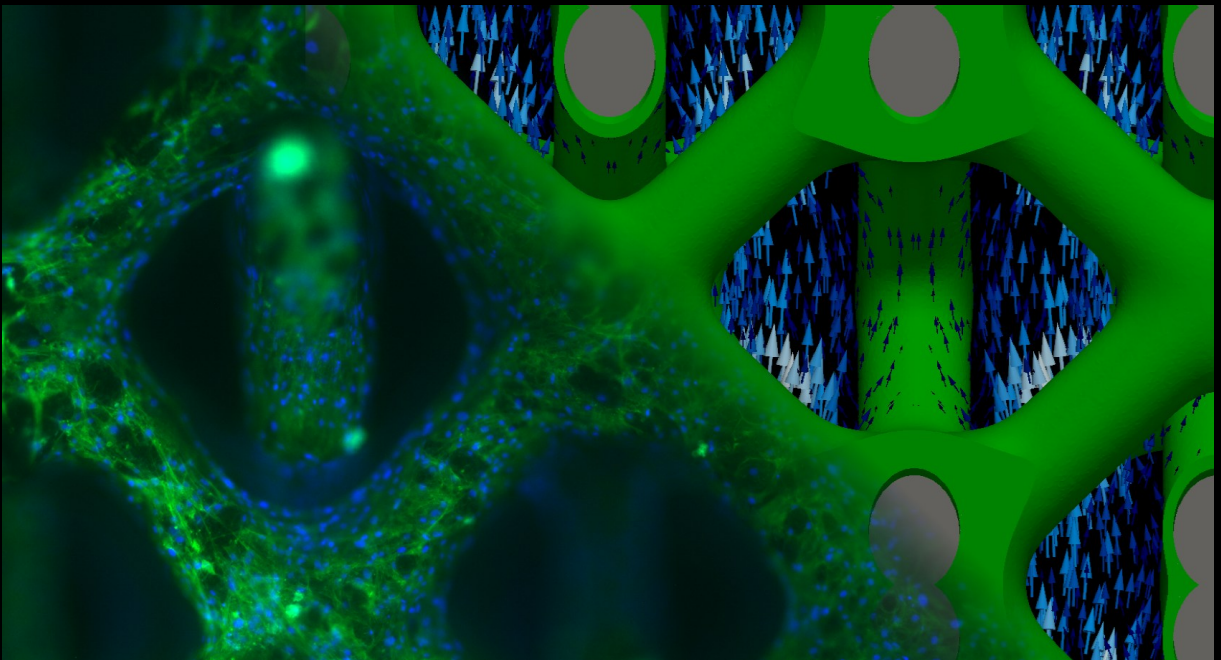


A multiphysics multiscale computational framework for the simulation of perfusion bioreactor processes in bone tissue engineering



Yann Guyot

Doctoral college of Aerospace
and Mechanical Engineering,
Faculty of Applied Sciences

Doctoral college of Aerospace and Mechanical Engineering,
Faculty of Applied Sciences.

A multiphysics multiscale computational framework for the simulation of perfusion bioreactor processes in bone tissue engineering

Author:

Yann Guyot

Supervisor:

Prof. Liesbet Geris

Jury Members:

Prof. Jean-Philippe Ponthot (ULg)

Prof. Maarten Arnst (ULg)

Prof. Davide Ruffoni (ULg)

Prof. Dominique Toye (ULg)

Prof. Jean-Marie Aerts (KU Leuven)

Prof. Hans Van Oosterwyck (KU Leuven)

Prof. Eirini Velliou (University of Surrey)

Dissertation presented in partial
fulfilment of the requirements for
the degree of Doctor in
Engineering Sciences



© ULG - Faculty of Applied Sciences Chemin des Chevreuils 1 BAT 52/3,
B-4000 Liège (Belgium)

Tous droits réservés. Aucun extrait de cet ouvrage ne peut être reproduit, ni saisi dans une banque de données, ni communiqué au public, sous quelque forme que ce soit, électronique, mécanique, par photocopie, film ou autre, sans le consentement écrit et préalable de l'éditeur.

All rights reserved. No part of the publication may be reproduced in any form by print, photoprint, microfilm or any other means without written permission from the publisher.

REMERCIEMENTS

Je tiens tout d'abord à remercier ma directrice de thèse, Liesbet Geris, pour la confiance qu'elle m'a accordée tout au long de ces quatre années, pour la qualité de ses enseignements en termes de biologie et de bio-ingénierie, pour m'avoir encouragé à participer à un maximum de conférences internationales, enrichissant ainsi mon niveau d'anglais et mes compétences en communication. Outre son appui scientifique, je voudrais particulièrement la remercier de m'avoir permis de travailler à mon rythme, d'avoir compris lorsque j'avais besoin de rentrer en France, de m'avoir laissé travailler du lieu de mon choix lorsque c'était possible, et d'avoir fait preuve de bienveillance à mon égard.

Je remercie également les professeurs Jean-Philippe Ponthot et Maarten Arnst de l'Université de Liège, pour avoir fait partie de mon comité de thèse et pour m'avoir apporté de précieux conseils. Je remercie également Prof. Dominique Toye d'avoir accepté de faire partie des membres du jury de cette thèse. I also would like to thank Prof. Jean-Marie Aerts and Prof. Hans Van Oosterwyck from KU Leuven, Prof. Davide Ruffoni from ULg and Prof. Eirini Velliou from University of Surrey for being part of my jury.

I want to say how very grateful I am to my friend Ioannis Papantoniou for his very useful advices, for always providing suggestions for the model, for his non negligible help for paper writing but also for all these nice moments and discussions around a beer. I also want to thank my friend Bart Smeets, it was a real pleasure to develop a model together. I also would like to thank all my colleagues from the Biomechanics Research Unit, here in Liège; Morgan, pour m'avoir supporté pendant ces quatre années; Varun, for having been a good friend but also my best english teacher so far; ainsi que Mohammad et Sébastien. I also would like to thank all my

colleagues from Prometheus in Leuven and the people of the bioreactor bench; Toon, I will always be your cells and you will always be my scaffold; Maarten, for having conducted essential experiments for models calibration; Gabriella, Niki, Guillaume, Akash, Hiroki, Tim, Johan, Aurélie, Inge and all the others for their contributions and every pleasant evenings in Leuven. Je remercie également Charles Dapogny pour m'avoir cédé les codes des ses programmes *mshdist* et *mmg3d-v5*.

Je tiens aussi à remercier les membres de ma famille; mes parents et mes grands-parents pour m'avoir soutenu depuis le début de mes études, ma tatie Marie-Pierre pour son soutien à la fois psychologique (et non, ça n'a rien à voir avec ce qui est à la campagne) mais aussi matériel quand ce fut nécessaire, ainsi que mes deux petits frères Damien et Cédric. Merci aussi à Thibaud pour nos longues conversations philosophiques et son soutien sans faille. Merci aussi à Virginie (ma petite gerbille) pour avoir toujours été à mes côtés. Merci aussi à Patrik pour nos sympathiques délires. Thanks also to James for all our nice moments. Je remercie aussi chaleureusement tout mes potes en France pour leurs jugements éclairés, nos nombreux fous rires, d'être on ne peut plus réceptifs à mes insanités, d'avoir su être là quand il le fallait, enfin tout simplement pour être là depuis si longtemps et de le demeurer. Merci à Anne et Babar pour m'avoir fait l'insigne honneur de me designer comme parrain de leur fils Marceau à une période ou rien ne pouvait me faire plus plaisir. Merci aussi à Lydia et Bichon ainsi qu'à Catherine et Jean-Marie pour s'être intéressés à ce que je faisais et pour toujours aussi bien nous accueillir chez eux.

Et pour finir, un petit clin d'œil à Marceau, Albane, Théa et Melina.

Yann
Décembre 2015, Liège

ABSTRACT

Bone tissue engineering is an interdisciplinary field that combines principles of life sciences and engineering in order to produce biological constructs that are able to heal, improve or replace damaged bone tissue. Despite an increasing amount of research, the field still suffers from a lack of reproducibility and quality control. In order to tackle these issues, process engineering and more precisely computational models can help to understand, predict and optimize the complex processes occurring during *in vitro* neotissue formation. In this thesis, the added value of computational modeling in the framework of bone tissue engineering was investigated at different length scales.

In the first chapter of this thesis, a three dimensional computational fluid dynamics (CFD) model of the whole scaffold and the bioreactor perfusion chamber was developed. Experimental data showed that scaffold location significantly affected cell content and neotissue distribution. Different successive positions of the empty scaffold were tested computationally and the optimal position was estimated *in silico* for different flow rates. The computational studies were compared to bioreactor experiments for two different scaffold positions at a specific flow rate. These results show that combining experimental characterization of neotissue formation with computational models for process optimization, can lead to bone tissue engineering constructs with improved quality attributes.

In the second part of this thesis, a model capturing neotissue growth on three dimensional structures was progressively developed. The Level Set Method was used to represent the curvature-dependent growth kinetics. This initial model was corroborated with previously obtained data for static culture experiments. Subsequently, a description of fluid flow was added to the

model in order to assess the local wall shear stress acting on the neotissue in perfusion conditions and to investigate the effect of these stresses on the neotissue growth rate. Finally, equations corresponding to mass transport of metabolic species were added to the model to quantify oxygen, glucose and pH, and their (positive or negative) effect on neotissue growth. Results from previously executed experiments were used to calibrate the model and dedicated experiments testing the validity of the model predictions are ongoing.

In the last part of this thesis, the flow induced mechanical stimuli on a cell attached to a three dimensional scaffold inside a perfusion bioreactor were investigated in greater detail. Hereto, a novel application of the Immersed Boundary Method was developed, where a single cell is represented as a deformable body embedded in a fluid environment. The model was able to investigate crucial physical parameters such as cell displacement and cortical tension due to flow and wall shear stress at the level of a single cell.

In conclusion, this PhD thesis shows the potential of using computational models as a tool for studying perfusion bioreactors processes at various length scales and demonstrates how these models can aid in the achievement of robust bioprocess control for regenerative medicine applications.

CONTENTS

Remerciements	i
Abstract	iii
List of figures	vi
List of tables	vii
List of abbreviations	ix
List of symbols	x
I Bioreactor chamber scale	1
II Neotissue scale	3
1 An <i>in silico</i> model to capture spatiotemporal stem cell growth kinetics in dynamic culture environments: incorporation of physicochemical parameters.	5
1.1 Introduction	6
1.2 Methods	8
1.2.1 Neotissue growth	8
1.2.2 Fluid flow equations	9
1.2.3 Nutrients and waste transport	10

1.2.4	Growth velocity expression	11
1.2.5	Initial and boundary conditions	13
1.2.6	Optimal medium refreshment	15
1.2.7	Experimental set-up and data analysis	15
1.3	Results	18
1.3.1	Experimental validation of the model	18
1.3.2	Scaffold geometry influence	18
1.3.3	Bioreactor flow rate influence	21
1.3.4	Intelligent medium refreshment procedure	22
1.4	Discussion	24
 III Single cell scale		27
 References		29
 Appendix A Reinitialization of the Level-Set with <i>mshdist</i>		49
 Appendix B Triply periodic minimal surface scaffold generation		51
 Appendix C Algorithm for model presented in chapter 7		53
 Appendix D Deformable cell model		55
D.1	Elastic model of the cortex	55
 Curriculum Vitae		59

LIST OF FIGURES

1.1	Schematic representation of the bioreactor.	16
1.2	Scaffold geometries investigated in this study.	17
1.3	Experimental data versus numerical results.	19
1.4	Spatial distribution within neotissue of pH and (oxygen). . .	20
1.5	Percentage of predicted scaffold filling (NV/AV) over time for every geometrical configuration.	21
1.6	Neotissue production over time for different bioreactor flow rates.	22
1.7	3 days medium refreshment compared to optimal medium refreshment.	23
A.1	Illustration of the reinitialization of the level-set with <i>mshdist</i>	50
B.1	Overall process to generate the <i>G7</i> scaffold and computational domain	52
C.1	Algorithm for model presented in chapter 7	54

LIST OF TABLES

1.1 Overview of all parameter values used in this study. 14

LIST OF ABBREVIATIONS

2D	two-dimensional
3D	three-dimensional
ATMP	advanced therapy medicinal product
BMP	bone morphogenetic protein
BTE	bone tissue engineering
Ca ²⁺	calcium ion
CaP	calcium phosphate
CE-nanoCT	contrast enhanced nanofocus X-ray computed tomography
CFD	computational fluid dynamic
DCR	diffusion-convection-reaction
ECM	extracellular matrix
FGF	fibroblast growth factor
hPDC	human periosteum derived stem cell
LSM	level set method
MSC	mesenchymal stem cell
ODE	ordinary differential equation
PDE	partial differential equation
TE	tissue engineering
TRL	technology readiness level
VEGF	vascular endothelial growth factor

LIST OF SYMBOLS

A_G	neotissue growth velocity constant
α_i	shear stress value thresholds
C_i	metabolites concentration
δ	micro neotissue pore size
δ_p	dirac function
φ	level set function
φ_{cell}	cell density
Γ	neotissue/void interface
Γ_{cell}	lagrangian representation of single cell
K_0	neotissue permeability
H	heaviside function
κ	mean curvature
μ	water viscosity
\mathbf{n}_Γ	neotissue surface normal
Ω_v	void domain
Ω_{nt}	neotissue domain
P	pressure
ψ	neotissue porosity
Q_i	perfusion bioreactor flow rates
ρ	water density
T	cortical tension
τ	wall shear stress
τ_{in}	inside neotissue wall shear stress
\mathbf{v}_G	neotissue growth velocity vector
V_G	neotissue growth velocity magnitude

CHAPTER 1

GENERAL INTRODUCTION

Bone is an intelligent material that is capable of load adaptation and scarless healing. However, sometimes the healing process does not lead to a successfully regenerated bone defect. In such cases, treatment strategies such as the use of living implants created from the patients' own cells might provide a good alternative to classical orthopaedic interventions. It is in this context of bone tissue engineering that this PhD is situated. The first chapter of this PhD dissertation provides a general introduction into the biological and engineering concepts that are needed to understand the following chapters. It starts with an introduction to general bone biology including structure, formation and repair, followed by an introduction to bone tissue engineering. The chapter continues with an overview of specific bioprocess engineering concepts related to bone tissue engineering and ends with an overview of computational tools used in the field of bone tissue engineering.

1.1 Bone structure and function

The skeleton is a rigid structure allowing the stability of the body, providing a structure to support, protect muscles and soft organs, serves as a calcium storage and is a blood cells source (from the marrow). This essential structure is composed of more than 270 bones in the human toddler, resulting due to fusion, into a total amount of 206 bones in the adult human skeleton. Depending on their function, bones can take different shapes, mostly divided into long (e.g. femur), short (e.g. the bones making up the

wrist and ankle) and flat bones (e.g. the ribs). Some bones are not part of these three families and are called irregular bones, such as the vertebrae that have a supporting role by constituting the spine as well as a protective role by surrounding the spinal cord. Most of the previously described bones show a similar structure. At the macroscopic scale, two types of bone tissue can be distinguished (see Fig. 1.1): the outer part, called cortical (compact) bone, providing stiffness and mechanical resistance, and the inner part, called trabecular (spongy or cancellous) bone consisting of a porous structure of interconnected trabeculae forming a host for nerves, blood vessels and marrow. Both cortical and trabecular bone are composed of collagen fibres (providing resilience) and mineral (providing rigidity). Bone tissue contains four types of cells: bone lining cells, osteoblasts, osteoclasts and osteocytes that all have a specific role (Hall, 2007). Osteoclasts are giant polynuclear cells (100 μm diameter in average) that are responsible for bone resorption. Osteoblasts are mononuclear differentiated mesenchymal stem cells (MSCs), they are responsible for new bone formation via deposition of collagen type 1 forming the osteoid. The third type of cells is the osteocytes, which are matured-osteoblasts that have been trapped in their own mineralized matrix, they act as sensors of mechanical stimuli and regulate the bone remodeling process by recruiting necessary osteoblasts or osteoclasts via biochemical signal transduction. Due to their shape (star-like), they form an interconnected network within the bone matrix. The last type of cells are the lining cells and like osteocytes, they are former osteoblasts however they have not been buried in the newly formed bone matrix, but remain flattened against the bone surface. They can be activated when new bone formation activity (such as after fracture) is required.

1.2 Bone formation and repair

1.2.1 Bone formation

Two different foetal bone development mechanisms can be distinguished: the endochondral (indirect) ossification and the intramembranous (direct) ossification (Shapiro, 2008). Intramembranous ossification mainly occurs in the formation of flat bones such as the skull and the pelvis. The MSCs form a cluster together and directly differentiate into osteoblasts. Then, due to this differentiation, they start to deposit collagen to form osteoid (non-mineralised bone extracellular matrix) that is subsequently mineralized as a result of the deposition of calcium salts in the collagen matrix. This process is called direct bone formation because of the direct differentiation

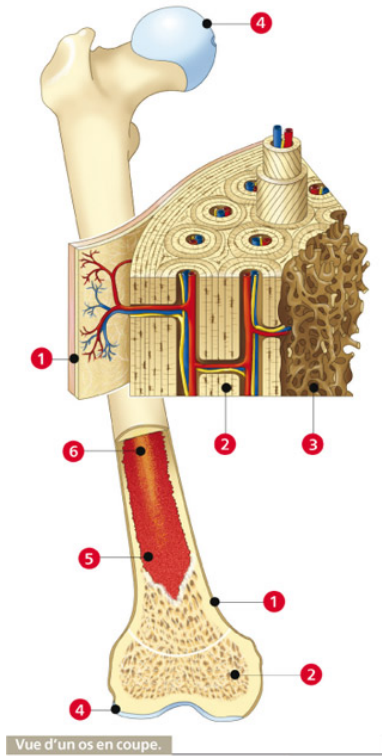


Figure 1.1: Schematic representation of a long bone. (1) Periosteum, (2) Cortical bone, (3) Trabecular bone, (4) Articular cartilage, (5) Red marrow, (6) yellow marrow. (<http://www.lecorpshumain.fr/corpshumain/1-os.html>)

of MSCs progenitor cells into the bone forming osteoblasts. When this direct differentiation does not take place and bone formation only occurs through an intermediate step of cartilage formation, we talk about secondary bone formation or endochondral ossification, the most common bone formation pathway, occurring mostly in long bone development. In this type of ossification, the clustered MSCs start to differentiate into chondrocytes (cartilage cells) and form a cartilaginous template. The differentiated cells within this template will start to proliferate, increasing the size of the construct and deposit a cartilage matrix. After some time, cells located in the centre of the construct will become hypertrophic, inducing blood vessels invasion. Due to the income of oxygen from blood flow, the hypertrophic

core is gradually broken down and replaced by bone and bone marrow, forming the so called primary ossification centre. Later, the epiphyseal parts are also invaded by blood vessels, initiating a second zone of bone formation, called the secondary centre of ossification. The remaining chondrocytes between the primary and secondary ossification centres, are organized in the growth plate that consists of different layers of cells in different stages of chondrogenic differentiation. The cells in the proliferative zone, keep proliferating and gradually move through the pre-hypertrophic to the hypertrophic zone, leading to a continuous longitudinal bone growth until, at the end of adolescence, hormonal changes close the growth plate. (Lenas and Luyten, 2011).

1.2.2 Bone healing

One of the most remarkable properties of bone, is its capacity to heal from injuries without any scars, which is not the case for most of the other tissues. The underlying mechanisms of bone healing are related to the previously described bone formation processes, with cell recruitment, proliferation and differentiation regulated by biochemical factors as well as mechanical factors active at the fracture site. The bone fracture repair in human can be divided into three different phases: the inflammatory phase, the reparative phase and finally the remodeling phase. During the first 5 days, the inflammatory phase consists of the formation of a hematoma within the fracture gap and the recruitment of MSCs, that, under the influence of growth factors such as bone morphogenetic protein (BMPs) and transforming growth factors $\beta 1$ (TGF- $\beta 1$) (BighamaSadegh and Oryan, 2014; Lieberman et al., 2002) and hypoxia due to the damaged blood vessels, will differentiate into chondrocytes. These chondrocytes will deposit cartilaginous matrix, providing a mechanical stabilization of the callus and marking the start of the reparative phase. Reminiscent of the developmental bone forming processes, the chondrocytes present in the callus will become hypertrophic, leading to the invasion of the fracture zone by blood vessel, inducing the formation of bone. This phase, depending on the size of the bone, takes one to two months. In the final remodeling phase, which is also the longest phase (several months to one year), the callus is progressively remodeled in order to retrieve the original pre-fracture geometry and structure (Papadimitropoulos et al., 2015). This indirect type of bone healing occurs in case of non-rigid fracture stabilization.

1.2.3 Non-healing defect

In 5% to 10% of bone fracture cases, the process of healing described above does not occur normally, leading to a delay in the repair or even to a non-union (Bhandari and Jain, 2009). These problems might come from several factors such as trauma, infection or skeletal abnormalities. The most common treatment strategy nowadays remains autologous bone grafting, where a sample of bone is harvested from the patient itself (for example from the iliac crest, due to the easily accessible location and the relatively large amount of bone tissue that can be harvested) and is further transplanted in the non-healing site (Jakob et al., 2012). However, this technique shows some important limitations such as donor site morbidity, increased risk of site infection and increased blood loss and surgery time (Arrington et al., 1996; Keating and McQueen, 2001). The use of synthetic materials as substitute for the previous limitations is explored, but their lack in terms of osteogenic (no cells seeded) and osteoinductive (no growth factors) properties reduces their healing potential. Due to lack of current ideal treatment options for non-healing fractures, research in past decades has been focusing on a novel and efficient strategy, that of bone tissue engineering (TE).

1.3 Bone tissue engineering

Tissue engineering is a strongly interdisciplinary field that combines principles and techniques of engineering, life sciences and chemistry in order to develop functional biological products that are able to heal, improve or even replace damaged tissues (Lanza et al., 2011). The main principle of TE is based on the elaboration of three dimensional (3D) *in vitro* constructs by combining scaffolds, cells, and biologically active molecules (Lanza et al., 2011). The most common paradigm implies five main steps (see Fig. 1.2):

1. Identification and harvesting of the progenitor cells from the patient
 2. Cellular proliferation
 3. Association of the cells to a scaffold (biocompatible material) as well as addition of suitable growth factors
 4. Expansion of the 3D construct (materials, cells, growth factors), with the potential help of a bioreactor system
 5. Implantation of the final biological construct into the patient.
-

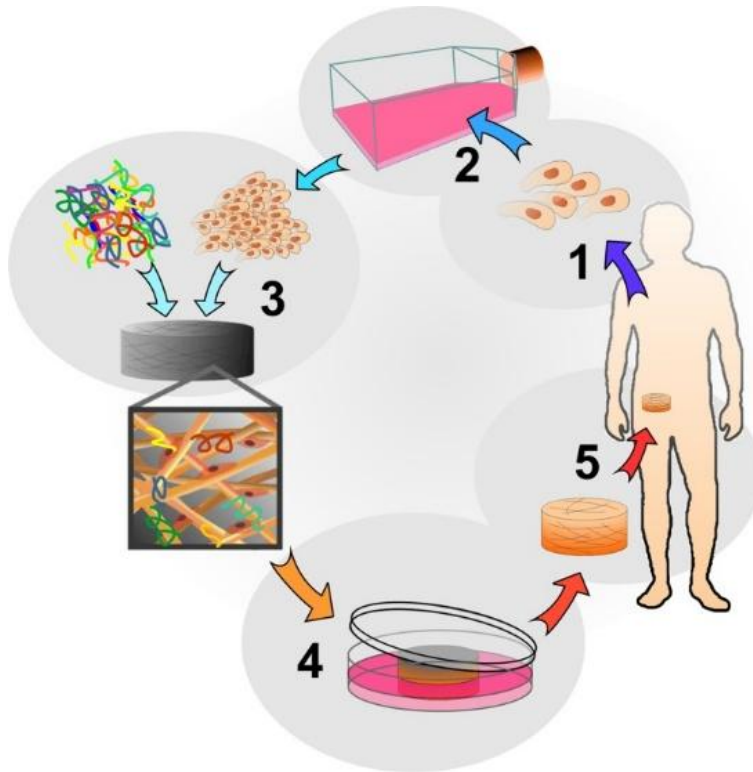


Figure 1.2: The classical Tissue Engineering paradigm
(<http://biomed.brown.edu>)

In bone tissue engineering (BTE), designing a relevant therapeutic bio-product includes three essential properties: osteogenicity, osteoconductivity and osteoinductivity (Shrivats et al., 2014). The first one implies that the cells in the construct are able to undergo osteogenesis, the biological process where osteoprogenitor cells such as MSCs differentiate into osteoblast or chondrocytes that further follow the above described bone regeneration cascades. Osteoconduction refers to a passive property of the biomaterial showing its ability to conduct bone formation on its surfaces. Finally, osteoinduction is related to the ability of the product to trigger osteogenesis, i.e. recruiting the osteoprogenitor cells (*in vivo*) as well as providing them suitable mechanical and biochemical stimulation for differentiation and matrix deposition. In order to create a viable tissue-engineered product, BTE is based on three key elements: cells (osteogenic), 3D biomaterial (osteoconductive) and growth factors (osteoinductive).

1.3.1 Cells

In order to achieve the osteogenicity criterion of a tissue engineered construct, the choice of a suitable cell source is crucial. As mentioned earlier, the fracture healing process is initiated by the recruitment of undifferentiated cells (MSCs) that are triggered by mechanical and chemical signalling to differentiate into osteo(chondro)genic cells in order to repair the fracture. Since tissue engineering has based its principles on mimicking (to a certain extent) that *in vivo* process, MSCs and their inherent multi-potency have extensively been used in BTE field (Dominici et al., 2006). Another reason for using progenitor cells is their ability for self-renewal, allowing them to expand *in vitro* and produce a large amount of available cells. Finally, using stem cells instead of differentiated cells such as osteoblast makes isolation and harvesting from the patient more feasible. Indeed, the extraction of osteoblast would implicate a bone biopsy, creating another bone defect, while MSCs can be isolated from the fracture site directly, from the bone marrow or the periosteum, also requiring a surgery, but not as invasive as for a bone piece harvest (Eyckmans and Luyten, 2006; van Gastel et al., 2012; Zhang et al., 2008).

1.3.2 Growth factors

As previously described, progenitor cells are widely used in the tissue engineering field, but biochemical cues are sometimes necessary to trigger the osteogenetic lineage and make stem cells differentiate into suitable bone forming cells. This osteoinductivity is generally (but not always) conducted with help of growth factors. Growth factors can be defined as protein-based agents that enter in the regulation process of the cell's behaviour. Several examples of growth factors included in bone generation and regeneration can be found, such as bone morphogenetic proteins (BMPs), fibroblast growth factors (FGF) and vascular endothelial growth factor (VEGF). A key aspect in bone engineering is to be able to efficiently deliver the growth factors with applicable procedures (Shrivats et al., 2014). One of the current delivery procedures consists of dip-coating the scaffold with growth factors, allowing gradient formation due to diffusion, and control the evolution of released amount inside the scaffold (Martin et al., 2004). Another technique (for *in vitro* delivery) consists in continuously providing the proteins through the use of a bioreactor system (Martin et al., 2004).

1.3.3 Scaffolds

The last aspect in the classical tissue engineering paradigm is the osteoconductivity, the ability to physically conduct bone formation. As explained earlier, natural bone tissue consists of cells embedded in an extracellular matrix. The role of the matrix is to provide a three dimensional structure for cells adhesion as well as proteins and nutrients supply, thus offering to cells a specific biomechanical and biochemical microenvironment. Consequently, providing an *in vitro* template (scaffold) will support and stimulate bone generation by providing the right microenvironment that allows and enhances cell proliferation and extracellular matrix deposition. There are several biomaterial properties required in order to conduct bone tissue regeneration. The scaffold has to be made of a biocompatible material, allowing cells to adhere to the surface. The biocompatibility includes the ability of the scaffold to, after eventual *in vivo* implementation, not being reject by the immune system. Another requirement is related to the scaffold architecture, which has to have interconnected pores to ensure cell proliferation and migration as well as subsequent ECM deposition. The porosity of the scaffold also has to permit diffusivity of chemical species to allow waste removal and nutrient supply, and, permit vascular invasion after implantation (Hollister, 2005; Hutmacher, 2000). Scaffolds can be made of polymers (Liu and Ma, 2004), metals (Sonnaert et al., 2015) or ceramics (Habraken et al., 2007), such as Calcium-Phosphate (CaP) based biomaterials (Bose and Tarafder, 2012). This latter type of biomaterials is designed to be fully replaced by cells and tissue. Although the scaffold has a primary role of supporting the neotissue¹ formation (osteoconductivity), its ability to stimulate the bone formation process (osteoinductivity) is also crucial, meaning that the scaffold should be designed in order to supply required cues for neotissue formation leading to additional different requirements. It has been shown that the scaffold stiffness has a real influence on cellular response due to external loading (Hutmacher et al., 2001). The biomaterial surface topography also has an important effect on cells fate, inducing stem cell differentiation towards the osteogenic lineage. The pore shape (via its influence on local wall shear stress experience by cells in the presence of fluid) and local curvature of the substrate surface has recently been shown to influence and, under some conditions, enhance bone formation (Knychala et al., 2013; Rumpler et al., 2008). These key geometrical aspects will be widely discussed in this PhD dissertation.

¹Neotissue is a term used in this PhD dissertation to indicate the combination of cells and the extracellular matrix they produce during culture.

1.4 Process engineering in tissue engineering

Despite the large amount of research and progress in the TE field, most of the studies are mainly focusing on the biological aspects to the detriment of the engineering part. Nowadays, most of the key steps involved in the elaboration of a functional autologous TE construct like cell isolation, expansion and 3D cultivation are performed manually and independently from each other, resulting in an important resources cost (both human and financial) and limiting the future translation of the field from the bench towards clinical application. To achieve a desired Advanced Therapy Medicinal Product (ATMP) that is approved by the regulatory agencies in Europe and elsewhere, all the aforementioned key steps must have their own dedicated processes. These processes must be set up in such a way as to ensure robustness, reproducibility, path-dependence (where a particular state depends on the preceding ones) and (semi-)autonomous, making the whole process more reliable (Archer and Williams, 2005). The setting-up of these processes will include the transition from the current laboratory-based manual interventions during culture to (fully) automated and controlled environments incorporating engineering technologies and tools, such as sensors (Lambrechts et al., 2014), bioreactors (Gaspar et al., 2012) and models (Geris, 2013).

1.4.1 Bioreactors

Static cell culture for 3D scaffolds shows several limitations. In static conditions, the supply of nutrients such as oxygen and the removal of waste products such as lactate are only performed by diffusion transport, leading to low (or high) concentrations of these products in the center of the scaffolds. This heterogeneous distribution of factors that are essential for proliferation or differentiation might negatively affect the final construct as it might lead to a non-homogenous neotissue distribution (Botchwey et al., 2003; Stiehler et al., 2009). This could in turn affect the maximal scaffold dimensions that can be allowed in culture, indeed, the more important the scaffold dimensions are, the more detrimental the effect of static culture conditions on the construct quality will be. To tackle this issue, the use of bioreactors has widely been accepted in the TE field. A bioreactor is a device or a system meant to grow cells or tissues in the context of cell culture. Dynamic bioreactor settings (such as perfusion) allow for a reduction of the side effects commonly associated with static culture (Volkmer et al., 2008). First of all, the mass transport is no longer only diffusion dependent but

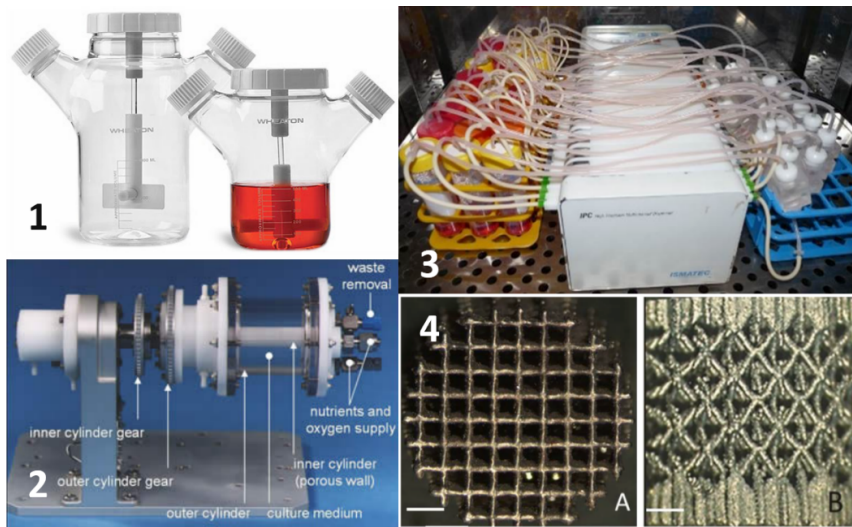


Figure 1.3: Bioreactors and scaffold: **(1)** Spinner flasks (<https://www.sks-science.com>). **(2)** Rotating wall vessels (<http://www.ukessays.com>) **(3)** Perfusion bioreactor used in this PhD work (**(left)**, medium reservoir; **(middle)** pump; **(right)** chamber) **(4)** Diamond shaped scaffold (**(A)** top view; **(B)** side view)

is increased and optimized due to fluid flow advection, resulting in a more homogenous distribution of nutrients and waste. Secondly, due to their dynamic environment, they will provide mechanical stimuli to the cells in the bioreactor through the fluid flow induced shear stress (Yeatts and Fisher, 2011).

A wide variety of bioreactor types has been proposed in the literature up till now, such as perfusion bioreactors, spinner flasks or rotating wall vessels (Sikavitsas et al., 2002). Spinner flasks consist of a recipient containing the scaffold and a stirring element allowing mass transport into the construct due to fluid rotation. Despite the fact that spinner flasks have shown beneficial effects on human MSCs (hMSCs) differentiation toward osteoblasts (Kim et al., 2007), this type of device has an important downside and that is that the size of the container as well as the rotation speed may induce turbulent flow, leading to high and uncontrolled shear stress distribution within the scaffold which in turn might have a detrimental effect on cell behaviour and neotissue growth (Meinel et al., 2004). Rotating wall vessels are made of two concentric cylinders. The outer one, containing culture medium and scaffolds is rotating horizontally around its axis. The

inner rotating wall is static and provides gas exchanges. This type of bioreactor has an advantage over the spinner flasks as not only they are able to provide sufficient oxygen to the cells, but they also do not induce turbulence. However, due to the large amount of constructs that is sometimes present in a single culture system, there are frequent collisions between the constructs and between the constructs and the rotating chamber walls, resulting in cell damage, detachment and possible matrix production (Yu et al., 2004). The last type of bioreactor presented in this introductory chapter are the perfusion bioreactors in which the scaffold seeded with cells is continuously or non-continuously perfused throughout the culture process. Perfusion bioreactors have properties that allow to address the problems indicated for the spinner flasks and rotating wall bioreactors (Zhao and Ma, 2005). The most common configuration of this type of bioreactor, and the one used in this PhD dissertation, consists of a culture chamber that contains the scaffold, a tubing circuit that connects the culture chamber to the culture media reservoir and a pump that will circulate the fluid through the entire bioreactor. Within this type of device, the cell microenvironment can be controlled by controlling the flow through the construct affecting nutrient supply and waste product removal. Moreover, perfusion of the neotissue will lead to changes in the flow-induced shear stress levels within the neotissue. The aspect of controlling the mechanical stimuli that cells will experience during the culture process can be important as it has been shown that it could affect functions such as proliferation and migration (Yeatts and Fisher, 2011). In the skeletal TE filed, this mechanical aspect can be very important as it can determine cell's lineage commitment, i.e. stem cell fate (chondrogenesis, osteogenesis, ...) (Song et al., 2013) or enhance extra-cellular matrix deposition (Papantoniou et al., 2013). Flow induced shear stress might depends upon several parameters, the most obvious being the pump flow rate that directly controls the fluid velocity. However, also the location of the scaffold within the perfusion chamber will have an effect on the flow profile and hence on the shear stress. Other essential parameters are the scaffold geometry, its porosity, pore size and pore shape which will significantly influence the inner flow pattern and thus the local shear stress distribution and magnitude. Finally, the stimulus experienced by the cells depends on their location within the construct. A cell located at the surface of the neotissue will not sense the same mechanical stimuli than one embedded in its own ECM inside the neotissue, and a cell attached to a scaffold strut perpendicular to the flow profile will sense more stress than one attached on a parallel strut.

In order to correctly assess the local (biological and mechanical) environment of cells during dynamic bioreactor culture and predict its effect on the neotissue growth, it is essential to develop computational tools that capture the biology and the mechanics of neotissue growth in dynamic cultures.

1.5 Computational tools for TE

Manufacturing reproducible and reliable products requires a stringent quality control system that is an integral part of the design process (quality by design). This is currently still a challenge due to a number of factors, amongst which is the intrinsic uncertainties resulting from cell's sensitivity to perturbation in the culture microenvironment. Mathematical models can be used to untangle the underlying mechanisms in every culture processes, for example intracellular molecular regulation determining cell fate, full tissue mechanics or environment control and be an *in silico* pre-testing tool for experiments. This section will discuss the state of the art in computational modeling for scaffolds and bioreactors process design across different length scales, starting from the whole culture chamber to the single cell behaviour under flow conditions.

Models capturing the way cells are growing on 3D surfaces and subsequently form a three dimensional biological construct are interesting tools to optimise the scaffold design. In (Bidan et al., 2012; Dunlop et al., 2010), the authors have depicted the importance of the scaffold pore geometry on the cells' behaviour and have developed models able to predict the evolution of the neotissue in 2D based on the local curvature of the tissue. As a consideration of third dimension is crucial to understand complete mechanism of neotissue growth in 3D structures, (Bidan et al., 2013) have extended their curvature-based model to 3D. The main disadvantage of the technique employed in their model is that the neotissue interface is treated explicitly, reducing the possibility to deal with complex geometries and eventual complete scaffold pore filling. Computational models have been used to investigate various aspects of the design of perfusion bioreactor systems as well as the tissue formation during dynamic culture within these systems. In (Olivares and Lacroix, 2012) and (Melchels et al., 2011), the authors have developed a computational model for the prediction of the spatial distribution of cells seeded onto different scaffold geometries

in a perfusion set-up. This model allows to investigate and optimise cell seeding efficiency on porous scaffolds which is an essential step in overall process of tissue formation inside the scaffold. Most computational models that have been presented in this context are based on Computational Fluid Dynamics (CFD) for determining the fluid induced wall shear stress on scaffold surface and attached cells, since mechanical stimuli have an important influence on cell proliferation and differentiation, as discussed in the previous section. Most of this studies consider an empty scaffold placed in the perfusion chamber, where Stokes or Navier-Stokes equations (depending on the corresponding Reynolds number which is related to the flow rate and dimensions of the system) are numerically solved resulting in the spatial wall shear stress distribution estimation (Cruel et al., 2015; De Boodt et al., 2010; Jungreuthmayer et al., 2008; Milan et al., 2009; Olivares et al., 2009; Truscetto et al., 2011; Zermatten et al., 2014). Despite the fact that the local wall shear stress distribution on the scaffold is often used as a design criterion for optimising scaffold geometry, it has a real meaning only for early culture days. Indeed, the 3D cell and tissue growth taking place in the scaffold will significantly influence the flow profile and the related shear stress distribution. In several studies (Hossain et al., 2015; Lesman et al., 2010; Nava et al., 2013), authors try to tackle this issue by proposing a method where the neotissue is considered as a solid phase with no flow permitted. Although this is already an improvement, this approach neglects the importance of the flow through the porous neotissue which can have a very important effect on the embedded cells and therefore on the overall neotissue growth rate and quality of the resulting construct. In (Chapman et al., 2014; Hossain S, 2015; Nava et al., 2013) the authors introduce a model where the neotissue growth rate depends upon the computed shear stress, whereby there is a specific shear stress range where the growth is optimal and a maximal shear stress value beyond which no growth occurs anymore. A third factor, besides geometry and mechanics that has a key role to play in the optimisation of bioreactor and scaffold design, is mass transport. A relevant design should allow for the provision of nutrients such as oxygen and glucose in a sufficient amount and the removal of waste product such as lactate from the neotissue to offer an optimal microenvironment to the cells. The incorporation of such a mass transport model for metabolites is generally made through the addition into the growth or flow model of Partial Differential Equations (PDEs) describing the spatio-temporal evolution of these metabolites. The typical PDEs used for this category of problems are Diffusion-Convection-

Reaction (DCR) equations. These equations, governing how a specific species concentration is spatially and temporally evolving in a domain, are composed of a diffusion term (second derivative in space) for the diffusivity of the species, a convection term (first derivative in space) for advection of the species (advection from the fluid velocity in the bioreactor), a reaction term describing the consumption or production of the species by the cells, and occasionally includes an external source term. This type of model is being used more and more extensively in the TE field to study *in vitro* bone and cartilage tissue culture set-ups (Chapman et al., 2014; Demol et al., 2011; Hossain et al., 2015; Hossain S, 2015; Nava et al., 2013; Pearson et al., 2015; Williams et al., 2002). Understanding and modeling the different phenomena occurring in bioreactors at the tissue scale is essential to control the process of an *in vitro* tissue engineered product. However, studying the local mechanical and geometrical environment at the level of a single cell or a small collection of cells might provide added insights into the cells experience (and respond to) their microenvironment. Recent publications have presented models for single cell attached to a scaffold under flow conditions *in vitro* (Vaez Ghaemi et al., 2015; Zhao et al., 2014) and *in vivo* (Vaughan et al., 2014, 2015; Verbruggen et al., 2014). These models are based on a Fluid-Structure Interaction (FSI) algorithm, where the cell is a deformable solid body, embedded within a fluid domain.

All the studies described above show that computational tools are increasingly used in the field of process engineering for tissue engineering. However, most of these works focus on a single aspect (biological, mechanical, micro-environmental, etc...). In order to address this issue and to bring a true impact on the bioprocessing field, the development of models incorporating several aspects together should be done in an integrative manner with strong links between the modeling and experimental communities.

CHAPTER 2

HYPOTHESIS AND OBJECTIVES

In the previous chapter some general notions of bone biology and tissue engineering were introduced as well as the issues with the current challenges in bioprocessing of tissue engineering constructs. An interdisciplinary integrative approach is needed in order to bring the tissue engineering products from the bench to the bedside. This PhD focusses on the development of computational tools that can play an important role in this translational process. In the first section of this chapter, the general aim of this work is explained. Subsequently, specific research objectives are formulated to investigate the validity of the stated hypotheses. Finally a number of methodological aspects (experimental, modeling and implementation) of this PhD are highlighted.

All the work presented in this dissertation is part of Prometheus, the division of Skeletal Tissue Engineering of the KU Leuven. Being part of this interdisciplinary group has influenced many choices during the entire PhD process. One of these choices was the use of the perfusion bioreactor already available in the laboratory. Another one concerned the scaffold geometries used for testing the models. In different chapters of this dissertation, the chosen geometries correspond to those used in the experiments providing the data for model calibration.

2.1 General hypothesis

In order to achieve a functional *in vitro* engineered bone tissue for clinical applications in regenerative medicine, the entire BTE field needs to incorporate several manufacturing requisites such as monitoring, control and automation. Inspiring from chemical engineering that uses modeling as a technique for process design by predicting the behavior of a given system, computational models applied to tissue engineering applications can help to the transition towards a more intelligent control by providing tools to the operator for predicting and optimizing 3D cell growth, based on the integration of different dynamic microenvironment aspects. The general hypothesis underlying this work is that **computational modeling – through an integrative approach – is capable of making a substantial contribution to the introduction and implementation of bioprocess engineering concepts in regenerative medicine**. Therefore, the main objective of this PhD work was to develop computational tools to predict and optimize biological outcomes from dynamic cell culture on three dimensional porous scaffold. For this purpose, three different models at three different length scales were developed. First, a CFD model of the whole bioreactor chamber was developed to assess the optimal position of the scaffold in the perfusion chamber in order to maximize biological outcomes. Secondly, a tissue scale model was designed able to capture the neotissue growth over culture time on the scaffold in a perfusion bioreactor. Finally, a single cell scale model was developed to simulate cell mechanical response under flow conditions.

2.2 Specific objectives

In order to assess the abovementioned hypothesis, a number of specific objectives were formulated. These specific objectives are elaborated in each of the following chapters of this PhD thesis. In essence, this work can be divided in three different sections corresponding to the three different spatial scales considered: chamber scale (cm), neotissue scale (mm) and cell scale (μm) (see Fig. ??)

- **Development of a model to determine optimal scaffold positioning in the bioreactor chamber.** The positioning of the scaffold inside the bioreactor was investigated by means of a CFD model. The steady state Navier-Stokes equations were solved numerically on a domain (the chamber) containing an obstacle (the
-

scaffold). Different successive positions of the empty square-shape scaffold were tested with different flow rates. For each configuration, the average flow velocity across the scaffold was calculated, and, based on this calculation, the optimal position was estimated for different flow rates (chapter 3).

- **Development of a novel neotissue growth model on 3D structures in a perfusion bioreactor set-up.** A computational model for simulating neotissue growth inside 3D scaffolds was developed. The overall design of the model can be divided in four successive steps. (1) The use of the Level Set Methods to implement curvature-based neotissue growth on complex 3D structures (chapter 4). (2) The coupling of this growth model with fluid flow throughout

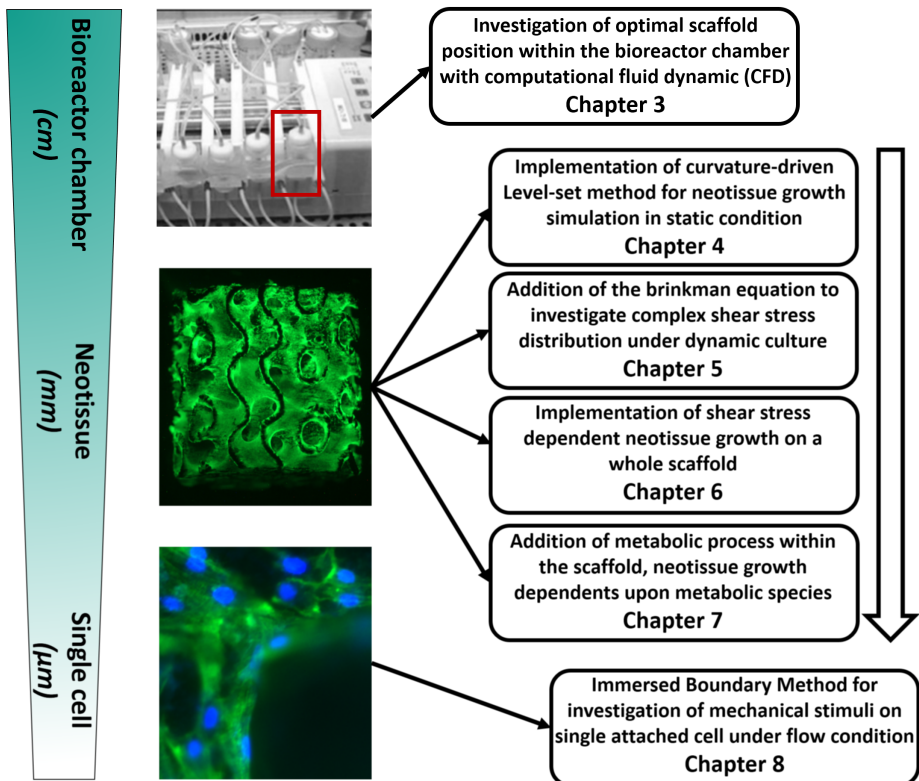


Figure 2.1: Schematic representation of the different scales and corresponding models presented in this PhD dissertation

the 3D structure, modeled by the Brinkman equation, in order to determine the wall shear stresses and the shear stress distribution throughout the neotissue (chapter 5). (3) Incorporation of the shear stress into the neotissue growth velocity (chapter 6). (4) Addition of a description of the metabolic activity inside the neotissue, affecting its growth rate (chapter 7). The complete model was used to *in silico* design an optimized scaffold geometry and optimized bioreactor settings (flow rate and refreshment rate) for maximal neotissue growth.

- **Development of a single cell model under flow conditions.** The effect of fluid flow on the deformation of single cells was investigated by means of a model coupling a computational model of cell deformation with a fluid solver through the Immersed Boundary Method (IBM). This model was used to investigate the mechanical stimuli caused by fluid flow at cell level (chapter 8).

2.3 Methodology

The integrative nature of the research described in this PhD thesis can be appreciated from the presence of both computational and experimental developments in the context of this study, as explained below.

2.3.1 Experimental aspects

Calibration and testing of the presented models was performed with the help of experimental data that was, partly, generated especially for the purpose of model validation by researchers from the Tissue Engineering Unit of the Skeletal Biology and Engineering Research Centre of the KU Leuven (I. Papantoniou, M. Sonnaert). The set-up used to generate this data consisted of a perfusion bioreactor in which cell-seeded titanium scaffolds were placed.

- **Cells.** The type of cells used in every experimental set-ups are human Periosteal Derived Cells (hPDCs), this candidate has been chosen for their pluripotency and their ability to form bone tissue engineered construct.
 - **Scaffold.** Titanium (Ti6Al4V) scaffolds were employed with two different regular pore shapes (square and diamond). The Ti6Al4V alloy (90% titanium, 6% aluminium, 4% Vanadium) is a clinically approved biomaterial used in many orthopaedic clinical applications.
-

The scaffolds were produced using a non-commercial, in-house-developed selective laser melting machine (S. Van Bael).

- **Bioreactor.** A perfusion bioreactor set-up was used, consisting of a chamber of 26 mm long, a culture medium reservoir of 12.8 ml, a peristaltic pump and tubing.

2.3.2 Modeling aspects

In order to realize the aforementioned objectives, a variety of computational techniques was used.

- **CFD Modeling.** To determine the optimal scaffold position inside the bioreactor chamber, the steady state Navier-Stokes equations were solved in a domain (the chamber) with an obstacle (the scaffold). Details and results for this model, along with experimental results are presented in chapter 3.
 - **Curvature-based neotissue growth model based on the Level Set Method.** The LSM was first introduced to track a moving interface between two different domains (Sethian, 1996). Due to its ability to capture, in a continuous manner, a moving interface on a computational mesh, this technique was employed to simulate the evolution of the interface between the neotissue and the void space. An additional advantage of the technique is its ability to deal with changes in interface topology, a possible phenomenon on complex 3D structures when two local neotissue surfaces merge together to form a single surface. The neotissue velocity was set to be dependent upon the local curvature on the surface. Details of this model as well as evaluation with experimental data are presented in chapter 4.
 - **Investigation of shear stress distribution during *in silico* neotissue growth.** The Brinkman equation was added to the curvature-based model in order to calculate the complex flow profile within scaffold pores. This equation allows to couple a Stokes regime (in the void) and a Darcy regime (in the neotissue, assumed to be a porous medium) in a configuration where the interface is not conform to the computational mesh. Two different shear stresses were estimated from the computational results, the wall shear stress acting on the surface of neotissue, and the shear stress occurring inside the neotissue on cells and matrix. This model is described in chapter 5.
-

- **Addition of the shear stress into the neotissue growth velocity.** The previously developed growth model was extended in order to include the computed surface wall shear stress into the growth velocity definition. The growth velocity was designed in order to be optimal within a specific range of shear stress values and zero in case of excessive values. The model was implemented on a entire scaffold with a diamond-shaped unit cell (chapter 6).
- **Addition of the metabolic activity into the neotissue growth velocity.** The previously developed model was completed with the integration of Diffusion-Convection-Reaction equations in order to take into account the metabolic activity occurring during dynamic culture. Equations for oxygen, glucose and lactate were added, and the previous curvature and shear stress based velocity was updated to take into account the detrimental effect on growth due to hypoxia, low glucose concentration or low pH value. This new model was tested on six *in silico* designed scaffolds (different triply periodic minimal surfaces) and was used to determine the optimal time point for medium refreshment during culture. This model is detailed in chapter 7.
- **Development of a single cell model under flow conditions.** In a collaborative effort with Bart Smeets (MeBioS, KU Leuven) a computational model of cell deformation was coupled with a fluid solver through the Immersed Boundary Method, where the cell, seen as a Lagrangian mesh, is immersed in Eulerian mesh where the flow is calculated. Four different realistic cell geometrical configurations were tested on different locations within the scaffold. Four mechanical measures were computed (total displacement, tension, pressure and wall shear stress) from the simulation results. Numerical details and results of this collaborative model are presented in chapter 8.

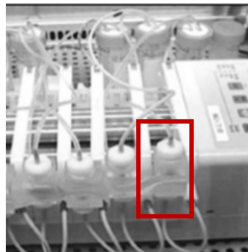
2.3.3 Implementation aspects

All the models presented in this PhD thesis (LSM, Navier-Stokes, Stokes, Brinkman, DCR equations) were implemented with finite element method with help of the free partial differential equation solver FreeFem++ (Hecht, 2012). The computational model for single cell deformation was implemented in DEMeter++ (Tijssens et al., 2003).

Part I

Bioreactor chamber scale

Bioreactor chamber
(cm)



Investigation of optimal scaffold
position within the bioreactor chamber
with computational fluid dynamic (CFD)
Chapter 3

CHAPTER 3

SPATIAL OPTIMIZATION IN PERFUSION BIOREACTORS IMPROVES BONE TISSUE-ENGINEERED CONSTRUCT QUALITY ATTRIBUTES

Ioannis Papantoniou^{1,2}, Yann Guyot^{1,3}, Maarten Sonnaert^{1,4}, Greet Kerckhofs^{1,3,4}, Frank P. Luyten^{1,2}, Liesbet Geris^{1,3}, Jan Schrooten^{1,4}

¹ Prometheus, Division of Skeletal Tissue Engineering, KU Leuven, Onderwijs en Navorsing 1 (+8), Herestraat 49 - PB813, B-3000, Leuven, Belgium.

² Skeletal Biology and Engineering Research Center, KU Leuven, Onderwijs en Navorsing 1 (+8), Herestraat 49 - PB813, B-3000, Leuven, Belgium.

³ Biomechanics Research Unit, Universite de Liège, Chemin des Chevreuils 1 - BAT 52/3, B-4000 Liège, Belgium.

⁴ Department of Metallurgy and Materials Engineering, KU Leuven, Kasteelpark Arenberg 44 – PB 2450, B-3001, Leuven, Belgium.

Adapted from: Papantoniou I., Guyot Y., Sonnaert M., Kerckhofs G., Luyten F. P., Geris L., and Schrooten J. (2014). **Spatial optimization in perfusion bioreactors improves bone tissue-engineered construct quality attributes.** *Biotechnology and Bioengineering*, 111(12), 2560-2570

3.1 Abstract

Perfusion bioreactors have shown great promise for tissue engineering applications providing a homogeneous and consistent distribution of nutrients and flow-induced shear stresses throughout tissue-engineered constructs. However, non uniform fluid-flow profiles found in the perfusion chamber entrance region have been shown to affect tissue-engineered construct quality characteristics during culture. In this study a whole perfusion and construct, three dimensional (3D) computational fluid dynamics approach was used in order to optimize a critical design parameter such as the location of the regular pore scaffolds within the perfusion bioreactor chamber. Computational studies were coupled to bioreactor experiments for a case-study flow rate. Two cases were compared in the first instance seeded scaffolds were positioned immediately after the perfusion chamber inlet while a second group was positioned at the computationally determined optimum distance were a steady state flow profile had been reached. Experimental data showed that scaffold location affected significantly cell content and neotissue distribution, as determined and quantified by contrast enhanced nanoCT, within the constructs both at 14 and 21 days of culture. However gene expression level of osteopontin and osteocalcin was not affected by the scaffold location. This study demonstrates that the bioreactor chamber environment, incorporating a scaffold and its location within it, affects the flow patterns within the pores throughout the scaffold requiring therefore dedicated optimization that can lead to bone tissue engineered constructs with improved quality attributes.

3.2 Introduction

The successful clinical use of tissue engineered (TE) products, as well as their commercial exploitation has been linked to the use of bioreactor-based manufacturing systems (Martin et al., 2004; Salter et al., 2012). The ability to generate reproducible culture conditions that may control cell proliferation and differentiation while minimizing operator-specific handling steps, relies on the development of bioreactor systems that will ensure the production of TE constructs of consistent quality (Martin et al., 2009; Papantoniou et al., 2013). One of the most widely used types of bioreactors in TE applications today is the perfusion bioreactor. Within perfusion bioreactors controlled culture environments can be developed, eliminating mass transport limitations observed in static culture (Bancroft et al., 2003;

Goldstein et al., 2001). These limitations may be overcome due to the introduction of convective nutrient and oxygen transport throughout the construct volume which is generated and enhanced by fluid flow through the scaffold (Bancroft et al., 2002; Goldstein et al., 2001; Grayson et al., 2008b). Moreover, in the case of bone TE, fluid flow shear stress provides biomechanical stimuli to the cultured cells enhancing extracellular matrix production and its mineralization, also improving its spatial distribution within scaffolds. (Datta et al., 2006; Bancroft et al., 2002; Sikavitsas et al., 2005; Grayson et al., 2008a; Li et al., 2009).

Computational fluid dynamics (CFD) modeling is a powerful tool that has been used extensively in TE for the characterization of complex flow fields developed throughout regular and irregular scaffolds during cell culture in bioreactors (for review see (Hutmacher and Singh, 2008)). Deciphering the complex relationship between the hydrodynamic environment and cultured TE construct properties is critical to the production of clinically useful tissues (Martin et al., 2004). For this purpose the quantification of flow-associated shear stresses as well as their spatial distribution within various scaffold geometries has been thoroughly investigated in perfused bioreactor setups (Boschetti et al., 2006; Jungreuthmayer et al., 2009; Porter et al., 2005; Raimondi et al., 2004; Cioffi et al., 2006; Maes et al., 2009; Voronov et al., 2010). However the focus of the majority of the aforementioned computational studies has been on analyzing local regions within empty scaffold geometries exposed to a flow field lacking a thorough link to the larger scale bioprocess environment. In a recent communication (Hidalgo-Bastida et al., 2012) suggested a cost-efficient computational strategy for the optimal design of perfusion bioreactors by using a volume averaged approach for the optimization of bioreactor chamber and scaffold designs. This approach provided useful information on the inlet velocity profile to the porous scaffold, which could serve as initial conditions for a more elaborate but localized CFD analyses. However simulations were not connected to any experiments in order to further validate their potential.

Whereas the main focus in bioreactor based TE has typically been on enhancing the functionality or maturation stage of the resulting engineered tissues, the potential for bioprocess optimization within bioreactor systems to minimize product variability should receive equal attention (Placzek et al., 2009; Martin et al., 2009). This could further aid in understanding biological responses observed during bioreactor culture by decoupling

the combined effects of process parameters. Recent publications have highlighted the importance of rational bioprocess design by incorporating quality engineering considerations defining process operation regimes where TE constructs may be manufactured with prerequisite quality specifications (McCoy and O'Brien, 2010; Papantoniou et al., 2013). In order to further enhance successful manufacturing of sensitive TE products, we should not only aim to define and maintain optimum bioprocess conditions but to also minimize or eliminate all possible sources of variation (Mason and Hoare, 2007). Minimizing bioreactor batch-to-batch variability by ensuring process reproducibility has been highlighted as an important factor for the further maturation of TE and successful translation into the clinic (Salter et al., 2012). Furthermore preventing the development of localized 'hot zones' within scaffolds (either excessive shear stress development or detrimental low mass transport regions) could be minimized by optimizing scaffold positioning and perfusion chamber geometry.

In this study a three dimensional (3D) fluid flow modeling approach was used in order to optimize a critical design parameter such as the position of the porous scaffolds in the perfusion bioreactor chamber. TE construct quality characteristics such as DNA content, homogeneity and quantity of the neotissues were assessed for scaffold batches cultured above and below the computationally determined critical length. Moreover the effect of scaffold location on the mRNA transcripts of two osteogenic markers, osteopontin (OPN) and osteocalcin (OCN) was evaluated. For a quantitative determination of the 3D distribution of the neotissue throughout the scaffold contrast enhanced nano-CT (CE-nanoCT), was employed (Papantoniou et al., 2014b). This allowed to link the experimentally determined quality attributes of the TE constructs to averaged process-scale environmental parameters.

3.3 Materials & Methods

3.3.1 Cell culture

Human periosteum derived cells (hPDCs) were isolated from periosteal biopsies of different donors as described previously (Eyckmans and Luyten, 2006). This procedure was approved by the ethics committee for Human Medical Research (KU Leuven) and with patient informed consent. hPDCs were expanded in Dulbecco's modified Eagle's medium with high-glucose (Invitrogen) containing 10% fetal bovine serum (BioWhittaker) and 1%

antibiotic–antimycotic (100 units/mL penicillin, 100mg/mL streptomycin, and 0.25mg/mL amphotericin B; Invitrogen). hPDCs were passaged at 80%–90% confluency.

3.3.2 Scaffold

3D additive manufactured open porous Ti6Al4V scaffolds (subsequently referred to as Ti scaffolds) of: $\emptyset = 6$ mm, $h = 6$ mm, porosity = $73 \pm 1\%$, strut diameter = 245 ± 2 μm and pore size = 755 ± 3 μm), produced on an in-house developed selective laser melting (SLM) machine, were used (for further details see Van Bael, 2011 #28). The design was based on a parametric unit cell which consists entirely of identical beams with constant circular cross-section (0.1 mm) and a beam length of 0.9 mm.

3.3.3 Perfusion Bioreactor

At the time of experiment, typically cells from passage 6 were trypsinized with Tryple Express (Invitrogen) and seeded on the scaffolds. A static drop-seeding protocol was used for seeding cells onto pre-wetted 3D Ti scaffolds. 200,000 cells per scaffold were seeded and left to attach overnight ($t=24$ h) with an average cell seeding efficiency of 60%. Scaffolds were positioned in the bioreactor perfusion chambers with a random orientation (regarding the direction of drop seeding) (Impens et al., 2010). The osteogenic medium used for this study contained Ca^{2+} (6mM) and P_i (4mM) and ascorbic acid at a concentration of 0.05 ng/ml (Chai et al. 2011). Scaffolds were cultured for 14 and 21 days. For dynamic culturing, TE constructs were cultured in an in-house developed perfusion bioreactor equipped with parallel perfusion circuits. Each perfusion chamber (Length=26 mm, Diameter=6mm), holding a single scaffold, was connected to an individual medium reservoir (disposable 50 ml Falcon tubes, BD Biosciences) containing 10 ml of cell culture medium via a Tygon (Cole Parmer) tubing and a two-stop tubing (BPT, Cole Parmer) connected to a peristaltic pump (IPC-24, Ismatec SA). Medium was refreshed every two days for the entire culture period. For each scaffold location 15 seeded scaffolds were cultured. Four scaffolds (TE constructs) for each experimental condition were used to determine average DNA content values per scaffold (at day 1, 14 and 21) and subsequent qPCR analysis (only for the day 14 and 21 groups). The remaining 3 TE constructs were analyzed via contrast enhanced nano-CT (at day 14 and 21). Experiments were randomized by culturing seeded scaffolds for both experimental conditions (scaffold locations) on parallel per batch, to avoid

batch to batch variation.

3.3.4 DNA content analysis

The PicoGreen buffer-submerged scaffolds were vortexed for 60s. After 60s of centrifugation at 13,000 rpm, 10 mL supernatant was diluted in 90 mL MiliQ water and briefly vortexed. 5 mL of the diluted sample was added to 195 mL of the earlier described working solution, after which the sample was briefly vortexed and incubated at room temperature for 5 min. The DNA concentration was then measured with the Qubit Fluorometer (Invitrogen). The measured value multiplied by 400 gave the actual DNA concentration in the initial sample (Chen et al., 2011). Four scaffolds for each experimental condition were used to determine average DNA content values per scaffold.

3.3.5 Quantitative PCR

RNA was extracted from four random, representative constructs for each culturing condition and time points using the RNeasy mini kit (Qiagen) and quantified using a Nanodrop ND-1000 spectrophotometer (Thermo Scientific). Complementary DNA was synthesized using the RevertAid H Minus First Strand complementary DNA synthesis kit (Fermentas). Sybr green quantitative polymerase chain reaction was performed for two different key osteogenic markers (OCN, OPN) (Chai et al., 2012a). The PCR reaction was cycled in a Rotor-Gene sequence detector (Qiagen) as follows: 95 °C for 3 min, 40 cycles of 95 °C for 3 s and 60 °C for 60s. Differences in gene expression were determined in comparison to HPRT and shown as $2^{-\Delta CT}$.

3.3.6 Contrast-Enhanced Nanofocus Computed Tomography (CE-nanoCT)

CE-nanoCT was performed on two random, representative constructs for each time point and culture condition. The constructs were fixed in 4% paraformaldehyde (Sigma) for two hours and stored in PBS prior to analysis. Hexabrix® 320 (Guerbet) was used as a contrast agent to visualize the neotissue (Papantoniou et al., 2014b). A Phoenix NanoTom S (GE Measurement and Control Solutions) with a 180 kV/15 W high-performance nanofocus X-ray tube was used to perform the CE-nanoCT. A tungsten target was operated at a voltage of 90 kV and a current of 170 μ A. An aluminum and copper filter, both 1mm thick were used to reduce beam hardening and metal artifacts. The exposure time was 500 ms, and a frame

averaging of 1 and image skip of 0 were applied, resulting in a scanning time of 20 min. The reconstructed images had an isotropic voxel size of 3.75 μm .

3.3.7 3D visualization, image processing and analysis

CTAn (Bruker micro-CT) was used for image processing as described in (Papantoniou et al., 2014b). Briefly, the neotissue domain was separated from the background noise and the scaffold using a 3-level Otsu thresholding method (Otsu, 1979). To analyze the volume of the Ti scaffolds the resulting dataset was thresholded to obtain binary images representing the scaffold. In order to reduce the influence of the partial volume effect and metallic artifacts introduced by the presence of the Ti6Al4V scaffold while analyzing the neotissue volume, the binarised images for the Ti6Al4V scaffold were dilatated by two voxels and subtracted from the 3-level thresholded dataset. The neotissue fraction was then binarized and the noise was eliminated by removing black speckles smaller than 500 pixels and white speckles smaller than 2000 voxels. To solidify the resulting structure, a ‘closing’ operation (2 voxels) was performed on the resulting images, providing final images used for the 3D analysis of the neotissue volume (Fig. 3.5A).

3.3.8 Live/Dead Assay

A Live/Dead viability/cytotoxicity kit (Invitrogen) was used to evaluate qualitatively cell viability and cell distribution by fluorescence microscopy. Constructs were rinsed with 1 ml PBS after which they were incubated in the staining solution (0.5 μl Calcein AM and 2 μl Ethidium Homodimer in 1 ml PBS) for 20 min in normal cell culture conditions. The constructs were imaged using a Leica M165 FC microscope.

3.3.9 Mathematical modeling

The culture medium Dulbecco’s modified Eagle’s medium, at 37°C (with a viscosity μ of 10^{-3} Pa s and density ρ of 1000 kg/m³) for each scaffold position was treated as a continuous medium solved by the incompressible Navier-Stokes equation ?? where \mathbf{u} and p are the fluid velocity and pressure gradient, respectively. The equation was solved in its steady state form.

$$\begin{aligned}\rho(\mathbf{u} \cdot \nabla \mathbf{u}) &= -\nabla p + \mu \Delta \mathbf{u} \\ \nabla \cdot \mathbf{u} &= 0\end{aligned}\tag{3.1}$$

Computational domains were created with the open source SALOME software (www.salomeplatform.org) and then for the purpose of

compatibility with FreeFem++ these geometries were meshed in an open source meshing software GMSH (geuz.org/gmsh/). Each domain was meshed with approximately 7.10^5 tetrahedrons. The non-linearity of the equation was treated with a Newton-Raphson algorithm that required approximately 2 hours to be solved. The wall of the perfusion chamber and the scaffold struts were treated as no-slip boundary condition ($\mathbf{u} = 0$). For the inlet of the flow a Poiseuille profile was imposed with the average velocity corresponding to the given flowrate. Finally, the outlet was set as free flow boundary conditions.

3.3.10 Critical length determination (L_{crit})

Scaffolds were positioned from the chamber inlet towards the exit with a step of $500\mu\text{m}$. In total, simulations for 7 flow rates were run. These flow rates corresponded to the span that is used for experimentation in our lab, coinciding with flow rates used for osteogenic differentiation studies in bioreactors of similar geometric features.

$$\text{Velocity magnitude : } \|\mathbf{u}\| = \sqrt{u_x^2 + u_y^2 + u_z^2}. \quad (3.2)$$

We define the average velocity magnitude difference across the planar (using the average value of the velocity function $\mathbf{u}(x, y, z)$ over the surface of the scaffold entrance and scaffold exit) (Fig. 3.1A) as:

$$\Delta\mathbf{u} = \left| \iint \|\mathbf{u}_{in}(x, y)\| dx dy - \iint \|\mathbf{u}_{out}(x, y)\| dx dy \right| \quad (3.3)$$

Where $\mathbf{u}_{in} = \mathbf{u}|_{z=\text{scaffold entrance}}$ and $\mathbf{u}_{out} = \mathbf{u}|_{z=\text{scaffold outlet}}$. In order to have the average velocity magnitude difference, $\Delta\mathbf{u}$ is divided by the surface (A) of the cross sections corresponding to $z=\text{scaffold entrance}$, (due to the symmetrical geometry of the scaffold, this surface area is the same at the entrance or at the exit of the scaffold). Simulations were run for consecutive scaffold locations (moving at the z -axis) starting from the perfusion chamber inlet (L_{entr}) with a step of $\Delta L=500 \mu\text{m}$ (Fig. 3.1). Convergence was reached when the average velocity magnitude difference (of scaffold entrance and outlet) between two consecutive scaffold positions (ΔL) was equal to zero i.e. $|\Delta\mathbf{u}_{L_{entr}+(j-1)\Delta L} - \Delta\mathbf{u}_{L_{entr}+j\Delta L}| = 0$ (Fig. 3.1). At that point the L_{crit} was determined for each flow rate and a steady state for the flow profile within the scaffold was reached. Positioning the scaffold downstream of the L_{crit} will not affect the flow profile at the inlet and within the scaffold. The maximum flow rate (in the geometric confines of the specific perfusion

chamber), where the previous convergence criterion could be satisfied was 4.4 ml/min.

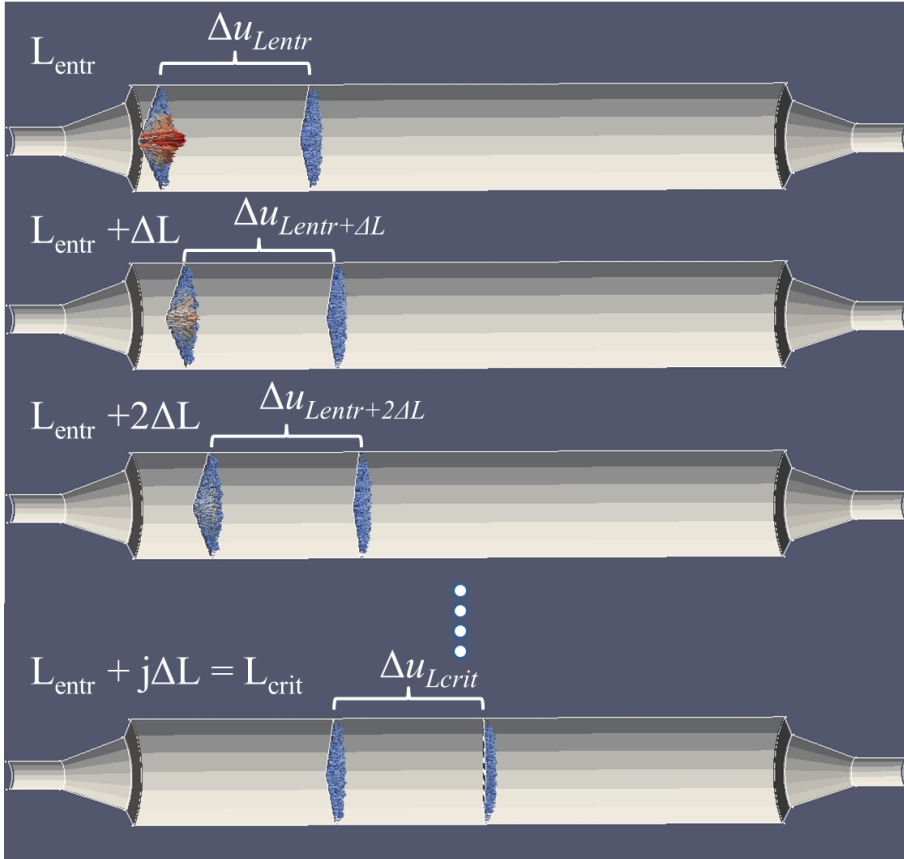


Figure 3.1: Schematic representation of sequential scaffold locations from L_{entr} to $L_{entr+\Delta L}$ ($\Delta L=500 \mu\text{m}$) for which CFD simulations were run. Planar sections represent scaffold entrance and exit and arrows velocity vectors. $\Delta\mathbf{u}_{L_{entr}}$ was calculated from eq (??) while as a convergence criterion for the determination of L_{crit} , the following was used: $|\Delta\mathbf{u}_{L_{entr+(j-1)\Delta L}} - \Delta\mathbf{u}_{L_{entr+j\Delta L}}| = 0$. At that point the L_{crit} was determined for each flow rate.

3.4 Results

3D CFD simulations were used to map the flow field within the bioreactor perfusion chamber and through the scaffold for the selected range of scaffold

locations and flow rates. Fig. 3.2C and 3.2D show the flow velocity values along the axis of symmetry of the scaffolds and perfusion chamber for two different scaffold positions (Fig. 3.2A,B). The flow field within the scaffold in the first case shows a high degree of inhomogeneity when compared with the second case.

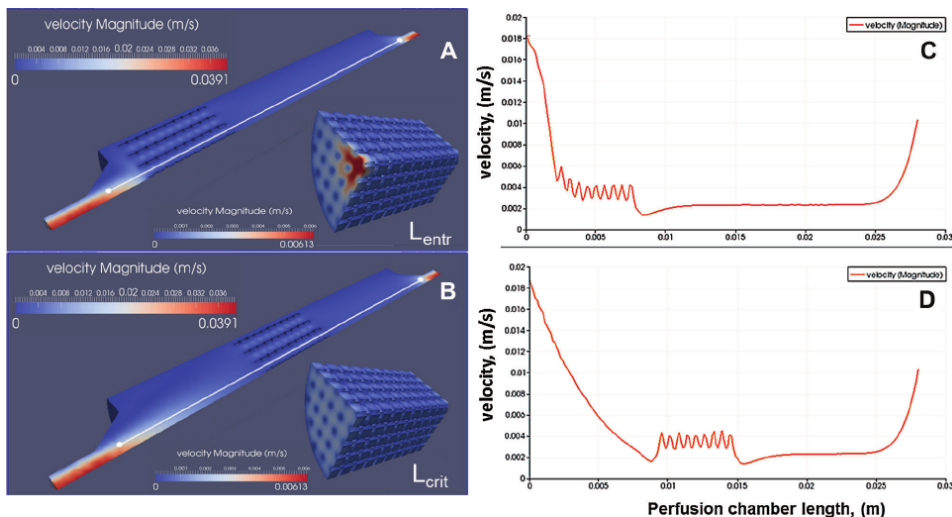


Figure 3.2: Longitudinal section of the perfusion bioreactor chamber showing scaffold velocity distribution, for a flow rate of 2ml/min, in the perfusion chamber and also within the scaffold for (A) L_{entr} positioning and (B) L_{crit} positioning. Flow velocity values along the axial direction (as indicated by the white lines) are shown for the (C) L_{entr} and (D) L_{crit} . Flow velocity fluctuations within the 3D scaffold show acceleration and deceleration through the pores.

Although the chamber inlet is designed with a smooth entrance to the perfusion chamber it is evident that the high inlet velocity from the narrow inlet tubing will substantially affect the flow field within the scaffolds. In order to determine minimum ‘safe’ distances as function of perfusion flow rate, a critical distance was defined (henceforth mentioned as L_{crit}) above which the average flow velocity magnitude difference (Δu) (between the scaffold entrance and scaffold outlet) between two consecutive scaffold locations was minimized for each flow rate. Fig. 3.3 shows the relationship between (Δu) and the distance of the scaffold from the entrance of the perfusion chamber. L_{crit} was determined as the distance from the perfusion chamber inlet, where this difference was minimized. This was also the

location where the pressure drop (Δp) across the scaffold was minimized reaching a plateau (data not shown). Based on the CFD results an empirical correlation between L_{crit} and flow rate (Q) was obtained for our bioreactor and scaffold geometry the following empirical power law correlation gave best fit: $L_{crit} = 2.66Q^{1.34}$ (Fig. 3.3C). Furthermore the maximum flow rate that would allow the development of an L_{crit} for the geometric features of the perfusion chamber used in this study, was also determined (= 4.4 ml/min). For this maximum feasible flow rate the average velocity magnitude difference between scaffold entrance and exit was $\Delta u = 10^{-6}$ m/s. The determination of the critical length after which a fully developed laminar profile can be obtained, could also show the limitations length-wise, of scaling-up (in this case using longer scaffolds) in a specific bioreactor setup, in order to maintain a minimal quality control.

As a case study, experiments were carried out for a flow rate of 2 ml/min to assess the effect of scaffold location on cell content, neotissue quantity and distribution throughout the scaffold during dynamic culture and also on osteogenic cell differentiation. Based on the CFD simulations (Fig. 3.3), the L_{crit} for a flow rate of 2 ml/min was determined to be 7 mm, thus scaffolds were positioned at the entrance and at 10 mm from the perfusion chamber entrance. This distance was chosen to be larger than the computational one to compensate for possible geometric manufacturing abnormalities across batch that could affect the flow profile during experiments, since steady state is reached by 7mm the flow profile across the scaffold should not be different from 7 to 10mm. Cells were cultured for 14 and 21 days. Fig. 3.4 shows representative fluorescent Live/Dead images of cells on the scaffold as function of culture duration. At 14 days of culture cell presence was seen to be inhomogeneous when scaffolds were positioned close to the perfusion chamber entrance with a substantial scaffold region with very low cells present. However constructs cultured above L_{crit} possessed a higher degree of homogeneity. This discrepancy seemed to diminish by culture day 21. Although the Live/Dead assay does not provide quantitative data regarding the presence of live and dead cells, there was a very low presence of dead cells (images not shown).

DNA analysis however showed a statistically significant lower cell content for scaffolds positioned at the entrance for both time points when compared with the corresponding scaffolds above L_{crit} (Fig. 3.5). For the two week culture time point L_{entr} scaffolds contained 69% of the cell number measured

for L_{crit} scaffolds. This difference was slightly reduced by culture day 21 where the cell number in L_{entr} was seen to be 75% of the corresponding L_{crit} cell content values.

CE-nanoCT was used to further investigate the 3D homogeneity of cell and ECM presence throughout the construct and provide quantitative volumetric information of its distribution. The results showed once more a lower presence of neotissue at the scaffold inlet in comparison to the rest of the scaffold with the quantity of the neotissue part increasing towards the scaffold outlet (Fig. 3.6B,C) for day 14 at L_{crit} . The first three pores of the scaffold were substantially affected containing only 25, 40, 65% compared to the equivalent pore filling of the L_{crit} scaffolds respectively, while the part of the scaffold closer to the outlet showed a higher content of neotissue. This inhomogeneity of neotissue presence within scaffolds continued to be present although to a lesser degree at day 21 resulting in 80% neotissue quantity in comparison to the L_{crit} scaffolds, which showed a homogeneous neotissue distribution for both culture time points (Fig. 3.6D,E). As a final test two commonly used genes related to stem cell osteogenic differentiation, osteopontin (OPN) and osteocalcin (OCN), were analyzed. In both cases a time dependent increase was observed from culture day 14 to day 21. However there was no significant difference of OCN and OPN gene expression between scaffolds positioned at the entrance and at L_{crit} (Fig. 3.7).

3.5 Discussion

The computational and experimental results presented in this study demonstrated that through a spatial optimization of scaffold positioning within perfusion bioreactor chambers, TE constructs with improved quality attributes, such as DNA content (i.e. cell content) and neotissue distribution were produced. For this study regular pore geometry scaffolds were used to minimize intra-scaffold niche variability and avoid the development of preferential flow pathways as has been seen for irregular scaffolds (Cioffi et al., 2006; Maes et al., 2012). The axial positioning of TE constructs within the bioreactor chamber was seen to affect the intra-scaffold hydrodynamic flow profile, for a given flow rate, resulting in a varied response on the aforementioned quality attributes, after two and three weeks of culture. The flow rate used in this study was chosen to maintain the shear stress distribution across the scaffold surface within a range of $1-5 \times 10^{-2}$ Pa,

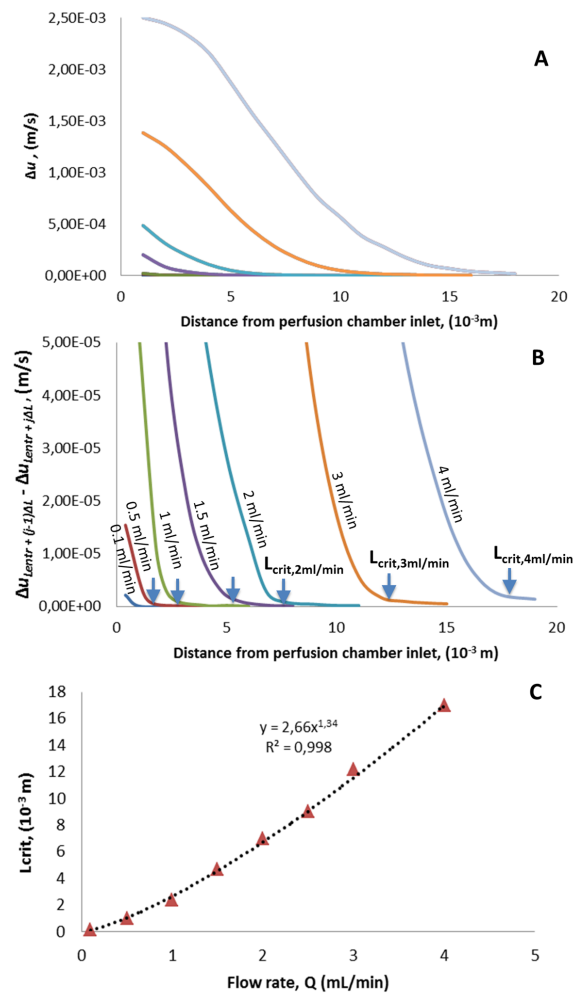


Figure 3.3: L_{crit} determination for increasing flow rates. The average velocity magnitude difference between scaffold entrance and outlet decreased as the scaffold was positioned away from the perfusion chamber inlet for all flow rates (A). Furthermore the difference of the same parameter between two consecutive scaffold locations was calculated and when a plateau was reached meaning the flow profile across the scaffold ceased to be a function of the scaffold location, steady state was assumed and the L_{crit} was obtained for each flow rate (B). An empirical correlation (power law giving best fit) between L_{crit} and the flow rates was obtained for the geometric characteristics of the specific bioreactor (C). A flow rate of 2 ml/min was used for the experimental case study.

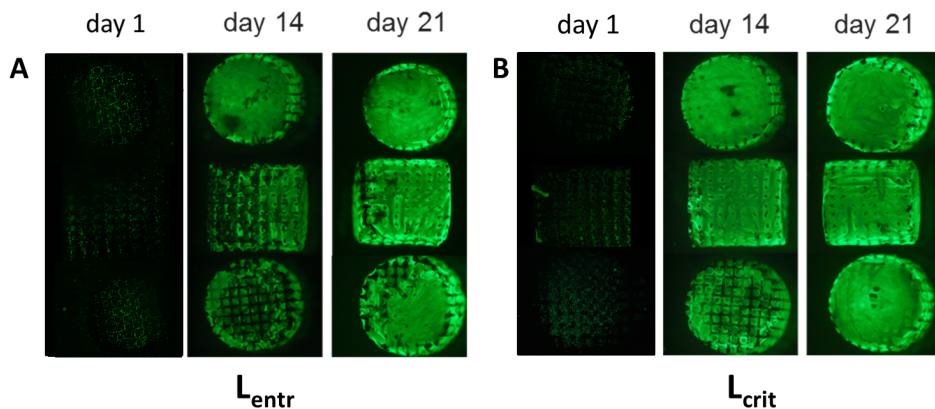


Figure 3.4: Representative Live/Dead stained images demonstrate the distribution of the cells in the scaffolds positioned at (A) L_{entr} where an inhomogeneous distribution may be seen at day 14 while by day 21 this is less pronounced, and (B) L_{crit} where cells seem to be present along the entirety of the scaffold. No statistically significant difference was seen for day 1 constructs between the two groups. Top images indicate the flow outlet while bottom images indicate flow inlet.

which has been reported in literature to enhance osteogenic differentiation when coupled to osteoinductive media (Cartmell et al., 2004). The axial positioning approach defined by the position L_{crit} minimized the development of localized ‘hot zones’ within the scaffolds during culture especially at the central and peripheral area of the scaffold entrance. Recently a cost-effective strategy for the spatial design and optimization of perfusion bioreactors, by representing the scaffold as a porous medium and employing the Brinkman equation to obtain cost-efficient fluid flow simulations for a number of scaffold positions and perfusion chamber geometries (Hidalgo-Bastida et al., 2012). In our study a volume-averaged approach was also used (data not shown) for a rapid evaluation of scaffold positioning in the perfusion chamber (for the same porosity as the scaffold employed in this study) that resulted in the same empirical correlation as the more detailed and computationally expensive real-scaffold geometry simulation using the Navier-Stokes equation (as shown in Fig. 3.1 and Fig. 3.2). However the limitation of this approach is the lack of information on the events occurring at smaller scales i.e. the fluid environment within the scaffold at the pore level and the shear stress distribution along the scaffold surface. The importance of being able to conduct multi-scale 3D

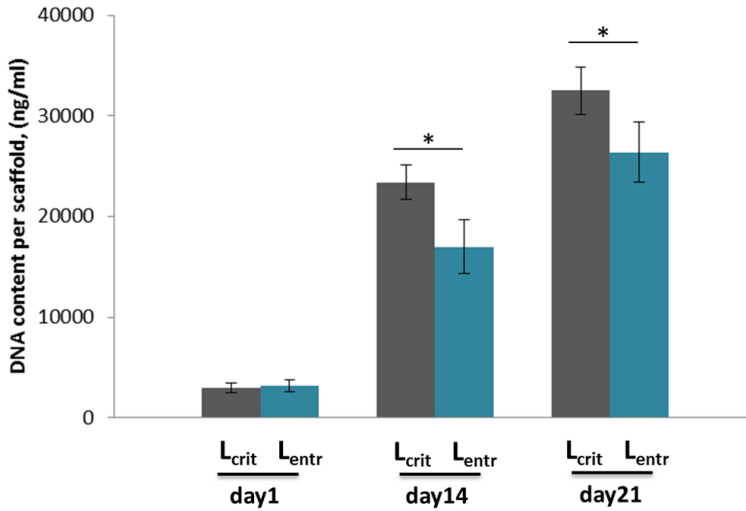


Figure 3.5: DNA content of scaffolds indicating cell content in scaffolds at 1, 14 and 21 days of culture, for groups ($n=4$) cultured at two different locations (L_{crit} and L_{entr}). (*: $p < 0.05$).

computer simulations was recently demonstrated by accurately simulating the flow field through an entire bioreactor chamber that enclosed an irregular scaffold. It affected flow and stresses within the pores throughout the scaffold and as such impacted the outcome of a cell seeding process simulated via a lattice-boltzman approach (Spencer et al., 2013). For this reason a real-scaffold geometry, instead of a volume averaged representation, was preferred in our computational model, since in this study a link between the process conditions and the shear stresses generated during culture was targeted. This approach also required experimental observations via a 3D analysis (CE-nanoCT). Inhomogeneous distribution of neotissue (cells and ECM) within TE scaffolds as a result of a range of fluid flow regimes has been reported by a number of studies during bioreactor culture (Du et al., 2009; Porter et al., 2007; Papantoniou et al., 2013; Plunkett et al., 2010; Mahmoudifar and Doran, 2005). In our study inhomogeneous neotissue distribution observed in Fig. 3.4 could be attributed to cell detachment due to exposure to fluid flow either to cell migration. However Live/dead images (Fig. 3.4) and DNA content per scaffold (Fig. 3.5) at day 1 show no discernible differences between the two scaffold locations indicating that the developed inhomogeneity at later time points (at L_{entr}) were not due to cell detachment upon exposure of cells to flow. The maximum wall shear stress

values obtained in this study varied from 0.065 to 0.04 Pa for the L_{entr} and L_{crit} scaffolds respectively. Cell detachment from surfaces due to fluid flow has been observed for shear stresses exceeding 1 Pa (for review see (McCoy and O'Brien, 2010) which is much higher than the fluid conditions to which cells in this work were exposed to, justifying our findings. However, cells attached to scaffolds via a 'bridged' morphology have been seen to detach at considerably lower flow rates than flattened cells within scaffolds and a critical shear stress value for bridged cell detachment was determined at 0.088 Pa (McCoy et al., 2012) a value closer to the max shear stress values determined along the L_{entr} scaffold struts (we should note that such values will be dependent upon scaffold material properties as well). It has been suggested that strut junctions act as nucleation spots for cells (Harley et al., 2008) in order to bridge the strut and subsequently grow in a 3D configuration driven by local curvature (Kommareddy et al., 2010; Knychala et al., 2013) until the entire void space of the scaffold is filled by neotissue (Joly et al., 2013; Papantoniou et al., 2014b). The lack of cell presence for the entrance region of L_{entr} scaffolds, could be explained by the fact that cells were experiencing shear stress levels that prohibited cell spreading in a bridged morphology close to strut junctions due to excessive cell deformation at those locations (Jungreuthmayer et al., 2009) rendering a proportion of the scaffold not suitable for void filling and 3D cell growth. This is also reflected by the lower DNA content of the L_{entr} scaffolds (Fig. 3.5). The gene expression level of osteopontin (OPN) and osteocalcin (OCN) was used as a mid-stage and late-stage marker of osteogenic differentiation respectively (Li et al., 2009). The expression levels of both genes have been seen to be enhanced by exposure to shear stress, in the presence of an osteogenic medium (Bancroft et al., 2002; Kreke et al., 2005; Goldstein et al., 2001). However, the relation between expression levels and the shear stress magnitude for both OCN and OPN has not yet been clarified (Grayson et al., 2011). In this study, the elevated gene expression levels of OPN and OCN from day 14 to day 21 and particularly the more pronounced upregulation of OCN shows the progression along an osteogenic cascade (Fig. 3.7). Osteogenic differentiation using the customized medium of this study has been shown to significantly upregulate a range of osteogenic genes such as RunX2, Osterix and ALP while also inducing mineralization of the extracellular matrix (Chai et al., 2012b).

However no statistical difference was observed between the gene expression of the L_{entr} and L_{crit} scaffold groups at 14 and 21 days of culture. This latter phenomenon could be explained by the fact that in the case of L_{entr}

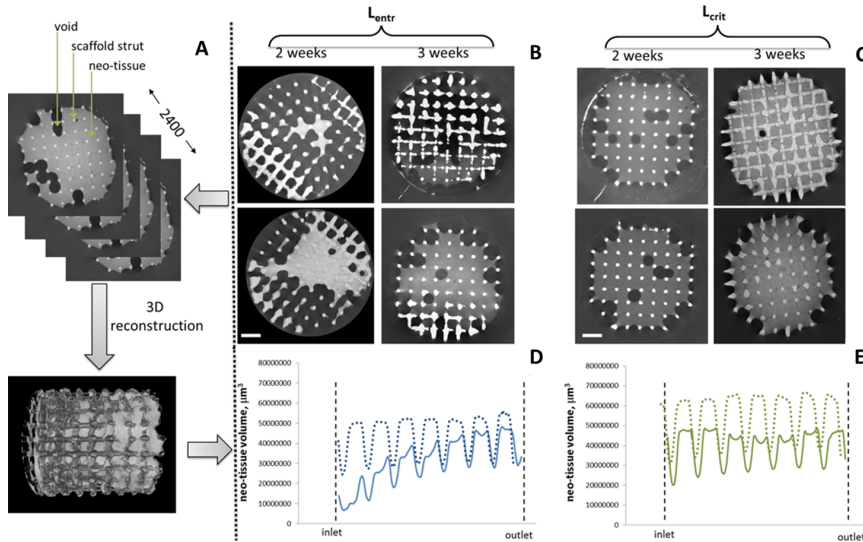


Figure 3.6: A 3D visualization of the neotissue distribution after reconstructed CT slices were obtained (A). Representative CE-nanoCT cross-sections at the entrance region of scaffolds at day 14 and 21 of culture positioned at (B) L_{entr} demonstrating low neotissue quantity and (C) L_{crit} showing high degree of filling. Images were subsequently 3D quantification of neotissue (composed of cells and ECM) and its distribution for (D) L_{entr} and (E) L_{crit} ; Continuous lines represent 14 days of culture and dashed lines represent 21 days of culture. Sudden drops in neotissue volume indicate zones with aligned scaffold struts where less void volume for neotissue growth is available at that section (scale bar = 1mm).

scaffold, cells were preferentially growing at scaffold regions where flow had already developed a homogenized flow profile similar to the one experienced by the cells in L_{crit} scaffolds, as observed by the CE-nanoCT data (Fig. 3.6). So in function of the position of the scaffold no gene expression differences were observed meaning that the cells' biological properties were not affected despite the discrepancies in DNA content.

In this study we extended the use of CE-nanoCT as a 'whole construct' 3D quality characterization method for the spatial optimization of the bioreactor process by quantifying neotissue distribution and quantity as a response to the intrascaffold flow field. The ability to use robust tools and methodologies such as CE-nanoCT to assess important and potentially critical quality characteristics of TE constructs such as neotissue quantity and homogeneity (across a whole scaffold) and maturation level

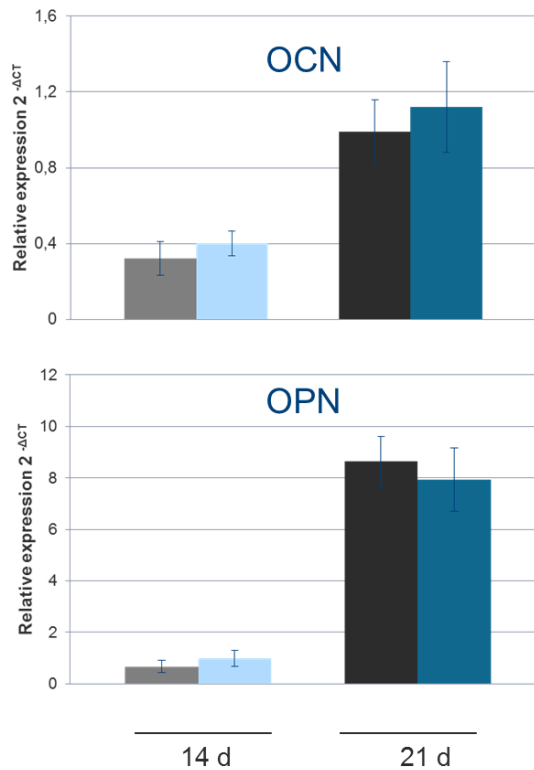


Figure 3.7: Gene expression of the cultured constructs by means of RT-PCR for OPN and OCN, relative to HPRT. No significant changes in expression of OPN, OCN were observed after 14 and 21 days between L_{entr} and L_{crit} scaffold groups (n=4).

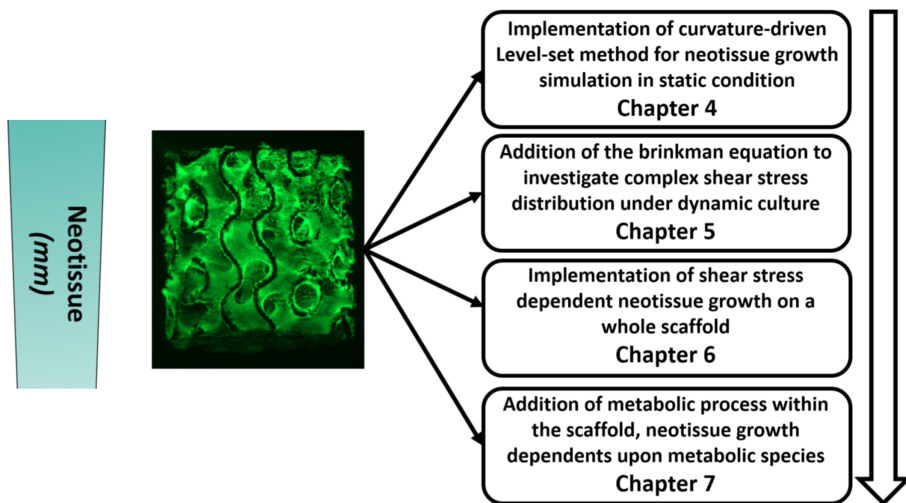
(ie mineralization (Porter et al., 2007), gives a new perspective to more integrated TE process design strategies whereby neotissue growth kinetics can be also taken into consideration. In order to fully exploit these advantages and link them meaningfully to the biological measurements and characterization, the development of computational tools that will be able to capture neotissue growth and its interplay with the surrounding dynamic culture environment will be essential, given recent developments on real-time and online measurement modalities (Mack et al., 2013).

In conclusion, by using ‘whole-perfusion-chamber’ 3D computational models (geometries composed of the perfusion chamber and the scaffold

architecture) it was possible to determine optimum scaffold locations where neotissue formation could occur without uncertainty derived from the surrounding flow field. These were subsequently coupled to a 3D ‘whole construct’ characterization technique which allowed to quantify the extent of the flow field effect on the distribution and amount of neotissue formed during 14 and 21 days. The biological state of the cells however was not influenced by the scaffold location. The development of 3D process-relevant models and characterization techniques will result in an improved understanding of the response of stem cells to culture conditions, enabling a tailored bioreactor and bioprocess design in respect to desired neotissue quality attributes, enabling ultimately a compliant translation to the clinic.

Part II

Neotissue scale



CHAPTER 4

A COMPUTATIONAL MODEL FOR NEOTISSUE GROWTH ON 3D SURFACES USING THE LEVEL SET METHOD: A BONE TISSUE ENGINEERING CASE STUDY

Yann Guyot^{1,2}, Ioannis Papantoniou^{1,3}, Yoke Chin Chai^{1,3}, Simon Van Bael^{4,6}, Jan Schrooten^{1,4}, Liesbet Geris^{1,2,5}

¹ Prometheus, Division of Skeletal Tissue Engineering, KU Leuven, Onderwijs en Navorsing 1 (+8), Herestraat 49 - PB813, B-3000, Leuven, Belgium.

² Biomechanics Research Unit, Universite de Liège, Chemin des Chevreuils 1 - BAT 52/3, B-4000 Liège, Belgium.

³ Skeletal Biology and Engineering Research Center, KU Leuven, Onderwijs en Navorsing 1 (+8), Herestraat 49 - PB813, B-3000, Leuven, Belgium.

⁴ Department of Metallurgy and Materials Engineering, KU Leuven, Kasteelpark Arenberg 44 – PB 2450, B-3001, Leuven, Belgium.

⁵ Department of Mechanical Engineering, Biomechanics Section, KU Leuven, Celestijnenlaan 300C – PB 2419, B-3001 Leuven, Belgium.

⁶ Department of Mechanical Engineering, Division of Production Engineering, Machine Design and Automation, KU Leuven, Celestijnenlaan 300b, 3001 Leuven, Belgium.

Adapted from: Guyot, Y., Papantoniou, I., Chai, Y. C., Van Bael, S., Schrooten, J., & Geris, L. (2014). **A computational model for cell/ECM growth on 3D surfaces using the level set method: a bone tissue engineering case study.** *Biomechanics and Modeling in Mechanobiology*, 13(6), 1361-1371.

4.1 Abstract

Three dimensional (3D) open porous scaffolds are commonly used in tissue engineering (TE) applications to provide an initial template for cell attachment and subsequent cell growth and construct development. The macroscopic geometry of the scaffold is key in determining the kinetics of cell growth and thus *in vitro* neotissue formation. In this study we developed a computational framework based on the Level Set Method to predict curvature-dependent growth of the cell/extracellular matrix domain within TE constructs. Scaffolds with various geometries (hexagonal, square, triangular) and pore sizes (500 and 1000 μm) were produced in house by additive manufacturing, seeded with human periosteum-derived cells and cultured under static conditions for 14 days. Using the projected tissue area as an output measure, the comparison between the experimental and the numerical results demonstrated a good qualitative and quantitative behavior of the framework. The model in its current form is able to provide important spatio-temporal information on final shape and speed of pore-filling of tissue engineered constructs by cells and extracellular matrix during static culture.

4.2 Introduction

Three dimensional (3D) porous scaffolds are commonly used in tissue engineering (TE) applications to provide an initial template for subsequent cell growth and construct development. Their architectural features, alongside with physicochemical characteristics, have been seen to play a significant role in important biological processes such as initial cell attachment (Melchels et al., 2010, 2011), cell growth and extracellular matrix (ECM) formation during 3D *in vitro* culture (Zeltinger et al., 2001a; Hollister et al., 2002; Van Bael et al., 2012). Geometrical scaffold properties such as pore size (Zeltinger et al., 2001b) and pore shape (Knychala et al., 2013), and more specific features such as curvature (Rumpler et al., 2008; Gamsjager et al., 2013) have been shown to constitute crucial design considerations in controlling cell fate both for *in vitro* (Rumpler et al., 2008) and *in vivo* applications (Bidan et al., 2012). (Nelson et al., 2005) studied the hypothesis that scaffold geometry controls the evolving multicellular construct geometry by defining patterns of mechanical stress throughout the structure thereby enhancing cell proliferation. Furthermore cell growth rate has been suggested to be dependent on mechanical stress, with a dependence of the rate of cell division on local stress regimes (Shraiman, 2005; Dunlop

et al., 2010).

Literature on the numerical exploration of growth kinetics of neotissue structures driven by the geometric properties of scaffolds (Rumpler et al., 2008; Bidan et al., 2012; Gamsjager et al., 2013; Knychala et al., 2013) is expanding rapidly. The concept of curvature controlled growth has been put forward by (Dunlop et al., 2010) to capture the previously mentioned dependence of cell growth kinetics on the local surface curvature of the substrate. (Rumpler et al., 2008), developed a 2D model capable of capturing *in vitro* curvature-driven cell growth by advecting the neotissue surface with a curvature-dependent velocity. They recently extended their model to 3D, based on an analytical computation of the curvature which depends on a sphere (mask) browsing digital image-sets of the geometries of interest, and compute the curvature within the mask (Bidan et al., 2013). A limitation of the aforementioned approach is its focus in symmetric 3D pore channel structures which cannot be extrapolated to complex and non-symmetrical scaffold geometries. Therefore, developing a model of curvature-dependent growth that readily and accurately allows simulation of neotissue growth over realistic convex or non-convex 3D scaffold geometries is important for the design of optimal TE scaffolds.

The development of additive manufacturing techniques has enabled the production of porous structures with controlled architectures suitable for TE applications (Van Bael et al., 2011; Sobral et al., 2011). However their design characteristics still lack features to guide cell fate. Studies regarding cell-material interactions often focus on surface topography, microenvironment niches and single cell observations (for review see (Higuchi et al., 2013; Lutolf and Hubbell, 2005) with limited translational relevance to TE. Currently a wide variety of regular and irregular 3D scaffolds is reported in literature, however regular pore geometry scaffolds seem to offer certain advantages by minimizing intra-scaffold variability. In this work as a case study 3D regular pore geometry Ti6Al4V (Ti) scaffolds were used, which in combination with human Periosteum Derived Cells (hPDCs) allow cell proliferation and differentiation to osteogenic phenotypes resulting in 3D mineralized constructs (Chai et al., 2012b; Papantoniou et al., 2013). Furthermore when implanted ectopically *in vivo* they have been shown to successfully induce bone formation (Chai et al., 2012a), thus constituting a promising system for further study.

A crucial parameter for robust TE process design will be the development of ‘realistic’ computational models that will be able to predict the behavior of such complex cell-scaffold systems under a range of culture process conditions. Expanding on the conclusions of the aforementioned experimental studies (Papantoniou et al., 2013) we developed a 3D *in silico* model based on the Level Set Method (presented in the next section). The aim of this paper is to present a computational framework capable of capturing the neotissue growth over a range of 3D geometries.

4.3 Materials & Methods

4.3.1 The Level Set Method

In order to accurately simulate time dependent events taking place in the neotissue component on the one hand and the remaining void space on the other, the Level Set Method (LSM) was used in this study (Sethian, 1999). The LSM is a numerical method mainly used in multiphasic fluid dynamics (AlMamani et al., 2008) or image processing (Machacek and Danuser, 2006) to follow an interface between two moving domains. This method has also been used to model 2D growth kinetics of biological systems such as tumours (Hogea et al., 2006) and soft tissues (Lappa, 2005, 2003a).

An important advantage of the LSM in the context of this study is its intrinsic way of computing the mean curvature. Indeed the curvature only depends on the level set function φ and the mesh size; hence it can be computed with minimal user intervention. The only element that the user has to provide is a meshed domain of the scaffold pore.

Define a domain $\Omega \subset \mathbf{R}^d$, $d = 2, 3$; and a decomposition of two subdomains Ω_{nt} and Ω_v (where Ω_{nt} is the neotissue area/volume and Ω_v the void area/volume) with the interface between them denoted as Γ and \mathbf{n}_Γ the normal to this interface. The role of the LSM is to track implicitly the interface $\Gamma(t)$ moving with a velocity \mathbf{v}_G . The main object of this method is a continuous scalar function φ defined on the domain. This level set function φ is a signed distance function chosen to be positive in Ω_{nt} , negative in Ω_v and zero on Γ . The interface tracking is described by an advection equation ?? of the level-set function φ on the whole domain Ω .

$$\begin{aligned}\frac{\partial\varphi}{\partial t} + \mathbf{v}_G \cdot \nabla\varphi &= 0 \\ \nabla\varphi \cdot \mathbf{n} &= 0\end{aligned}\tag{4.1}$$

The interface advection velocity \mathbf{v}_G , is determined in a similar manner to that reported in other curvature-controlled models (Rumpler et al., 2008). In (Rumpler et al., 2008), the authors describe that the neotissue interface moves faster where its local curvature κ is higher. Therefore, in this study, we define \mathbf{v}_G as follows (see Fig. 4.1):

$$\mathbf{v}_G = -V_G * \mathbf{n}_\Gamma\tag{4.2}$$

$$V_G = \begin{cases} \kappa, & \text{if } \kappa < 0. \\ 0, & \text{if } \kappa \geq 0. \end{cases}\tag{4.3}$$

In this study, by using the LSM, the neotissue interface growth direction will be always from the surface of the strut towards the void pore ($\varphi < 0$) space as observed experimentally (Papantoniou et al., 2013; Van Bael et al., 2012), this is the reason why equation ?? is with a negative sign, indeed in our definition, the normal is toward the tissue, so the growth velocity has to be along the opposite of the gradient of φ . As previously stated, the curvature of the interface as well as its normal are intrinsically computed with respect to the level-set function φ , and their expression is as follows:

$$\begin{aligned}\mathbf{n}_\Gamma &= \frac{\nabla\varphi}{|\nabla\varphi|} \\ \kappa &= \nabla \cdot \mathbf{n}_\Gamma\end{aligned}\tag{4.4}$$

The curvature calculated in Eq. ?? corresponds to the mean curvature, similar to what was used by (Bidan et al., 2012, 2013).

4.3.2 Implementation

The full model was implemented using the finite element method (FEM) with an open source partial differential equation solver FreeFem++ (Hecht, 2012). This solver is well adapted for the type of model developed in this study due to its ability to deal with complex geometries and meshes, and its simplified way to treat any type of partial differential equation (PDE) by

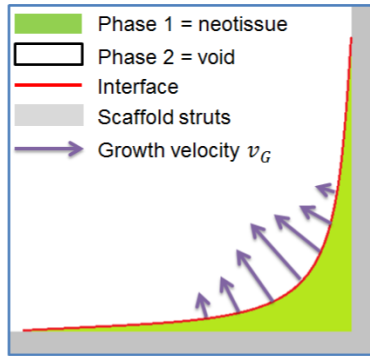


Figure 4.1: Schematic representation of the Level Set Method. The neotissue interface ($\varphi = 0$) is represented in *red*, the neotissue domain ($\varphi > 0$) in *green* and the “empty” domain ($\varphi < 0$) in *white*. Arrows represent the curvature-controlled velocity.

implementing its variational form. As a first step, relevant geometries were created with the (free) software SALOME (www.salome-platform.org) and then for the purpose of compatibility with FreeFem++, these geometries were meshed in an open source meshing software GMSH (geuz.org/gmsh/). To initialize the LSM, an initial distance function, φ_0 , was defined in the domain Ω at the boundaries corresponding to the scaffold struts. Due to the very nature of distance functions, the level set function φ is not differentiable at certain locations (i.e. where gradient discontinuities may be found), thus the normal \mathbf{n}_Γ and the curvature κ are not properly defined everywhere in the domain. In order to overcome this issue, an artificial diffusion term was added in the definition of \mathbf{n}_Γ and κ (equations ??), leading to the equations shown in ??.

$$\begin{aligned} \mathbf{n}_\Gamma &= \frac{\nabla\varphi}{|\nabla\varphi|} + \varepsilon\Delta\mathbf{n}_\Gamma \\ \kappa &= \nabla \cdot \mathbf{n}_\Gamma + \varepsilon\Delta\kappa \end{aligned} \quad (4.5)$$

The result of adding this numerical diffusion to the equations is shown in Fig. 4.2. After verification on a simple test problem allowing direct comparison with an analytical solution (Fig. 4.2A), the parameter ε in equations ?? was chosen to be equal to 10^{-4} for all the simulations in this study. If ε is too small, the numerical diffusion term in the smoothing procedure is negligible and oscillations appear in the calculation of the curvature leading to loss

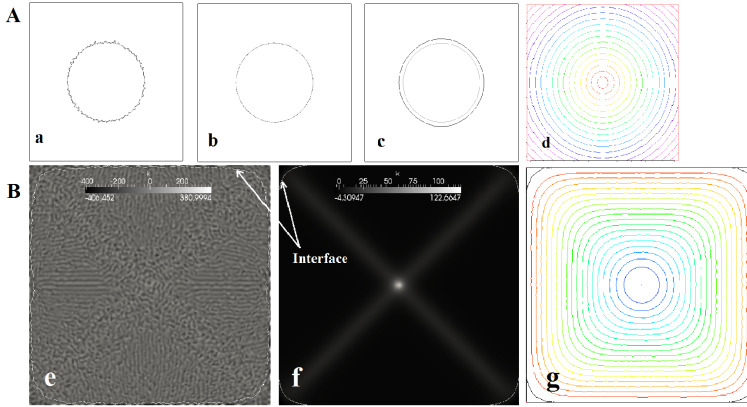


Figure 4.2: Effect of adding numerical diffusion in the calculation of the curvature. **(A)** Comparison between analytic solution of curvature ($1/\text{radius}$) (in *grey*) and numerical solution (in *black*) for the curvature of a circle function of radius 0.25 in the unit square (d) for (a) 10^{-6} , (b) 10^{-4} , (c) 10^{-2} . **(B)** Calculation of the curvature κ of a distance function in the square. The interface ($\varphi = 0$) is represented with a white line. In (e) no numerical diffusion was added during the calculations so oscillations appear and the interface is not smooth. In (f) the curvature is correctly smoothed by diffusion and the interface is smooth due to the addition of a limited amount of numerical diffusion in the calculations. (g) represents the iso-levels of the [Equation] function (with in black, the interface).

of smoothness in the definition of the interface. Contrarily, if ε is too high, excessive diffusion is added leading to a smooth but erroneous calculation of the curvature.

Once \mathbf{n}_Γ and κ are computed, the advection velocity \mathbf{v}_G is updated and equation (4.1) is solved. It is well known that this kind of equation (pure convection) solved with the finite element method leads to oscillations. To avoid this oscillatory behaviour, the addition of a stabilization term (under many different forms) has been frequently described in the literature (Bochev et al. 2004). The drawback of this method is its computational cost. A cost efficient computational approach, implemented in FreeFem++, is the method of characteristics (Polyanin et al., 2002). This method consists of reducing a PDE to a system of ordinary differential equations (ODEs) along curves called ‘characteristics’; the resolution of these ODEs along those curves leads to the solution of the original PDE.

Advecting a distance function is known to result in distortion of the level

set, that could eventually lead to numerical error. In order to avoid such troubles, the level set function φ is reinitialized using the technique developed in (Dapogny and Frey, 2012) and the related open source software *mshdist* (<http://ljk.imag.fr/membres/Charles.Dapogny/software.html>) was employed.

4.3.3 Experimental data

In this study, results presented in (Van Bael et al., 2012) were used in a first calibration and testing round. The setup of the experiment is briefly repeated below. Six distinct unit cells were used which can be classified according to their shape as triangular, hexagonal and square, and according to their pore size. The pore sizes (measured in a 2D horizontal plane, cf Fig. 4.3 first row) used in this study were 500 and 1000 μm (Fig. 4.3). The outer dimensions of the scaffold were 6mm height and 6mm diameter. Scaffolds were produced by a non-commercial, in-house-developed selective laser melting machine using Ti6Al4V powder (Raymor Industries Inc., Canada) as described in Van Bael et al. (2012). Each scaffold was drop seeded with 200,000 human periosteum-derived cells (hPDCs) (passage 5, additional details on the cell source can be found in Bari et al. (2006)) in 60 μl cell suspension and incubated statically for 1h at 37°C to facilitate cell attachment, before being transferred to a rotator to perform dynamic rotation seeding. Cell seeding efficiencies between 80 and 95% with significantly higher amounts of cells present on the small pore scaffolds which have the largest surface area (see (Van Bael et al., 2012) for extensive discussion). After 6h, the cell-seeded scaffolds were transferred to a 48-well plate and cultured in GM for 14 days. Medium was refreshed thrice a week. Cell growth on scaffolds was evaluated using the Live-Dead viability/cytotoxicity staining (In vitrogen, USA) performed according to the provider's instructions. Homogeneous cell growth over the whole 3D surface was observed. Pictures of the growing neotissue domain (top and bottom of scaffold) were taken for 7 and 14 days of culture

4.3.4 Objectives of this study

The aim of this study is to develop a computational framework that will enable modeling of the neotissue growth in porous structures. In this study porous structures with various pore geometries and sizes were used. Cell seeding on these porous structures was represented by the initial condition in which the geometries were 'seeded' with a 20 μm thin layer of neotissue on

the struts (Fig. 4.3). For computational cost and accuracy, the simulation was performed on a single scaffold pore. Due to the regular geometry of the scaffolds used in this study this simplification does not limit the generalization of the model predictions. Results are shown either for the entire pore or for half a pore in order to be able to investigate neotissue evolution within the pore.

Given the current absence of biological mechanistic details in the definition of the parameters describing neotissue growth a calibration procedure was carried out based on experimental *in vitro* data to obtain a first assessment of the quantitative capabilities of the developed framework. Calibration of the model consisted of linking the simulation time (described by the number of iterations t using the fixed computational time step) to absolute time (days in culture). The parameter used for least square fitting was defined as the ratio of the 2D projected void pore surface, S_v (white part in Fig. 4.1) before and after cell culture (determined for both simulations and experiments). For the calculation of projected void pore surface from the experimental results, an average value was determined over 6 pores. First the simulation time t (in this study, t is non dimensional) needed to reach the projected void pore surface ratio equal to that of the experimentally measured one at culture day 7 was determined by best least square fitting for the hexagonal geometry. Subsequently t^2 was used to predict S_v values at day 14 for all geometries.

4.4 Results

The *in vitro* experimental results were used to compare and calibrate the models (Fig. 4.5). Values of ‘projected tissue area’ (as a percentage of initial void area) obtained from live/dead images of the *in vitro* constructs, provided 2D information regarding the development of neotissue construct in a static 3D culture over time. The comparison between *in silico* and *in vitro* results demonstrated a satisfying qualitative agreement in terms of shape. By least square fits a single calibration parameter (relating simulated time to experimental time) for all geometries of a same pore size was determined and led to good results. For the small pore size $t=1500$ iterations corresponded to 7 days and $t=3000$ to 14 days of culture (Fig. 4.5A) while for the large pore size $t=7000$ iterations corresponded to 7 days and $t=14000$ iterations to 14 days of culture (Fig. 4.5B). A quantitative evaluation of the projected tissue areas (both for computational and experimental

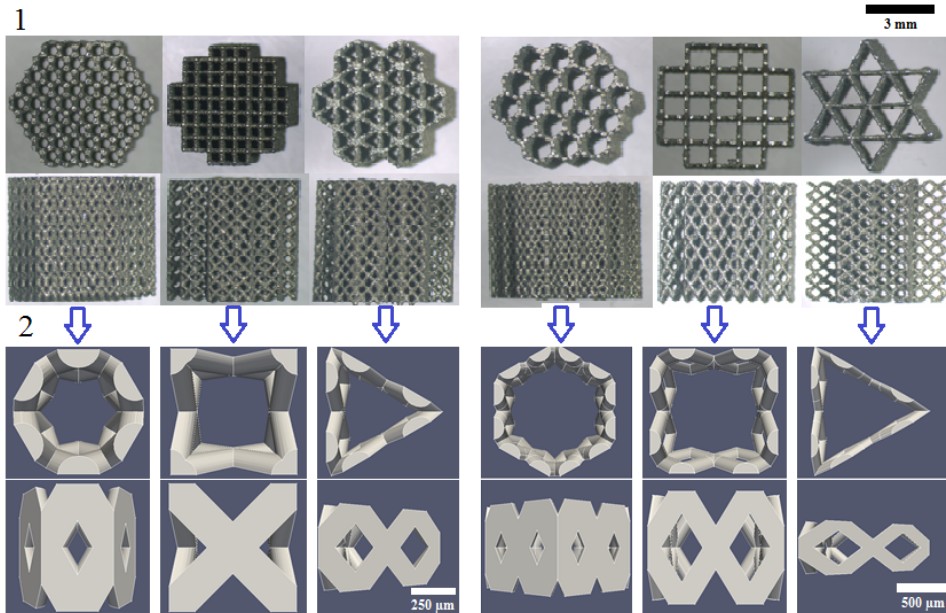


Figure 4.3: (1) Different scaffold geometries (hexagon, square and triangle) used in this study for pore size equal to $500\ \mu\text{m}$ (left) and 1mm (right). (2) Corresponding single pore for numerical simulations.

results) of the aforementioned images is shown in Fig. 4.6A and 4.6B. As an interpretation, the model predicts two important successive stages during growth process. The first one correspond to the filling of the vertical small spaces between struts and the second one is the filling of the pore itself. Indeed, for instance, on 1mm pore size, the hexagon presents very small vertical spaces leading to an acceleration at the very first steps; at the contrary, triangle shapes presents big vertical spaces that are not even filled in during the simulations and did not enter into the second growth stage. A good correspondence between computational and experimental results was obtained where the simulated projected tissue area was systematically less than one standard deviation away from the experimentally observed mean projected tissue area. In more complex geometries, such as the one shown in Fig. 4.6, particular behavior such as bridging between different local surfaces during neotissue growth can be observed which is treated automatically with the LSM in contrast to other techniques that previously have been reported to implement curvature-dependent growth.

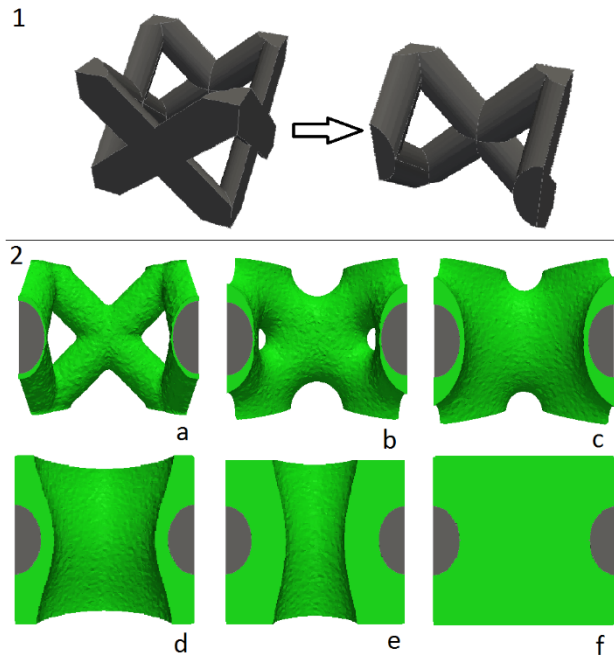


Figure 4.4: Neotissue growth in squared shape pore. **(1)** Pore geometry (left) an cut in half (right) for better visualization. **(2)** neotissue growth (green) at (a) initial state, (b)15%, (c)30%, (d)50%, (e)75%, (f)100% of filling.

4.5 Discussion

This study provides a ‘proof of concept’ on the use of the LSM as a tool to investigate 3D neotissue growth on a range of titanium alloy (Ti6Al4V) scaffold architectures that are relevant to tissue engineering (TE) applications. The preference of cells to spontaneously grow in a 3D neotissue network structure rather than in a flattened 2D manner when cultured *in vitro* on 3D scaffolds has been reported in numerous studies (Papantoniou et al., 2013, 2014b; Knychala et al., 2013; Grayson et al., 2004). In this study a range of pore geometries was studied. Initial results showed that the curvature-driven growth was correctly implemented capturing known qualitative features of neotissue growth. Irrespective of the initial pore shape (Kommareddy et al., 2010; Rumpler et al., 2008), all simulations eventually resulted in ‘spherical’ or ‘cylindrical’ geometries with positive curvatures at the corners leading to higher velocities of interface growth, as observed by others (Knychala et al., 2013; Rumpler et al., 2008), and

negative curvatures at the middle of the struts. Hexagonal pore scaffolds possessing a shape that is closest to that of a circle, showed a faster growth of the neotissue domain, while triangular pore scaffolds were seen to induce the slowest growth, in agreement with what has been observed in our experiments and reported in literature to date (Knychala et al., 2013; Rumpler et al., 2008; Bidan et al., 2013).

The use of curvature-driven growth models has been shown to be an efficient approach when investigating biological constructs in 2D (Knychala et al., 2013; Rumpler et al., 2008; Bidan et al., 2012). However, due to the complexity of many scaffold geometries and a lack of symmetry (regarding the different axes), 2D approximations were employed limiting thus their predictive capabilities regarding neotissue distribution in 3D structures with realistic design features. This study proposed a 3D modeling approach able to interpret a local change in the curvature and to use it to guide the growth rate. Furthermore it showed that the LSM is a powerful approach in the context of curvature driven growth simulation due to its intrinsic evaluation of the direction of interface motion and curvature, reducing in this way user intervention. In previous studies in both 2D (Bidan et al., 2012) and 3D (Bidan et al., 2013), a mask was used over a digital (pixelated) images to determine the local curvature of the construct and use it to update the interface. This approach, although allowing for easy implementation of novel geometries due to the explicit use of CT data as input, requires substantial input by the user when choosing an efficient mask size. Additionally, upscaling to 3D was not straightforward, especially when dealing with complex pore structures, combining larger and smaller curvatures. In this study, the user intervention was strongly reduced due to the model's ability to determine the local curvature by itself. This study shows the potential of the LSM in capturing curvature driven neotissue growth on different geometries including complex, irregular and non-symmetric shapes. Due to the very nature of the LSM and its ability to treat changes in topology, this model was able to simulate particular behavior such as bridging between two local surfaces when moving in the same direction (Fig. 4.7).

Despite the advantages inherent to the use of the LSM for simulating neotissue growth, the model in its current form faces a number of limitations. Indeed, even though user intervention was minimized, a mesh of the pore domain still has to be constructed. The mesh size has to be of sufficient quality, as an overly coarse mesh could lead to incorrect results.

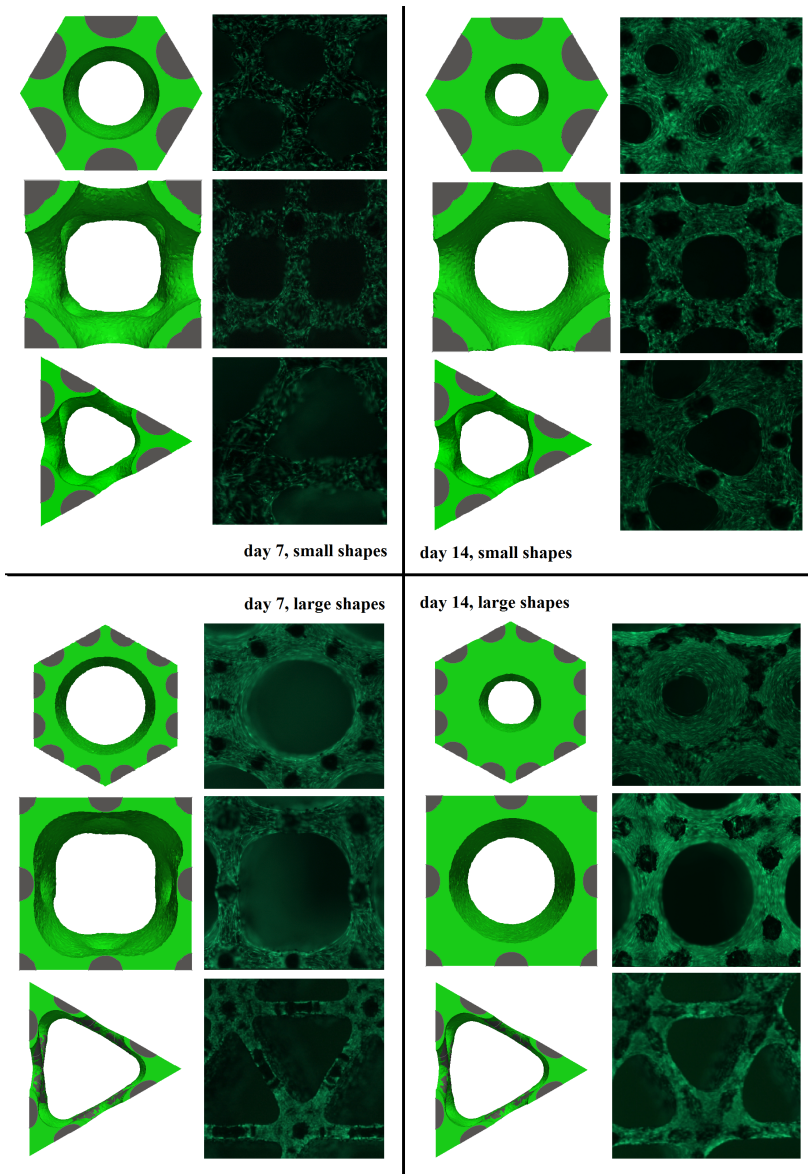


Figure 4.5: Qualitative comparison between simulations and experiments. Computational results are shown on the white background, experimental results (live-dead staining) are shown on the black background at day 7 (left) and day 14 (right) for the 0.5 mm (top) and 1mm (bottom) scaffold geometries.

Additionally, during the calibration phase, a factor 5 difference in the ratio experimental time vs simulation time was found between geometries with 1mm vs 500 μm pore size. One would expect that due to any nutrient transport restrictions within the small pores, growth would be relatively slower. However, the difference between the two empty volumes, may lead to a significant increase of necessary culture time to fill the pore. This means that although the parameters defining the growth rate for various geometries with a similar pore size are equal, these parameters need to be altered when larger pore sizes are modeled. Currently the growth rate only depends on the local curvature.

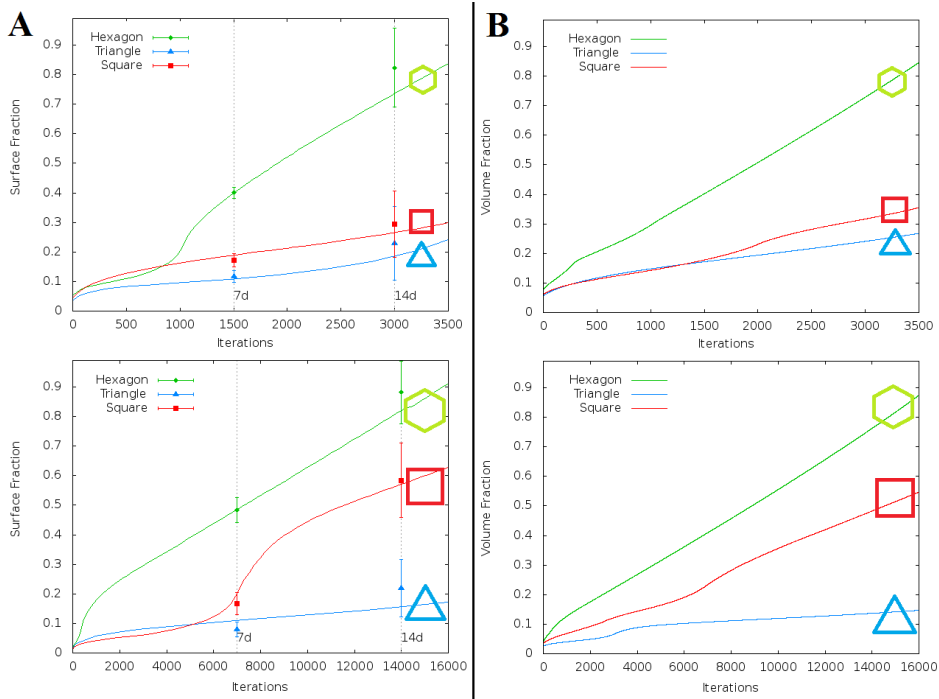


Figure 4.6: (A) Quantitative comparison between simulations and experiments. Surface fraction from a cross section (continuous line) for 0.5 mm (top) and 1mm (bottom) geometries versus experimental projected area (data points, average \pm standard deviation for 6 pores). (B) Volume fraction (continuous line) for 0.5 mm (top) and 1mm (bottom) geometries

Potentially the introduction of other influencing factors in equation 4.2 such as mass transport, oxygen consumption and medium composition

could help to explain the difference in calibration factor between geometries with small and large pore sizes. The introduction of space and time dependent parameters representing the biology in a more mechanistic way will be the subject of future work. When considering mass transport in the model, a coupling with fluid dynamics also needs to be established. The Level Set Method has already been successfully used in conjunction with fluid dynamic and oxygen and nutrient consumption models in the simulation of cartilage growth in an *in vitro* culture system (Lappa, 2003b, 2005). Whereas the model by (Lappa, 2005) was limited to 2D, the multiphysics approach of combining curvature-dependent growth with fluid dynamics could be extended to the third dimension. Finally the quantitative calibration/testing carried out in this study was based on ‘2D projected void areas’ which constitutes a considerable simplification since both computational and experimental results were obtained in 3D settings. In order to overcome this limitation it is necessary to develop and use more realistic and information-rich validation techniques. The use of computer tomography techniques such as microCT, nanoCT and CE-nanoCT to analyze and monitor 3D neotissue growth (Voronov et al., 2012; van Lenthe et al., 2007; Papantoniou et al., 2014b) on complex geometries could offer substantial improvement to the model by allowing for a more accurate validation of neotissue growth kinetics and is something that will be further pursued.

The results obtained by this study provide crucial feedback that would allow the intelligent design of (3D porous) TE scaffolds that may actively guide 3D cell growth and final neotissue construct characteristics. Based on the presented computational tool a wide range of biologically relevant 3D scaffold designs could be tested *in silico* prior to the manufacturing phase. Furthermore, given the additional complexities introduced by the use of dynamic culture conditions i.e. in bioreactor setups, a multiphysics model could pose as an attractive platform for further integrated studies on the interplay between scaffold design features and process conditions and their decoupled and combined effect on neotissue growth.

In this study we developed an LSM based computational framework to predict the final shape of a biological construct in static culture conditions for a given scaffold geometry. Various geometries and pore sizes were examined both experimentally and numerically and a good qualitative and quantitative behavior of the framework was demonstrated. The model in

its current form is able to provide important information on the shape and the speed of the filling of tissue engineered constructs by neotissue.

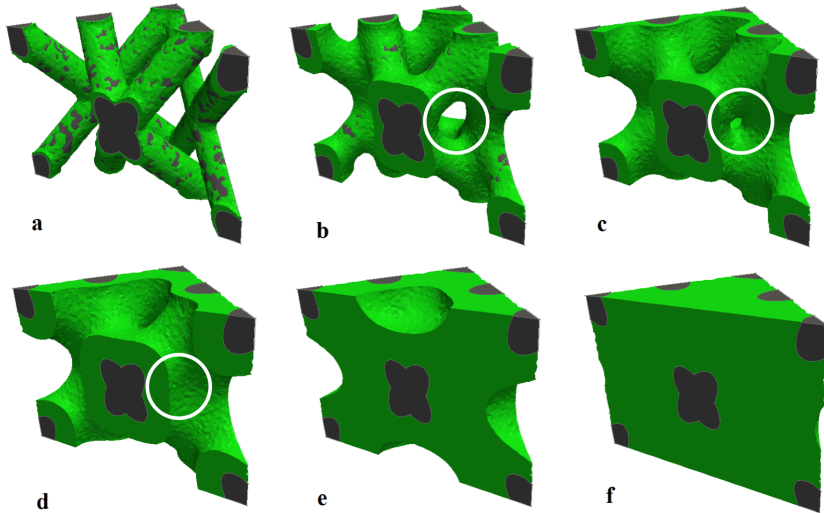


Figure 4.7: Neotissue growth on a complex geometry with diamond shaped pores. Results are shown for different degrees of pore filling: 8% (a), 15% (b), 30% (c), 50% (d), 75% (e) and 98% (f) . The pore has being cut in half (diagonally) for a better visualisation of the simulated growth. These results illustrate the bridging process (white circle) and the subsequent change in topology when two local surfaces move in the same direction.

CHAPTER 5

A THREE-DIMENSIONAL COMPUTATIONAL FLUID DYNAMICS MODEL OF SHEAR STRESS DISTRIBUTION DURING NEOTISSUE GROWTH IN A PERFUSION BIOREACTOR

Yann Guyot^{1,2}, Frank P. Luyten^{1,3}, Ioannis Papantoniou^{1,3}, Jan Schrooten^{1,4}, Liesbet Geris^{1,2,5}

¹ Prometheus, Division of Skeletal Tissue Engineering, KU Leuven, Onderwijs en Navorsing 1 (+8), Herestraat 49 - PB813, B-3000, Leuven, Belgium.

² Biomechanics Research Unit, Universite de Liège, Chemin des Chevreuils 1 - BAT 52/3, B-4000 Liège, Belgium.

³ Skeletal Biology and Engineering Research Center, KU Leuven, Onderwijs en Navorsing 1 (+8), Herestraat 49 - PB813, B-3000, Leuven, Belgium.

⁴ Department of Metallurgy and Materials Engineering, KU Leuven, Kasteelpark Arenberg 44 – PB 2450, B-3001, Leuven, Belgium.

⁵ Department of Mechanical Engineering, Biomechanics Section, KU Leuven, Celestijnenlaan 300C – PB 2419, B-3001 Leuven, Belgium.

Adapted from: Guyot, Y., Luyten, F. P., Schrooten, J., Papantoniou, I., & Geris, L. (2015). **A three-dimensional computational fluid distribution during neotissue growth in a perfusion bioreactor.** *Biotechnology and bioengineering*, 112(12), 2591-2600.

5.1 Abstract

Bone tissue engineering strategies use flow through perfusion bioreactors to apply mechanical stimuli to cells seeded on porous scaffolds. Cells grow on the scaffold surface but also by bridging the scaffold pores leading a fully filled scaffold following the scaffold's geometric characteristics. Current computational fluid dynamic approaches for tissue engineering bioreactor systems have been mostly carried out for empty scaffolds. The effect of 3D cell growth and extracellular matrix formation (termed in this study as neotissue growth), on its surrounding fluid flow field is a challenge yet to be tackled. In this work a combined approach was followed linking curvature driven cell growth to fluid dynamics modeling. The Level Set Method (LSM) was employed to capture neotissue growth driven by curvature, while the Stokes and Darcy equations, combined in the Brinkman equation, provided information regarding the distribution of the shear stress profile at the neotissue/medium interface and within the neotissue itself during growth. The neotissue was assumed to be micro-porous allowing flow through its structure while at the same time allowing the simulation of complete scaffold filling without numerical convergence issues. The presented computational framework is used on different scaffold pore geometries demonstrating its potential to be used a design tool for scaffold architecture taking into account the growing neotissue.

5.2 Introduction

Perfusion bioreactors have been extensively explored for the production of bone forming tissue engineered constructs by supporting cell growth, metabolism, and differentiation. Attempts to culture *in vitro* three dimensional (3D) tissue engineered (TE) constructs in static conditions typically resulted in an outer shell of viable cells, while the inner core became necrotic due to limited diffusive delivery of nutrients. Using bioreactors, cell proliferation and cell survival have been enhanced substantially when compared with static setups, by improving mass transport of oxygen and nutrients throughout the TE construct during cell growth (Martin et al., 2004). However, fluid flow exerts stresses on the cultured cells affecting functions such as migration, proliferation and apoptosis (McCoy and O'Brien, 2010). Furthermore shear stress can determine lineage commitment Song et al. (2013) but also promote osteogenic differentiation of bone marrow stromal, periosteum and adipose derived mesenchymal

stem (stromal) cells, and enhance extra-cellular matrix deposition (McCoy and O'Brien, 2010; Rauh et al., 2011; Papantoniou et al., 2013).

In order to understand and characterize complex flow fields which are developed throughout regular and irregular scaffolds during cell culture in bioreactors, computational fluid dynamics (CFD) modeling has been extensively used in tissue engineering (for review see (Hutmacher and Singh, 2008)). The quantification of flow-associated shear stresses as well as their spatial distribution within various 3D scaffold geometries has been thoroughly investigated in perfused bioreactor setups (Raimondi et al., 2004; Porter et al., 2005; Cioffi et al., 2006; Jungreuthmayer et al., 2009; Maes et al., 2009; Voronov et al., 2010). In previous studies, local shear stresses were defined as a function of flow rate of the culture medium, bioreactor configuration, porosity and porous scaffold micro-architecture (Voronov et al., 2010; Pham et al., 2012). However the majority of CFD studies to date used empty scaffold geometries to calculate shear stress magnitude and distribution across the empty scaffold surface i.e. wall shear stress. They did not take into account the dynamics of the changing 3D environment as a result of cell/tissue growth. Efforts to mimic 3D cell growth on regular scaffolds were limited to a swelling of the scaffold struts (Lesman et al., 2010) or the use of a growing biomass (Nava et al., 2013), in both cases modeling the cell layer to be impermeable whilst not being able to reach a full filling of the scaffold void.

3D cell growth and neotissue formation starts with 2D cell migration and proliferation on the strut surface, followed by cells bridging the scaffold void spaces and growing in the third dimension with matrix deposition. This will eventually lead to complete scaffold void filling as evidenced recently via synchrotron and nano-CT imaging (Voronov et al., 2012; Papantoniou et al., 2014a). This means that estimation of wall shear stress values in empty scaffold geometries would only be indicative of the shear stress experienced by cells during early culture time points. A current bottleneck to further advance and utilize CFD strategies in the TE field is the inclusion of a domain composed of cells and extracellular matrix (a growing permeable neotissue) on real scaffold geometries as recently stated (Hendrikson et al., 2014). This way the whole range of fluid-flow associated stresses exerted on cells during neotissue growth could be determined.

In this paper we present a computational strategy that will help understand shear stress magnitude and distribution along the fluid-neotissue interface but also within the permeable 3D neotissue during growth in a perfusion bioreactor. To achieve this, the Level Set Method (LSM) was employed capturing neotissue growth on 3D macro-porous Titanium scaffolds over time leading to complete scaffold pore closure (filling). Computational neotissue growth was driven by the local curvature as previously described (Bidan et al., 2013; Guyot et al., 2014) (chapitre 4). At various degrees of scaffold filling, the steady Brinkman equation was used to continuously describe both flow through a micro-porous medium (neotissue) and free flow through the macro-porous scaffold void. This shear stress mapping will allow to eventually link experimentally determined biological responses (i.e. cell phenotype) to the actual shear stress regime that cells experience during 3D neotissue growth in perfusion bioreactors.

5.3 Materials & Methods

5.3.1 Ti6Al4V scaffolds

Regular, 3D additive manufactured Ti6Al4V scaffolds (diameter 6 mm, height 6mm) were produced in-house using selective laser melting, based on a diamond-shaped unit cell (Fig. 5.1B) and a square unit cell (Van Bael et al., 2012) (Fig. 5.1C). Strut diameter for both scaffolds was 200 μm . Prior to use, the scaffolds were ultrasonically cleansed for 10 min over three wash steps in acetone, ethanol and distilled water. Subsequently they received an alkali treatment with 5M sodium hydroxide (Sigma-Aldrich) at 60°C for 24 h, rinsed with distilled water and finally sterilized in a steam autoclave. Prior to cell seeding, all scaffolds were prewetted by vacuum impregnation in cell culture medium for 2 h in a humidified incubator.

5.3.2 Human periost-derived cells (hPDCs)

hPDCs were isolated from periosteal biopsies of different donors, as described previously . This procedure was approved by the Ethics Committee for Human Medical Research (KU Leuven) and by the patients' informed consent. hPDCs were expanded in Dulbecco's modified Eagle's medium (DMEM) with high glucose (Invitrogen), containing 10% fetal bovine serum (FBS; Gibco), 1% sodium pyruvate (Invitrogen) and 1% antibiotic-antimycotic (100 units/ml penicillin, 100 mg/ml streptomycin and 0.25 mg/ml amphotericin B; Invitrogen).

5.3.3 Scaffold seeding

The cells were seeded at 5700 cells/cm² and passaged at 80–90% confluence. Prior to the 3D culture experiments, cells were harvested using Triple Express (Invitrogen) and drop-seeded by a single drop onto the scaffolds at a density of 200 000 cells/60 μ l drop, as performed in earlier studies (Papantoniou et al., 2013). 45 min after seeding, 60 μ l culture medium was added and 135 min later the medium volume was topped up to 1 ml. Seeded scaffolds were incubated overnight under standard culture conditions (37°C, 5% CO₂, 95% relative humidity) before being positioned in the perfusion chamber.

5.3.4 Bioreactor culture

Seeded scaffolds were cultured in the perfusion bioreactors for up to 21 days. The perfusion chamber was 26 mm long with a diameter of 6 mm, holding a single scaffold. This chamber was connected to an individual medium reservoir (disposable 50 mL Falcon tubes, BD Biosciences) containing 10 mL of cell culture medium via a Tygon1 (Cole Parmer, Antwerp, Belgium) tubing and a two-stop tubing (BPT, Cole Parmer) connected to a peristaltic pump (IPC-24, Ismatec, SA). Culture medium was refreshed every 2 days for the entire culture period. All seeded scaffolds were positioned 10mm from the inlet of the perfusion chamber so that a steady state flow profile was reached as shown in (Papantoniou et al., 2014a).

5.3.5 SEM imaging

The micro-porosity of the neotissue between cells and extracellular matrix was approximated by scanning electron microscopy (SEM) coupled with energy-dispersive X-ray (EDAX) analysis (FEI XL30 FEG) at 10 kV. Briefly, the cultures were rinsed twice with PBS, fixed with 2.5% glutaraldehyde (in PBS) for 1h, and postfixed in 1% osmium tetroxide for 2h before dehydrated in 50%, 75%, 95%, and 100% ethanol solutions. Finally, the samples were chemically dried with hexamethyldisilazane for 3 min and goldsputtered before SEM analysis.

5.3.6 Live/Dead Assay

The live/dead viability/cytotoxicity kit (Invitrogen) was employed to evaluate qualitatively cell viability and cell distribution and growth by fluorescence microscopy. Constructs were rinsed with 1 mL PBS after which

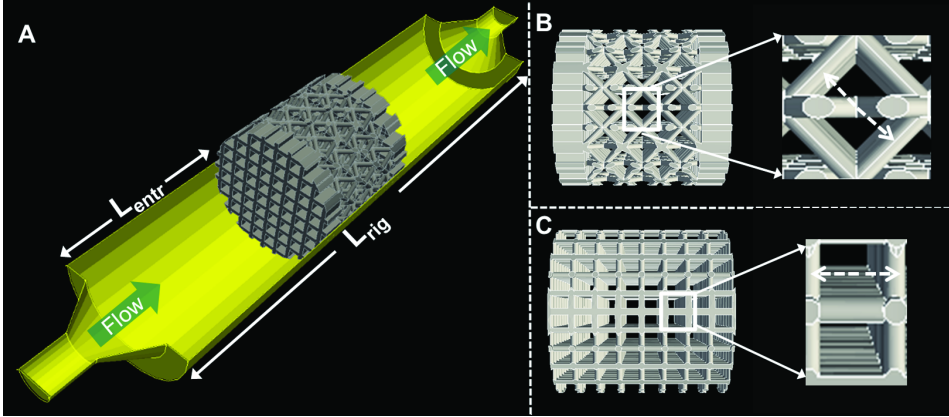


Figure 5.1: (A) Image indicating the the perfusion rig dimensions ($D_{rig}=6\text{mm}$, $L_{rig}=26\text{mm}$) and scaffold position which was $L=10\text{mm}$ from the entrance of the rig. Both scaffolds had the same external dimensions $D_{scaff}=6\text{mm}$ and $L_{scaff}=6\text{mm}$, also the same strut thickness was used for both pore designs were $D_{strut}=200\mu\text{m}$. (B) ‘Diamond’ scaffold pore size was $750\mu\text{m}$ from the centre of one strut to the other as shown by the dashed arrows. (C) ‘Square’ pore scaffold pore size was $650\mu\text{m}$.

they were incubated in the staining solution (0.5 ml Calcein AM and 2 ml Ethidium Homodimer in 1 mL PBS) for 20 min in normal cell culture conditions. The constructs were imaged using a Leica M165 FC microscope.

5.3.7 Computational framework

Neotissue growth with Level Set Method (LSM)

The evolution of the neotissue topology occurring during the growth process was numerically treated with the LSM which has been developed to deal with moving interfaces. This technique has been used here for its ability to track the front-line between neotissue and void space in a mesh-free manner. In this study, the simulated moving interface Γ represents the border between the neotissue domain Ω_{nt} and the void domain Ω_v . The principle of LSM is based on a continuous distance function φ defined on the whole domain Ω with the following properties:

$$\begin{cases} \varphi > 0, & \text{in } \Omega_{nt}. \\ \varphi < 0, & \text{in } \Omega_v. \\ \varphi = 0, & \text{on } \Gamma. \end{cases} \quad (5.1)$$

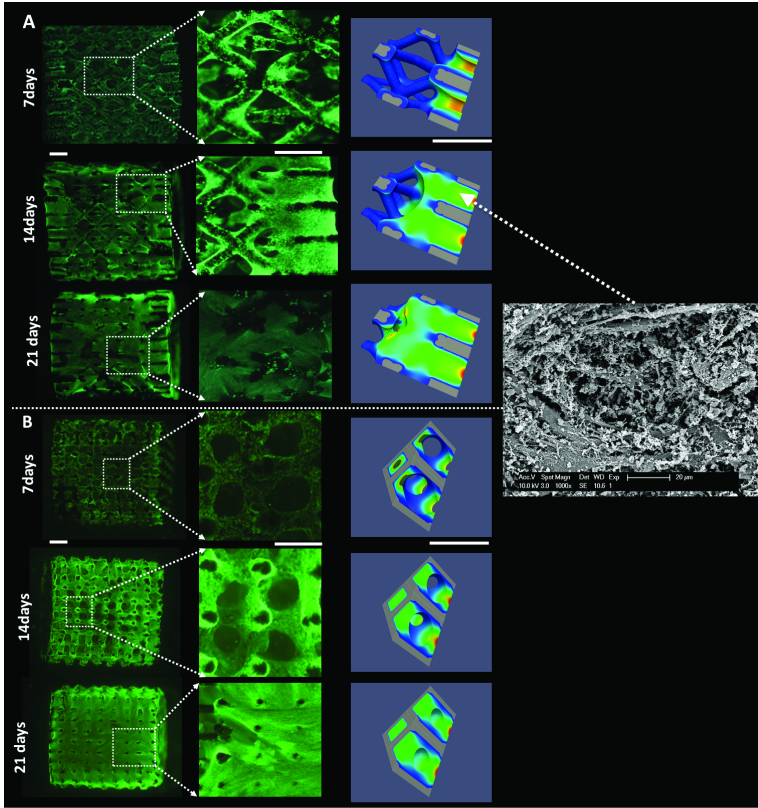


Figure 5.2: Live/dead staining indicating three dimensional neotissue growth during culture over a culture period of 21 days in perfusion bioreactors in two different scaffolds designs: **(A)** ‘diamond’ and **(B)** ‘square’. In both cases neotissue eventually fills the scaffold void by day 21, (scale bar = 800 μm). SEM indicates a representative microporosity of the growing neotissue.

To simulate the evolution of the system, the time dependent advection equation ?? is solved with a given velocity \mathbf{v}_G .

$$\begin{aligned} \frac{\partial \varphi}{\partial t} + \mathbf{v}_G \cdot \nabla \varphi &= 0 \\ \nabla \varphi \cdot \mathbf{n} &= 0 \end{aligned} \quad (5.2)$$

Neotissue growth kinetics are curvature-dependent meaning that neotissue grows faster where the curvature is higher and also that it does not grow if the curvature is negative or equal to zero. To tackle this, the advecting

velocity \mathbf{v}_G of equation ?? has the following expression:

$$\mathbf{v}_G = -V_G * \mathbf{n}_\Gamma \quad (5.3)$$

$$V_G = \begin{cases} \kappa, & \text{if } \kappa < 0. \\ 0, & \text{if } \kappa \geq 0. \end{cases} \quad (5.4)$$

with $\mathbf{n}_\Gamma = \frac{\nabla\varphi}{|\nabla\varphi|}$ representing the normal at the interface pointing towards the neotissue, and $\kappa = \nabla \cdot \mathbf{n}_\Gamma$ representing the mean curvature. Growth simulations were run thanks to the model developed in a previous study (Guyot et al., 2014) (chapter 4) providing several neotissue topologies. From these results, geometries corresponding to 10% to 90% of scaffold pore filling were taken as starting points for the flow simulations (see below).

Fluid flow model

Neotissue growth leads to changes in morphology affecting the fluid behavior over time. Two fluid flow regimes can be distinguished one within the void but also in the neotissue. In the void part, due to a low Reynolds number, the flow profile can be estimated with Stokes equation ??.

$$\begin{aligned} -\mu\Delta\mathbf{u} + \nabla p &= 0 \text{ in } \Omega_v \\ \nabla \cdot \mathbf{u} &= 0 \text{ in } \Omega_v \end{aligned} \quad (5.5)$$

Due to the presence of cells and extracellular matrix in the neotissue part (see Fig. 5.2), the flow profile in this region cannot be estimated with a simple Stokes equation. To address this we consider this region as a porous medium with a given permeability K_0 and so the flow profile will be governed by the Darcy equation ??.

$$\begin{aligned} \frac{\mu}{K_0}\mathbf{u} + \nabla p &= 0 \text{ in } \Omega_{nt} \\ \nabla \cdot \mathbf{u} &= 0 \text{ in } \Omega_{nt} \end{aligned} \quad (5.6)$$

In equations ?? and ??, μ represents the viscosity, \mathbf{u} the fluid velocity and p the pressure. Due to the LSM definition of the neotissue topology, the interface would not be conform with the computational mesh, and so equations ?? and ?? could be difficult to couple together. One solution to

this problem is to model the flow with a penalization technique and the Brinkman equation ??.

$$\begin{aligned} \frac{\mu}{K} \mathbf{u} - \mu \Delta \mathbf{u} + \nabla p &= 0 \text{ in } \Omega \\ \nabla \cdot \mathbf{u} &= 0 \text{ in } \Omega \end{aligned} \quad (5.7)$$

This technique is based on a penalization of the term K in the neotissue domain. For that purpose, a smooth space and time dependent Heaviside function H was calculated with the following equation:

$$H(\varphi) \begin{cases} 0, & \varphi < -\varepsilon \\ \frac{1}{2} + \frac{\varphi}{2\varepsilon} + \frac{1}{2\varepsilon} \sin\left(\frac{\pi\varphi}{\varepsilon}\right), & -\varepsilon < \varphi < \varepsilon \\ 1, & \varphi > \varepsilon \end{cases} \quad (5.8)$$

It should be noted that equation ?? does not take into account time, this corresponds to the fact that the flow is calculated only on given neotissue geometries in order to estimate the mechanical stimuli at that degree of scaffold filling. The parameter ε was taken to be equal to $1.5 \cdot h$, with h the mesh size.

K is then updated according to the following equation:

$$K(\mathbf{x}) = 10^{-4}(1 - H) + K_0 H \quad (5.9)$$

The permeability of the neotissue K_0 was calculated using a random fibers approximation to simulate the random unstructured cell and extracellular matrix construct. To tackle this issue, K_0 was estimated according to (Nabovati et al., 2009), based on a method to approximate the permeability of a random fibers web, resulting in the following expression for K_0 :

$$K_0 = 0.491 \delta^2 \sqrt{\frac{1 - \psi_0}{1 - \psi} - 1}^{-2.31} \quad (5.10)$$

In this equation, ψ represents the micro-porosity of the neotissue. According to (Nabovati et al., 2009) ψ_0 is called the ‘‘percolation threshold’’, and it corresponds to a threshold porosity where fluid flow is permitted through the micro-porous medium. We assumed that such a threshold did not exist, so ψ_0 was set to zero. An important parameter is δ , which corresponds to the average size of the micro-porosity of the neotissue. Two values for δ , 25 and 50 μm were used based on experimental SEM observations,

accounting for the fact that the micro-porosity could be affected by the culture environment. Finally, a poiseuille flow corresponding to the average inlet velocity was applied as a dirichlet boundary condition at the entrance of the domain. Symmetry boundary conditions ($\mathbf{u} \cdot \mathbf{n} = 0$) were applied on each lateral side, free flow condition at the exit of the domain, and wall boundary conditions on the scaffold struts ($\mathbf{u} = 0$).

Shear stress estimation

Wall shear stress τ at the interface between neotissue and void was calculated by:

$$\tau = \sqrt{\tau_{12}^2 + \tau_{23}^2 + \tau_{13}^2} \quad \text{where} \quad \tau_{ij} = \mu \left(\frac{\partial u_i}{\partial x_j} + \frac{\partial u_j}{\partial x_i} \right)$$

In addition the shear stress associated with the interstitial flow through the micro-porous neotissue τ_{in} was calculated based on the method presented in (Whittaker et al., 2009). The interstitial velocity magnitude $u_{in} = |\mathbf{u}|/\psi$ was calculated, assuming that the micro-porous neotissue is composed of cylindrical ducts of diameter δ . Hence, the flow profile in each duct can be seen as a Poiseuille flow with a local radial coordinate r , and the following velocity profile:

$$u_p = 2u_{in} \left(1 - \left(\frac{2r}{\delta} \right)^2 \right) \quad (5.11)$$

The inner neotissue shear stress would be:

$$\tau_{in} = \mu \left| \frac{\partial u_p}{\partial r} \right|_{r=\delta/2} \approx \frac{8\mu u_{in}}{\delta} \approx \frac{8\mu |\mathbf{u}|}{\delta\psi} \quad (5.12)$$

Implementation details

The full implementation of the model presented above has been carried out with Freefem++ (Hecht, 2012). For each geometry (diamond and square), the curvature driven growth model (Guyot et al., 2014) (chapter 4) was run. From these simulations, neotissue topologies corresponding to 10, 20, ..., 90% of scaffold filling were calculated and used as input for the fluid model using the Brinkman equation. The Brinkman equation was solved using the parallelization method of domain decomposition, where the problem is distributed over and solved on 12 cores.

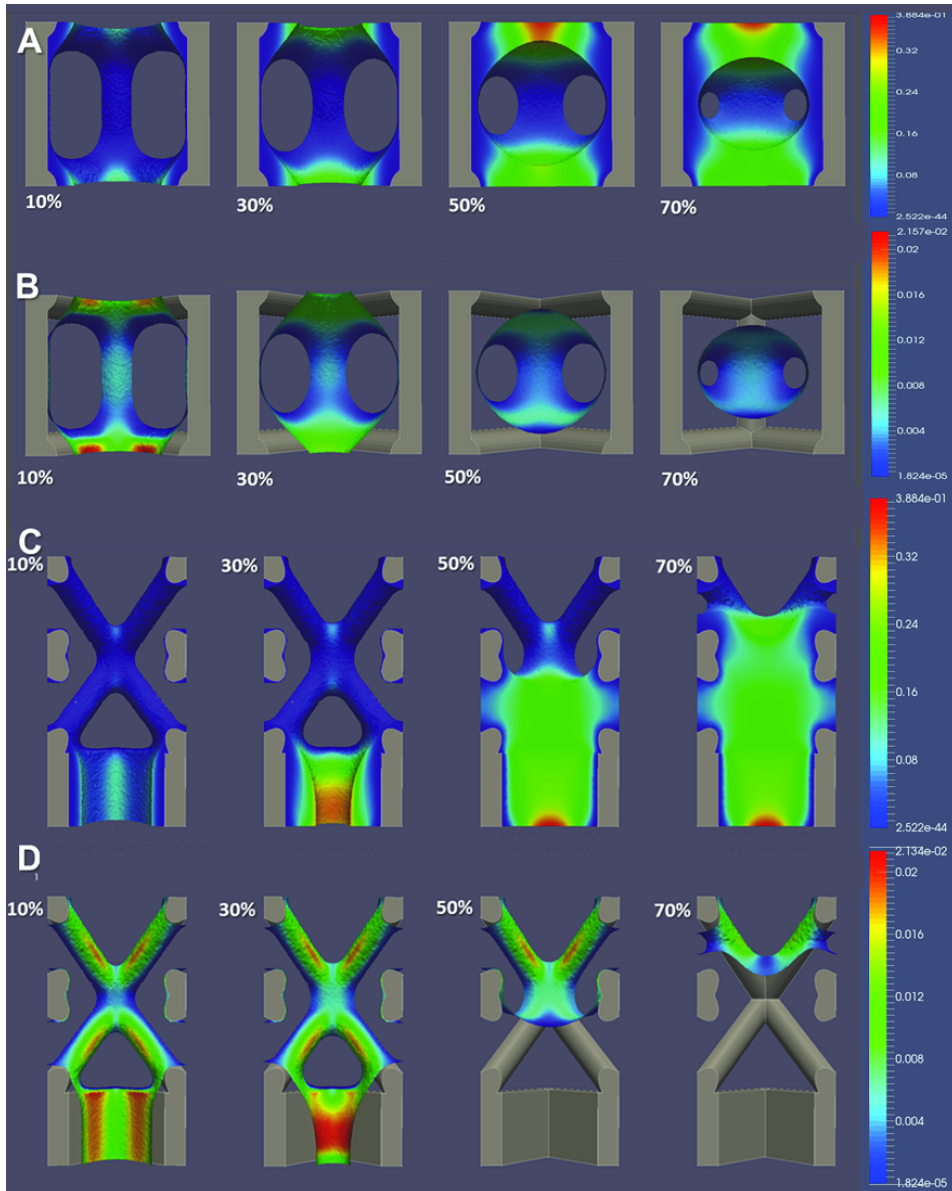


Figure 5.3: (A,C) Inner and (B,D) interface shear stress magnitude (Pa) and distribution during neotissue growth and gradual ‘closure’ of the void in scaffolds with (A,B) square and (C,D) diamond pore shape. Neotissue microporosity used for this simulation was $50\ \mu\text{m}$.

		Scaffold pore size (μm)	Average shear stress (mPa)	Inlet velocity ($\mu\text{m/s}$)
Surface shear stress	(Maes et al., 2009)	180	1.4	34
	(Cioffi et al., 2006)	100	3.28-3.94	53
	(Lesman et al., 2010)	500	11	5000
	(Nava et al., 2013)	300	5	100
	(Zermatten et al., 2014)	220	3.08	66
	(Hossain S, 2015)	1000	40	230
	This study, τ	600	3.4-8	1200
Single cell/ μ-porosity/ inner shear stress	(Zhao et al., 2014)	180	50-250	300
	(Jungreuthmayer et al., 2009)	96	30	235
	This study, τ_{in}	600	10-250	1200

Table 5.1: A comparison between empty scaffold shear stress values calculated in literature and interface shear stress values obtained in this study. In the second group the inner shear stresses obtained for the neotissue part were compared to literature shear stress values for bridging single cell models, please note that shear stress units are in mPa.

5.4 Results & Discussion

Live/dead images in Fig. 5.2 show typical 3D cell growth and neotissue formation over time during culture in a perfusion bioreactor for two different scaffold designs with square and diamond pore shapes. In both cases the initial scaffold void was substituted gradually by neotissue. Cells seeded on 3D scaffolds have been seen to be able to bridge across pores of 70 μm entering a 3D growth phase followed by neotissue formation in static conditions.

In previous studies we have also observed this behavior for bioreactor based cell cultures in scaffolds of larger pores ($\sim 750 \mu\text{m}$) (Papantoniou et al., 2014a,b). The growing neotissue is a permeable micro-porous structure as can be observed in the SEM image (Fig. 5.2). Neotissue growth will subsequently influence the fluid flow profile in the remaining scaffold void space but also the fluid flow derived shear stress distribution and magnitude within the neotissue itself. The flow rate used in this study was 1 ml/min, for which the cells used in this study have been observed to be able to grow up to 100% scaffold filling in a similar bioreactor set-up (Sonnaert et al.,

2014). In this study, 100% scaffold filling was indeed reached for both pore shapes as shown in Fig. 5.2. Their growth under a constant flow rate meant that cells experienced a cascade of increasing shear stresses until complete filling was reached. Two fluid flow regimes could be distinguished, one for free fluid flow and one within the micro-porous neotissue itself. Hence a dynamic multiphase approach was best suited to capture the aforementioned events.

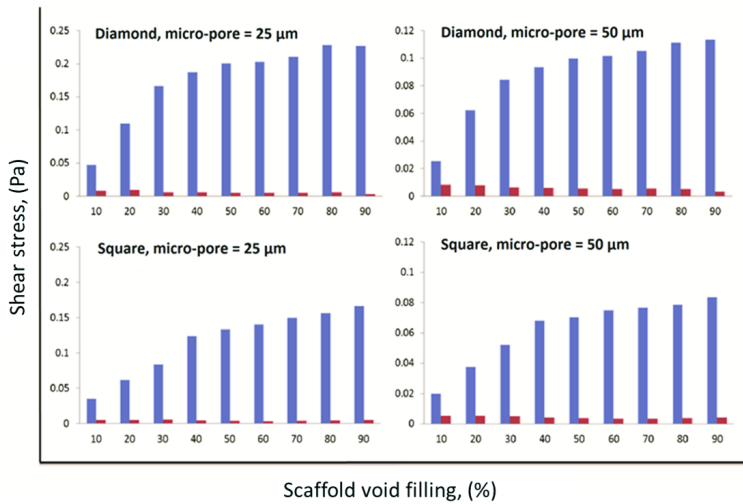


Figure 5.4: Average inner (blue bars) and interface (red bars) shear stress values for both scaffold geometries and micro-porosities investigated in this study for a range of scaffold void filling percentages.

Starting from two different scaffold designs, cell growth was simulated following a curvature-dependent growth mechanism (Bidan et al., 2012, 2013; Guyot et al., 2014) (chapter 4). Once coupled with fluid flow equations, computer simulations were run to study shear stress magnitude and distribution over time. The average inlet velocity used at the entrance of a single scaffold pore was (0.0012 m/s) and corresponded to a 1 ml/min perfusion flow rate for the geometric features of the bioreactor. Fig. 5.3 shows the gradual closure and the development of the correspondingly changing flow profiles for the two different scaffold designs. Shear stress values were determined both at the interface of the neotissue with the free flow domain and also within the neotissue itself. For the square design, the average interface shear stress values evolved from 0.0034 to 0.005 Pa while

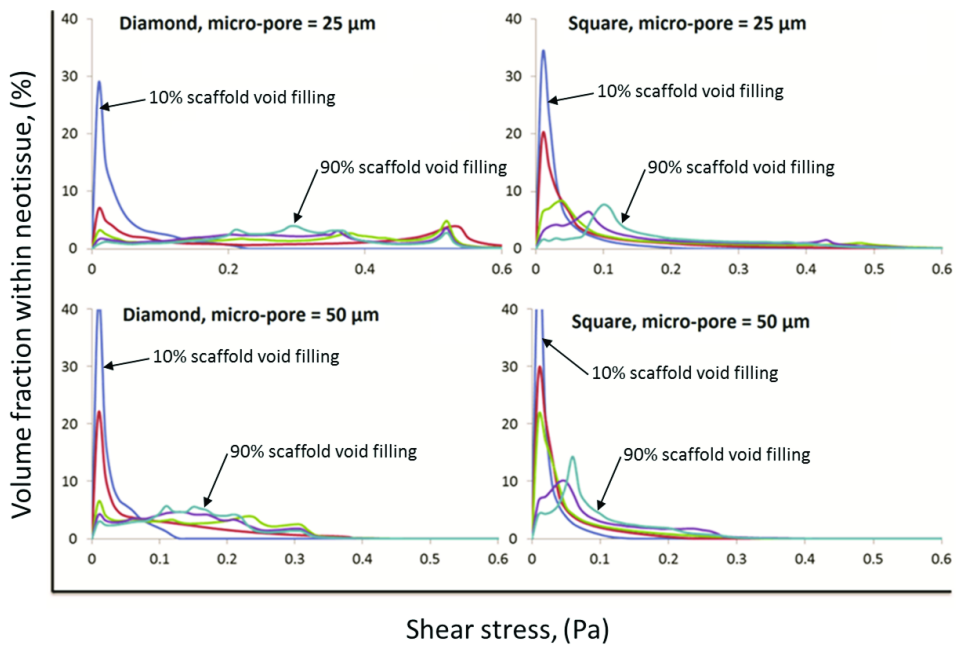


Figure 5.5: Shear stress distribution within the neotissue during growth. Different colors represent the filling percentage of the scaffold void during neotissue growth, (dark blue: 10%, mauve: 30%, green: 50%, purple: 70%, light blue: 90%.)

for the diamond design the average interface shear stress values evolved from 0.004 to 0.008 Pa during the filling of the scaffold macro-pores. Interface shear stress values reported here ranged from being comparable (for i.e. 10% filling) to two orders of magnitude higher (for i.e. 60% filling upwards) compared to the ones calculated for empty scaffold geometries in CFD modeling studies to date, as seen in Table 1. The average shear stresses developed within the growing neotissue were higher as expected, evolving from 0.04 to 0.28 Pa in the diamond pore shape scaffold and from 0.03 to 0.18 Pa in the square pore shape scaffold during the filling of the scaffold macro-pores. Additionally, the absolute values of the shear stresses were dependent on the micro-porosity of the neotissue domain (Fig. 5.4). Fig. 5.5 shows the shear stress distribution within the neotissue for different degrees of scaffold filling. Following this distribution for different degrees of scaffold filling (different colors), it demonstrates the shift from lower towards higher shear stress values within the neotissue due to the scaffold filling. The geometric homogeneity of the square pore scaffold was reflected on the shear stress distribution inside the neotissue which was narrower for the square

pore scaffolds than for the diamond pore scaffolds. Furthermore it should be noted that average inner shear stress values calculated here, especially in conditions with high degrees of scaffold filling, were closer to calculated values experienced by cells in the *in vivo* setting, reported to range from 0.8 Pa onwards (Weinbaum et al., 1994) or, as calculated more recently, from 0.1-10 Pa experienced by osteocytes due to fluid flow via canaliculi (Verbruggen et al., 2014). Interestingly, these shear stress levels also closely compared with recent work focusing on shear stresses experienced by single cells bridging across scaffold pore struts (Jungreuthmayer et al., 2009; Zhao et al., 2014).

In this study a number of simplifications were made that warrant further investigation in future work. First and foremost it will be necessary to couple the shear stress experienced by the cells (and calculated in this study) to the neotissue growth rate. Various studies have shown the influence of mechanical stimuli on the behavior of cells (McCoy and O'Brien, 2010; Rauh et al., 2011; Papanтониου et al., 2013). Adding a more detailed description of the neotissue constituents (cells and extracellular matrix (ECM)) and/or additional variables such as oxygen and glucose will allow to capture additional biological behavior observed in bioreactor experiments. These observations include the decrease in neotissue micro-porosity due to ECM production, the cellular lineage commitment and the oxygen consumption during culture.

5.5 Conclusion

In conclusion, this framework provides insight into the dynamic microenvironment to which cells are exposed in TE perfusion bioreactors. The development of such a model generates an additional level of control by allowing operators to deliver controlled shear stress magnitudes to cells during growth, e.g. by adapting flow rates during neotissue growth in order to maintain fixed shear stress magnitudes and profiles causing minimal culture environment variation. Moreover this model could be used for an *in silico* evaluation and screening of scaffold designs, including their impact on neotissue growth and exposure to stress profiles, avoiding costly and time consuming *in vitro* experiments.

CHAPTER 6

COUPLING CURVATURE-DEPENDENT AND SHEAR STRESS STIMULATED NEOTISSUE GROWTH IN DYNAMIC BIOREACTOR CULTURES: A 3D COMPUTATIONAL MODEL OF A COMPLETE SCAFFOLD.

Yann Guyot^{1,2}, Ioannis Papantoniou^{1,3}, Frank P. Luyten^{1,3}, Liesbet Geris^{1,2,4}

¹ Prometheus, Division of Skeletal Tissue Engineering, KU Leuven, Onderwijs en Navorsing 1 (+8), Herestraat 49 - PB813, B-3000, Leuven, Belgium.

² Biomechanics Research Unit, Universite de Liège, Chemin des Chevreuils 1 - BAT 52/3, B-4000 Liège, Belgium.

³ Skeletal Biology and Engineering Research Center, KU Leuven, Onderwijs en Navorsing 1 (+8), Herestraat 49 - PB813, B-3000, Leuven, Belgium.

⁴ Department of Mechanical Engineering, Biomechanics Section, KU Leuven, Celestijnenlaan 300C – PB 2419, B-3001 Leuven, Belgium.

Adapted from: Guyot, Y.; Papantoniou, I.; Luyten, F. P. & Geris, L. **Coupling curvature-dependent and shear stress stimulated neotissue growth in dynamic bioreactor cultures: a 3D computational model of a complete scaffold.** *Biomechanics and modeling in mechanobiology*,

Accepted for publication

6.1 Abstract

The main challenge in tissue engineering consists in understanding and controlling the growth process of *in vitro* cultured neotissues towards obtaining functional tissues. Computational models can provide crucial information on appropriate bioreactor and scaffold design but also on the bioprocess environment and culture conditions. In this study the development of a 3D model using the Level Set Method to capture the growth of a microporous neotissue domain in a dynamic culture environment (perfusion bioreactor) was pursued. In our model, neotissue growth velocity was influenced by scaffold geometry as well as by flow induced shear stresses. The neotissue was modeled as a homogenous porous medium with a given permeability and the Brinkman equation was used to calculate the flow profile in both neotissue and void space. Neotissue growth was modeled until the scaffold void volume was filled thus capturing already established experimental observations, in particular the differences between scaffold filling under different flow regimes. This tool is envisaged as a scaffold shape and bioprocess optimization tool with predictive capacities. It will allow control fluid flow during long-term culture, whereby neotissue growth alters flow patterns, in order to provide shear stress profiles and magnitudes across the whole scaffold volume influencing, in turn, the neotissue growth.

6.2 Introduction

Skeletal Tissue Engineering (TE) strategies hold a great promise for the regeneration of bone and cartilage based on the combination of bioreactors, 3D biomaterials and mesenchymal stem cells (MSCs). MSCs are progenitor cells crucial for skeletal TE applications due to their ability to undergo osteogenic and chondrogenic differentiation under the influence of various biochemical, biophysical and, importantly, biomechanical cues. Perfusion bioreactors have been extensively employed for the expansion and differentiation of MSCs providing sufficient mass transport for cell growth and differentiation (Sikavitsas et al., 2005; Grayson et al., 2011; Sonnaert et al., 2014). Furthermore, shear stress can determine early stem cell lineage commitment (Song et al., 2013) but also promote terminal osteogenic differentiation of bone marrow, periosteum and adipose derived MSCs and enhance extracellular matrix (ECM) deposition (McCoy and O'Brien, 2010; Rauh et al., 2011; Papantoniou et al., 2013). There is a substantial body of literature illustrating the osteogenic effect of mechanical stimulation

either due to fluid flow or mechanical compression (or stretching) on the differentiation of MSCs when cultured in dynamic environments seeded on 3D scaffolds *in vitro* (Wang and Chen, 2013; Delaine-Smith and Reilly, 2011).

In scaffold-based perfusion bioreactor culture, 3D cell growth and neotissue formation has been observed to begin with 2D cell proliferation on the scaffold strut surface. Subsequently, cells bridge scaffold struts and start growing towards the pore void followed by ECM deposition. Eventually, 3D cell growth will result in scaffold void filling, something that has been studied recently using computed tomography imaging techniques (Voronov et al., 2012; Papantoniou et al., 2014b). The calculation of wall shear stress values in empty scaffold geometries are therefore indicative of the shear stress experienced by cells during early culture time (Truscello et al., 2011). A current challenge to further advance and utilize computational modeling strategies in the TE field is to comprise a domain composed of cells and ECM (a growing permeable neotissue) on real 3D scaffold geometries. There are intriguing 2D studies investigating this (Sacco et al., 2011; Hossain et al., 2015) however it was recently shown that without the third dimension, model parameters were overestimated losing accuracy in the representation of neotissue growth (Nava et al., 2013).

Computational fluid dynamics (CFD) modeling has been extensively used in the field of TE (for review see (Hutmacher and Singh, 2008; Hossain et al., 2012; Patrachari et al., 2012)). The quantification of flow-associated shear stresses as well as their spatial distribution within various 3D scaffold geometries has been thoroughly investigated in perfused bioreactor setups (Raimondi et al., 2004; Porter et al., 2005; Boschetti et al., 2006; Cioffi et al., 2006; Jungreuthmayer et al., 2009; Maes et al., 2009; Voronov et al., 2010). In previous studies, local shear stresses were defined as a function of flow rate of the culture medium, bioreactor configuration, porosity and porous scaffold micro-architecture (Voronov et al., 2010; Pham et al., 2012). Most 3D CFD studies to date only use empty scaffold geometries to calculate shear stress magnitude and distribution across the empty scaffold surface i.e. wall shear stress. The aforementioned studies do not take into account the transient nature of the 3D neotissue domain as a result of neotissue growth which has been observed experimentally (Papantoniou et al., 2013). There have been few attempts to capture 3D neotissue growth on scaffolds, limited to gradually increasing scaffold struts (Lesman et al., 2010), representing

the neotissue layer as an impermeable domain. A recent interesting study describes the growth of a ‘biomass’ domain (similar to what we term neotissue in this study) whose growth was coupled to oxygen concentration and shear stress (Nava et al., 2013).

In addition to flow associated shear stress, neotissue growth kinetics have been also linked to the geometric features of scaffolds. Pore size (Zeltinger et al., 2001b), pore shape (Knychala et al., 2013), and more specific features such as local curvature (Rumpler et al., 2008; Gamsjager et al., 2013) have been demonstrated to control cell fate both for *in vitro* (Rumpler et al., 2008; Guyot et al., 2014) and *in vivo* applications (Bidan et al., 2012) (Bidan et al. 2012). Building on our previous studies where we investigated the effect of local curvature on *in vitro* 3D growth (Guyot et al., 2014) and where we used the evolving neotissue growth in a 3D scaffold to accurately determine the shear stress values in both the void space and the neotissue during the bioreactor culture process (Guyot et al., 2015), this study demonstrates the added value of using also the shear stress as a parameter that influences the neotissue growth. Hereto this study shows the development of a Level Set based computational tool able to capture the difference in growth of a microporous neotissue domain in a dynamic culture environment (perfusion bioreactor) under different flow rates. Capturing this difference is only possible by the explicit incorporation of flow-induced shear stresses as a parameter in the calculation of the neotissue growth velocity (alongside the scaffold geometry which was already present (Guyot et al., 2014)). This tool provides the ability to steer fluid flow during long term culture in order to provide given shear stress profiles and magnitudes across the whole scaffold volume.

6.3 Methods

In this section, the model describing the neotissue growth, the calculation of the flow-induced shear stresses and the influence of the latter on the former will be explained.

6.3.1 Neotissue growth via the Level Set Method

The growth induced changes in the neotissue topology during the culture process can be seen as a moving interface between two different domains (Sethian, 1996): in this study, one domain represents the neotissue volume Ω_{nt} , and the other one is the void Ω_v , separated by an interface Γ , with a

normal \mathbf{n}_Γ (see Fig. 6.1B). The Level Set Method is a technique that has been developed to deal with this kind of moving interfaces and it is used in the context of this study to simulate the evolution of the frontline Γ between neotissue and void space in a mesh-free manner. The principle of the LSM consists in defining a signed distance function φ in $\Omega = \Omega_{nt} \cup \Omega_v$ with the following properties:

$$\begin{cases} \varphi > 0, & \text{in } \Omega_{nt}. \\ \varphi < 0, & \text{in } \Omega_v. \\ \varphi = 0, & \text{on } \Gamma. \end{cases} \quad (6.1)$$

In order to capture the evolution of the moving interface Γ , the following transient advection equation is solved with a given growth velocity \mathbf{v}_G .

$$\begin{aligned} \frac{\partial \varphi}{\partial t} + \mathbf{v}_G \cdot \nabla \varphi &= 0 \\ \nabla \varphi \cdot \mathbf{n} &= 0 \end{aligned} \quad (6.2)$$

With $\mathbf{v}_G = -V_G * \mathbf{n}_\Gamma$, and $\mathbf{n}_\Gamma = \frac{\nabla \varphi}{|\nabla \varphi|}$. The expression of the growth velocity magnitude will be described later. The initial configuration of the distance function corresponds to a homogenous single cell layer over the scaffold struts with a thickness equal to 20 μm (Darling and Guilak, 2008). The time discretization of equation ?? was done using the backward Euler method and the advection term was treated with the method of characteristics. For more details about the implementation, please refer to (Guyot et al., 2014) (chapter 4).

6.3.2 Shear stress distribution

During dynamic culture, the neotissue grows, eventually filling up the whole scaffold void. These changes affect the flow patterns developed, depending on the presence (or not) of neotissue and so the flow profile has to be treated differently in Ω_{nt} and Ω_v (as described in detail in (Guyot et al., 2015)). In Ω_v , due to a low Reynolds number ($\text{Re} < 1$), the flow profile was approximated via the Stokes equation ?. In Ω_{nt} , the complex structure of the neotissue can be seen as a homogenous porous medium with a given permeability K_0 , leading to the flow profile being calculated with the Darcy equation ?. According to the definition of the LSM, the interface Γ is never conforming to the computational mesh, resulting in difficulties to

couple equation ?? and ?? together with suitable boundary conditions at the interface. To overcome this, the Brinkman equation ?? was used to calculate the flow profile in the whole domain Ω (see Fig. 6.1C). A no-slip boundary condition was applied on the scaffold surface as well as on the chamber walls. The scaffold was placed at a sufficient distance from the inlet avoiding refluxes occurring at the entrance of the scaffold (Papantoniou et al., 2014a), so the boundary condition for the inflow was set to a Poiseuille profile with a velocity \mathbf{u} corresponding to the given flow rate Q .

$$\begin{aligned} -\mu\Delta\mathbf{u} + \nabla p &= 0 \text{ in } \Omega_v \\ \nabla \cdot \mathbf{u} &= 0 \text{ in } \Omega_v \end{aligned} \quad (6.3)$$

$$\begin{aligned} \frac{\mu}{K_0}\mathbf{u} + \nabla p &= 0 \text{ in } \Omega_{nt} \\ \nabla \cdot \mathbf{u} &= 0 \text{ in } \Omega_{nt} \end{aligned} \quad (6.4)$$

$$\begin{aligned} \frac{\mu}{K}\mathbf{u} - \mu\Delta\mathbf{u} + \nabla p &= 0 \text{ in } \Omega \\ \nabla \cdot \mathbf{u} &= 0 \text{ in } \Omega \end{aligned} \quad (6.5)$$

This technique can be seen as a penalization method, indeed, when K is equal to the neotissue permeability K_0 in Ω_{nt} , it makes the Stokes term in ?? negligible. At the contrary, when K is set to a highest value in Ω_v , it leads to the Darcy term to be close to zero. To avoid numerical problems, this switch between the two values was implemented using a space and time dependent smeared out Heaviside function H (eq. ??), and K was updated according to this function ?? ($\varepsilon = 1.5 \times h$, with h the mesh size).

$$H(\varphi) = \begin{cases} 0, & \varphi < -\varepsilon \\ \frac{1}{2} + \frac{\varphi}{2\varepsilon} + \frac{1}{2\varepsilon} \sin\left(\frac{\pi\varphi}{\varepsilon}\right), & -\varepsilon < \varphi < \varepsilon \\ 1, & \varphi > \varepsilon \end{cases} \quad (6.6)$$

$$K(\mathbf{x}) = 10^{-4}(1 - H) + K_0H \quad (6.7)$$

The parameter K_0 was estimated using the random fibers theory approximation. In (Nabovati et al., 2009), the authors provide an

approximation of the permeability of a porous media made of a random fiber web:

$$K_0 = 0.491\delta^2 \sqrt{\frac{1 - \psi_0}{1 - \psi} - 1}^{2.31} \quad (6.8)$$

In this equation, ψ represents the porosity of the media (neotissue, assumed to be equal to 90% in this study, which is in the range of porosities of soft tissues and hydrogels) and ψ_0 corresponds to a percolation threshold or a threshold porosity where flow is permitted (set to zero in this study). Finally, δ represents the micro-pore size of the neotissue and was set to 50 μm , assuming the pore size equal to half to one third of the size of a fully spread cell of the type used in this study (Eyckmans et al., 2012). In this study, we distinguished two different wall shear stresses acting on cells depending on their location. The first one (τ) is the shear stress acting on the interface due to the different flow profiles from either side and is calculated with the usual definition:

$$\tau = \sqrt{\tau_{12}^2 + \tau_{23}^2 + \tau_{13}^2} \quad \text{where} \quad \tau_{ij} = \mu \left(\frac{\partial u_i}{\partial x_j} + \frac{\partial u_j}{\partial x_i} \right)$$

The second one (τ_{in}) is the shear stress acting within the neotissue, it is associated with the interstitial flow through the micro-porous neotissue and is approximated following the method presented in (Whittaker et al., 2009). This method is based on the fact that the micro-porous neotissue is assumed to be composed of cylindrical ducts of diameter δ . Since the Darcy equation just gives the average (Darcy) velocity \mathbf{u} , the interstitial velocity magnitude u_{in} is calculated from results of equation ?? and is turned into a Poiseuille velocity profile (u_p) in a cylindrical channel in order to have an analytical expression of local wall shear stress (on the wall of the cylindrical ducts, representing here the micro-pores), allowing for the estimation of τ .

$$u_{in} = |\mathbf{u}|/\psi \quad (6.9)$$

$$u_p = 2u_{in} \left(1 - \left(\frac{2r}{\delta} \right)^2 \right) \quad (6.10)$$

$$\tau_{in} = \mu \left. \frac{\partial u_p}{\partial r} \right|_{r=\delta/2} \approx \frac{8\mu u_{in}}{\delta} \approx \frac{8\mu |\mathbf{u}|}{\delta\psi} \quad (6.11)$$

6.3.3 Neotissue growth velocity

A key parameter of the study is the local growth velocity of the neotissue. In (Guyot et al., 2014) (chapter 4), this space dependent velocity was only depending on the local mean curvature of the interface as it has been shown in (Bidan et al., 2012; Rumpler et al., 2008). Another important growth influencing factor is the local shear stress on cells. In (Nava et al., 2013), authors present a biomass growth model for cartilage describing an interface moving in time in function of the fluid-induced shear stress and in (Chapman et al., 2014) the authors introduce a growth model for cell aggregates in hollow fiber bioreactors where cell population growth increased or decreased depending on wall shear stresses experienced by cells. In this study, a similar approach is used and the local neotissue growth velocity magnitude V_G is described as a function of both the mean curvature and the flow-induced shear stress:

$$V_G = A \times f(\tau) \times g(\kappa) \quad (6.12)$$

The neotissue growth velocity parameter A was estimated from the experimental data obtained for the low flow rate results obtained in (Papantoniou et al., 2014b) using a trial and error approach and was set equal to $4.10^{-14}m^2/s$. As described extensively in (Guyot et al., 2014), the basis of the influence of curvature on the neotissue growth comes from the observation that neotissue grows faster where the curvature is higher and that it does not grow if the curvature is negative or equal to zero (Bidan et al., 2013). The mean curvature influence function $g(\kappa)$ can therefore be expressed mathematically as follows:

$$g(\kappa) = \begin{cases} \kappa, & \text{if } \kappa < 0. \\ 0, & \text{if } \kappa \geq 0. \end{cases} \quad (6.13)$$

where κ is the local mean curvature ($\kappa = \nabla \cdot \mathbf{n}_\Gamma$) and the second row of equation ?? depicts that there is no growth when the curvature is null or negative. The negative sign in equation ?? comes from the fact that according to our definition of φ , the normal \mathbf{n}_Γ points toward neotissue, so growth has to be towards the opposite of $\nabla\varphi$. The surface shear stress influence function $f(\tau)$ (unit less) was inspired by (Nava et al., 2013) (Fig. 6.1D) and defined as a continuous function.

Parameter	Value	References
Neotissue porosity, ψ	90%	(Guyot et al., 2015)
Neotissue micro-pore size, δ	50 μm	(Guyot et al., 2015)
Neotissue growth rate, A	$4 \cdot 10^{-14} \text{m}^2/\text{s}$	Determined from (Papantoniou et al., 2014b)
Minimal shear stress value enhancing neotissue growth, α_1	0.01	Determined from (Chapman et al., 2014)
Maximal shear stress value enhancing neotissue growth, α_2	0.03	Determined from (Chapman et al., 2014)
Detrimental shear stress value, α_3	0.05	Determined from (Chapman et al., 2014)

Table 6.1: Model parameters used for the calculation of the neotissue growth rate v_G .

$$f(\tau) = \begin{cases} 0.5 + \frac{0.5\tau}{\alpha_1} & 0 \leq \tau < \alpha_1 \\ 1 & \alpha_1 \leq \tau < \alpha_2 \\ \frac{\tau - \alpha_3}{\alpha_2 - \alpha_3} & \alpha_2 \leq \tau < \alpha_3 \\ 0 & \alpha_3 \leq \tau \end{cases} \quad (6.14)$$

This function was established in order to have an optimal shear stress influence that enhances the growth ($\alpha_1 \leq \tau < \alpha_2$), and a critical threshold ($\alpha_3 \leq \tau$) above which shear stress inhibits the cells and growth cannot occur anymore, in this study α_1 , α_2 and α_3 were respectively set to 0.01, 0.03 and 0.05 Pa (Chapman et al., 2014). Table 6.1 summarizes all the parameters used in the calculation of the neotissue growth velocity V_G .

6.3.4 Implementation

The full model was implemented with the free partial differential equation solver FreeFem++ (Hecht, 2012). The computational domain (see Fig. 6.1A) chosen consisted of the part of the perfusion bioreactor chamber comprising the entire scaffold including 2mm of the chamber at each scaffold side. This was done in order to avoid numerical refluxes and was meshed with approximately 3 million tetrahedrons. The numerical problem was solved in parallel using a 12 cores facility. In order to avoid unnecessary computational effort, the Brinkman equation was solved on only one quarter

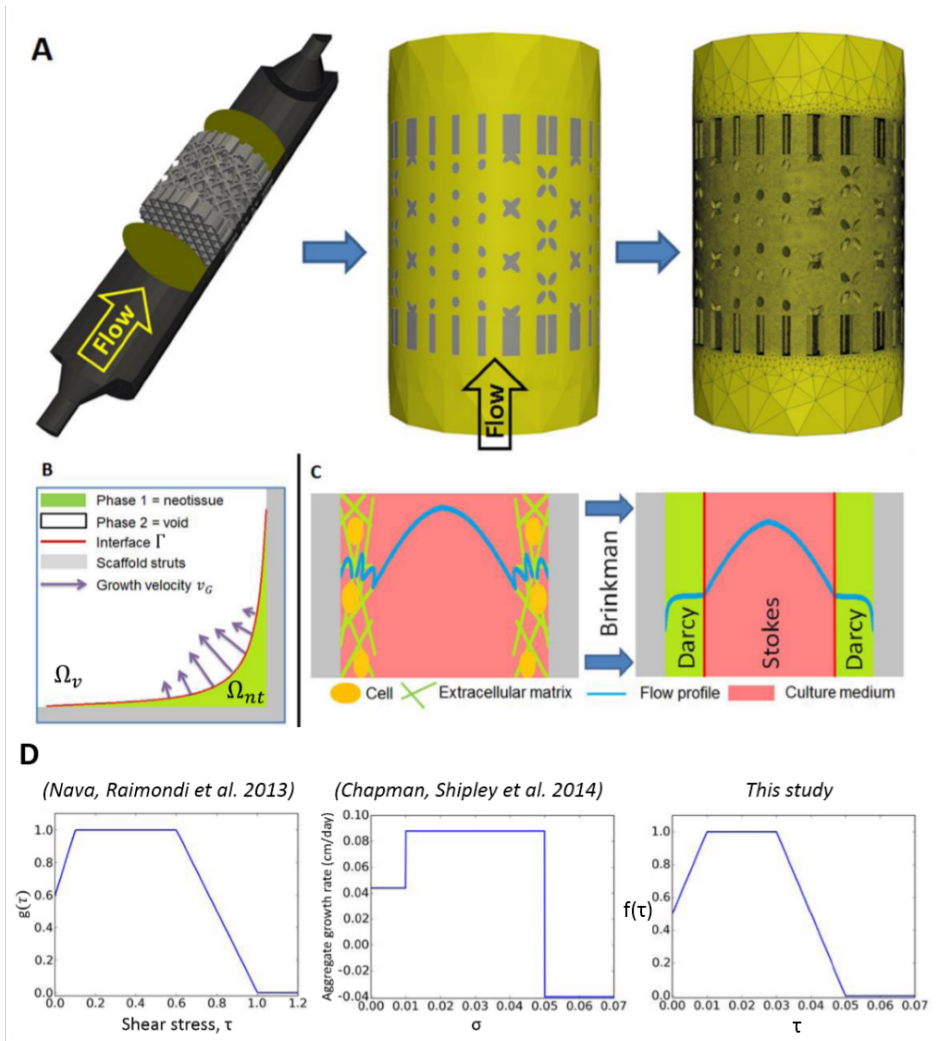


Figure 6.1: (A) Representation of the scaffold and the bioreactor chamber, the region of interest is delimited by two yellow circles. The scaffold is then removed from a cylinder representing the delimited area. Finally, a mesh is created in the computational domain. (B) Schematic representation of curvature driven neotissue growth using the Level Set Method. (C) Schematic representation of the Brinkman approximation used in this study. (D) The influence of shear stress on the neotissue growth velocity in this study (right) is a combination of the continuous shape proposed by (Nava et al., 2013) (left) and the values by (Chapman et al., 2014) (middle).

of the full mesh cut along the flow axis and with respect to symmetrical boundary condition.

6.3.5 Summary of Experimental set-up

In this study, results presented in (Papantoniou, Sonnaert et al. 2014) were used in a first calibration and validation set-up. The set-up of the experiment is briefly repeated below. Three-dimensional additive manufactured open porous Ti6Al4V scaffolds (diameter = 6 mm, h = 6 mm, porosity = $73\% \pm 1\%$, strut diameter = 245 ± 2 μm and pore size = 755 ± 3 μm), produced on an in-house developed selective laser melting (SLM) machine (Van Bael et al., 2011) were used. Human Periosteal Derived Stem Cells (hPDCs, one of the known sources of MSCs) were isolated from periosteal biopsies of different donors as described previously (Eyckmans and Luyten, 2006) and expanded in culture flasks. When a sufficient amount of these cells was produced in this 2D culture (number of population doublings = 15), cells were harvested by trypsinization with Tryple Express (Invitrogen) and seeded on the scaffolds, which marked the start of the bioreactor experiment. The TE constructs were cultured in an in-house developed bioreactor for 14, 21 and 28 days under dynamic culture conditions ($n = 9$ per flow rate – triplicates per time point). Two different perfusion flow rates were used: 4 mL/min (Q_1 , high) and 0.04 mL/min (Q_2 , low). After culture, three constructs for each time point were prepared for Contrast-Enhanced nanofocus Computed Tomography (NEnanoCT) imaging (Kerckhofs et al., 2013) allowing for visualization and quantification of the neotissue volume formed inside the constructs.

6.4 Results

The model was run for different flow rates according to the experimental set up described in (Papantoniou et al., 2014b). Simulations show a significant difference between the two conditions regarding the total amount of neotissue that has been produced at different time points (Fig. 6.2 and Fig. 6.3). Indeed, under the high flow rate, the local shear stress acting on the neotissue interface is higher than for the lowest flow rate, resulting in an acceleration of neotissue growth. Although differences can be observed between the simulations and experiments, the simulations are capable of capturing the experimentally observed differences between the two flow rates in terms of volume filling (Fig. 6.3B). The model was also able to compute quantitative data (shown in Fig. 6.4) regarding important culture variables

during neotissue growth such as pressure drop across the scaffold along the flow axis, average surface and inner shear stresses, giving an overview of different mechanical stimuli acting on cells over culture time.

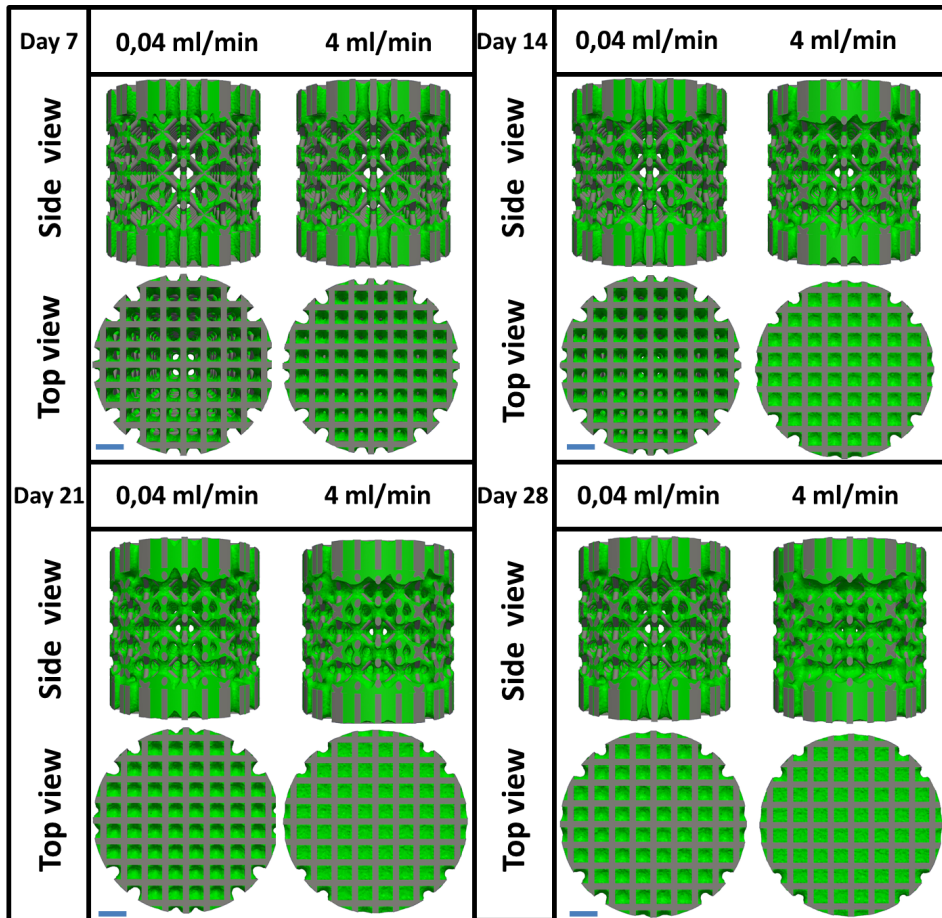


Figure 6.2: Neotissue growth (green) on scaffold (grey) at different time points for two different flow rates and two different views (direction of flow rate is from bottom to top in side view). Gradual scaffold pore closure can be observed. Scale bar represents 1 mm.

The pressure drop (Fig. 6.4A) across the scaffold varied from almost 4 Pa in the first days of culture to 11 Pa at day 28 for the high flow rate Q_1 , while it ranged from 0.03 Pa to 0.08 Pa for the low flow rate Q_2 in an equivalent period of time. The surface shear stresses (Fig. 6.4B) and

inside shear stresses (Fig. 6.4C) differed by a factor of 100 between the two different flow rates. For both flow rates, the inner shear stress, the stress acting on cells embedded into the neotissue, can be around 3 (for early time points) to 20 (for late time points) times bigger than the interface shear stress acting on cells at interface in contact with the free flow. Fig. 6.5 shows how the flow regime changes from when the scaffold is almost empty (Fig. 6.5A) to where it is partially filled (Fig 6.5B). Fig 6.6 depicts the local growth velocity v_G showing the influence of the distributed shear stress as well as the local mean curvature of the surface. Maximal neotissue growth velocities of 3 and 7 $\mu\text{m}/\text{day}$ were obtained for the low and high flow rates respectively.

6.5 Discussion

Understanding spatiotemporal cell growth in dynamic cultures constitutes a challenge in TE, in particular the quantification, distribution and interplay between scaffold geometry, shear stress and neotissue growth. The present model provides a foundation that will allow the quantitative investigation of the effect of shear stresses on cell growth and ECM production, which today is still not well understood. The most important contribution of this study is the extension of a previously developed model of local curvature-dependent neotissue growth to incorporate the influence of the local shear stresses on the neotissue growth, on complete scaffolds in 3D. The importance of 3D models in comparison to 2D has been shown by (Nava et al., 2013), the latter suffering from a lack of accurate representation which leads to loss of information and an incorrect parameter estimation. Recent experimental observations have revealed that hPDCs (the MSC source used in this study) may grow in the third dimension by bridging scaffold struts, leading to complete filling of scaffold pores when cultured in perfusion bioreactors in glucose based growth medium (Sonnaert et al., 2014) and in growth factor containing osteogenic medium (Papantoniou et al., 2013). NanoCT imaging has been employed to confirm that complete pore closure could be obtained depending on bioreactor operating conditions (Papantoniou et al., 2014b). Similar 3D cell growth behavior upon seeding on scaffolds has been also observed for other cell types such as human bone marrow MSCs (Zhao and Ma, 2005; Li et al., 2009), primary fibroblasts (Joly et al., 2013) and cell lines such as MC3T3-E1 pre-osteoblast cells (Kommareddy et al., 2010). This opens the possibility to create 3D *in vitro* tissue-like structures where cells may grow independently of the initial scaffold surface allowing

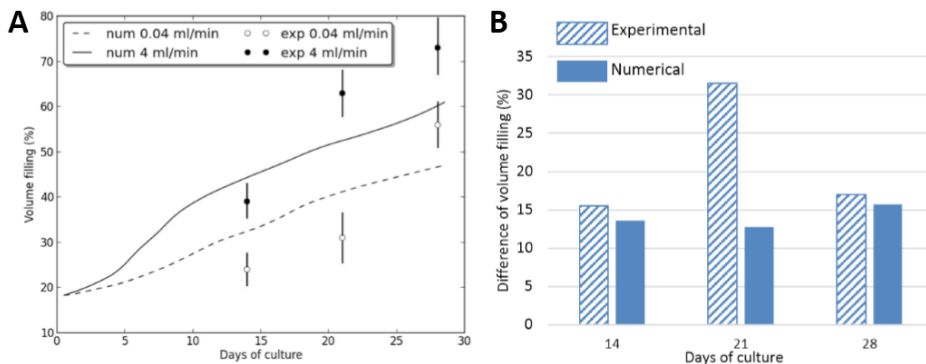


Figure 6.3: Comparison between simulations and experimental results (Papantoniou et al., 2014b). **(A)** Evolution of volume filling over culture time for the two different flow rates used in this study. Experimental results are presented through the mean and standard deviation ($n=3$). **(B)** Quantitative differences in volume filling between the different flow rates, indicating that the simulated differences are similar to those experimentally observed.

for the study of the interaction between cells and their own ECM and the culture environment. Additionally, this means that when simulating the experimentally observed void filling due to 3D neotissue growth, models should take into account the specificity of the experimentally used cell type (Chapman et al., 2014). In this work we attempt to investigate this for adult stem cell types in particular for hPDCs.

Neotissue growth kinetics in 3D dynamic and scaffold-based culture set ups, has been linked with oxygen level (Zhao and Ma, 2005), shear stress (Nava et al., 2013) and scaffold geometry - in particular curvature (Bidan et al., 2013; Knychala et al., 2013). In our study, oxygen was not investigated since for the flow rate and scaffold dimensions used in this work, taking into account the oxygen consumption rate of hPDCs (Lambrechts et al., 2014), there is no significant oxygen drop detected from inlet to outlet. Therefore the assumption that the whole cell population is exposed to the same level of dissolved oxygen tension (atmospheric) seems to be justified. When other flow regimes and/or other cell types will be studied, this assumption has to be re-evaluated. An additional assumption was the existence of an initial single cell layer at the start of the simulations. This layer was assumed to be 20 μm based on 2D suspended MSC diameter values (Darling and Guilak, 2008), leading to an initial filling percentage of 18%. Provided that a high

number of cells is used for cell seeding (Chen et al., 2011), a homogeneous distribution can indeed be achieved across the scaffold. This step has been studied in detail for regular geometry scaffolds (Melchels et al., 2011). The initial filling percentage is likely an overestimation of the real filling and is (in its current way of calculating) dependent on the available surface of the scaffold under study. With the currently used measurement technique (NanoCT) the experimental value for the initial filling cannot be obtained due to the absence of matrix produced by the cells immediately after seeding. This parameter therefore merits further study in future work. Neotissue shrinkage/loss due to cell death was not incorporated in the presented model, however, there is a possibility that this shrinkage/loss occurs for those cases where excessively harsh culture conditions are developed i.e. very low dissolved oxygen tension (anoxia) and glucose concentration or high lactate concentration (Flaibani et al., 2009). Further efforts are required in order to incorporate the aforementioned physico-chemical components in our model. However this is out of the scope of the present study, where geometry and fluid dynamics are the main regulators of neotissue growth.

In this study neotissue growth velocity was coupled to the local scaffold topography (curvature) (Guyot et al., 2014) (chapitre 4) and local fluid flow induced shear stress. Shear stress was modeled to enhance increasingly neotissue growth from 0 to α_1 reaching a maximum value between α_1 and α_2 (equal to 0.01 and 0.03 Pa respectively). The lower amount of neotissue observed at the periphery of the scaffolds is due to the low values of fluid flow induced shear stresses at that location. This in turn is due to the flow demonstrating a Poiseuille profile when entering the scaffold, thereby positively influencing to a greater extent the neotissue formation at the center of the scaffold. When the shear stress reaches α_3 threshold equal to 0.05 Pa, its effect on neotissue growth was modeled to change into a prohibitive one with decreasing neotissue growth for increasing shear stresses beyond α_3 . Experimental observations of 0.015 Pa as an optimum shear stress level for human bone marrow MSCs cultured in perfusion bioreactors confirmed this hypothesis (Li et al., 2009). A similar range of shear stresses has been reported for human bone marrow MSCs by (Grayson et al., 2011) although these values referred to empty scaffold geometries. We have recently experimentally observed the adverse effects of excessive shear stress on neotissue growth by hPDCs in perfusion bioreactors resulting in inhomogeneous tissue engineered constructs (Papantoniou et al., 2014b). This was observed for shear stress values in excess of 0.05 Pa

which is the threshold value used in this study. Interestingly (McCoy et al., 2012) estimated a critical threshold for human bone MSC detachment from irregular scaffolds at 0.088 Pa closely matching the one used here, taking into account the differences in scaffold architecture and cell type.

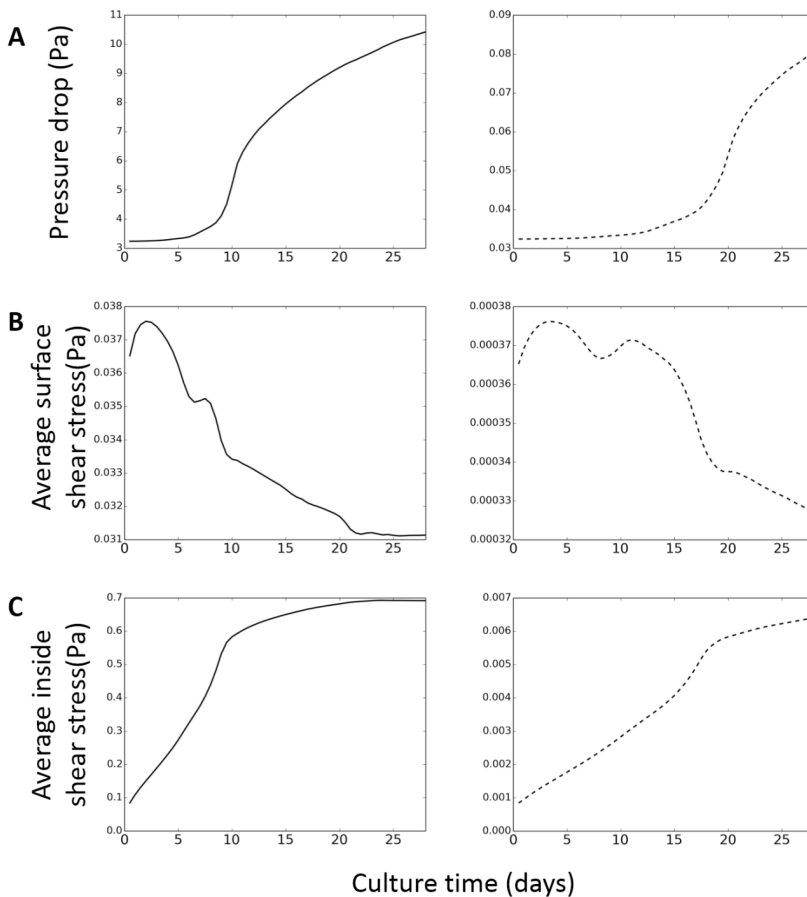


Figure 6.4: Mechanical characterization of the predicted tissue growth for flow rates Q_1 (4ml/min, left) and Q_2 (0.04ml/min, right). **(A)** Pressure drop between the entrance and the exit of the scaffold. **(B)** Average neotissue surface shear stress. **(C)** Average inside neotissue shear stress. Notice the difference in scale on the vertical axes between left and right figures.

The growth velocity term A was estimated in a trial and error fashion based on in-house experimental observations (Papantoniou et al., 2014b)

measuring neotissue growth on the simulated scaffold for the low flow rate Q_2 . The prediction obtained for the high flow rate Q_1 shows an increase in volume filling, similar to the experimental data (Fig. 6.3B). The discrepancy observed between experimental and computationally-derived neotissue growth kinetics seen in Fig. 6.3 could be attributed to numerical and physical factors. For the former (numerical factor), we did not go through an objective and rigorous optimization process to find the value for A because of the insufficient quantity of experimental data available. In a follow-up study, dedicated experimental data will be generated to parametrize the model. As to the latter (physical factor), neotissue growth kinetics do not solely depend upon scaffold geometry and shear stress magnitude. The introduction in the model of additional physico-chemical parameters that are well known for their influence on neotissue growth such as dissolved oxygen tension (Grayson et al., 2008a; Dos Santos et al., 2010), glucose concentration (Saki et al., 2013) and lactate concentrations in the medium, could help to improve the agreement between experimentally and computationally determined values. Even though for the experiments used in this study (Papantoniou et al., 2014b), no global changes in oxygen tension were observed between the inlet and outlet for the flow rate and cell source used, the model allows to quantify these variable throughout the entire scaffold, potentially showing pockets of decreased oxygen tension (and neotissue growth) coming from improper perfusion due to local geometrical particularities. Additionally, the possibility that higher flow rates might lead to the secretion of more ECM could also explain to a certain extent the differences in volume filling patters between simulations and experiments.

In a very interesting recent study, neotissue was modeled in 3D by (Nava et al., 2013) using the arbitrary Lagrangian–Eulerian (ALE) method to implement mesh movement. However, the flow was only modeled in the void space, which is acceptable for the early growth phase, but is not suitable to simulate complete filling of the scaffold. In this study, we employed the Level Set Method to represent neotissue growth as described previously in (Guyot et al., 2014, 2015) (chapitre 4,5). This method, separating the movement of the interface from the definition of the mesh allows tracking the neotissue kinetics until full scaffold pore filling is reached. A maximal neotissue growth velocity of 3 and 7 $\mu\text{m}/\text{day}$ was obtained for the low and high flow rates respectively as seen in Fig. 6.6. The average growth velocities from the present study are the same order of magnitude than the ones estimated in (Nava et al., 2013) which were in the order of 1 $\mu\text{m}/\text{day}$ and

higher than the values adopted in previous tissue growth models (Sacco et al., 2011). This could be due to the fact that chondrocytes modeled in that work are slow proliferating cells compared to hPDCs.

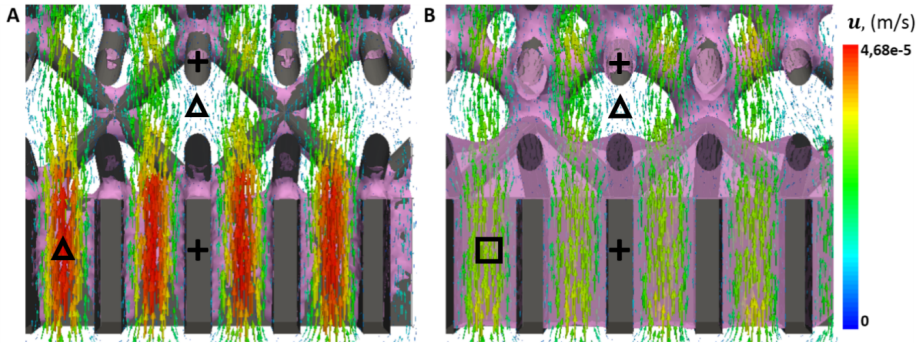


Figure 6.5: Close-up view on a section of the scaffold illustrating the different flow profiles (\mathbf{u}) at early (A) and late (B) time points (neotissue volume is indicated in pink). In image (A), the scaffold is almost empty, so the flow is mostly ruled by the Stokes equation leading to Poiseuille flow in the bottom part. In (B), the bottom part of the scaffold is completely filled with neotissue, so the flow profile in this area is ruled by the Darcy equation. +=scaffold, □=neotissue, Δ=void.

Numerical predictions obtained in this study (Fig. 6.4 and Fig. 6.5) are in general agreement with published literature with regard to the range of shear stresses calculated at the neotissue interphase during neotissue growth (Boschetti et al., 2006; Cioffi et al., 2006; Lesman et al., 2010; Nava et al., 2013). However shear stresses developed within the neotissue (τ_{in}) were seen to be an order of magnitude higher than the surface shear stresses. It is interesting to note that the average values obtained for inner shear stress for the high flow rate in this work, reaching 0.7 Pa, compared closely to the ones determined for native bone (1–3 Pa) (Zeng et al., 1994), closer than what has been reported to date for tissue engineered constructs. In this study it was assumed that the pores within the neotissue had a size of 50 μm , this was justified, for our case study, for large hPDC cells whose size has been shown to range between 100–150 μm when fully spread (Eyckmans et al., 2012). This value could become smaller upon 3D confluency when cells ECM secretion might lead to fuller neotissue structures. Interestingly, the calculated inner neotissue (microporous) shear stress magnitude for the selected neotissue pore size matched closely to those determined via single cell simulations (Jungreuthmayer et al., 2009; Verbruggen et al., 2014; Zhao

et al., 2014). Empty scaffold simulations may be useful for early time points and have been successfully used to determine stem cell lineage commitment (Song et al., 2013) however for later culture time points these models seem to be insufficient.

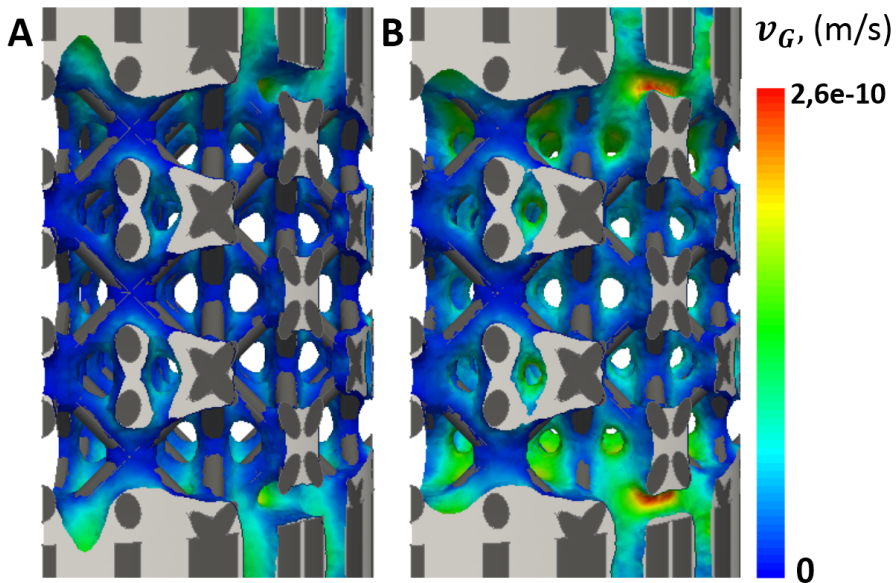


Figure 6.6: Local distribution of the neotissue growth velocity v_G (m/s) at the neotissue-void interface at 28 days for flow rates Q_2 (0.04ml/min, left) and Q_1 (4ml/min, right). The neotissue is indicated in light grey).

Using the whole scaffold geometry it was also possible to determine changing pressure drop values during neotissue growth and subsequent scaffold pore closure. The maximum pressure drop values obtained for the high flow rate, for completely full scaffolds, equaled to 11 Pa for the parameters of this study (cylindrical scaffold dimensions $d = 6 \text{ mm}$, $h = 6 \text{ mm}$; neotissue porosity 90%, pore size = $50 \text{ }\mu\text{m}$). This value is close to pressure drop measured computationally in microporous polyester scaffolds in flow through perfusion bioreactors ($\Delta P = 46 \text{ Pa}$, scaffold $h = 20 \text{ mm}$, $d = 100 \text{ mm}$, flow rate 10 ml/min (Podichetty et al., 2014) but also with experimentally measured pressure drop values for chitosan-gelatin scaffolds (with 80-92% porosity and pore size $\sim 100 \text{ }\mu\text{m}$, $d = 100 \text{ mm}$, $h = 2 \text{ mm}$ (Podichetty et al., 2012)). Pressure drop is a parameter that can be measured

online during bioreactor culture and, when linked to this whole-scaffold model, could provide a non-invasive readout to monitor neotissue growth in perfusion bioreactors. The continuous secretion of ECM, in particular upon reaching 3D ‘confluency’, is expected to lead a decrease in neotissue permeability. This will occur mostly towards the later stages of perfusion culture. To achieve this in the present model a time-dependent parameter could be coupled to the porosity parameter making it decrease over time, reflecting ECM deposition. This could be experimentally validated by measuring pressure drop across the tissue engineered construct over time, for fixed flow rates.

Scaffold design in perfusion bioreactors can affect neotissue growth in two ways. First, due to their geometry, the scaffolds provide topographies that will enhance 3D cell growth and neotissue formation (Melchels et al., 2010; Van Bael et al., 2012). Second, their design will define fluid flow patterns throughout the entirety of the scaffold affecting the mechanical stimuli exerted on the cells (Hutmacher and Singh, 2008) and the resulting growth kinetics. The computational tool developed in this study could be used to assess biomechanical regimes that will develop in a particular scaffold during neotissue growth but also to evaluate the effect of specific geometries using scaffold CAD designs on these regimes. This model could also suggest ‘ideal’ geometries where shear stress variation exerted on cells across the scaffold could be minimized, resulting thus in a more homogeneous cell population phenotype. The spatiotemporal mapping of shear stress levels will allow to more accurately link phenotypic responses in bioreactors (Yu et al., 2004; Grayson et al., 2011) with the experienced biomechanical microenvironment. Moreover, already observed phenomena such as shear stress dependent ECM secretion and mineralization (Bancroft et al., 2003; Papantoniou et al., 2013) could be also linked to the experienced microenvironment. For their validation such models will require 3D tools of high resolution such as NanoCT as presented here or synchrotron X ray microCT as reported elsewhere (Voronov et al., 2012).

6.6 Conclusion

In this study, a 3D model of microporous neotissue growth in a dynamic culture environment was presented in which the neotissue growth velocity depends on scaffold geometry and fluid flow induced shear stress. The obtained simulation results showed a correspondence with established

experimental observations. Although the model can be extended to include additional determinants of the growth process, in its current state it is already able to act as a scaffold shape and bioprocess optimization tool, allowing for a control of the flow-induced mechanical stimulation and growth of the neotissue.

CHAPTER 7

AN *IN SILICO* MODEL TO CAPTURE SPATIOTEMPORAL STEM CELL GROWTH KINETICS IN DYNAMIC CULTURE ENVIRONMENTS: INCORPORATION OF PHYSICOCHEMICAL PARAMETERS.

Yann Guyot^{1,2}, Maarten Sonnaert^{1,5}, Ioannis Papantoniou^{1,3}, Frank P. Luyten^{1,3}, Liesbet Geris^{1,2,4}

¹ Prometheus, Division of Skeletal Tissue Engineering, KU Leuven, Onderwijs en Navorsing 1 (+8), Herestraat 49 - PB813, B-3000, Leuven, Belgium.

² Biomechanics Research Unit, Universite de Liège, Chemin des Chevreuils 1 - BAT 52/3, B-4000 Liège, Belgium.

³ Skeletal Biology and Engineering Research Center, KU Leuven, Onderwijs en Navorsing 1 (+8), Herestraat 49 - PB813, B-3000, Leuven, Belgium.

⁴ Department of Mechanical Engineering, Biomechanics Section, KU Leuven, Celestijnenlaan 300C – PB 2419, B-3001 Leuven, Belgium.

⁵ Department of Materials Engineering, KU Leuven, Heverlee, Belgium.

Adapted from: Guyot, Y.; Sonnaert, M.; Papantoniou, I.; Luyten, F. P. & Geris, L. **An *in silico* model to capture spatiotemporal stem cell growth kinetics in dynamic culture environments: incorporation of physicochemical parameters.**

In preparation

The previous chapters described the curvature-based neotissue growth model and the influence of fluid flow-induced mechanics on growth velocity. In the present chapter, this model is further extended in order to take into account physicochemical parameters such as metabolic species. Three mass transport equations corresponding to glucose, lactate and oxygen concentrations were added to the model. The neotissue growth velocity was updated in order to take into account the detrimental effect of low glucose, oxygen and pH on neotissue growth. The model was first corroborated by comparing neotissue volume and lactate production with experimental data. Then, in order to show the ability of the model to be used as a bioprocess optimization tool, different scaffold geometries and flow rates were tested. Finally, the model was used to find optimal time point for culture medium refreshment.

7.1 Introduction

Bone Tissue Engineering is a promising strategy in the regenerative medicine field for treating bone diseases and overcoming the increasing shortage of donor grafts (Amini et al., 2012). The most common *in vitro* strategies encompass three different elements (Leijten et al., 2015), the first of which is a bioreactor that is able to supply nutrients, remove metabolic waste and provide suitable mechanical stimuli to the cells. The second element is three dimensional (3D) biomaterial such as a scaffold made of titanium or calcium-phosphate providing a geometrical base for 3D cell growth and extracellular matrix (ECM) deposition. The last element is a population of mesenchymal stem cells (MSCs), progenitor cells, that is able to differentiate following the osteogenic pathway depending on the biochemical and biomechanical environment (Grayson et al., 2011; Sonnaert et al., 2014).

The use of perfusion bioreactor set-ups, amongst other, focuses on delivering mechanical stimuli via flow induced shear stress. Indeed, the wall shear stresses that MSCs experience were shown to determine their viability, enhance proliferation and induce osteogenic differentiation (McCoy and O'Brien, 2010; McCoy et al., 2012; Papantoniou et al., 2013; Song et al., 2013). Computational fluid dynamics (CFD) modeling has been introduced as a tool to characterize the flow pattern in (empty) scaffolds to quantify the local flow induced shear stresses acting on the attached cells (Raimondi et al., 2004; Boschetti et al., 2006; Cioffi et al., 2006; Jungreuthmayer et al., 2009; Maes et al., 2009; Voronov et al., 2010). However, most of these studies

focus on empty scaffold set-ups and investigate the flow profile in the absence of neotissue (cells and their ECM). As the neotissue growth and its eventual filling of the scaffold (as observed for instance in (Papantoniou et al., 2014b)) will significantly affect the flow profile, studying an empty scaffold study could be inadequate to determine the mechanical environment that cells will experience over culture time. In (Lesman et al., 2010; Hossain S, 2015), the authors do consider growth of the neotissue but they model the neotissue volume as an impermeable structure which leads to overestimated surface shear stresses. The neotissue is a permeable structure permitting flow (Papantoniou et al., 2014a) and therefore it is important to consider the fluid velocity field within the neotissue. For this purpose, the present work uses a previously developed technique to compute the complex flow profile both in the free volume and the neotissue volume of the scaffold (Guyot et al., 2015) (chapter 5).

Apart from mechanical stimuli, a large body of literature reveals the impact of physicochemical stimulants on stem cell activity, such as molecular gradients of oxygen, glucose and growth factors (Carrier et al., 2002; Zhao and Ma, 2005; Radisic et al., 2006; Malda et al., 2007; Wang et al., 2009; Spitters et al., 2014). Molecular gradients occur when the distribution of a molecule is not spatially homogeneous as determined by diffusion and/or convection principles (Berg, 1993). As suggested for oxygen (Grayson et al., 2006; Markway et al., 2010) and trophic factors (Caplan and Dennis, 2006), the response of stromal cells depends on concentrations for a particular molecule. For instance low glucose and oxygen concentration in the system could lead to cell death whereas an important amount of lactate will decrease the medium pH and inhibits cell proliferation capacity (Wuertz et al., 2009). Despite the importance of these physicochemical factors on the outcome of the bioreactor process, their local quantification (through e.g. sensors) remains problematic thereby severely limiting the product quality control and the translation to clinical practice. Mathematical models and computational simulations can play a significant role in the quantification of the complex physicochemical environment within the scaffold. *In silico* predictions of the final bioreactor process outcome can guide the optimization of process parameters such as scaffold geometry, fluid flow rate, nutrient concentration and medium refreshment frequency. The physicochemical cell environment within a bioreactor set-up has recently been computationally investigated in (Nava et al., 2013; Hossain et al., 2015; Hossain S, 2015). In these studies, the authors introduced oxygen, glucose

and lactate with help of diffusion-convection-reaction equations to determine the local concentration of these metabolic species in the context of bioreactor processes geared towards *in vitro* cartilage growth. A similar approach will be presented in this work, three partial differential equations (PDE) for the aforementioned species (oxygen, glucose and lactate) were included and the neotissue growth velocity was defined in order to be dependent upon their local concentration.

In this study, a complete model for 3D neotissue growth based on the Level Set Method (LSM) (Sethian, 1999) is presented. This model is able, over the entire bioreactor culture period, to capture the changes in neotissue topology, estimate the local flow-induced mechanical stimuli on the cells and quantify the local biochemical variables such as pH and their subsequent effect on neotissue growth. The presented model is first calibrated by comparison of the computed neotissue volume fraction and cumulative lactate production with experimental in-house data obtained for two different scaffold geometries. Subsequently, in order to test its predictive capacities, four additional geometries were designed *in silico* and assessed on their capacity for neotissue growth during *in silico* culture. Fluid flow influence on the culture process was investigated on a selected scaffold shape (the one showing the maximal neotissue volume at day 21) via a variation of the bioreactor flow rates within a common experimental range of values. Finally, in order to show that the presented model can be seen as an optimization tool for the bioreactor cell culture process, an intelligent strategy for medium refreshment was designed, based on the computed local pH within the neotissue.

7.2 Methods

7.2.1 Neotissue growth

In this section a brief overview is presented of the LSM used to track the moving interface between neotissue. For more explanations, implementation details and limitations, please refer to (Guyot et al., 2014) (chapter 4). In (Sethian, 1999), the author provides a numerical technique called Level Set Method (LSM) that is able to simulate a moving front and can be applied to capture the evolution of the interface between the neotissue and void during bioreactor culture process. The neotissue volume, called Ω_{nt} , and the void volume, called Ω_v , are separated by an interface called Γ . The LSM is based on the definition of a continuous signed distance function φ defined on the

whole computational domain Ω with the following assumption:

$$\begin{cases} \varphi > 0, & \text{in } \Omega_{nt}. \\ \varphi < 0, & \text{in } \Omega_v. \\ \varphi = 0, & \text{on } \Gamma. \end{cases} \quad (7.1)$$

The evolution of the interface is then computed using an advection equation with a velocity \mathbf{v}_G normal to the interface (\mathbf{n}_Γ) with homogenous Neumann boundary conditions (\mathbf{n} is the normal of the computational domain).

$$\begin{aligned} \frac{\partial \varphi}{\partial t} + \mathbf{v}_G \cdot \nabla \varphi &= 0 \\ \nabla \varphi \cdot \mathbf{n} &= 0 \end{aligned} \quad (7.2)$$

$$\mathbf{v}_G = -V_G * \mathbf{n}_\Gamma \quad (7.3)$$

One of the major issues of this study was to find the most suitable expression for the spatially dependent growth velocity magnitude V_G , a whole section is dedicated to this definition later.

7.2.2 Fluid flow equations

The topological changes in term of neotissue volume during growth affect significantly the flow profile inside the bioreactor (Guyot et al., 2015). At the micro-scale, the neotissue is made of cells and ECM and can therefore neither be seen as a simple void volume where the Stokes equations govern the flow profile nor as a full solid volume where no flow can occur. In order to simulate the flow behavior within the complex geometry of neotissue, it is modeled as a porous medium with permeability K_0 leading to flow governed by the Darcy equations. Due to the definition of the LSM, the interface Γ is not conform with the computational mesh, for this reason the Brinkman equation 1.6 with its penalization term \mathbf{K} was introduced.

$$\begin{aligned} -\mu \Delta \mathbf{u} + \nabla p &= 0 \text{ in } \Omega_v \\ \nabla \cdot \mathbf{u} &= 0 \text{ in } \Omega_v \end{aligned} \quad (7.4)$$

$$\begin{aligned} \frac{\mu}{K_0} \mathbf{u} + \nabla p &= 0 \text{ in } \Omega_{nt} \\ \nabla \cdot \mathbf{u} &= 0 \text{ in } \Omega_{nt} \end{aligned} \quad (7.5)$$

$$\begin{aligned} \frac{\mu}{K} \mathbf{u} - \mu \Delta \mathbf{u} + \nabla p &= 0 \text{ in } \Omega \\ \nabla \cdot \mathbf{u} &= 0 \text{ in } \Omega \end{aligned} \quad (7.6)$$

As previously mentioned, equation 1.6 can be seen as a penalization equation with the spatially and temporal dependent parameter K that act as a switch between the two different volumes. In the neotissue volume Ω_{nt} , $K = K_0$ making the Stokes term in 1.6 negligible. Conversely, in the void Ω_v , $K \gg K_0$ making the Darcy term in 1.6 negligible. The jump between the two different behaviors was implemented with help of a smeared-out Heaviside function H , with the following definition ($\varepsilon = 1.5h$, h the mesh size):

$$H(\varphi) = \begin{cases} 0, & \varphi < -\varepsilon \\ \frac{1}{2} + \frac{\varphi}{2\varepsilon} + \frac{1}{2\varepsilon} \sin\left(\frac{\pi\varphi}{\varepsilon}\right), & -\varepsilon < \varphi < \varepsilon \\ 1, & \varphi > \varepsilon \end{cases} \quad (7.7)$$

$$K(\mathbf{x}) = 10^{-4}(1 - H) + K_0 H \quad (7.8)$$

The parameter 10^{-4} was chosen as low as possible to reduce the jump between the two extreme values for K and as big as possible to not affect the Stokes behavior in the void. K_0 was estimated according to (Nabovati et al., 2009) where the authors presented an equation to approximate the permeability of a porous medium made of random fiber web :

$$K_0 = 0.491\delta^2 \sqrt{\frac{1 - \psi_0}{1 - \psi} - 1}^{-2.31} \quad (7.9)$$

The parameter ψ_0 was defined as the percolation threshold, a porosity from where flow is permitted, it was set to zero in this study. ψ represents the porosity of the porous medium and was assumed to be equal to 90% (same order of magnitude as many natural soft tissues and hydrogels) and δ represents the micro-pore (neotissue pore) and was chosen equal to 50 μm corresponding to one third of the size of a spread attached cell used in this study (Eyckmans et al., 2012).

7.2.3 Nutrients and waste transport

One of the advantages of using a perfusion bioreactor set-up is to continuously supply nutrients such as oxygen and glucose and remove

metabolic waste such as lactate (Hossain et al., 2015). In order to take this behavior into account in the model, three convection-diffusion-reaction equations were added as governing equation for metabolic species transport.

$$\frac{\partial C_i}{\partial t} + \mathbf{u} \cdot \nabla C_i - \nabla \cdot (D_i \nabla C_i) = -R_i \quad (7.10)$$

Where C_i represents the species concentration with $i = g$ for glucose, $i = o$ for oxygen and $i = l$ for lactate. D_i represents the diffusion coefficient for each species i . As said previously, the neotissue can be seen as a porous medium, affecting the diffusion behavior of species through it. To address this effect, D_i was defined as a spatially dependent function with following definition:

$$D_i = D_{i_{water}}(1 - H) + D_{i_{water}}\psi H, \quad (7.11)$$

with $D_{i_{water}}$ corresponding to the diffusivity of the species i in water and the right term of equation 1.11 representing diffusion through the porous medium. In equation 1.10, the right hand side term describes the production or consumption of the species by the cells and was modeled with Michaelis-Menten kinetics:

$$R_o = H\varphi_{cell} \frac{V_o C_o}{K_o + C_o} \quad (7.12)$$

$$R_g = H\varphi_{cell} \frac{V_g C_g}{K_g + C_g} \quad (7.13)$$

φ_{cell} is the cell density within the neotissue and H is the previously defined Heaviside function in order to allow consumption or production only in the neotissue volume. As we assume the metabolic state of the hPDCs during the bioreactor process studied in this work to be glycolytic, cells break a molecule of glucose into two lactate molecules resulting in the production of lactate governed by the following algebraic relation:

$$R_l = -2R_g \quad (7.14)$$

7.2.4 Growth velocity expression

The local growth velocity magnitude V_G is a key parameter in this study. Indeed, the velocity at which the cells colonize the full 3D scaffold depends on several geometrical, physical and chemical factors, and was expressed as the following equation (for a graphical representation, see Fig. 7.1):

$$V_G = A_G \times f(\tau) \times g(\kappa) \times h_1(C_o) \times h_2(C_g) \times h_3(pH) \quad (7.15)$$

A_G was determined according to experimental data in a fitting procedure. In (Bidan et al., 2012) or (Rumpler et al., 2008), authors show that this velocity is highly dependent on the local mean curvature of the surface of tissue in contact with the void space. Following this observation, the first version of the model was a curvature dependent model (Guyot et al., 2014) (chapter 4), and the curvature κ was defined as follow $\kappa = \nabla \cdot \mathbf{n}_\Gamma$ and $\mathbf{n}_\Gamma = \frac{\nabla\varphi}{|\nabla\varphi|}$. In order to avoid tissue losses on areas with negative curvature, the curvature dependents term in 1.15, $g(\kappa)$, was expressed as follows:

$$g(\kappa) = \begin{cases} \kappa, & \text{if } \kappa < 0. \\ 0, & \text{if } \kappa \geq 0. \end{cases} \quad (7.16)$$

To take into account the mechanical stimulation provided by the flow to the cells, (Nava et al., 2013; Hossain et al., 2015) or (Chapman et al., 2014), authors describe a function that is able to take into account an optimal shear stress (τ) range enhancing growth as well as a detrimental value of τ that inhibits growth. This function was inspired by (Nava et al., 2013) and defined as follow:

$$f(\tau) = \begin{cases} 0.5 + \frac{0.5\tau}{\alpha_1} & 0 \leq \tau < \alpha_1 \\ 1 & \alpha_1 \leq \tau < \alpha_2 \\ \frac{\tau - \alpha_3}{\alpha_2 - \alpha_3} & \alpha_2 \leq \tau < \alpha_3 \\ 0 & \alpha_3 \leq \tau \end{cases} \quad (7.17)$$

Between α_1 and α_2 , shear stress has a beneficial effect (compared to static conditions) on cells enhancing the growth ($f = 1$) and above the threshold α_3 the shear stress has a detrimental effect and inhibits the cellular activity resulting in an arrest of the growth ($f = 0$). The influence of oxygen and glucose concentrations were taken into account with the help of the functions h_i , reducing the velocity lower when the level of these species decreases:

$$h_1(C_o) = \frac{C_o}{K_o + C_o} \quad (7.18)$$

$$h_2(C_g) = \frac{C_g}{K_g + C_g} \quad (7.19)$$

Finally, the negative influence of lactate on the neotissue growth was incorporated with the introduction of the local pH and its negative effect on cells when the medium becomes more and more acidic. In (Hossain et al.,

2015), authors give a linear relation between the local lactate concentration and the pH , with the following expression:

$$pH = 7.4 - 0.0406C_l \quad (7.20)$$

In (Wuertz et al., 2009), authors determined a detrimental effect on cells starting from a pH of 7.1 with a decrease in the cell proliferation while the pH was linearly decreasing. From their results, the influencing function $h_3(pH)$ was determined:

$$H(\varphi) = \begin{cases} 0, & pH \leq 6.375 \\ \frac{4}{3}pH - 8.5, & 6.375 < pH \leq 7.1 \\ 1, & pH > 7.1 \end{cases} \quad (7.21)$$

An overview of all parameter values used in this study is provided in Table 7.1.

7.2.5 Initial and boundary conditions

At the start of the bioreactor culture, $2e5$ cells were (manually) drop-seeded onto the scaffold. For the numerical analysis, initial seeding was assumed to be homogeneous throughout the entire scaffold represented through an initial function φ . This initial layer was assumed to be $20 \mu\text{m}$ based on the reported diameters of MSCs in 2D culture (Darling and Guilak, 2008). An example of this monolayer is depicted in Fig. 7.1. Assuming a cell seeding efficiency of 60% (experimental evaluation is ongoing), the seeded cell amount distributed into the initial monolayer of $20 \mu\text{m}$ thick resulted in an initial cell density φ_{cell} of approximately $2.5e13$ cells/ m^3 for the scaffolds used in the bioreactor experiments. The value was assumed not to change over time and was used for all scaffold designs (see Fig. 7.2 for an overview of the different scaffold designs) and culture conditions tested in the all *in silico* experiments reported in this study unless specifically mentioned otherwise.

In (Papantoniou et al., 2014b), authors determined a minimal distance between the inlet of the bioreactor chamber and the scaffold to allow the flow pattern to fully develop, avoiding inhomogeneity in neotissue formation in the final biological construct. In this study, the scaffold was assumed to be at a sufficient distance from the chamber inlet as to allow a Poiseuille flow to be used as a Dirichlet boundary condition at the bottom of the computational domain for equation 1.6 (see Fig. 7.1). No-slip boundary conditions were

Parameter	Value	References
Neotissue porosity, ψ	90%	(Guyot et al., 2015)
Neotissue micro-pore size, δ	50 μm	(Guyot et al., 2015)
Neotissue growth rate, A_G	5.6e-14 m^2/s	(Papantoniou et al., 2014b)
Minimal shear stress value enhancing neotissue growth, α_1	0.01	(Chapman et al., 2014)
Maximal shear stress value enhancing neotissue growth, α_2	0.03	(Chapman et al., 2014)
Detrimental shear stress value, α_3	0.05	(Chapman et al., 2014)
$D_{o_{water}}$, oxygen diffusivity in water	2.1e-9 m^2/s	(Palsson BO, 2004)
$D_{g_{water}}$, glucose diffusivity in water	5.65e-9 m^2/s	(Hazwani Suhaimi, 2015)
$D_{l_{water}}$, lactate diffusivity in water	1.4e-9 m^2/s	(Hossain et al., 2015)
V_o , oxygen consumption rate	1.09e-17 mol/cell/s	(Lambrechts et al., 2014)
V_g , glucose consumption rate	9.5e-17 mol/cell/s	(Zhou et al., 2013)
K_o , Michaelis-Menten constant for oxygen	1.82e-3 mM (2 %)	(Carlier et al., 2014)
K_g , Michaelis-Menten constant for glucose	0.3 mM	(Hossain et al., 2015)
φ_{cell} , cell density within neotissue	2.5e13 cells/ m^3 (except for lower cell seeding efficiency test on D_c scaffold)	-

Table 7.1: Overview of all parameter values used in this study.

assigned to the chamber wall as well as on the scaffold surface, and free-flow conditions were applied on top of the domain. The bioreactor set-up is a closed loop, so all nutrients and waste products that leave the chamber from the top are automatically entering the scaffold from the bottom after having made a complete run-through of the bioreactor system. Hereto, the Dirichlet boundary conditions for glucose and lactate at the bottom of the chamber were set to the concentration of the corresponding species at the top of the domain at the previous time step (Δt) ($C_{i_{bottom}}^t = C_{i_{top}}^{t-\Delta t}$), with the time step chosen to match the time needed to complete one cycle (for 1 ml/min and the total volume being 12.8 ml, the time step was 12.8 min). Although the bioreactor can be seen as a close loop, it is not perfectly sealed

and oxygen can constantly enter the system through the tubing connecting the bioreactor chamber with the medium reservoir, leading to a Dirichlet boundary condition for oxygen always equal to the dissolved concentration in water (21%, $C_{o_{bottom}} = 0.192\text{mM}$) (Demol et al., 2011). The culture medium was refreshed every 3 days, resulting in a re-initialization of the bottom boundary condition for glucose and lactate at their initial value at the corresponding time points ($C_{g_{bottom}} = 25\text{mM}$, $C_{l_{bottom}} = 0\text{mM}$ at $t = 3k$ days, $k \in \mathbf{N}$).

7.2.6 Optimal medium refreshment

One of the key factors of the bioreactor process is the refreshment of the culture medium, in order to remove accumulated waste as well as supply fresh nutrients. Currently, this process follows a 3 days basis protocol and the presented model can be used as a tool for the optimization of this refreshment protocol. The criterion for medium refreshment (modeled as the re-initialization of the inlet boundary conditions for glucose and lactate) will no longer be the time passed since the last refreshment but rather the volume of neotissue (here arbitrarily chosen at 20% of the total volume) where the pH has dropped below 7.1, being the threshold where pH starts to have a detrimental effect on cell growth.

7.2.7 Experimental set-up and data analysis

Cell culture Human periosteum derived cells (hPDCs) were isolated from periosteal biopsies of different donors as described previously (Eyckmans and Luyten, 2006). This procedure was approved by the ethics committee for Human Medical Research (KU Leuven) and with patient informed consent. hPDCs were expanded in Dulbecco's modified Eagle's medium with high-glucose medium (Invitrogen) containing 10% fetal bovine serum (BioWhittaker) and 1% antibiotic-antimycotic (100 units/mL penicillin, 100 mg/mL streptomycin, and 0.25 mg/mL amphotericin B; Invitrogen). hPDCs were passaged 6 times at 80%–90% confluency prior to their use in this study.

Scaffold 3D additively manufactured open porous Ti6Al4V scaffolds (henceforth referred to as Ti scaffolds) of: diameter = 6 mm, h = 6 mm, porosity = $73 \pm 1\%$, strut diameter = $245 \pm 2 \mu\text{m}$ and pore size = $755 \pm 3 \mu\text{m}$, produced on an in-house developed selective laser melting (SLM) machine, were used.

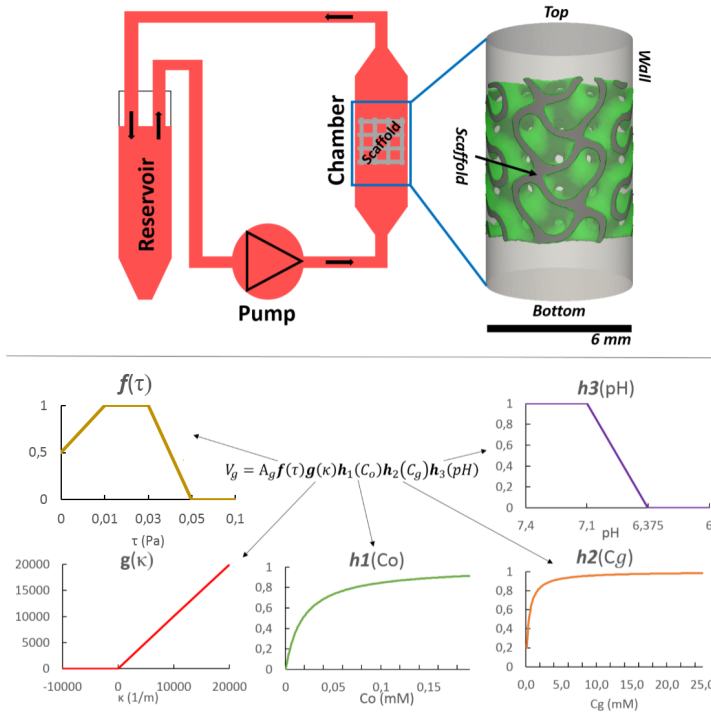


Figure 7.1: (top, left) Schematic representation of the bioreactor. (top, right) Volume corresponding to the computational domain with the scaffold in the middle ($G10$), the green volume represents the initial neotissue distribution with a thickness of $20 \mu\text{m}$. (bottom) Graphical representation of the growth velocity V_G .

Perfusion Bioreactor Prior to the start of the experiment, cells were trypsinized with Tryple Express (Invitrogen) and seeded on the scaffolds. A static drop-seeding protocol was used for seeding cells onto pre-wetted 3D Ti scaffolds. $2e5$ cells per scaffold were seeded and left to attach overnight ($t=24\text{h}$). Scaffolds were positioned in the bioreactor perfusion chambers with a random orientation (top-bottom) with respect to the direction of drop seeding (Impens et al., 2010). Scaffolds were cultured for 14 and 21 days. For dynamic culturing, TE constructs were placed in an in-house developed perfusion bioreactor equipped with parallel perfusion circuits. Each perfusion chamber (Length=26 mm, Diameter=6mm), holding a single scaffold, was connected to an individual medium reservoir containing 10 ml of cell culture medium via a Tygon (Cole Parmer) tubing and a two-

stop tubing (BPT, Cole Parmer) connected to a peristaltic pump (IPC-24, Ismatec SA). Medium was refreshed every three days for the entire culture period. For each scaffold location 15 seeded scaffolds were cultured. Four scaffolds (TE constructs) for each experimental condition were used to determine average DNA content values per scaffold (at day 1, 14 and 21) and subsequent qPCR analysis (only for the day 14 and 21 groups). The remaining 3 TE constructs were analyzed via contrast enhanced nanofocus Computed Tomography (Nano-CT) at day 14 and 21.

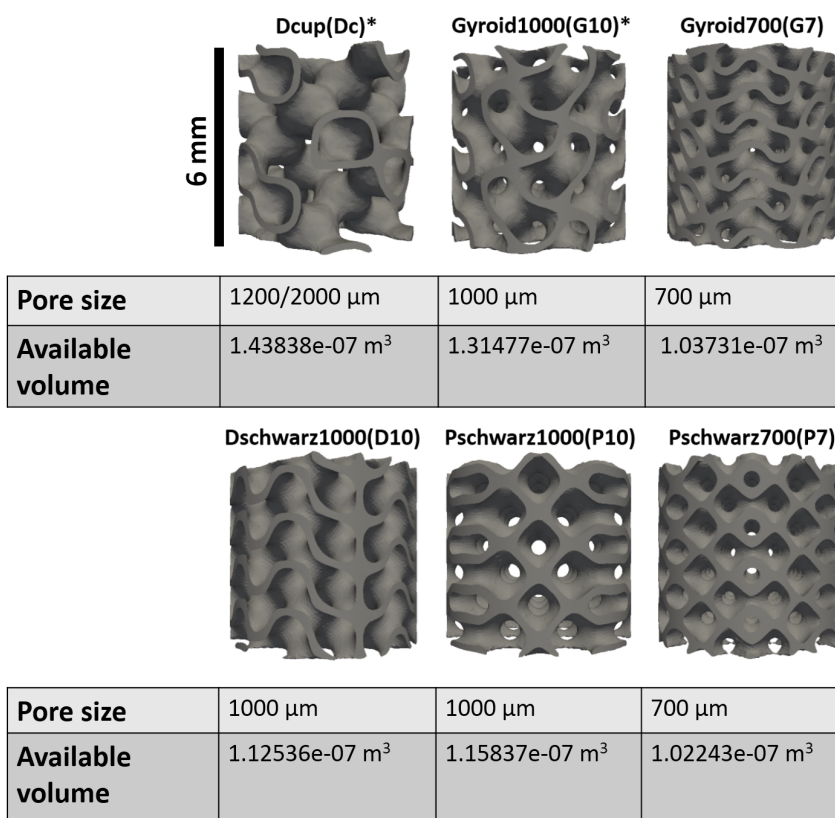


Figure 7.2: Scaffold geometries investigated in this study. Scaffold used in the experimental corroboration of the model are indicated with an *.

Live/Dead assay A Live/Dead viability/cytotoxicity kit (Invitrogen) was used to evaluate qualitatively cell viability and cell distribution by fluorescence microscopy. Constructs were rinsed with 1 ml PBS after which

they were incubated in the staining solution (0.5 μ l Calcein AM and 2 μ l Ethidium Homodimer in 1 ml PBS) for 20 min in normal cell culture conditions. The constructs were imaged using a Leica M165 FC microscope.

7.3 Results

7.3.1 Experimental validation of the model

Fig. 7.3 shows the comparison between experimental data and computational results. After fitting of the Ag parameter through an iterative procedure using the lactate concentration of the large gyroid ($G10$) scaffold, a good qualitative and quantitative correlation was obtained for the $G10$ scaffold not only for neotissue volume (around 22% at day 21) (Fig. 7.3 (bottom)) but also for cumulative lactate production (Fig. 7.3 (middle)). For scaffold Dcup (Dc), no three dimensional growth was observed experimentally, with a neotissue volume remaining the same over time (around 6%) (Fig. 7.3 (bottom)). Corresponding computational results show a similar behavior with a neotissue volume not exceeding 9% at day 21. However, the computed cumulative lactate was over-estimated by a factor two. This difference might come from the absence of 3D growth, resulting in 2D confluency and a possible effect on the cells' metabolic activity. This difference might also come from a lower cell seeding efficiency on the Dc scaffold, possibly due to pore shape anisotropy, resulting in a lower overall cell density. In order to investigate this hypothesis, a cell seeding efficiency of 30% was tested on the Dc geometry. Fig. 7.3 (middle) shows the results of considering such cell seeding efficiency and a better correlation for cumulative lactate production was obtained, while having no effect on the total neotissue volume. Fig. 7.4 shows the local pH , oxygen and lactate calculated in this study.

7.3.2 Scaffold geometry influence

The capacity of predicting the evolution of the 3D neotissue growth was tested on four additional different scaffold geometries. These configurations have been designed following Schwarz minimal surfaces (*Primitive* (P), *Diamond* (D), *Gyroid* (G)). These geometries have been used widely in the tissue engineering field, showing an optimal stress distribution under compression (Shin et al., 2012), improving cell seeding efficiency (Melchels et al., 2010) or showing a homogenous wall shear stress distribution under flow conditions (Melchels et al., 2011). Since the macro-pore size has a

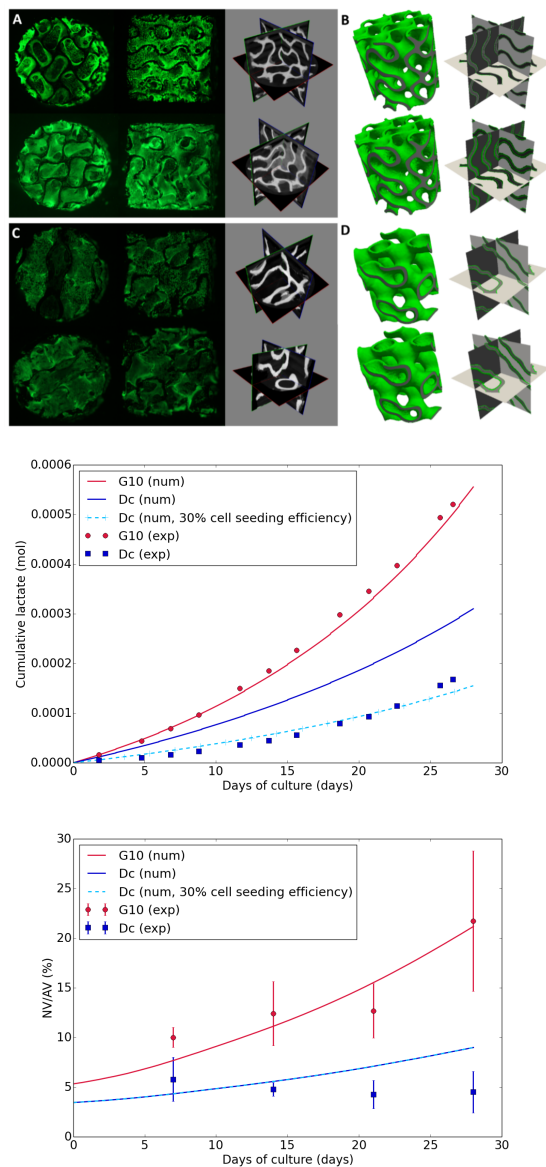


Figure 7.3: Experimental data versus numerical results. **(A, C)**, live/dead staining and CE-NanoCT slices at day 28 for (*G10*) and (*Dc*) respectively. **(B, D)**, Corresponding numerical output of the model at day 28 for (*G10*) and (*Dc*) respectively. **(Middle)**, Cumulative lactate prediction over time (continuous line) for (*G10*, red) and (*Dc*, blue) compared to experimental data. **(Bottom)**, Percentage of predicted scaffold filling (NV/AV) over time (continuous line) compared to experimental data (dots). The light blue dashed line represents (*Dc*) numerical results with a cell seeding efficiency equal to 30%.

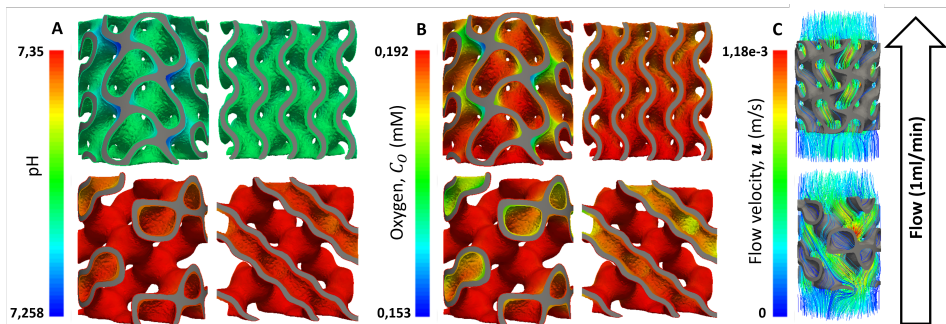


Figure 7.4: Spatial distribution within neotissue of pH (A) and (oxygen) (B) at 28 days for the experimentally tested scaffold geometries ($G10$ (top), Dc (bottom)). For each geometry, a cut has been proceeded for inside visualization (right part). Flow streamlines colored by velocity (C).

real influence on cell proliferation, various pore sizes were tested see Fig. 7.2. Fig. 7.5 shows the comparison of these six geometries regarding the evolution of void filling. Simulations have been executed with a volumetric flow rate of 1 ml/min for 21 culture days, corresponding to common bioreactor settings and times. The graph represents the relative percentage of volume occupied by neotissue over culture time (neotissue volume (NV) / available volume (AV)). There is a clear difference in terms of filling between scaffolds with a macro-pore size higher than 1 mm and those with a pore size lower or equal than 700 μm . Scaffolds with large pores show a very open geometry leading to a low curvature, negatively affecting the growth velocity resulting in a void filling never exceeding 40%. The study case named (Dc) presents a pathological case due to on the one hand this scaffold not being isotropic and having two characteristic macro-pore sizes (2mm/1.2mm) leading to two different local velocities. On the other hand, due to this strong anisotropy, fluid flow adopts preferential paths where macro-pores are bigger, creating zones almost devoid of flow, particularly in the small pores. This spatial difference in flow pattern applies to the local part of the scaffold (and so the neotissue) with low oxygen and glucose as well as high lactate concentration due to the absence of medium renewal. The resulting neotissue formed in such an anisotropic scaffold is low and spatially inhomogeneous showing the importance of considering isotropic scaffolds. Scaffolds with lower pore sizes show better results in terms of void filling with the complete inside volume filled with neotissue in the $G7$ case. In the $P7$ case, there are still a few void volumes localized within the scaffold. This geometry, contrary to $G7$, shows narrowing of the walls along

the flow path, eventually leading to a local increase of the wall shear stresses under a given flow condition. This spatial variation of in the mechanical stimuli distribution along the scaffold may have a detrimental effect on cells resulting in a slowing down or even stopping the tissue growth.

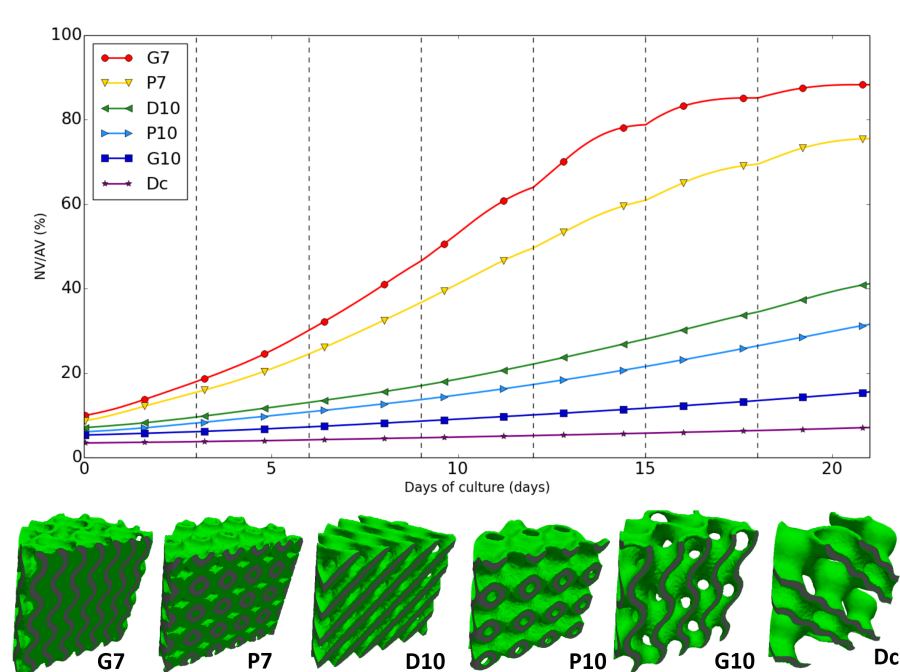


Figure 7.5: (top) Percentage of predicted scaffold filling (neotissue volume (NV) / available volume (AV)) over time for every geometrical configuration (the vertical dash lines correspond to medium refreshment). (bottom) 3D representation of the neotissue at 28 days for the seven scaffolds (a cut has been proceeded for better visualisation).

7.3.3 Bioreactor flow rate influence

The influence of the flow rate on cells and the resulting neotissue growth was investigated on the scaffold geometry that presented the highest amount of void filling in the previous section, *G7*, by varying the bioreactor flow rate in a typical experimental range, starting from 0.03 ml/min to 4 ml/min. Fig. 7.6 shows the evolution of the neotissue growth depending on the inlet velocity. It can be observed that a flow rate equal to 2 ml/min has a maximal improving effect on growth velocity compared to the 1 ml/min case, due to a

larger surface area exposed to a shear stress value between 0.01 and 0.03 Pa. At the contrary, a decrease in the flow rate shows a continuous decrease in the neotissue growth velocity due to a larger surface area of tissue exposed to shear stress value lower than 0.01 Pa. From the bar chart (Fig. 7.6, insert), it can be observed that a neotissue volume fraction equal to 80% has been reached in 14 days for a c flow rate equal to 2 ml/min, while 21 days are necessary for a flow rate equal to 0.5 ml/min.

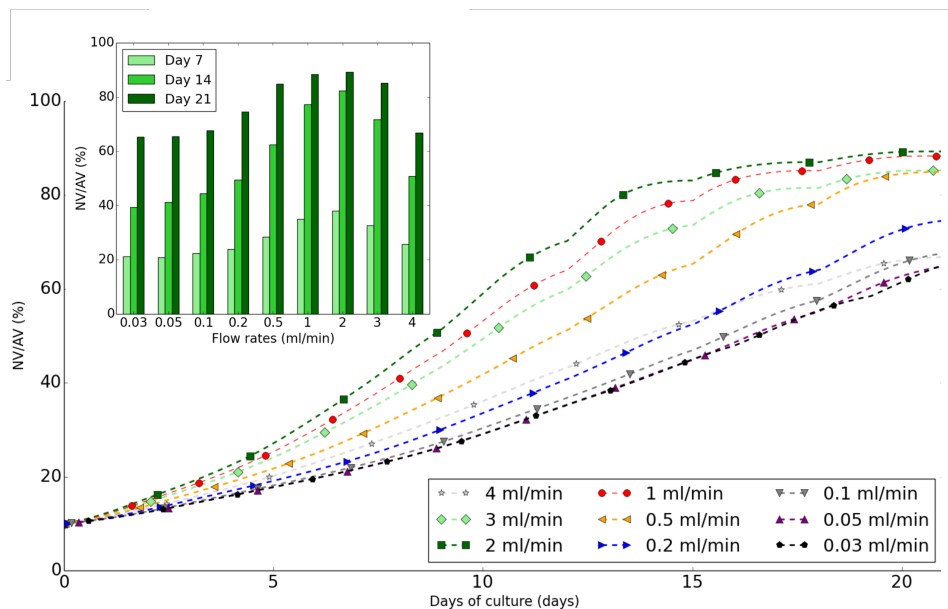


Figure 7.6: Neotissue production over time for different bioreactor flow rates. (Insert): NV/AV at day 7, 14, 21 for all flow rates.

7.3.4 Intelligent medium refreshment procedure

The capacity of the model to provide intelligent medium refreshment time points to the operator was investigated on the previous scaffold geometry $G7$ with a flow rate equal to 1 ml/min. Fig. 7.7 shows the comparison between the usual 3 days culture medium refreshment procedure and the optimal one, based on the percentage of neotissue presenting a pH value lower than 7.1. During the first 10 days, the two configurations had the same behavior due to the low volume of neotissue, producing not enough lactate to have a detrimental effect on cells. Towards the end of the culture

period, in the configuration with the 3 days refreshment protocol, the growth presented some jumps in the production rate at the re-initialization points. This was due to the pH reaching the level of detrimental values before the medium was changed. Under the optimal refreshment configuration, based on local pH values in a fraction of the neotissue, no such jumps appeared and neotissue growth rate was continuous, to finally present more neotissue formed at day 21. Due to the low amount of neotissue in the early days, the total nutrients consumed and lactate produced was very low and the medium did not need to be changed before day 5.5. In the later stage, due to a large amount of tissue, these species were highly consumed or produced, resulting in medium that needed to be changed much more frequently (upto more more than once perday). One can notice that the number of medium re-initialization time points is higher in the optimized configuration, resulting in using a larger amount of medium and so increasing the total cost of the experiment. This result corresponds to the best case scenario, where the medium was changed after the pH value starts to become lower than 7.1 in at least 20% of the neotissue. According to equation 7.21, the growth velocity magnitude barely starts to decrease at this pH value. An alternative could be, for example, to consider lower thresholds for the pH or larger affected neotissue volumes for medium changes to be recommended.

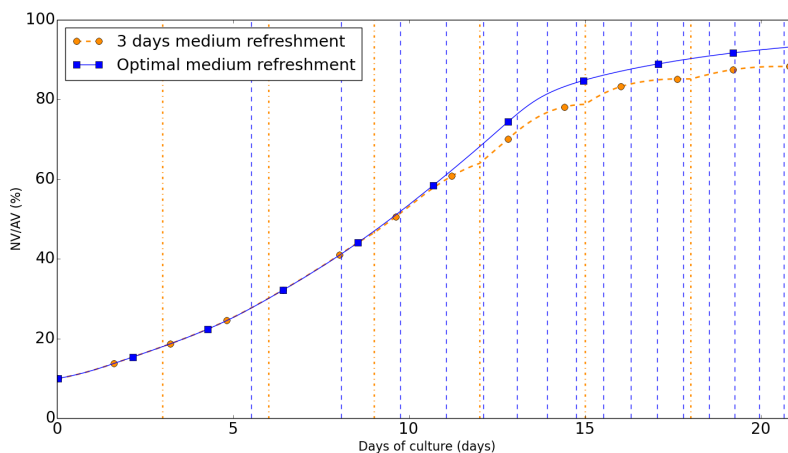


Figure 7.7: 3 days medium refreshment (orange) compared to optimal medium refreshment (blue). Dashed lines correspond to the time points where the medium was changed.

7.4 Discussion

In this work, a computational tool to predict and optimize *in vitro* neotissue growth on 3D scaffolds within a perfusion bioreactor was developed. Three important aspects occurring in the bioreactor were taken into account, (i) the neotissue growth, spatially simulated with the Level Set Method, (ii) the complex fluid dynamics with a specific description of flow inside the neotissue and (iii) the metabolic processes, with mass transport equations for oxygen and glucose consumption as well as lactate production. The influence of all these aspects on local neotissue growth velocity was coupled in a single equation. The model was first evaluated using experimental data obtained on two different scaffold designs by comparing neotissue volume fraction and cumulative lactate concentration at four time point during cultures. Then, in order to show that this model can be seen as an optimizing tool, five other scaffolds geometries were tested and the total *in silico* neotissue volumes produced were assessed. As fluid flow has a substantial effect on the cells, five different volumetric flow rates were tested in order to find the ideal flow rate for maximal neotissue production. Finally, an intelligent culture medium refreshment protocol was established based on the local pH value.

Nowadays, most of *in vitro* bioreactor cultures are based on trial and error methods, potentially wasting time and products. The presented model could tackle this issue by providing to the operator an *in silico* tool for culture preprocessing. The scaffold and its geometrical aspects can be tested *in silico* before any experiment takes place and an optimal scaffold shape can be selected in order to have maximal neotissue production in the shortest period of time. The bioreactor settings such as flow rate can also be pre-tested and optimized in order to avoid detrimental effects of flow on the neotissue growth but at the same time keep providing sufficient waste product removal and nutrients supply. During growth, the neotissue colonized the void and eventually filled up completely the scaffold. These changes in neotissue topologies affect the flow profile by narrowing the zone where the flow is governed by the Stokes equation, resulting in an increase in the shear stress on the neotissue-void interface thereby negatively affecting the growth velocity. For instance, a flow rate of 4 ml/min was seen to hinder growth beyond a filling of 68% *in silico*. In (Sonnaert et al., 2014) a flow rate above 4 ml/min was seen to be detrimental for further cell growth, giving confidence results obtained in this study. To avoid this negative effect, an intelligent algorithm could be implemented where the model automatically

adapts the bioreactor flow rate over time, providing, for example, on a daily basis feedback to the operator regarding the optimal flow rate settings to use.

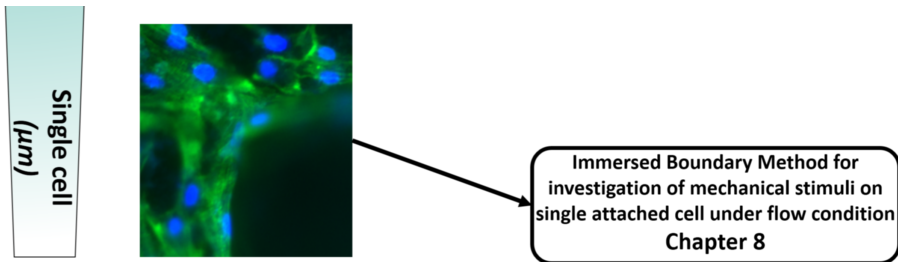
Another important aspect in cell culture is medium refreshment. Currently, most of the experiments are conducted with fixed culture medium exchanges carried out every three days. This study showed that this method might be suboptimal especially towards later time points where increased cell numbers will alter more rapidly the surrounding culture environment. In Fig. 7.6, it was shown that a more intelligent refreshment procedure could be considered, with a frequency starting from once a week at the start of the culture, gradually increasing to more than once a day due to neotissue growth, showing another facet of this model for experimental optimization.

One of the limitations of this study is the absence of an equation for the representation of cell density evolution. Indeed, in all cases, the model was assuming a constant cell density corresponding to the one calculated based on the initial cell amount within the initial monolayer volume (representing the initial film seeded on the scaffold struts). Taking into account the evolution of cell density inside the tissue might have a non-negligible effect on the computed growth. Due to proliferation or decay, the amount of consumed nutrients and produced lactate might be different and subsequently indirectly alter the growth velocity. The cell density could also have a direct effect on growth, with a local acceleration where this value is high and a deceleration effect (to even a complete stop) where this value is low or null due to cell death. This issue will be addressed in future work where equations for cell density, such as the ones presented in (Carlier et al., 2014), will be added.

The *in silico* tests conducted in this study have showed optimal neotissue formation for a scaffold with design *G7*, cultured under a flow of 2 ml/min with an adaptive medium refreshment protocol. The scaffold with design *G7* is currently being manufactured and the validation experiments confirming (or infirming) the model predictions will be started as soon as the scaffolds are available. In a future step, a parameters sensitivity analysis will be conducted in order to accurately estimate the neotissue growth rate A_G .

Part III

Single cell scale



CHAPTER 8

IMMERSED BOUNDARY MODELS FOR QUANTIFYING FLOW-INDUCED MECHANICAL STIMULI ON STEM CELLS SEEDED ON 3D SCAFFOLDS IN PERFUSION BIOREACTORS

Yann Guyot^{1,2,*}, Bart Smeets^{1,3,5,*}, Tim Odenthal³, Ramesh Subramani³,
Frank P. Luyten^{1,4}, Herman Ramon³, Ioannis Papantoniou^{1,4}, Liesbet
Geris^{1,2,5}

¹ Prometheus, Division of Skeletal Tissue Engineering, KU Leuven, Onderwijs en Navorsing 1 (+8), Herestraat 49 - PB813, B-3000, Leuven, Belgium.

² Biomechanics Research Unit, Universite de Liège, Chemin des Chevreuils 1 - BAT 52/3, B-4000 Liège, Belgium.

³ Division of Mechatronics, Biostatistics and Sensors (MeBioS) Kasteelpark Arenberg 30 - box 2456 3001 Leuven, Belgium.

⁴ Skeletal Biology and Engineering Research Center, KU Leuven, Onderwijs en Navorsing 1 (+8), Herestraat 49 - PB813, B-3000, Leuven, Belgium.

⁵ Department of Mechanical Engineering, Biomechanics Section, KU Leuven, Celestijnenlaan 300C – PB 2419, B-3001 Leuven, Belgium.

* *these authors share the first authorship*

Adapted from: Y. Guyot, B. Smeets, T. Odenthal, R. Subramani, F. P. Luyten, H. Ramon, I. Papantoniou & L. Geris, **Immersed Boundary Models for quantifying flow-Induced mechanical stimuli on stem cells seeded on 3d scaffolds in perfusion bioreactors.**

Submitted to PLoS Computational Biology

The work described in this chapter is the result of an equal partnership with Bart Smeets, who developed the cell deformation model with Tim Odenthal (see (Odenthal et al., 2013) and appendix D).

8.1 Abstract

Perfusion bioreactors regulate flow conditions in order to provide cells with oxygen, nutrients and flow-associated mechanical stimuli. Locally, these flow conditions can vary depending on the scaffold geometry, cellular confluency and amount of extra cellular matrix deposition. In this study, a novel application of the immersed boundary method was developed, representing a detailed deformable cell attached to a 3D scaffold inside a perfusion bioreactor and exposed to microscopic flow. The immersed boundary model allowed to predict the mechanical effects of the local flow conditions on the cell. Incorporating stiffness values measured with atomic force microscopy and micro-flow boundary conditions obtained from computational fluid dynamics simulations on the entire scaffold, we compared cell deformation, cortical tension, normal and shear pressure for different cell shapes and locations. We observed a large effect of the precise cell location on the local shear stress and predicted flow-induced cortical tensions in the order of $5 \mu\text{J}/\text{m}^2$ which is at the lower end of the range reported in the literature. The proposed method provides an interesting tool to study perfusion bioreactors processes down to the level of the individual cell's micro-environment which can further aid in the achievement of robust bioprocess control for regenerative medicine applications.

8.2 Introduction

The culture of stem cell populations in dynamic set-ups, for instance perfusion bioreactors, is of great potential for the production of bone tissue engineered constructs (Yeatts and Fisher, 2011). Amongst others, these systems provide controlled biomechanical stimuli, such as fluid flow-induced shear stresses, that will mimic the *in vivo* environment (bone) contributing to the generation of bone graft substitutes. Shear stress might significantly affect stem cell properties during dynamic culture in bioreactors as it has been associated to early stem cell lineage commitment (Song et al., 2013) and osteogenic priming (Sonnaert et al., 2014) in the absence of inductive growth factors, while it has been observed to promote osteogenic differentiation of bone marrow, periosteum and adipose derived mesenchymal stem cells in the presence of osteoinductive growth factors (Meinel et al., 2004; Frohlich et al., 2009; Grayson et al., 2011). Osteogenic differentiation has been further linked to shear stress magnitude with dose dependent enhancement of extra-cellular matrix deposition and subsequent

mineralization by the cultured cells (Sikavitsas et al., 2002; McCoy and O'Brien, 2010; Rauh et al., 2011; Papantoniou et al., 2013).

In order to characterize the dynamic environment throughout cell seeded scaffolds in perfusion bioreactors, many Computational Fluid Dynamics (CFD) model studies have been presented the past decade (Boschetti et al., 2006; Maes et al., 2009; Olivares et al., 2009; Hidalgo-Bastida et al., 2012; Podichetty et al., 2014). However, the majority of these studies considered empty scaffold geometries without incorporating a cell domain. Recently this was addressed by representing the growing neotissue as a porous medium, modeling the effect of neotissue growth on the flow profile (Hossain et al., 2015; Guyot et al., 2015). Yet these models predicted the local distribution of shear stresses and pressure through a volume averaged porous domain and did not take into account the local mechanical and geometrical environment of individual cells.

Mechano-transduction of stress induced by shear flow conditions is highly localized at specific areas of the cell's interface with its environment, such as focal adhesions, FAs (Shemesh et al., 2005), and primary cilia. The latter have been shown to be involved in the osteogenic response of bone cells to dynamic shear flow conditions (Malone et al., 2007), as well as in remodeling of the extracellular matrix (Weinbaum et al., 1994). The amount of force perceived at the level of FAs as a result of external flow conditions is influenced by the cell's mechanical properties, cell shape and the geometry of its microscopic environment (e.g. location of attachment points, and presence of extracellular matrix (ECM)). In this respect, the concept of cell cortical tension has gained a renewed interest in the last years as a mediator of mechano-transduction processes (Heisenberg and Bellaiche, 2013). Cortical tension is created by the cell itself through active acto-myosin contractility, resulting in a pre-stressed cytoskeleton. External flow however, can also contribute to locally elevated levels of cortical tension, especially close to attachment point such as FAs. This passive source of cortical tension, as well as its importance relative to the cell-generated active tension, has not yet been investigated for perfusion cell culture systems. Therefore there is a scaling gap from small scale i.e. 'single cell' to the 'neotissue/whole scaffold' macro-scale that needs to be bridged and computational models using realistic single cell geometries are a prima candidate for the job (Zhao et al., 2015).

Computational models of cell deformation due to shear flow have been developed considering the cell as a 2D Gaussian interface (Lee et al., 2012) or a 3D linear elastic solid (Dailey H, 2007; Slomka and Gefen, 2010). The latter uses a mixed Lagrangian-Eulerian formulation to solve the Fluid-Structure interaction (FSI) problem, with a coupling through continuity boundary conditions. For larger deformations, the interaction between cell and fluid has been addressed by means of the level-set method (Yang et al., 2008). Alternatively, the Immersed Boundary Method (IBM) is able to explicitly take into account discrete entities in the cell's cortex and, possibly, its internal cytoskeletal structure. It has been used to model the movement and deformation of vesicles, red blood cells and bacteria under flow conditions (Zhang et al., 2009; Lushi et al., 2014). An FSI model for osteoblasts attached to scaffold struts was recently published (Zhao et al., 2015), with a simple rigid single cell consisting of half a sphere with two focal adhesion points. In the work presented in this study, more realistic cell shapes are included, which are not rigid but deformable under the flow. Still, the cytoskeleton constitutes a highly complex material and its mechanical behaviour differs between various temporal and spatial scales, (Fabry et al., 2001). Hence at present, only a highly simplified mechanical representation of a complete attached cell is computationally feasible.

The main purpose of this study is to use the IBM to investigate fluid-induced mechanical stimuli on progenitor cells (human periosteal derived cells, hPDCs) attached to regular pore scaffolds inside a perfusion bioreactor set-up. Each cell is represented by a simplified model of the cortical shell, similar to (Odenthal et al., 2013), supplemented with discrete Focal Adhesions (FAs) and an elastic nucleus. A multi-scale modeling approach is presented, consisting of a CFD analysis at the scaffold macroscopic (tissue) scale in order to determine suitable input boundary conditions at the microscopic scale (single cell scale) where the fluid-structure interaction is modeled via the IBM. The impact on the calculated mechanical stimuli of the spatial location of the cells within the scaffold during flow perfusion was investigated. To illustrate how (location-induced) geometrical differences might affect the biomechanical environment of single cells, three locations and corresponding geometries of cells were chosen: one cell spread along the direction of the flow (A), one facing the flow (F) and one bridging between two struts (B). The present model was furthermore employed to investigate the impact of fluid flow on small clusters of cells attached in the scaffold. In order to investigate some effects of mutual shielding, a ‘three

cells configuration' (T) facing the flow was presented (Fig. 8.2)).

8.3 Methods

Fig 8.1 provides an overview of the different length scales that were considered in this study and Fig. 8.2 shows the location of the different cells as mentioned above. The following sections explain the deformable cell model and the coupling between the deformable cell and the fluid flow in the scaffold.

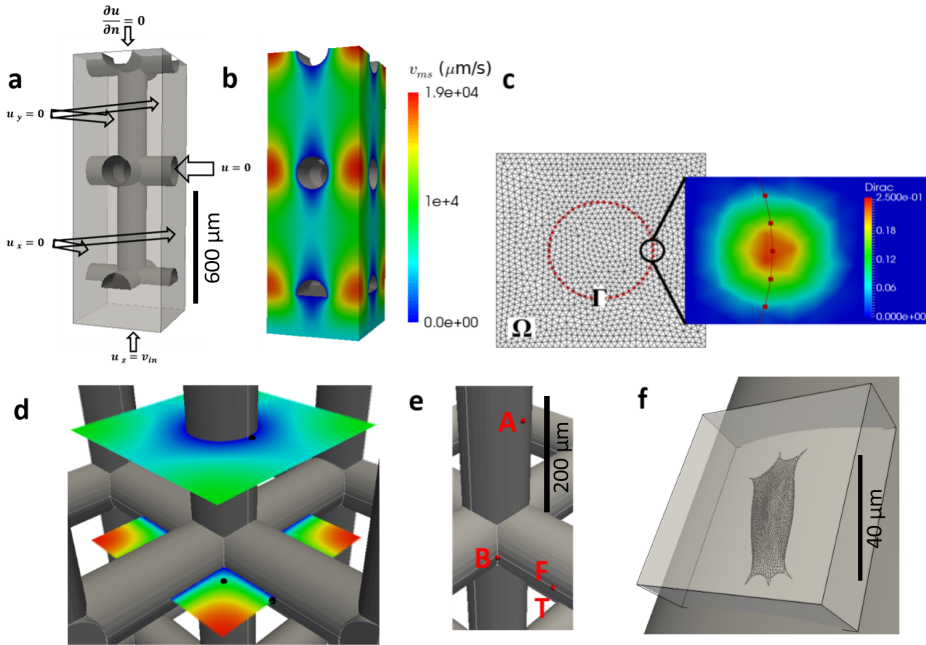


Figure 8.1: Overview of the computational domains. **a)** The computational domain and boundary conditions at the macro-scale. **b)** Computed flow velocity magnitude used as input for the micro-scale models. **c)** Immersed Boundary method representation, Ω and Γ_{cell} are respectively the Eulerian and Lagrangian mesh (left), with an illustration of the smoothed dirac δ_p distribution (right). **d)** Black dots represent the three locations where the micro-scale dirichlet boundary conditions for flow velocity are extracted. **e)** Red dots represent the three locations of cells: along flow (A), bridging (B), facing the flow (F) and ‘three cell cluster configuration’ (T). **f)** Micro-scale domain; the grey cylinder is the scaffold strut, the box is the Eulerian mesh Ω and the cell is the Lagrangian mesh Γ_{cell} .

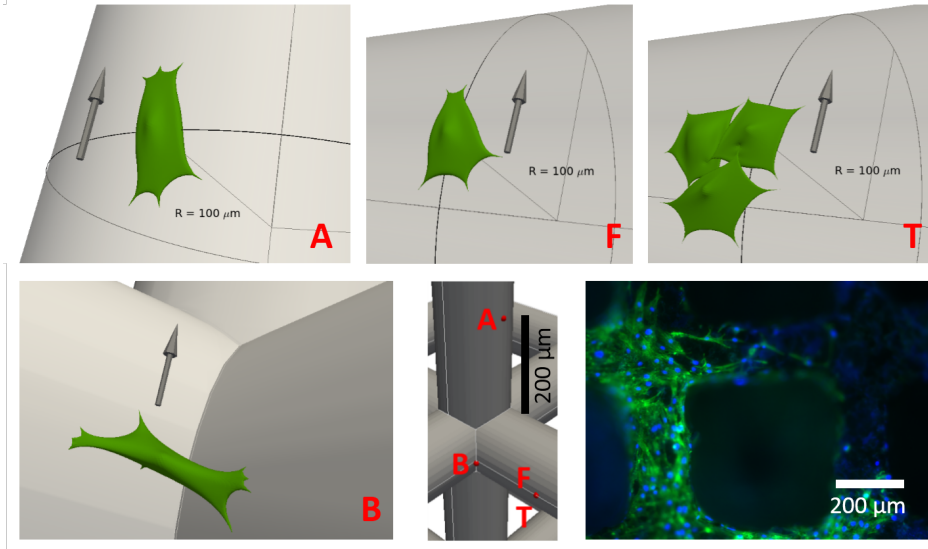


Figure 8.2: Geometrical initial representations of the 4 studied cell configurations. Along the flow (A), facing the flow (F), the three cells clump (T) and the corner bridging cell (B). Bottom right: DAPI/Phalloidin staining of cells attached on scaffold struts.

8.3.1 Immersed Boundary Method

The IBM has been developed for simulating deformable membranes in fluid flow, based on a combination of an Eulerian and a Lagrangian approach (Peskin, 2002). The deformable object (the cell in this study), is represented by a discretized membrane/cortex $\Gamma_{cell}(t)$ and is able to move freely through the fixed Eulerian mesh Ω on which the flow is computed (Fig. 8.1C). The interconnection between both lattices is accomplished by means of a smoothed Dirac function δ_p . In the 3D mesh Ω , the equations for incompressible Stokes flow are solved (as appropriate for the low Reynolds numbers typically encountered in bioreactors), written as

$$\begin{aligned} -\mu\Delta\mathbf{u} + \nabla p &= \mathbf{F} \text{ in } \Omega \\ \nabla \cdot \mathbf{u} &= 0 \text{ in } \Omega \end{aligned} \quad (8.1)$$

with suitable boundary conditions which are explained in following section. In Eq. ??, \mathbf{u} represents the fluid velocity, p the pressure and μ the viscosity. The influence of the cell boundary $\Gamma_{cell}(t)$ immersed in the fluid is taken

into account through the distributed force density and can be expressed as:

$$\mathbf{F}(\mathbf{x}, t) = \int_{\Gamma_{cell}(t)} f(s, t) \delta_p(\mathbf{x} - \mathbf{X}(s, t)) ds \quad (8.2)$$

Here, \mathbf{x} are the Eulerian coordinates and $\mathbf{X}(s, t)$ are the discretized cell membrane coordinates indicating the position of the membrane at time t . As mentioned previously, the interaction between both meshes is realized through the introduction of a dirac function δ_p defined by the following continuous function of the distance r :

$$\delta_p(r) = \begin{cases} \frac{1}{4} (1 + \cos(\frac{\pi r}{2})), & |r| \leq 2 \\ 0, & |r| > 2 \end{cases} \quad (8.3)$$

Using Eq. ??, Eq. ?? can be rewritten in a discrete formulation

$$\mathbf{F}(\mathbf{x}, t) = \sum_{i=1}^N f^i(s, t) \delta_p^h(\mathbf{x} - \mathbf{X}(s, t)) \quad (8.4)$$

with N the number of nodes of the cell membrane, h the Eulerian mesh size and

$$\delta_p^h(\mathbf{x}) = \frac{1}{h^3} \delta_p\left(\frac{x}{h}\right) \delta_p\left(\frac{y}{h}\right) \delta_p\left(\frac{z}{h}\right) \quad (8.5)$$

Once the flow is computed, the membrane positions are updated using the following equation of motion:

$$\frac{d\mathbf{X}(s, t)}{dt} = \mathbf{U}(\mathbf{X}(s, t), t) \quad (8.6)$$

with \mathbf{U} the interpolated flow velocity on $\Gamma_{cell}(t)$ which can be expressed as follows:

$$\mathbf{U}(\mathbf{X}(s, t), t) = \int_{\Omega} \mathbf{u}(\mathbf{x}, t) \delta_p(\mathbf{x} - \mathbf{X}(s, t)) d\mathbf{x} \quad (8.7)$$

8.3.2 Mechanical representation of the cell

The mechanical representation of a cell in the Eulerian domain relies on the work presented in (Odenthal et al., 2013) where the underlying mechanisms and assumptions are discussed in detail. Briefly, the model assumes that most of the cytoskeletal material is present in a relatively thin cortical

shell and that an elastic description of deformations at short timescales is adequate. The immersed boundary which represents the cell is composed of a triangulated surface with a stretching stiffness k_s and a bending energy k_b (Fig. 8.3). The linear spring force between two connected nodes at distance

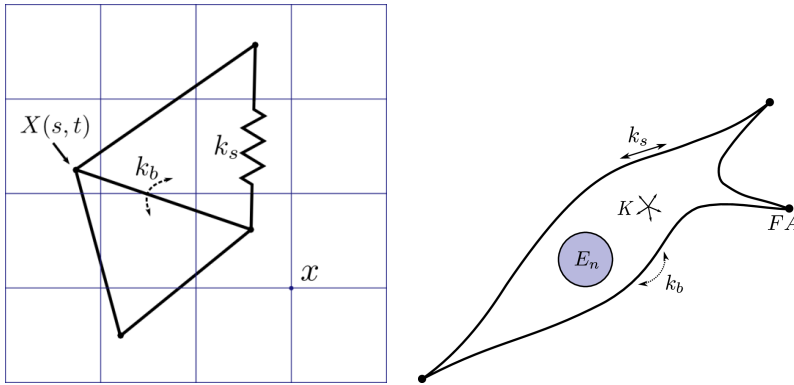


Figure 8.3: Mechanical representation of the cell. **Left:** Lagrangian elastic boundary of the cell with stretching stiffness k_s , bending stiffness k_b and integration points $\mathbf{X}(s, t)$, immersed in an Eulerian lattice with positions \mathbf{x} . **Right:** Mechanical representation of a cell attached to a scaffold, approximated through the use of a cortical shell model with stretching and bending stiffness (resp. k_s and k_b), volume compression modulus K and nucleus stiffness E_n . Discrete attachment points representing focal adhesions (FA) connect the cell to the rigid scaffold.

d^{ij} and resting length d_0^{ij} is expressed as:

$$f_s^{ij} = k_s(d^{ij} - d_0^{ij}) \quad (8.8)$$

A moment of bending is computed between two adjacent triangles with angle θ^{ij} and resting angle θ_0^{ij} :

$$M_b^{ij} = k_b \sin(\theta^{ij} - \theta_0^{ij}) \quad (8.9)$$

A force corresponding to this moment is applied to the non-common points of each of the two triangles, and a compensating force is applied to the common edge points, ensuring that the total force on the cell remains unchanged. The bending force for each node is denoted as f_b^i . This type of bending stiffness is commonly found in the literature for Red Blood Cell models (Fedosov et al., 2010). The cell's volume is maintained through an effective bulk modulus K . For this, an internal pressure P_v is computed

based on a cell's volume V and equilibrium volume V_0 :

$$P_v = K \cdot \frac{V_0 - V}{V} \quad (8.10)$$

Subsequently, a force $f_v^i = P_v A^i n^i$ is obtained for each node i with A^i and n^i respectively the area and outward normal unit vector of each node, both of which are calculated using a discrete version of the Laplace-Beltrami operator. Furthermore, the nucleus is represented as a solid, elastic sphere with Young's modulus E_n for which contact with the cortical nodes is considered Hertzian, i.e.

$$f_n^i = \frac{4E_n \sqrt{R_n}}{3} \delta_n^i \quad (8.11)$$

for a nucleus with radius R_n indenting a node i with overlap distance δ_n^i . Discrete attachment points serve as Focal Adhesions (FAs). These points are placed outside of the fluid domain and are therefore not displaced by the fluid. Finally, the total force per node $f^i(s, t)$ is computed as the sum of all aforementioned partial forces:

$$f^i(s, t) = f_s^i + f_b^i + f_v^i + f_n^i. \quad (8.12)$$

8.3.3 Initialization of the cell geometry

In order to obtain realistic shapes of spread-out and stretched-out cells on cylindrical scaffold struts, we perform a separate relaxation simulation. Hereto we start with a spherical geometry, generated from a subdivided icosahedron (Odenthal et al., 2013), and slowly translate pre-selected adhesion points towards specific attachment points on the scaffold, which are obtained by displacing the nodes normal to the sphere's surface and subsequently projecting them on the scaffold surface (Fig. 8.4). During this process, the 'free' nodes of the cell relax towards an energy-minimizing equilibrium. The node displacements are calculated in the absence of flow, by solving for the velocity $\nu(s, t)$:

$$\Gamma \cdot \nu(s, t) = f(s, t), \quad (8.13)$$

in which $f(s, t)$ are the internal mechanical forces and Γ is an arbitrary friction matrix. It is clear that this does not simulate the way that real cells obtain their spread out configuration, but it should be pointed out that the fundamental mechanisms of protrusions, contractility and mature focal adhesions will produce very similar shapes with elongated, curvature minimizing surfaces.

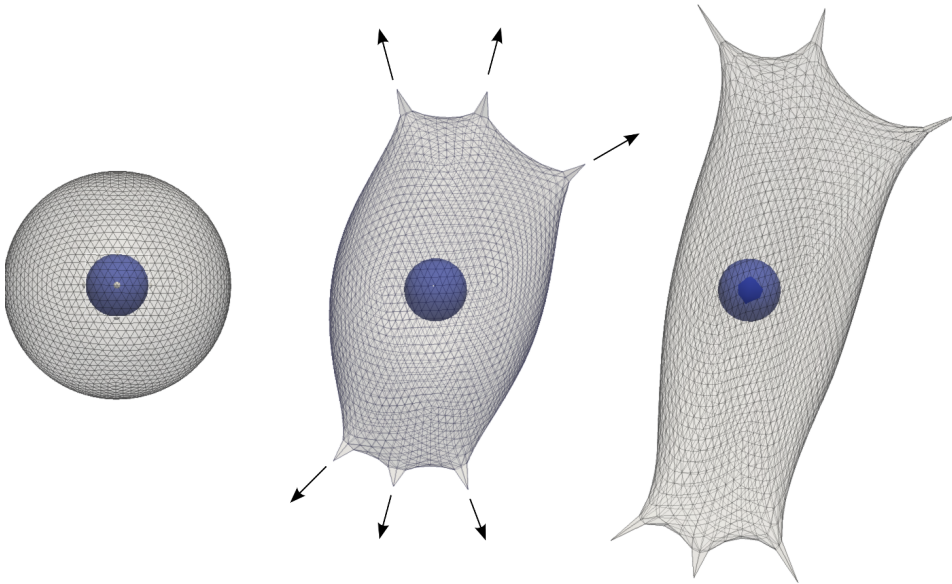


Figure 8.4: Geometrical model of the cell. **From left to right:** An example of the procedure for obtaining geometries of cells attached in flow, starting from a perfect sphere. The blue sphere inside the cell represents the nucleus.

8.3.4 Atomic Force Microscopy measurements of cell cortical stiffness

Cell cortical stiffness was measured using Atomic Force Microscopy (AFM). Measurements were performed using a Nanowizard 3 BioScience AFM (JPK) with a working range of $100 \times 100 \times 15 \mu\text{m}$ mounted on the stage of an inverted microscope (Olympus 1) placed on a vibration-isolation table. A V-shaped gold-coated silicon nitride cantilever with a four-sided pyramidal tip (BudgetSensors) with a nominal tip radius r_{in} of 15 nm and an opening angle θ of 35 degrees was used as the probe. The spring constant k_{spring} of the cantilever was ca. 0.3 Nm^{-1} . Exact values have been calibrated using the thermal fluctuation method. Force curves have been recorded at $5 \mu\text{m/s}$ approach and retract speed, of which only the approach curves have been analyzed to arrive at the instantaneous Young's modulus using the Sneddon model for forces $>200 \text{ pN}$. We neglect the information at low indentations, since according to (Rico et al., 2005), the Sneddon model is sufficient at higher indentation δ , allowing us to extract the cortical Young's modulus

E_c as:

$$F = \frac{E_c \tan(\theta)}{\sqrt{2}(1 - \nu^2)} \delta, \quad (8.14)$$

where F is the measured force. Assuming a Poisson's ratio ν of 0.5 (Charras et al., 2001), we can fit this formula to the typical force-indentation curves obtained by AFM for every pixel on the cell's surface (we use the Levenberg-Marquard algorithm in MINPACK through its python-interface provided by SciPy for curve-fitting). To extract the stiffness of the cortical layer, we select regions on the cell away from the nucleus where the average cell height is very low so that we can assume that the measured stiffness is indeed the compressive stiffness of the cell's cortex and not dominated by effects from bending of the cortical layer or the intra-cellular fluid (see supplementary Fig. 8.12-S). The complete selection procedure consists of the following steps (Rico et al., 2005):

1. Fit Eq. ?? to all the force-distance curves obtained on the cell (typically 16x16 or 32x32). To obtain a robust fit, it has been proven beneficial to estimate the contact-point ($\delta = 0$) at the same time as the apparent cortical Young's modulus.
2. Select thin extensions of the cell.
3. Calculate local slopes of the smoothed surface and reject angles with respect to the vertical >20 degrees to minimize artifacts due to tip-sliding or lateral cell movement.
4. Reject bad fits based on a χ^2 -statistic (rare).

The remaining apparent cortical Young's moduli are averaged per patch on the cell and the distribution of these is shown in Fig. 8.5d, the global average over all measured cells and all patches is 3.5 ± 2 kPa.

8.3.5 Calibration of cell mechanical model

For a relatively thin cortical 'sheet', and assuming the cortex to consist out of some homogenous elastic material, the stretching stiffness k_s and bending energy k_b can be related to the cortical Young's modulus E_c and the cortical thickness t_c :

$$k_b = \frac{E_c t_c^3}{12(1 - \nu_c^2)} \quad (8.15)$$

$$k_s = \frac{2E_c t_c}{\sqrt{3}} \quad (8.16)$$

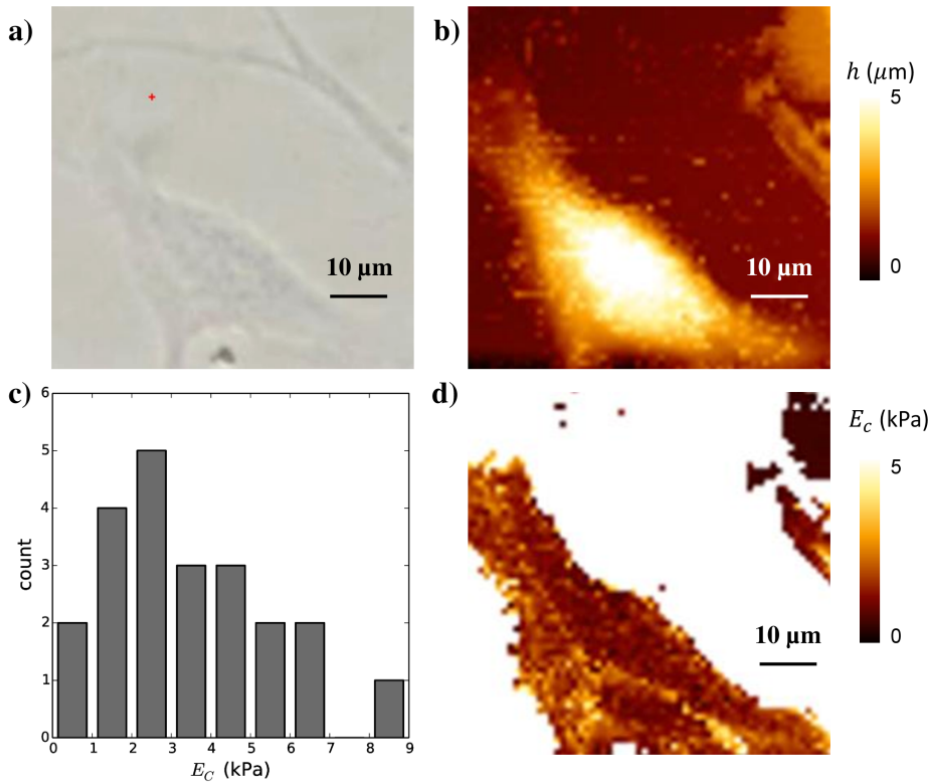


Figure 8.5: AFM measurements of the cell cortical stiffness. **a)** Optical image of the cell, **b)** AFM height map, **c)** histogram of cortical Young's modulus E_c from $N=13$ cells (in which in total 22 different cortex regions were sampled), **d)** Young's modulus image.

where we usually assume the Poisson's ratio of the actin cortex ν_c to be 0.5 (Docheva et al., 2008). Having determined the effective stiffness of the cortical shell and its thickness, these formulas allow us to calculate the parameters of the mechanical cell model. To cross-validate our procedure, these estimated mechanical parameters can be compared to simulated Micropipette Aspiration (MA) experiments. Hereto, a simulation was set up where a spherical cell is aspirated into a thin cylindrical structure with a rounded tip and radius R_p (Fig. 8.6). The relationship between the applied under-pressure in the pipette and the aspirated length L_p of the cell expresses an effective equilibrium Young's Modulus E_∞ which can be compared to experimental values obtained using the same technique

(Hochmuth, 2000):

$$\Delta P = \frac{2\pi}{3} E_\infty \frac{L_p}{R_p} \Phi \quad (8.17)$$

where $\Phi \approx 2.1$ is a scaling factor. The cell's Young's modulus obtained by this procedure (Fig. 8.6) from the parameter values estimated from the AFM measurements (Table 1) compare well to measured values from MSCs; e.g. (Sliogeryte et al., 2014) report Young's moduli in the range of 150-350 Pa.

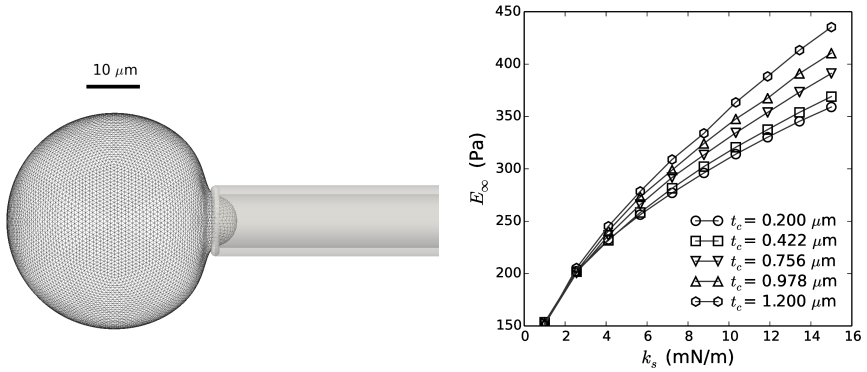


Figure 8.6: Determination of cell stiffness through micropipette aspiration. **Left:** Visualization of simulated micropipette aspiration experiment. **Right:** Equilibrium Young's Modulus E_∞ as a function of stretching stiffness k_s for varying cortical thickness t_c .

Parameter	Symbol	Value	Unit	Source
Viscosity	μ	0.001	Pa · s	Water at 293K
Bending energy cortex	k_b	8.5e-17	Nm	AFM; Eq. 8.15
Cortical stiffness	k_s	2.34e-3	N/m	AFM; Eq. 8.16
Bulk modulus	K	200	Pa	Assumption
Young's modulus nucleus	E_n	1000	Pa	(Guilak et al., 2000)
Poisson's ratio nucleus	ν_n	0.5	-	(Guilak et al., 2000)

Table 8.1: List of parameters used in this study

8.3.6 Preprocessing and Boundary conditions

The fluid environment around a single cell attached to the scaffold is calculated by solving the immersed boundary problem at the scale of the investigated cell. For this purpose, the Eulerian computational domain Ω corresponds to a box of a few hundreds microns wide/long containing the cell and not the whole scaffold pore (Fig. 8.1F). In order to have an estimation of the flow magnitude to be used as a Dirichlet boundary condition on domain Ω when solving Eq. 8.1 for the micro-scale problem, Stokes equation was solved on an entire pore of the scaffold (Fig. 8.1A) and the calculated flow velocity \mathbf{v}_{ms} was used to extract a suitable boundary condition \mathbf{v}_{ib} for the IBM problem. An inlet velocity corresponding to the bioreactor flow rate Q_{in} was set at the entrance of the pore and symmetry boundary conditions were applied on each sides of the pore (Fig. 8.1A).

8.3.7 Implementation

The Immersed Boundary implementation was realized using the Finite Element software FreeFEM++ (Hecht, 2012), which solves the Stokes flow problem, with the Lagrangian forces computed in a coupled module implemented in the particle-based simulation platform DEMeter++ (Tijsskens et al., 2003).

8.4 Results and Discussion

Four potentially relevant mechanical measures were computed for cells experiencing flow conditions inside a scaffold pore: nodal displacement, cortical tension, normal pressure and local shear stress. Moreover, we compared between four different geometries as illustrated in Fig. 8.2: a cell on a cylindrical strut with flow parallel to the cylinder axis (A), a cell on a cylindrical strut with flow perpendicular to the cylinder axis (F), a small cluster of three interconnected cells on a cylindrical strut with flow perpendicular to the cylinder axis (T) and a single cell attached on a strut junction, forming a bridge between two perpendicular struts (B). All cells were attached with discrete FAs located on the surface of the struts and which did not displace. All aforementioned geometries are regularly encountered in experimental set-ups where cells are attached to titanium scaffold struts (Fig. 8.2). In the following section, we will discuss for each of these geometries the effect of flow on the four mechanical measures.

Fig. 8.7 summarizes the effect of flow on the nodal displacements D . Very low displacements were obtained for flow parallel to the cylindrical strut, while intermediate displacements were found for flow perpendicular to the cylindrical strut and relatively high displacements were observed for the cell forming a bridge at a scaffold corner. For inlet bioreactor flow rates in the order of 1 ml/min, maximal displacements are in the range of 30 nm which have been previously reported as a critical displacement for the detachment of mesenchymal stem cells of bridged morphology from irregular scaffolds (Jungreuthmayer et al., 2009; McCoy et al., 2012). However, these studies were carried out using a one-way fluid–structure interaction (FSI) approach and did not consider the influence of cellular deformation on the surrounding fluid flow, something that in this study was included (two way interaction between cell and fluid).

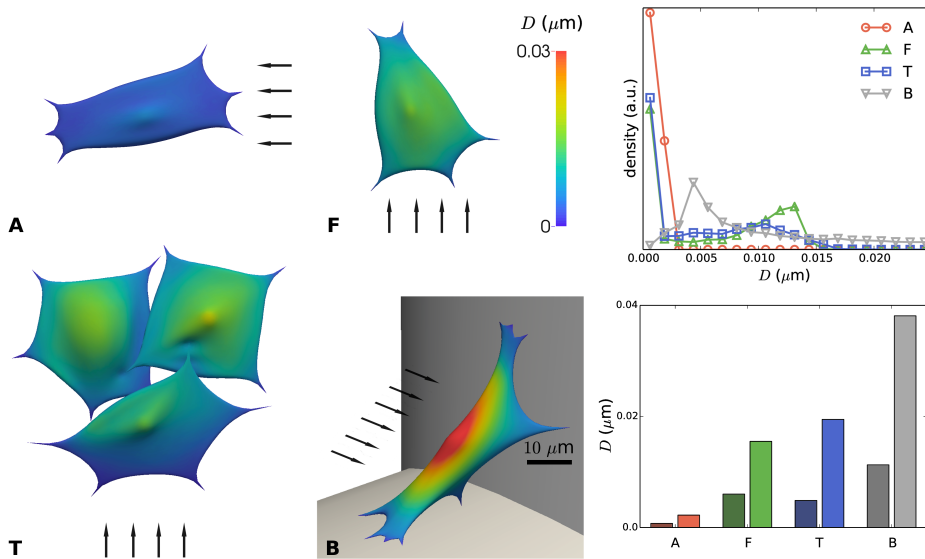


Figure 8.7: Displacement D of the immersed boundary due to flow, relative to the no-flow condition, for distinct configurations (A,F,T and B) of cells on scaffold struts. **Left:** color map showing local displacements. The arrows indicate the direction of the flow; scale bar 10 μm . **Top right:** distribution of the displacements for A, F, T, B. a.u.: arbitrary units. **Bottom right:** mean nodal displacement (dark color) and maximal nodal displacement for cases A, F, T and B.

These deformation value ranges are much smaller than typical deformations of cells in tissue: e.g. for chondrocytes in mature cartilage, strains

higher than 20% (i.e. more than $1\ \mu\text{m}$) have been measured upon tissue compression (Guilak et al., 1995). It should be stressed that our simulations report the instantaneous elastic response in deformation to a step increase in flow velocity, and neglect the viscous deformations that might occur when cells are exposed to constant flow conditions for a long time (i.e days).

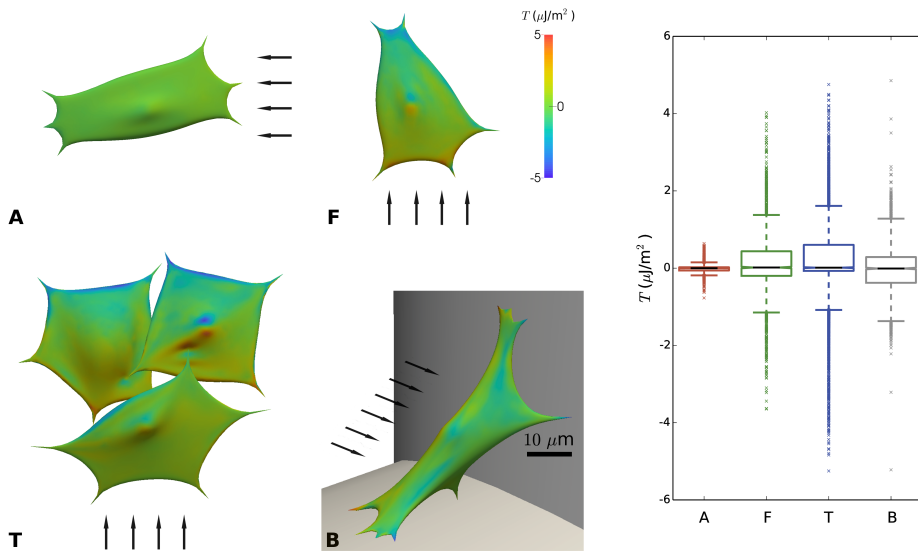


Figure 8.8: Cortical tension T due to imposed flow for distinct configurations (A, F, T and B) of cells on scaffold struts. Positive values indicate tensile conditions, while negative values indicate compressed conditions. **Left:** color map showing local tension. The arrows indicate the direction of the flow; scale bar $10\ \mu\text{m}$. **Right:** Boxplot showing distribution of tension for cases A, F, T and B.

In Fig. 8.8, the distribution of cortical tension T is shown for the four different geometrical configurations. Positive values of T indicate tensile conditions, whereas negative values of T indicate compressive stresses in the cortical shell. Unlike the cell deformations, which were maximal for the cell bridging between two struts (B), the maximal tension T occurs for cells on cylindrical struts with flow perpendicular to the strut (F) and (T). Moreover, maximal cortical tensions are observed close to the nucleus and close to FAs, with tensile stresses occurring at the side of incoming flow and compressive stresses at the side of out-going flow. Maximal tensions, which are highly localized, are around $5\ \mu\text{J}/\text{m}^2$. For comparison, these values are several orders of magnitude below the values for membrane rupture. Other experimental studies have looked at the induction of blebbing, for

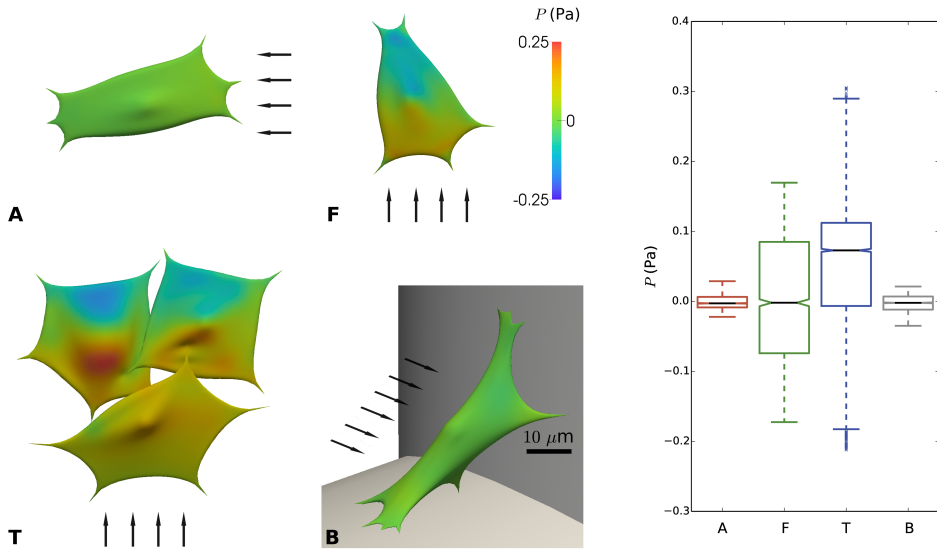


Figure 8.9: Pressure P on the cell surface due to imposed flow for distinct configurations (A, F, T and B) of cells on scaffold struts. **Left:** color maps showing local pressure. The arrows indicate the direction of the flow; scale bar 10 μm . **Right:** boxplot showing distribution of pressure for cases A, F, T and B.

which they reported that cortical tensions of at least $200 \mu\text{J}/\text{m}^2$ (Tinevez et al., 2009) were required, while inside blebs, cortical tensions between 10 and $100 \mu\text{J}/\text{m}^2$ (Peukes and Betz, 2014) were measured. The cell's acto-myosin contractility alone creates an average resting cortical tension in the order of $0.5 \mu\text{J}/\text{m}^2$ (Dai et al., 1999). In other words, the predicted additional cortical tension due to shear flow is relatively low, but it cannot be excluded that these tensions could result in some conformational changes in the cytoskeleton.

Fig. 8.9 shows the distribution of the fluid pressure P on each cell's surface. Cells located in the configuration where the flow is facing the strut, i.e. where the flow velocity is the highest (F and T), show the largest variation in the pressure distribution, reaching a maximal amplitude of about 0.5 Pa. Contrarily, cells located in (A) and (B) display few pressure differences due to the low velocity magnitude and very small changes in the flow streamlines.

Fig. 8.10 shows the flow induced shear stress τ across the examined cells.

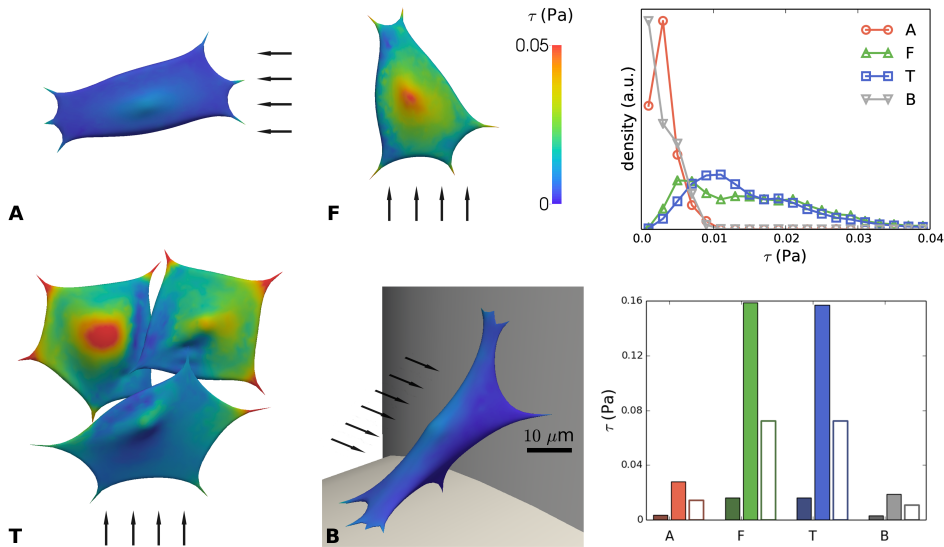


Figure 8.10: Shear stress τ on the cell surface due to imposed flow for distinct configurations (A,F,T and B) of cells on scaffold struts. **Left:** color maps showing local shear stress. The arrows indicate the direction of the flow; scale bar 10 μm . **Top right:** distribution of shear stress for A,F,T,B. **Bottom right:** mean shear stress (dark color) and maximal shear stress (light color) for cases A, F, T and B. The empty bars indicate the shear stress on the empty scaffold strut at the cell's location (computed at the macro-scale).

While the average value of τ taken over the entire cell-surface (including the 'bottom' of the cells, facing the strut) is generally low due to the reduced flow speed and related shear stress at the bottom of the cell, it is very interesting to compare the maximum wall shear stress values at the top of the cells. Due to their location (F) and (T) configurations show the highest magnitude with a value reaching up to 0.16 Pa while cells located in (A) and (B) show a low value of shear stress, around 0.02-0.03 Pa. *In vivo*, cells in the bone tissue have been found to experience shear stresses of 0.8-3.0 Pa during routine physical activity (Weinbaum et al., 1994). Comparing to the expected wall shear stresses in an empty scaffold, we see that the maximum stresses predicted by the IBM are generally about twice as high, while the average stress over the complete cell surface is significantly lower. This clearly indicates the importance of taking the shape and mechanical response of the cells into account for estimating their relevant wall shear stress. Regarding the (F) and T configurations,

as expected, the distribution of shear stress is more homogenous with half of the cell surface exposed to a higher value than 0.015 Pa, while the two other configurations present most of their surface exposed to low shear stress value (below 0.005 Pa). For the flow rate level used in this study, we have previously reported the effect of increasing flow rates resulting in osteogenic priming of hPDCs in the absence of supplementary growth factors (Sonnaert et al., 2014) with genes such as osterix and bone sialoprotein being slightly upregulated. Additionally, again for similar flow rates and in the presence of osteoinductive medium, hPDCs were seen to secrete higher levels of ECM and to enhance mineralization for increasing flow rates (Papantoniou et al., 2013). It has been observed (McCoy et al., 2012) that for a shear stress value exceeding a threshold value of 0.088 Pa, human MSCs can detach from the scaffold surface and by doing so negatively affect the final properties of tissue engineered constructs, resulting in an inhomogenous distribution of neotissue across the scaffold (Papantoniou et al., 2014a). This illustrates the importance of having a numerical model such as the one presented in this study, to quantify and characterize the mechanical environment that cells experience in novel scaffold designs in order to avoid the development of suboptimal or detrimental mechanical regimes.

Fig. 8.11 shows the results of a parameter study where both the inlet flow velocity Q_{in} and the cortical stiffness k_s were varied for configuration (F). From Q_{in} the Dirichlet boundary conditions in the micro-scale model were determined using a CFD simulation of the complete scaffold pore (Fig. 8.1A). The resulting maximal deformation, pressure, shear stress and cortical tension were quantified. One might notice that the dependence on Q_{in} is linear, which is due to the Stokes flow regime, which would be valid for the investigated range of flow rates. Except for the the maximal deformations, the effect of the cells' stiffness is very small.

8.5 Conclusions and outlook

In the presented work, a novel application of the immersed boundary method was developed, representing a deformable cell exposed to microscopic flow and attached to a 3D scaffold inside a perfusion bioreactor. Cells were represented by a deformable Lagrangian surface mesh, which was immersed in an Eulerian fluid domain, with flow in the Stokes regime. We demonstrated the effect of shear flow for multiple realistic geometrical cell configurations and strut locations inside a regular pore scaffold. This

tool can be used to estimate shear flow conditions directly on the surface of individual cells, and assess the micro-scale variability of mechanical conditions inside single scaffold pores. The instantaneous cell stiffness was measured using AFM experiments on hPDCs, and the mechanical model was calibrated using micro-pipette aspiration simulations in the range of short term deformations. Simulations confirmed that mechanical cues originating from the flow are highly dependent on the exact geometry of the cell and its environment. For example, a cell on a cylindrical strut with flow perpendicular to the strut will experience a much larger shear stress than a cell on a similar strut with parallel flow. This should be a major consideration when designing novel scaffold designs. Moreover, it

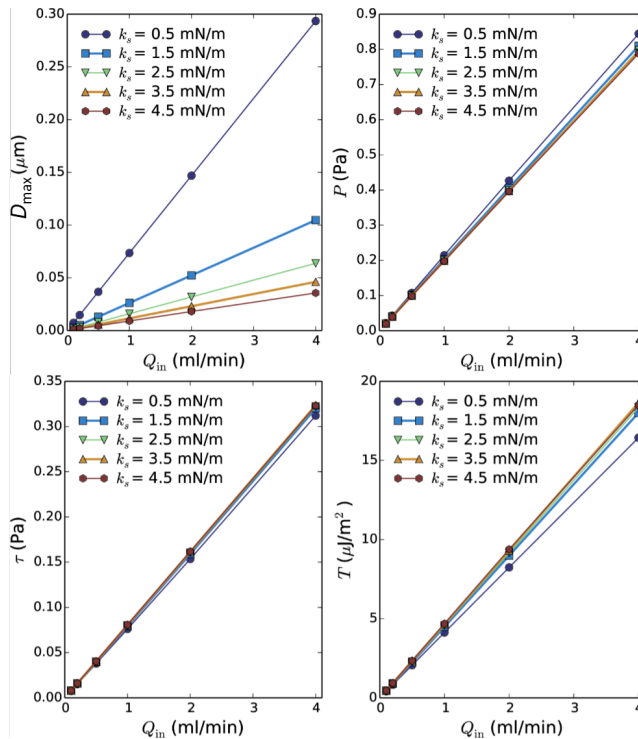


Figure 8.11: Results of a parameter study varying inlet volumetric flow rate and cortex stiffness. **Top left:** maximal local displacement; **Top right:** maximal normal pressure; **Bottom left:** maximal local shear stress and **Bottom right:** maximal local tension.

was found that wall shear stress calculated in the empty scaffold would underestimate the actual maximal wall shear stress experienced by the cells by a factor of two in the investigated cases. Furthermore, the model was used

to estimate the additional instantaneous flow-induced cell deformation, tension and pressure. Compared to the cell-generated deformation and tension due to acto-myosin activity these values are very small for the applied flow conditions, making it unlikely that they would trigger a biological response, at least for the instantaneous elastic deformation. The effect of shear flow on the long timescale viscous-like deformation of living cells remains to be investigated. This would also require a more elaborate description of the cell's mechanical behavior, which for this study was greatly simplified and limited to linearly elastic deformation. Furthermore, to simulate adhesion and detachment behaviour (e.g. in very high shear flows), the presented methodology has to be extended since adhesion is only implicitly captured by placing FAs out of the fluid domain thereby fixing them in space independently of applied forces. A parameter study showed linear behaviour in the relevant cell-mechanical and flow parameters, showing that the model can be used to inter-/extrapolate to different cell types and flow conditions. For a cell of thickness $5\ \mu\text{m}$ facing flow on a strut of diameter $200\ \mu\text{m}$, the wall shear stress can be estimated as: $\tau \approx 0.08Q_{in}$. Evidently, the maximal wall shear stress experienced by a cell does not seem to depend strongly on the cell's mechanics. This implies that even though a cell may undergo structural changes (e.g. migration, re-alignment), it can still reliably 'sense' the shear flow (e.g. with its primary cilium). This study constitutes an important step towards model-based control of a cell's biophysical micro-environment (stem cell niche engineering) in a perfusion bioreactor.

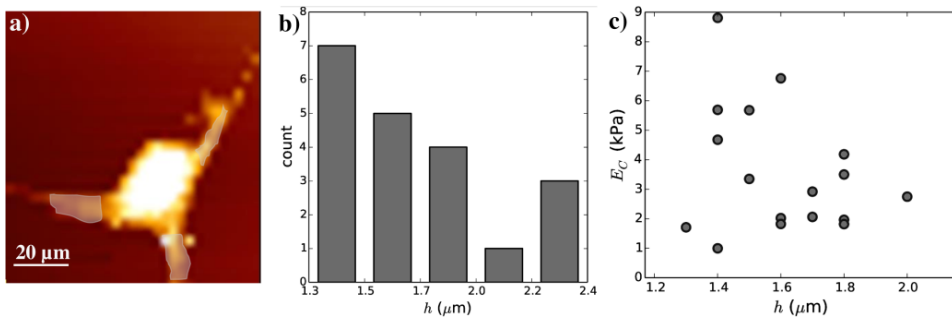


Figure 8.12: Supplementary figure : Additional data on AFM experiments: **a)** Selection of regions on the cellular extension used for the cortex-stiffness analysis, **b)** Average thickness h of all thus selected regions, **c)** Young's modulus E_c vs. thickness h for all regions, no correlations are apparent.

CHAPTER 9

GENERAL CONCLUSION

This final chapter summarizes the work presented in this thesis. It starts with an extended summary and is followed by an overview of the most important contributions of this PhD work to the field of bioprocessing for bone tissue engineering as well as its valorisation potential. At the end of the chapter a number of limitations and potential directions for future research are discussed.

9.1 Summary

The first chapter of this dissertation introduced some biological aspects necessary for the further understanding of the work, like the general biology of bone, properties of bone tissue, the fracture healing process and causes of non-healing. Skeletal tissue engineering was introduced as a promising strategy for treatment of impaired fracture healing cases. Subsequently, process engineering was introduced as a key factor for the production of a viable and clinically relevant tissue engineered construct. Finally, computational models were presented as fundamental tools for helping to tackle remaining issues in the process of engineering a living implant, such as monitoring, quality control and reproducibility.

Chapter 2 presented the main hypothesis of this PhD thesis, i.e. the elaboration of a multi-physics multi-scale computational framework capable of making a substantial contribution to the introduction and implementation of bioprocess engineering concepts in regenerative medicine.

In chapter 3, a computational fluid dynamic approach using the Navier-Stokes equations was applied to model perfusion bioreactors experiments in order to understand the influence of scaffold location within the bioreactor chamber on neotissue growth and estimate the critical distance the scaffold should be placed from the inlet to obtain optimal neotissue distribution. Computationally, different flow rates and positions were tested in order to estimate the optimal distance from the inlet based on the average flow velocity throughout the scaffold. Experimentally, two groups of cell-seeded scaffold were tested, the first one was positioned immediately at the chamber inlet while the second one was placed at the critical distance estimated from the numerical simulations. Experimental data showed significant differences between the two groups in terms of cell content and tissue distribution, as quantified by contrast-enhanced nanofocus computed tomography (CE-nanoCT).

Chapter 4 introduced the concept of the Level-Set Method for simulating neotissue growth by tracking the evolution of the interface between neotissue and void on 3D scaffold. The growth velocity was dependent on the local curvature, exploiting the curvature-dependence nature of neotissue growth reported in the literature. An *in silico* study was conducted, recapitulating a previously executed experiment in which different scaffold geometries (hexagonal, triangular, and square) and macro-pore sizes (500 and 1000 μm) were seeded with hPDCs and cultured in static conditions for 14 days. A qualitative and quantitative comparison was carried out between experimental data and numerical results based on the projected tissue area, and a good correlation between both was demonstrated, demonstrating the relevance of the model.

In order to further extend the previously described static model to dynamic culture conditions (perfusion bioreactor processes) to estimate the fluid induced mechanical microenvironment that cells are exposed to during culture, equations governing the flow behaviour were added to the model (as described in chapter 5). The flow regime into the neotissue (assumed to be a porous media) was governed by the Darcy equation while the free flow was governed by the Stokes equation. The coupling between the two regimes was performed in a continuous manner with the help of the Brinkman equation in its penalisation form. From the computed fluid velocity, information regarding the shear stress distribution at neotissue-void interface and within

the neotissue itself was provided. The model was tested on two scaffold macro-pore geometries (square and diamond). Results showed a significant difference between the two obtained shear stresses (interface vs inside), with the interface shear stress value inferior to inside neotissue value by one order of magnitude.

In chapter 6, the model presented above was further extended to take into account the influence of fluid flow on the neotissue growth velocity. This was obtained by adding to the hitherto only curvature-dependent neotissue growth velocity a factor describing the influence (both beneficial and detrimental) of flow-induced shear stress. The model was implemented on an entire scaffold (cylinder, 6 mm x 6 mm) with a diamond shaped unit cell. The model was used to simulate the difference in neotissue growth velocity for two different flow rates for which experimental data was available. Without performing a rigorous fitting procedure, a rough correspondence between experiments and simulations was observed whereby it was clearly demonstrated that the model was able to quantitatively capture the difference in neotissue growth velocity between the two flow rates.

Chapter 7 described the last extension of the neotissue growth model which pertained to the incorporation of a description of metabolic activity within the scaffold. Three additional Diffusion-Convection-Reaction equations corresponding to oxygen, glucose and lactate concentration were implemented. The influence of these three metabolites on local neotissue growth was introduced in the definition of the growth velocity by adding three factors describing the detrimental effect of low oxygen and glucose concentration and high pH value (a linear approximation of pH was calculated based on lactate concentration). The model was validated by comparison of the simulation outcome with neotissue growth and lactate production data obtained in a dedicated dynamic culture experiment on two in-house triply periodic surface scaffolds. Thereafter, several simulations were conducted in order to explore the potential of the model as a tool for designing experiments in the context of bioprocessing for bone tissue engineering. Five different scaffold geometries with specific macro-pore sizes were designed *in silico* and the most efficient design in terms of scaffold filling was selected. Several flow rates were tested on the selected geometry to demonstrate the importance of a critical flow regime selection. Finally, an optimal *in silico* medium refreshment procedure based on local pH inside

the neotissue was implemented. This procedure was able to suggest optimal medium refreshment time points to enhance neotissue distribution within the scaffold.

Finally, chapter 8 demonstrated the use of the Immersed Boundary Method for quantifying the local mechanical stimuli experienced by an hPDC attached to a 3D scaffold exposed to microscopic flow. A pre-processing CFD procedure was used to estimate the fluid velocity boundary condition at microscopic scale. Atomic Force Microscopy was employed to provide experimental input on the stem cell stiffness. Four relevant mechanical measures were extracted from the simulations, i.e. total displacement, cortical tension, hydrostatic pressure and wall shear stress. The model predicted a significant difference between wall shear stress computed on empty scaffolds struts and the actual maximum and average value acting on the cell.

9.2 General contributions and valorisation potential

This section describes the main contributions and valorisation potential of the work presented in this PhD dissertation (schematically summarized in Fig. 9.1). Besides providing additional insight and quantification of the local biological and mechanical environment throughout the growing neotissue, the presented models can serve as design tools to come up with rational choices for the design of scaffold geometries and bioprocess settings for perfusion bioreactor systems.

Chapter 3 presented a whole perfusion chamber CFD analysis taking into account the bioreactor chamber geometry as well as the exact scaffold architecture. Using such a spatially accurate procedure, it was possible to determine with precision the fluid environment at macro-pore scale and provide an accurate process design criterion via the determination of the local flow velocity within the scaffold. More specifically, using this approach, it was possible to determine, for each flow rate, the optimal scaffold position. This allows to reduce the variation introduced by the local flow environment and to improve the final biological construct, for example, by enhancing quality attributes such as cell content and ECM distribution. The development of this kind of integrative strategy, using at the same time experimental characterisation via CE-nanoCT for quantifying

neotissue formation and computational models for optimisation, might result in a better understanding of the stem cell response to dynamic culture conditions, allowing dedicated design of suitable bioreactor and process regarding the desired neotissue quality.

In chapter 4, the curvature-driven 3D neotissue growth model based on Level-Set Method was introduced, and further extended until chapter 7 in order to take into account cell response to the complex flow environment, nutrient concentration and local pH value. In its initial version (chapter 4), the model was able to qualitatively and quantitatively capture experimental data obtained from a static 3D cell culture experiments on different scaffold geometries and macro-pore sizes. The present model constitutes an alternative to already existing curvature-based neotissue growth models presented in the literature. First of all it extends the models of curvature driven growth from 2D (Rumpler et al., 2008; Bidan et al., 2012; Knychala et al., 2013) and simple 3D geometries (Bidan et al., 2013) to complex 3D structures which are often present when dealing with porous scaffold. Indeed, due to the very nature of the LSM, the model was able to deal with very important changes in the surface topology, allowing the model to predict neotissue formation on any kind of scaffold shape. The use of this type of geometrically based model constitutes a determinant tool for intelligent scaffold architecture design, allowing the production of structures able to actively guide 3D cell growth and finally enhance the construct's characteristics in terms of quality.

Subsequently, the model was extended to simulate dynamic culture conditions with the help of the Brinkman equations governing the flow to investigate the local shear stresses that cells are exposed to during the culture process. This addition of equations governing the fluid velocity profile both in the culture medium as well as in the growing neotissue (considered as a porous medium), constitutes a novelty in modeling neotissue growth under dynamic conditions. Indeed, most of the studies reported in the literature focus on calculating the shear stress on empty scaffolds (De Boodt et al., 2010; Cruel et al., 2015) or consider the neotissue as an impermeable volume where no flow is allowed (Lesman et al., 2010; Nava et al., 2013; Hossain S, 2015). These approaches might be sufficient to capture the initial stages of neotissue formation but are inadequate to capture the later stages as the growing tissue is a porous tissue allowing flow through its own micro-pores thereby changes its surrounding flow

environment. Results presented in chapter 5 show the ability of the model developed in this PhD to tackle the aforementioned issue by calculating the level of shear stress not only on the interface between neotissue and culture medium (void space), but also within the biological construct itself, where an approximation based on the computed interstitial fluid velocity was made. The computed inner shear stress was around 10 to 50 times higher than surface shear stress, showing the non-negligibility of the influence of the progressing neotissue-void interface and the porous nature of the neotissue on the results obtained with the fluid equations. The model contributes to the optimisation of perfusion bioreactor culture by providing an insight into the dynamic microenvironment to which cells are exposed in perfusion bioreactors. Like for the pure geometrical model (chapter 4), taking into account the flow might provide guidance for optimal scaffold architecture design.

After establishment of the ability to compute the local flow profile under dynamic culture conditions, the model was extended in order to take into account the influence of the computed surface shear stress on the definition of the neotissue growth velocity (chapter 6). Since the mechanical stimuli that cells are exposed to have been shown to dramatically affect the cell's behaviour and proliferation, an expression depicting the shear stress' stimulatory effect in a specific range of shear stress values (0.01-0.03 Pa) and its detrimental effect for high values (>0.05 Pa) were added into the neotissue growth velocity definition. Using this type of "flow-induced neotissue growth" model was already present in the literature (Hossain S, 2015; Nava et al., 2013; Chapman et al., 2014), but these models were conducted on 2D cross sections or reduced control 3D volumes and were not considering flow within the neotissue. To the best of the author's knowledge, the results presented in chapter 6 showed for the first time this type of fully coupled and 3D model on a complete scaffold geometry. The model was able to clearly demonstrate the effect of shear stress on neotissue growth by simulating the growth under two different flow rates and comparing the results with in-house experimental data. Using this tool, the operator could adapt the bioreactor flow settings during culture in order to maintain an optimal shear stress magnitude and distribution throughout the neotissue resulting in minimizing the uncertainties and maximizing the final biological construct quality. The final version of the curvature-driven 3D neotissue growth model initiated at chapter 4, was presented in chapter 7. With the help of DCR equations, a simple representation of metabolic

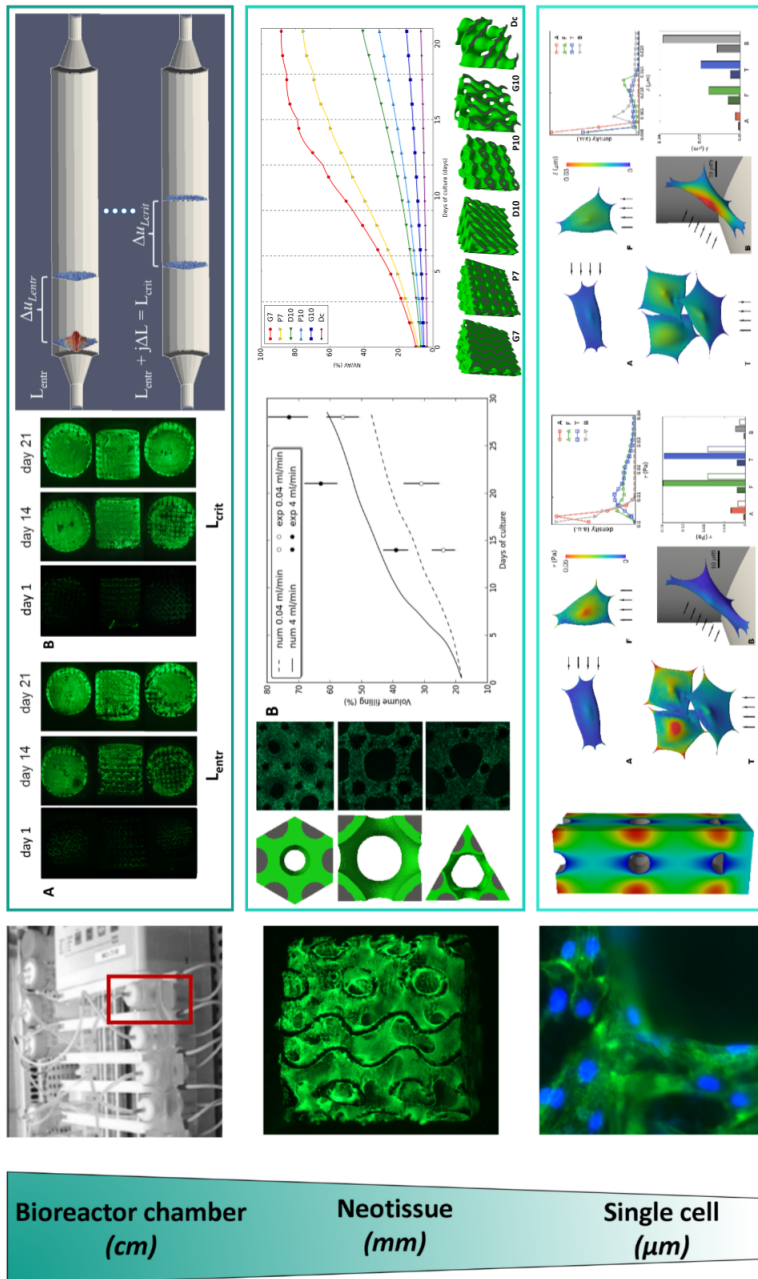


Figure 9.1: Schematic representation of the main contributions of this dissertation

activity was incorporated into the model in order to capture its effect (being negative or positive) on neotissue growth velocity. After calibration of the model by comparing the computed neotissue volume fraction with the experimentally obtained values for two in-house scaffold designs, the model demonstrated its ability to play a role in the design of optimised bioreactor processes. Indeed, this final version constitutes not only a tool for intelligent scaffold geometry design where several designs can be tested *in silico* in order to find the best candidate for 3D cell growth guidance, or a tool for controlling the flow-induced shear stress on the cells by *in silico* varying the flow rate and selecting the optimum fluid velocity; but also contributes to a better understanding of the local effect of metabolite concentrations on neotissue growth. Knowing with precision the local concentration of nutrients and waste products within the scaffold and particularly in the neotissue could lead to additional factors for scaffold geometry design and flow rate determination. Indeed, depending on the scaffold geometry, some isolated zones might appear where the flow is very low, resulting in high waste and low nutrients concentrations in these zones due to lack of convection. Designing a new and efficient scaffold geometry should avoid such zones and in order to enhance the final construct quality. Also for the determination of the flow rate, the local metabolite concentrations should be considered as a too low velocity could not be sufficient to remove waste and replenish the nutrients, potentially creating undesired gradients that might negatively affect the final biological outcomes. Finally, this model can also provide to the operator a more objective criterion for fixing the medium refreshment frequency. Nowadays, experimental procedures include a refreshment of the medium every 2-3 days throughout the entire culture period, without taking into account the evolution of neotissue inside the scaffold. The current model is able to compute *in silico* an adaptive medium refreshment frequency based on predefined criteria such as the local pH value into the system. The elaborated example shows that refreshing the medium when the pH drops below a given threshold in a predefined fraction of the total neotissue volume, leads to a lower frequency of medium change in the early days of culture due to low volume of neotissue and a high frequency in later days. All the above mentioned model features lead to designate the present model as an important tool for the design of new experiments investigating 3D cell growth in a perfusion bioreactor and with implications for the improvement of scaffolds, bioreactors and bioprocess design settings. The use of such tools is required to bring the field of tissue engineering closer to robust and reliable clinical translation.

The final chapter of this thesis, chapter 8, discussed a micro scale model where a cell, immersed in a microfluidic environment represented by an Eulerian mesh, is described by a fully deformable Lagrangian mesh. The model was conducted regarding different cell shapes and locations into the scaffold. Despite the previous models' ability to give insights into the mechanical microenvironment that cells are exposed to under dynamic culture conditions (by calculating the shear stresses inside the neotissue), the present model is able to simulate in a detailed way the precise shear flow conditions on individual cells and thus to provide a better estimation of the micro-scale fluid-induced mechanical stimuli acting on each cell. The model showed that a cell located in a position where it faces the flow, experiences a much larger shear stress than one in a position where the flow is parallel to the cell. Furthermore, the model showed that the maximal shear stress on an individual cell is twice higher than on an empty struts (at the same location) and as such emphasizes again the importance of not considering CFD analyses on empty scaffolds as a sufficient design criterion. Even though the model's length scale is an order of magnitude below that of the models presented in chapter 4 to 7, it can still be considered as a useful tool for scaffold and bioprocess design as it can provide insight into the importance of the cell location within the construct which can be used in the design of optimal scaffold geometries and culture conditions. In conclusion, this chapter constitutes an additional step towards control of the micro-environment in a perfusion bioreactor bioprocess, based on *in silico* simulations.

Recently, the Avicenna Consortium edited a roadmap on *In Silico* Clinical Trials, referring to “the use of individualised computer simulation in the development or regulatory evaluation of a medicinal product, medical device or medical intervention” (Viceconti et al., 2015). The consortium gives an overview on how biomedical products are developed from initial design phase until (and including) the regulatory phase, and how *In Silico* Clinical Trials are or could be used. In relation to the biomedical device industry, they stated that “Modeling and simulation are used extensively in the early design phase, but primarily using computer-aided design and engineering software for the device design and for some very basic functional assessment related to mechanical strength, pressure drops, etc.” Even so, modeling and simulation tools are becoming increasingly accepted by regulators as an integral part of the preclinical dossier that

is submitted to seek permission to take a proposed medical device to the next phase of clinical testing (U.S.-FDA, 2014). Although the development of Advanced Therapy Medicinal Products provide many more challenges than the development of medical devices, the basic tools developed for the latter can be extended to make progress for the former. As such, even if the models presented in this PhD work are at this stage not yet related to very specific clinical applications, they have a vocation to be early design phase tools in the conception of Advanced Therapy Medicinal Products. Throughout this dissertation, achievements have clearly demonstrated that the elaboration of a computational framework can contribute to the introduction and implementation of bioprocess engineering concepts in regenerative orthopaedics, supporting the hypothesis formulated at the start of this work. The clearest articulations of these contributions are listed below, Fig. 9.2 shows schematically how this contributions relate to the Technology Readiness Levels (TRL) used to indicate the level of translation of new technologies into practice.

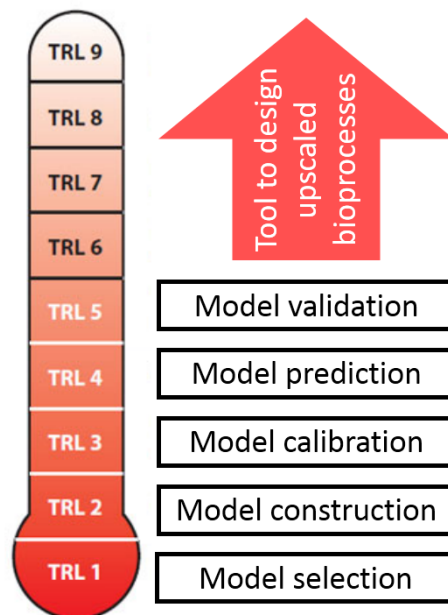


Figure 9.2: Technology Readiness Level (TRL) representation of the work accomplished in this PhD. (image adapted from <http://blog.vegenov.com/voie-express-innovation-europe-pme/>)

- **Bioreactor chamber design.** Combining experimental characterisation and computational models has shown in chapter 3 to be able to optimize the biological outcomes from dynamic culture conditions by finding a critical scaffold location within the bioreactor chamber.
- **Scaffold geometry design.** The 3D neotissue growth model (chapters 4-7) as well as the micro-scale model (chapter 8) have demonstrated their capability as a design tool for scaffold geometries optimisation by showing the essential impact of the local substrate curvature and possible “zone” with low nutrients concentration, or the importance of cells position and alignment or not with flow. This work has shown that the step of designing an intelligent scaffold architecture is crucial in the elaboration of a good quality tissue engineered construct.
- **Perfusion flow rate selection.** Perfusion flow rate selection. Every chapter of this PhD work has shown the fundamental effect of the flow profile on neotissue formation. Computational models can help to understand the flow-induced mechanical stimuli on single cell or neotissue, to assert the total level of shear stress during dynamic culture process, to predict the cell response and to give to the operator an insight of the overall process in order to adapt the perfusion flow rate to have an optimal and well-controlled biological construct.
- **Culture medium composition and refreshment time point.** Computational models have shown (chapter 7) their ability to estimate the chemical composition of the culture medium (pertaining to a certain number of metabolites) and its subsequent change over time. *In silico* models can be used as non-invasive tools for investigating local gradients and concentrations of metabolic species and related pH value. They can also provide critical time points when the medium must be changed to avoid local detrimental pH values, and so, provide to the operator more optimized and control-oriented parameters for enhancing the neotissue quality attributes.

In conclusion, this PhD work has contributed to integrate bioprocess engineering concepts into the tissue engineering field by providing computational tools to enhance control, prediction and optimisation of perfusion bioreactor processes.

9.3 Limitations and future perspectives

In the previous section, it has been shown that the current computational framework developed in this thesis can already contribute to integrate bioprocess engineering concepts in the development of TE products. However, many computational and experimental challenges still need to be addressed in order to have more realistic models, a better understanding of the underlying biological processes, a better quantification of the micro-environment during dynamic culture and, ultimately, an outright contribution of the models to the development of TE products fit for use in the clinics.

9.3.1 Computational perspectives

The first limitation and the next issue to be tackled in the 3D neotissue growth model is the absence of local cell density evolution. Indeed, in its current form, the model considers a homogenous and time independent cell density within the neotissue. However it has been observed experimentally that the cell population does change during culture due to proliferation within the already produced neotissue and cell migration due to random motion, haptotaxis or chemotaxis. In order to tackle this issue, an equation governing cell density, like the one presented in (Geris et al., 2006), has to be implemented. Cell density distribution will have a direct effect on neotissue scaffold filling by adding a new term in the definition of the growth velocity corresponding to its surface value. However, it would also have an indirect effect by consuming or producing more (or less, due to eventual apoptosis) nutrients and waste products, or, by increasing or decreasing the local permeability of the neotissue affecting the local flow profile. The addition of such an equation in the model raises implementation questions. The LSM is based on a fictitious domain approach, where the moving interface (neotissue interface in our case) is not conform to the mesh, and, the cell density evolution has a meaning only in the neotissue volume, leading to a discontinuity. This calls for a remeshing procedure in order to avoid undesired numerical effects at the interface which would considerably increase the computational cost, or for the use of the extended finite element method (X-FEM) to treat the said discontinuity.

Another limitation of this model is the assumption of an initial cell layer covering the totality of the scaffold surface. This might cause an overestimation of neotissue formation in cases where confluency of the initial

cell layer does not correspond to the experimental reality. Indeed, the optimisation of the cell seeding procedure and ensuing efficiency is a research field on its own and still suffers from uncertainties (Sobral et al., 2011; Wendt et al., 2003). Computer models of the seeding procedure have been reported in the literature, often focusing on a particular aspect of the procedure such as cellular adhesion or the dynamic (Olivares and Lacroix, 2012). Building on that body of work, an *in silico* procedure mimicking the underlying process of cell adhesion and scaffold seeding might be incorporated into the current model for neotissue growth in order to initiate the growth process correctly.

The current version of the growth model only takes into account glucose, oxygen and lactate. However, other metabolic species like glutamine or glutamate are also essential factors in the overall bioprocess, and suitable equations might be added into the model in order to simulate their evolution and their influence on the local pH value, to further refine the growth velocity definition. Another aspect of cell culture that the model could help to understand, predict and optimise is the potential differentiation of the cultured stem cells into various lineages. This differentiation can be either a result from the flow-induced mechanical stimuli acting on the cells in the neotissue (Lacroix and Prendergast, 2002; Geris et al., 2008; Isaksson et al., 2008); or it can be the result of the supplementation of the medium with factors known for their induction of differentiation. For the former, the deformation of the newly formed neotissue due to flow needs to be further elaborated. This could be tackled by the introduction of a poroelasticity model (Biot equations for example) (Cowin, 1999). The basis of this type of mechanical models is to consider the porous medium filled with fluid as an elastic body where the pressure drop acts as a body force. However implementing this type of behaviour in the model will create discontinuity (since only the neotissue, and not the void, is concerned with this description) and will raise the same questions for treating this discontinuity as discussed for the incorporation of cell density as a model variable (see above). For the latter, as an example, by adding calcium, phosphate and osteogenic growth factors to the medium, cells inside the neotissue have been shown to progress along the osteogenic lineage and to induce mineralisation of the deposited neotissue, forming osteoinductive mineralized carriers as described in (Chai et al., 2014). Adding additional equations to the model to describe the actions and interactions of these medium supplements, might result in having a non-invasive analysis tool of

to analyse the species' local gradients as well as the spatial distribution of the mineralized matrix within the neotissue. This could help to optimize the final quality of the construct in terms of osteoinductivity for future *in vivo* applications.

The final goal of an *in vitro* tissue engineered construct is to be implanted *in vivo* (ectopically or orthotopically) to assert its bone forming capacity. In order to address this aspect *in silico*, a coupling to other models describing essential *in vivo* processes (such as (Carlier et al., 2014)) might be considered. Briefly, the *in silico* engineered neotissue construct could be placed into an *in silico* large bone defect to observe the bone formation and bone ingrowth into the construct. The result of the *in vivo* model, in terms of amount of bone tissue formed as well as its location provides feedback to the bioreactor culture model, suggesting further optimisation of the scaffold geometry and bioreactor processes (see Fig. 9.3).

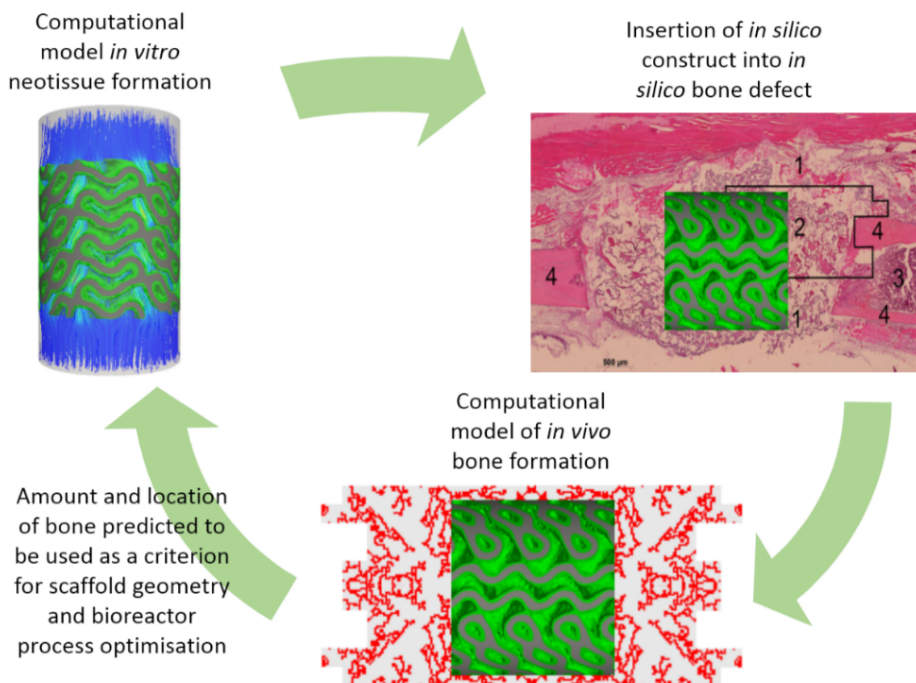


Figure 9.3: Schematic representation of possible interaction between *in silico* models representing the *in vitro* and *in vivo* phases of bone tissue engineering. (images related to the *in vivo* model from (Carlier et al., 2014))

Regarding the micro-scale model, several limitations are present, like the absence of the investigation of long time-scale effects on cell deformation and potential cell migration, as well as a more elaborated description of mechanical behaviour, since in its current state, it is limited to linear elastic deformations. Additionally, the possible effect of cell detachment from the substrate due to shear flow should be one of the next steps in improving the model. Indeed, during dynamic cell seeding procedures or early culture days, cells might detach from the scaffold surface, having a potential dramatic effect on the final construct properties. In (Sanz-Herrera and Reina-Romo, 2011), a model for cell adhesion is presented in which ligand-receptor interaction is described with linear springs. Understanding the adhesion process of suspended cells and determining the critical flow regime where cells will detach are key factors in TE.

9.3.2 Experimental perspectives

During the elaboration of the neotissue growth model, some assumptions and approximations were made, like the estimation of shear stress values having an positive or negative on hPDCs or the relation between growth velocity and curvature. In order to have both a qualitative and a quantitative representation of the bioprocess as well as better parameters estimations, some new experiments must be performed.

Experiments have been conducted on very complex scaffold structures, resulting in the difficulty to read clearly every underlying biological processes. For this purpose, simplified scaffold geometries like cylindrical channels should be manufactured. This will allow to understand more easily the relation between curvature and growth, since curvature can be analytically calculated in a cylinder and neotissue growth velocity more easily observed in a single channel geometry. Recently, a first step in this direction was taken by (Herklotz et al., 2015). In such a simplified set-up, even the influence of the flow might be studied in more detail, as the cylindrical shape will result in a Poiseuille flow profile where shear stress value can easily be extracted and related to neotissue growth. In order to model the adhesion and detachment of cells on surfaces, a simplified set up could be envisaged. With help of a microfluidic device, it can be easily observed under what range of fluid velocity cells are able to attach and above what flow rate threshold cells will detach.

REFERENCES

- AlMamani, T., Udaykumar, H. S., Marshall, J. S., and Chandran, K. B. (2008). Micro-scale dynamic simulation of erythrocyte-platelet interaction in blood flow. *Annals of Biomedical Engineering*, 36(6):905–920.
- Amini, A. R., Laurencin, C. T., and Nukavarapu, S. P. (2012). Bone tissue engineering: recent advances and challenges. *Critical Reviews in Biomedical Engineering*, 40(5).
- Archer, R. and Williams, D. J. (2005). Why tissue engineering needs process engineering. *Nature biotechnology*, 23(11):1353–1355.
- Arrington, E. D., Smith, W. J., Chambers, H. G., Bucknell, A. L., and Davino, N. A. (1996). Complications of iliac crest bone graft harvesting. *Clinical orthopaedics and related research*, 329:300–309.
- Bancroft, G. N., Sikavitsas, V. I., and Mikos, A. G. (2003). Design of a flow perfusion bioreactor system for bone tissue-engineering applications. *Tissue Engineering*, 9(3):549–554.
- Bancroft, G. N., Sikavitsast, V. I., van den Dolder, J., Sheffield, T. L., Ambrose, C. G., Jansen, J. A., and Mikos, A. G. (2002). Fluid flow increases mineralized matrix deposition in 3d perfusion culture of marrow stromal osteoblasts in a dose-dependent manner. *Proceedings of the National Academy of Sciences of the United States of America*, 99(20):12600–12605.
- Berg, H. C. (1993). *Random walks in biology*. Princeton University Press.
- Bhandari, M. and Jain, A. K. (2009). Bone stimulators: Beyond the black box. *Indian journal of orthopaedics*, 43(2):109.

- Bidan, C. M., Kommareddy, K. P., Rumpler, M., Kollmannsberger, P., Brechet, Y. J. M., Fratzl, P., and Dunlop, J. W. C. (2012). How linear tension converts to curvature: Geometric control of bone tissue growth. *PLoS One*, 7(5).
- Bidan, C. M., Wang, F. M., and Dunlop, J. W. (2013). A three-dimensional model for tissue deposition on complex surfaces. *Comput Methods Biomech Biomed Engin.*
- BighamaSadegh, A. and Oryan, A. (2014). Basic concepts regarding fracture healing and the current options and future directions in managing bone fractures. *International wound journal.*
- Boal, D. H. and Rao, M. (1992). Topology changes in fluid membranes. *Physical Review A*, 46(6):3037.
- Boschetti, F., Raimondi, M. T., Migliavacca, F., and Dubini, G. (2006). Prediction of the micro-fluid dynamic environment imposed to three-dimensional engineered cell systems in bioreactors. *J Biomech*, 39(3):418–25.
- Bose, S. and Tarafder, S. (2012). Calcium phosphate ceramic systems in growth factor and drug delivery for bone tissue engineering: a review. *Acta biomaterialia*, 8(4):1401–1421.
- Botchwey, E. A., Dupree, M. A., Pollack, S. R., Levine, E. M., and Laurencin, C. T. (2003). Tissue engineered bone: Measurement of nutrient transport in three dimensional matrices. *Journal of Biomedical Materials Research Part A*, 67(1):357–367.
- Caplan, A. I. and Dennis, J. E. (2006). Mesenchymal stem cells as trophic mediators. *Journal of cellular biochemistry*, 98(5):1076–1084.
- Carlier, A., van Gastel, N., Geris, L., Carmeliet, G., and Van Oosterwyck, H. (2014). Size does matter: an integrative in vivo-in silico approach for the treatment of critical size bone defects.
- Carrier, R. L., Rupnick, M., Langer, R., Schoen, F. J., Freed, L. E., and Vunjak-Novakovic, G. (2002). Effects of oxygen on engineered cardiac muscle. *Biotechnology and bioengineering*, 78(6):617–625.
- Cartmell, S., Huynh, K., Lin, A., Nagaraja, S., and Guldberg, R. (2004). Quantitative microcomputed tomography analysis of mineralization within three-dimensional scaffolds in vitro. *Journal of Biomedical Materials Research Part A*, 69A(1):97–104.
- Chai, Y. C., Geris, L., Bolander, J., Pyka, G., Van Bael, S., Luyten, F. P., and Schrooten, J. (2014). In vivo ectopic bone formation by devitalized mineralized stem cell carriers produced under mineralizing culture condition. *BioResearch open access*, 3(6):265–277.
-

- Chai, Y. C., Roberts, S. J., Desmet, E., Kerckhofs, G., van Gestel, N., Geris, L., Carmeliet, G., Schrooten, J., and Luyten, F. P. (2012a). Mechanisms of ectopic bone formation by human osteoprogenitor cells on cap biomaterial carriers. *Biomaterials*, 33(11):3127–42.
- Chai, Y. C., Roberts, S. J., Van Bael, S., Chen, Y., Luyten, F. P., and Schrooten, J. (2012b). Multi-level factorial analysis of ca^{2+}/π supplementation as bio-instructive media for in vitro biomimetic engineering of three-dimensional osteogenic hybrids. *Tissue Eng Part C Methods*, 18(2):90–103.
- Chapman, L. A., Shipley, R. J., Whiteley, J. P., Ellis, M. J., Byrne, H. M., and Waters, S. L. (2014). Optimising cell aggregate expansion in a perfused hollow fibre bioreactor via mathematical modelling. *PLoS One*, 9(8):e105813.
- Charras, G., Lehenkari, P. P., and Horton, M. (2001). Atomic force microscopy can be used to mechanically stimulate osteoblasts and evaluate cellular strain distributions. *Ultramicroscopy*, 86(1):85–95.
- Chen, Y., Bloemen, V., Impens, S., Moesen, M., Luyten, F. P., and Schrooten, J. (2011). Characterization and optimization of cell seeding in scaffolds by factorial design: quality by design approach for skeletal tissue engineering. *Tissue Engineering Part C: Methods*, 17(12):1211–1221.
- Cioffi, M., Boschetti, F., Raimondi, M. T., and Dubini, G. (2006). Modeling evaluation of the fluid-dynamic microenvironment in tissue-engineered constructs: A micro-ct based model. *Biotechnology and bioengineering*, 93(3):500–510.
- Cowin, S. C. (1999). Bone poroelasticity. *Journal of biomechanics*, 32(3):217–238.
- Cruel, M., Bensidhoum, M., Nougulier-Lehon, C., Dessombz, O., Becquart, P., Petite, H., and Hoc, T. (2015). Numerical study of granular scaffold efficiency to convert fluid flow into mechanical stimulation in bone tissue engineering. *Tissue Engineering Part C: Methods*.
- Dai, J., Ting-Beall, H. P., Hochmuth, R. M., Sheetz, M. P., and Titus, M. A. (1999). Myosin i contributes to the generation of resting cortical tension. *Biophysical journal*, 77(2):1168–1176.
- Dailey H, Yalcin H, G. S. (2007). Fluid-structure modeling of flow-induced alveolar epithelial cell deformation. *Computers & structures*, 85(11):1066–1071.
- Dapogny, C., Dobrzynski, C., and Frey, P. (2014). Three-dimensional adaptive domain remeshing, implicit domain meshing, and applications to free and moving boundary problems. *Journal of Computational Physics*, 262:358–378.
- Dapogny, C. and Frey, P. (2012). Computation of the signed distance function to a discrete contour on adapted triangulation. *Calcolo*, 49(3):193–219.
-

- Darling, E. M. and Guilak, F. (2008). A neural network model for cell classification based on single-cell biomechanical properties. *Tissue Eng Part A*, 14(9):1507–15.
- Datta, N., Pham, Q. P., Sharma, U., Sikavitsas, V. I., Jansen, J. A., and Mikos, A. G. (2006). In vitro generated extracellular matrix and fluid shear stress synergistically enhance 3d osteoblastic differentiation. *Proceedings of the National Academy of Sciences of the United States of America*, 103(8):2488–2493.
- De Boodt, S., Truscello, S., Özcan, S. E., Leroy, T., Van Oosterwyck, H., Berckmans, D., and Schrooten, J. (2010). Bi-modular flow characterization in tissue engineering scaffolds using computational fluid dynamics and particle imaging velocimetry. *Tissue Engineering Part C: Methods*, 16(6):1553–1564.
- Delaine-Smith, R. M. and Reilly, G. C. (2011). The effects of mechanical loading on mesenchymal stem cell differentiation and matrix production. *Vitam Horm*, 87:417–480.
- Demol, J., Lambrechts, D., Geris, L., Schrooten, J., and Van Oosterwyck, H. (2011). Towards a quantitative understanding of oxygen tension and cell density evolution in fibrin hydrogels. *Biomaterials*, 32(1):107–18.
- Discher, D. E., Boal, D. H., and Boey, S. K. (1998). Simulations of the erythrocyte cytoskeleton at large deformation. ii. micropipette aspiration. *Biophysical Journal*, 75(3):1584–1597.
- Docheva, D., Padula, D., Popov, C., Mutschler, W., Clausen-Schaumann, H., and Schieker, M. (2008). Researching into the cellular shape, volume and elasticity of mesenchymal stem cells, osteoblasts and osteosarcoma cells by atomic force microscopy. *Journal of cellular and molecular medicine*, 12(2):537–552.
- Dominici, M., Le Blanc, K., Mueller, I., Slaper-Cortenbach, I., Marini, F., Krause, D., Deans, R., Keating, A., Prockop, D., and Horwitz, E. (2006). Minimal criteria for defining multipotent mesenchymal stromal cells. the international society for cellular therapy position statement. *Cytotherapy*, 8(4):315–317.
- Dos Santos, F., Andrade, P. Z., Boura, J. S., Abecasis, M. M., Da Silva, C. L., and Cabral, J. (2010). Ex vivo expansion of human mesenchymal stem cells: a more effective cell proliferation kinetics and metabolism under hypoxia. *Journal of cellular physiology*, 223(1):27–35.
- Du, D. J., Furukawa, K. S., and Ushida, T. (2009). 3d culture of osteoblast-like cells by unidirectional or oscillatory flow for bone tissue engineering. *Biotechnology and Bioengineering*, 102(6):1670–1678.
- Dunlop, J. W. C., Fischer, F. D., Gamsjager, E., and Fratzl, P. (2010). A theoretical model for tissue growth in confined geometries. *Journal of the Mechanics and Physics of Solids*, 58(8):1073–1087.
-

- Eyckmans, J., Lin, G. L., and Chen, C. S. (2012). Adhesive and mechanical regulation of mesenchymal stem cell differentiation in human bone marrow and periosteum-derived progenitor cells. *Biol Open*, 1(11):1058–68.
- Eyckmans, J. and Luyten, F. P. (2006). Species specificity of ectopic bone formation using periosteum-derived mesenchymal progenitor cells. *Tissue Eng*, 12(8):2203–13.
- Fabry, B., Maksym, G. N., Butler, J. P., Glogauer, M., Navajas, D., and Fredberg, J. J. (2001). Scaling the microrheology of living cells. *Phys Rev Lett*, 87(14):148102.
- Fedosov, D. A., Caswell, B., and Karniadakis, G. E. (2010). Systematic coarse-graining of spectrin-level red blood cell models. *Comput Methods Appl Mech Eng*, 199(29-32).
- Fedosov, D. A., Lei, H., Caswell, B., Suresh, S., and Karniadakis, G. E. (2011). Multiscale modeling of red blood cell mechanics and blood flow in malaria. *PLoS Comput. Biol*, 7(12):e1002270.
- Flaibani, M., Magrofuoco, E., and Elvassore, N. (2009). Computational modeling of cell growth heterogeneity in a perfused 3d scaffold. *Industrial & Engineering Chemistry Research*, 49(2):859–869.
- Frohlich, M., Grayson, W. L., Marolt, D., Gimble, J. M., Kregar-Velikonja, N., and Vunjak-Novakovic, G. (2009). Bone grafts engineered from human adipose-derived stem cells in perfusion bioreactor culture. *Tissue Engineering Part A*, 16(1):179–189.
- Gamsjager, E., Bidan, C., Fischer, F., Fratzl, P., and Dunlop, J. (2013). Modelling the role of surface stress on the kinetics of tissue growth in confined geometries. *Acta biomaterialia*, 9(3):5531–5543.
- Gaspar, D. A., Gomide, V., and Monteiro, F. J. (2012). The role of perfusion bioreactors in bone tissue engineering. *Biomatter*, 2(4):167–175.
- Geris, L. (2013). *Computational modeling in tissue engineering*. Springer.
- Geris, L., Gerisch, A., Maes, C., Carmeliet, G., Weiner, R., Vander Sloten, J., and Van Oosterwyck, H. (2006). Mathematical modeling of fracture healing in mice: comparison between experimental data and numerical simulation results. *Medical and Biological Engineering and Computing*, 44(4):280–289.
- Geris, L., Vandamme, K., Naert, I., Vander Sloten, J., Duyck, J., and Van Oosterwyck, H. (2008). Application of mechanoregulatory models to simulate peri-implant tissue formation in an in vivo bone chamber. *Journal of biomechanics*, 41(1):145–154.
-

- Goldstein, A. S., Juarez, T. M., Helmke, C. D., Gustin, M. C., and Mikos, A. G. (2001). Effect of convection on osteoblastic cell growth and function in biodegradable polymer foam scaffolds. *Biomaterials*, 22(11):1279–1288.
- Grayson, W. L., Bhumiratana, S., Cannizzaro, C., Chao, P. H., Lennon, D. P., Caplan, A. I., and Vunjak-Novakovic, G. (2008a). Effects of initial seeding density and fluid perfusion rate on formation of tissue-engineered bone. *Tissue Eng Part A*, 14(11):1809–20.
- Grayson, W. L., Chao, P. H., Marolt, D., Kaplan, D. L., and Vunjak-Novakovic, G. (2008b). Engineering custom-designed osteochondral tissue grafts. *Trends Biotechnol*, 26(4):181–9.
- Grayson, W. L., Ma, T., and Bunnell, B. (2004). Human mesenchymal stem cells tissue development in 3d pet matrices. *Biotechnol Prog*, 20(3):905–12.
- Grayson, W. L., Marolt, D., Bhumiratana, S., Frohlich, M., Guo, X. E., and Vunjak-Novakovic, G. (2011). Optimizing the medium perfusion rate in bone tissue engineering bioreactors. *Biotechnol Bioeng*, 108(5):1159–70.
- Grayson, W. L., Zhao, F., Izadpanah, R., Bunnell, B., and Ma, T. (2006). Effects of hypoxia on human mesenchymal stem cell expansion and plasticity in 3d constructs. *Journal of cellular physiology*, 207(2):331–339.
- Guilak, F., Ratcliffe, A., and Mow, V. C. (1995). Chondrocyte deformation and local tissue strain in articular cartilage: a confocal microscopy study. *Journal of Orthopaedic Research*, 13(3):410–421.
- Guilak, F., Tedrow, J. R., and Burgkart, R. (2000). Viscoelastic properties of the cell nucleus. *Biochemical and biophysical research communications*, 269(3):781–786.
- Guyot, Y., Luyten, F. P., Schrooten, J., Papantoniou, I., and Geris, L. (2015). A three-dimensional computational fluid dynamics model of shear stress distribution during neotissue growth in a perfusion bioreactor. *Biotechnol Bioeng*.
- Guyot, Y., Papantoniou, I., Chai, Y. C., Van Bael, S., Schrooten, J., and Geris, L. (2014). A computational model for cell/ecm growth on 3d surfaces using the level set method: a bone tissue engineering case study. *Biomech Model Mechanobiol*, 13(6):1361–71.
- Habraken, W., Wolke, J., and Jansen, J. (2007). Ceramic composites as matrices and scaffolds for drug delivery in tissue engineering. *Advanced drug delivery reviews*, 59(4):234–248.
- Hall, S. J. (2007). *Basic biomechanics*. McGraw-Hill Boston, MA:.
-

-
- Harley, B. A., Kim, H. D., Zaman, M. H., Yannas, I. V., Lauffenburger, D. A., and Gibson, L. J. (2008). Microarchitecture of three-dimensional scaffolds influences cell migration behavior via junction interactions. *Biophysical Journal*, 95(8):4013–24.
- Hazwani Suhaimi, Shuai Wang, D. B. D. (2015). Glucose diffusivity in cell culture medium. *Chemical Engineering Journal*, 269(323–327).
- Hecht, F. (2012). New development in freefem++. *Journal of Numerical Mathematics*, 20(3–4):251–265.
- Heisenberg, C. P. and Bellaiche, Y. (2013). Forces in tissue morphogenesis and patterning. *Cell*, 153(5):948–62. Heisenberg, Carl-Philipp Bellaiche, Yohanns eng Research Support, Non-U.S. Gov't Review 2013/05/28 06:00 Cell. 2013 May 23;153(5):948–62. doi: 10.1016/j.cell.2013.05.008.
- Hendrikson, W. J., van Blitterswijk, C. A., Verdonschot, N., Moroni, L., and Rouwkema, J. (2014). Modeling mechanical signals on the surface of micro and cad based rapid prototype scaffold models to predict (early stage) tissue development. *Biotechnol Bioeng*, 111(9):1864–75.
- Herklotz, M., Prewitz, M. C., Bidan, C. M., Dunlop, J. W., Fratzl, P., and Werner, C. (2015). Availability of extracellular matrix biopolymers and differentiation state of human mesenchymal stem cells determine tissue-like growth in vitro. *Biomaterials*, 60:121–129.
- Hidalgo-Bastida, L. A., Thirunavukkarasu, S., Griffiths, S., Cartmell, S. H., and Naire, S. (2012). Modeling and design of optimal flow perfusion bioreactors for tissue engineering applications. *Biotechnology and Bioengineering*, 109(4):1095–1099.
- Higuchi, A., Ling, Q. D., Chang, Y., Hsu, S. T., and Umezawa, A. (2013). Physical cues of biomaterials guide stem cell differentiation fate. *Chem Rev*, 113(5):3297–328.
- Hochmuth, R. M. (2000). Micropipette aspiration of living cells. *J Biomech*, 33(1):15–22. Hochmuth, R M eng HL23728/HL/NHLBI NIH HHS/ Research Support, U.S. Gov't, P.H.S. Review 1999/12/28 J Biomech. 2000 Jan;33(1):15–22.
- Hogea, C. S., Murray, B. T., and Sethian, J. A. (2006). Simulating complex tumor dynamics from avascular to vascular growth using a general level-set method. *journal of mathematical biology*, 53(1):86–134.
- Hollister, S. J. (2005). Porous scaffold design for tissue engineering. *Nature materials*, 4(7):518–524.
-

- Hollister, S. J., Maddox, R. D., and Taboas, J. M. (2002). Optimal design and fabrication of scaffolds to mimic tissue properties and satisfy biological constraints. *Biomaterials*, 23(20):4095–103.
- Hossain, M. S., Bergstrom, D. J., and Chen, X. B. (2015). Prediction of cell growth rate over scaffold strands inside a perfusion bioreactor. *Biomech Model Mechanobiol*, 14(2):333–44.
- Hossain, M. S., Chen, X., and Bergstrom, D. (2012). Investigation of the in vitro culture process for skeletal-tissue-engineered constructs using computational fluid dynamics and experimental methods. *Journal of biomechanical engineering*, 134(12):121003.
- Hossain S, Bergstrom D.J., C. X. (2015). A mathematical model and computational framework for three-dimensional chondrocyte cell growth in a porous tissue scaffold placed inside a bi-directional flow perfusion bioreactor. *Biotechnology and Bioengineering*, 9999:1–10.
- Hutmacher, D. W. (2000). Scaffolds in tissue engineering bone and cartilage. *Biomaterials*, 21(24):2529–2543.
- Hutmacher, D. W., Schantz, T., Zein, I., Ng, K. W., Teoh, S. H., and Tan, K. C. (2001). Mechanical properties and cell cultural response of polycaprolactone scaffolds designed and fabricated via fused deposition modeling. *Journal of biomedical materials research*, 55(2):203–216.
- Hutmacher, D. W. and Singh, H. (2008). Computational fluid dynamics for improved bioreactor design and 3d culture. *Trends Biotechnol*, 26(4):166–172.
- Impens, S., Chen, Y., Mullens, S., Luyten, F., and Schrooten, J. (2010). Controlled cell-seeding methodologies: A first step toward clinically relevant bone tissue engineering strategies. *Tissue Eng Part C Methods*, 16(6):1575–1583.
- Isaksson, H., van Donkelaar, C. C., Huiskes, R., and Ito, K. (2008). A mechano-regulatory bone-healing model incorporating cell-phenotype specific activity. *Journal of theoretical biology*, 252(2):230–246.
- Jakob, M., Saxer, F., Scotti, C., Schreiner, S., Studer, P., Scherberich, A., Heberer, M., and Martin, I. (2012). Perspective on the evolution of cell-based bone tissue engineering strategies. *European Surgical Research*, 49(1):1–7.
- Joly, P., Duda, G. N., Schone, M., Welzel, P. B., Freudenberg, U., Werner, C., and Petersen, A. (2013). Geometry-driven cell organization determines tissue growths in scaffold pores: consequences for fibronectin organization. *PLoS One*, 8(9):e73545.
-

- Jungreuthmayer, C., Donahue, S. W., Jaasma, M. J., Al-Munajjed, A. A., Zanghellini, J., Kelly, D. J., and O'Brien, F. J. (2008). A comparative study of shear stresses in collagen-glycosaminoglycan and calcium phosphate scaffolds in bone tissue-engineering bioreactors. *Tissue Engineering Part A*, 15(5):1141–1149.
- Jungreuthmayer, C., Jaasma, M. J., Al-Munajjed, A. A., Zanghellini, J., Kelly, D. J., and O'Brien, F. J. (2009). Deformation simulation of cells seeded on a collagen-gag scaffold in a flow perfusion bioreactor using a sequential 3d cfd-elastostatics model. *Medical engineering & physics*, 31(4):420–427.
- Keating, J. and McQueen, M. (2001). Substitutes for autologous bone graft in orthopaedic trauma. *JOURNAL OF BONE AND JOINT SURGERY-BRITISH VOLUME-*, 83(1):3–8.
- Kerckhofs, G., Sainz, J., Wevers, M., Van de Putte, T., and Schrooten, J. (2013). Contrast-enhanced nanofocus computed tomography images the cartilage subtissue architecture in three dimensions. *European cells & materials*, 25.
- Kim, H. J., Kim, U., Leisk, G. G., Bayan, C., Georgakoudi, I., and Kaplan, D. L. (2007). Bone regeneration on macroporous aqueous derived silk 3d scaffolds. *Macromolecular bioscience*, 7(5):643–655.
- Knychala, J., Bouropoulos, N., Catt, C., Katsamenis, O., Please, C., and Sengers, B. (2013). Pore geometry regulates early stage human bone marrow cell tissue formation and organisation. *Annals of biomedical engineering*, 41(5):917–930.
- Kommareddy, K. P., Lange, C., Rumpler, M., Dunlop, J. W. C., Manjubala, I., Cui, J., Kratz, K., Lendlein, A., and Fratzl, P. (2010). Two stages in three-dimensional in vitro growth of tissue generated by osteoblastlike cells. *Biointerphases*, 5(2):45–52.
- Kreke, M. R., Huckle, W. R., and Goldstein, A. S. (2005). Fluid flow stimulates expression of osteopontin and bone sialoprotein by bone marrow stromal cells in a temporally dependent manner. *Bone*, 36(6):1047–1055.
- Lacroix, D. and Prendergast, P. (2002). A mechano-regulation model for tissue differentiation during fracture healing: analysis of gap size and loading. *Journal of biomechanics*, 35(9):1163–1171.
- Lambrechts, T., Papantoniou, I., Sonnaert, M., Schrooten, J., and Aerts, J. M. (2014). Model-based cell number quantification using online single-oxygen sensor data for tissue engineering perfusion bioreactors. *Biotechnol Bioeng*, 111(10):1982–92.
- Lanza, R., Langer, R., and Vacanti, J. P. (2011). *Principles of tissue engineering*. Academic press.
-

- Lappa, M. (2003a). The growth and the fluid dynamics of protein crystals and soft organic tissues: models and simulations, similarities and differences. *J Theor Biol*, 224(2):225–240.
- Lappa, M. (2003b). Organic tissues in rotating bioreactors: fluid-mechanical aspects, dynamic growth models, and morphological evolution. *Biotechnol Bioeng*, 84(5):518–32.
- Lappa, M. (2005). A cfd level-set method for soft tissue growth: theory and fundamental equations. *Journal of Biomechanics*, 38(1):185–190.
- Lee, A. M., Berny-Lang, M. A., Liao, S., Kanso, E., Kuhn, P., McCarty, O. J., and Newton, P. K. (2012). A low-dimensional deformation model for cancer cells in flow. *Phys Fluids (1994)*, 24(8):81903.
- Leijten, J., Chai, Y. C., Papantoniou, I., Geris, L., Schrooten, J., and Luyten, F. (2015). Cell based advanced therapeutic medicinal products for bone repair: Keep it simple? *Advanced drug delivery reviews*, 84:30–44.
- Lenas, P. and Luyten, F. P. (2011). An emerging paradigm in tissue engineering: From chemical engineering to developmental engineering for bioartificial tissue formation through a series of unit operations that simulate the in vivo successive developmental stages†. *Industrial & Engineering Chemistry Research*, 50(2):482–522.
- Lesman, A., Blinder, Y., and Levenberg, S. (2010). Modeling of flow-induced shear stress applied on 3d cellular scaffolds: implications for vascular tissue engineering. *Biotechnology and bioengineering*, 105(3):645.
- Li, D. Q., Tang, T. T., Lu, J. X., and Dai, K. R. (2009). Effects of flow shear stress and mass transport on the construction of a large-scale tissue-engineered bone in a perfusion bioreactor. *Tissue Engineering Part A*, 15(10):2773–2783.
- Lieberman, J. R., Daluiski, A., and Einhorn, T. A. (2002). The role of growth factors in the repair of bone. *The Journal of bone & joint surgery*, 84(6):1032–1044.
- Liu, X. and Ma, P. X. (2004). Polymeric scaffolds for bone tissue engineering. *Annals of biomedical engineering*, 32(3):477–486.
- Lushi, E., Wioland, H., and Goldstein, R. E. (2014). Fluid flows created by swimming bacteria drive self-organization in confined suspensions. *Proc Natl Acad Sci U S A*, 111(27):9733–8.
- Lutolf, M. P. and Hubbell, J. A. (2005). Synthetic biomaterials as instructive extracellular microenvironments for morphogenesis in tissue engineering. *Nature Biotechnology*, 23(1):47–55.
-

-
- Machacek, M. and Danuser, G. (2006). Morphodynamic profiling of protrusion phenotypes. *Biophysical Journal*, 90(4):1439–1452.
- Mack, J. J., Youssef, K., Noel, O. D. V., Lake, M. P., Wu, A., Iruela-Arispe, M. L., and Bouchard, L. S. (2013). Real-time maps of fluid flow fields in porous biomaterials. *Biomaterials*, 34(8):1980–1986.
- Maes, F., Claessens, T., Moesen, M., Van Oosterwyck, H., Van Ransbeeck, P., and Verdonck, P. (2012). Computational models for wall shear stress estimation in scaffolds: A comparative study of two complete geometries. *Journal of biomechanics*, 45(9):1586–1592.
- Maes, F., Ransbeeck, P., Van Oosterwyck, H., and Verdonck, P. (2009). Modeling fluid flow through irregular scaffolds for perfusion bioreactors. *Biotechnology and Bioengineering*, 103(3):621–630.
- Mahmoudifar, N. and Doran, P. M. (2005). Tissue engineering of human cartilage in bioreactors using single and composite cell-seeded scaffolds. *Biotechnology and Bioengineering*, 91(3):338–355.
- Malda, J., Klein, T. J., and Upton, Z. (2007). The roles of hypoxia in the in vitro engineering of tissues. *Tissue engineering*, 13(9):2153–2162.
- Malone, A. M., Anderson, C. T., Tummala, P., Kwon, R. Y., Johnston, T. R., Stearns, T., and Jacobs, C. R. (2007). Primary cilia mediate mechanosensing in bone cells by a calcium-independent mechanism. *Proc Natl Acad Sci U S A*, 104(33):13325–30.
- Markway, B. D., Tan, G.-K., Brooke, G., Hudson, J. E., Cooper-White, J. J., and Doran, M. R. (2010). Enhanced chondrogenic differentiation of human bone marrow-derived mesenchymal stem cells in low oxygen environment micropellet cultures. *Cell transplantation*, 19(1):29–42.
- Martin, I., Smith, T., and Wendt, D. (2009). Bioreactor-based roadmap for the translation of tissue engineering strategies into clinical products. *Trends Biotechnol*, 27(9):495–502.
- Martin, I., Wendt, D., and Heberer, M. (2004). The role of bioreactors in tissue engineering. *Trends Biotechnol*, 22(2):80–6.
- Mason, C. and Hoare, M. (2007). Regenerative medicine bioprocessing: Building a conceptual framework based on early studies. *Tissue Engineering*, 13(2):301–311.
- McCoy, R. J., Jungreuthmayer, C., and O’Brien, F. J. (2012). Influence of flow rate and scaffold pore size on cell behavior during mechanical stimulation in a flow perfusion bioreactor. *Biotechnology and bioengineering*, 109(6):1583–1594.
-

- McCoy, R. J. and O'Brien, F. J. (2010). Influence of shear stress in perfusion bioreactor cultures for the development of three-dimensional bone tissue constructs: a review. *Tissue Engineering Part B: Reviews*, 16(6):587–601.
- Meinel, L., Karageorgiou, V., Fajardo, R., Snyder, B., Shinde-Patil, V., Zichner, L., Kaplan, D., Langer, R., and Vunjak-Novakovic, G. (2004). Bone tissue engineering using human mesenchymal stem cells: effects of scaffold material and medium flow. *Annals of biomedical engineering*, 32(1):112–122.
- Melchels, F. P., Barradas, A. M., Van Blitterswijk, C. A., De Boer, J., Feijen, J., and Grijpma, D. W. (2010). Effects of the architecture of tissue engineering scaffolds on cell seeding and culturing. *Acta Biomaterialia*, 6(11):4208–4217.
- Melchels, F. P., Tonnarelli, B., Olivares, A. L., Martin, I., Lacroix, D., Feijen, J., Wendt, D. J., and Grijpma, D. W. (2011). The influence of the scaffold design on the distribution of adhering cells after perfusion cell seeding. *Biomaterials*, 32(11):2878–2884.
- Milan, J.-L., Planell, J. A., and Lacroix, D. (2009). Computational modelling of the mechanical environment of osteogenesis within a polylactic acid–calcium phosphate glass scaffold. *Biomaterials*, 30(25):4219–4226.
- Nabovati, A., Llewellyn, E., and Sousa, A. (2009). A general model for the permeability of fibrous porous media based on fluid flow simulations using the lattice boltzmann method. *Composites: Part A*, 40:860–869.
- Nava, M. M., Raimondi, M. T., and Pietrabissa, R. (2013). A multiphysics 3d model of tissue growth under interstitial perfusion in a tissue-engineering bioreactor. *Biomech Model Mechanobiol*, 12(6):1169–79.
- Nelson, C. M., Jean, R. P., Tan, J. L., Liu, W. F., Sniadecki, N. J., Spector, A. A., and Chen, C. S. (2005). Emergent patterns of growth controlled by multicellular form and mechanics. *Proceedings of the National Academy of Sciences of the United States of America*, 102(33):11594–11599.
- Odenhal, T., Smeets, B., Van Liedekerke, P., Tijssens, E., Van Oosterwyck, H., and Ramon, H. (2013). Analysis of initial cell spreading using mechanistic contact formulations for a deformable cell model. *PLoS Comput Biol*, 9(10):e1003267.
- Olivares, A. L. and Lacroix, D. (2012). Simulation of cell seeding within a three-dimensional porous scaffold: a fluid-particle analysis. *Tissue Engineering Part C: Methods*, 18(8):624–631.
- Olivares, A. L., Marsal, A., Planell, J. A., and Lacroix, D. (2009). Finite element study of scaffold architecture design and culture conditions for tissue engineering. *Biomaterials*, 30(30):6142–6149.
-

- Otsu, N. (1979). Threshold selection method from gray-level histograms. *Ieee Transactions on Systems Man and Cybernetics*, 9(1):62–66.
- Palsson BO, B. S. (2004). Scaling up for ex vivo cultivation. in: *Tissue engineering*. Pearson Education, London.
- Papadimitropoulos, A., Scotti, C., Bourguine, P., Scherberich, A., and Martin, I. (2015). Engineered decellularized matrices to instruct bone regeneration processes. *Bone*, 70:66–72.
- Papantoniou, I., Chai, Y. C., Luyten, F. P., and Schrooten, J. (2013). Process quality engineering for bioreactor-driven manufacturing of tissue-engineered constructs for bone regeneration. *Tissue Engineering Part C-Methods*, 19(8):596–609.
- Papantoniou, I., Guyot, Y., Sonnaert, M., Kerckhofs, G., Luyten, F. P., Geris, L., and Schrooten, J. (2014a). Spatial optimization in perfusion bioreactors improves bone tissue-engineered construct quality attributes. *Biotechnol Bioeng*, 111(12):2560–70.
- Papantoniou, I., Sonnaert, M., Geris, L., Luyten, F. P., Schrooten, J., and Kerckhofs, G. (2014b). Three-dimensional characterization of tissue-engineered constructs by contrast-enhanced nanofocus computed tomography. *Tissue Eng Part C Methods*, 20(3):177–87.
- Patrachari, A. R., Podichetty, J. T., and Madihally, S. V. (2012). Application of computational fluid dynamics in tissue engineering. *Journal of bioscience and bioengineering*, 114(2):123–132.
- Pearson, N. C., Waters, S. L., Oliver, J. M., and Shipley, R. J. (2015). Multiphase modelling of the effect of fluid shear stress on cell yield and distribution in a hollow fibre membrane bioreactor. *Biomechanics and modeling in mechanobiology*, 14(2):387–402.
- Peskin, C. S. (2002). The immersed boundary method. *Acta numerica*, 11:479–517.
- Peukes, J. and Betz, T. (2014). Direct measurement of the cortical tension during the growth of membrane blebs. *Biophysical journal*, 107(8):1810–1820.
- Pham, N. H., Voronov, R. S., VanGordon, S. B., Sikavitsas, V. I., and Papavassiliou, D. V. (2012). Predicting the stress distribution within scaffolds with ordered architecture. *Biorheology*, 49(4):235.
- Placzek, M. R., Chung, I. M., Macedo, H. M., Ismail, S., Blanco, T. M., Lim, M., Cha, J. M., Fauzi, I., Kang, Y., Yeo, D. C. L., Ma, C. Y. J., Polak, J. M., Panoskaltsis, N., and Mantalaris, A. (2009). Stem cell bioprocessing: fundamentals and principles. *Journal of the Royal Society Interface*, 6(32):209–232.
-

- Plunkett, N. A., Partap, S., and O'Brien, F. J. (2010). Osteoblast response to rest periods during bioreactor culture of collagen-glycosaminoglycan scaffolds. *Tissue Eng Part A*, 16(3):943–51.
- Podichetty, J. T., Bhaskar, P. R., Khalf, A., and Madihally, S. V. (2014). Modeling pressure drop using generalized scaffold characteristics in an axial-flow bioreactor for soft tissue regeneration. *Annals of biomedical engineering*, 42(6):1319–1330.
- Podichetty, J. T., Dhane, D. V., and Madihally, S. V. (2012). Dynamics of diffusivity and pressure drop in flow-through and parallel-flow bioreactors during tissue regeneration. *Biotechnology progress*, 28(4):1045–1054.
- Polyanin, A., Zaitsev, V., and Moussiaux, A. (2002). *Handbook of First Order Partial Differential Equations*. Taylor and Francis, London.
- Porter, B., Zauel, R., Stockman, H., Guldberg, R., and Fyhrie, D. (2005). 3-d computational modeling of media flow through scaffolds in a perfusion bioreactor. *Journal of Biomechanics*, 38(3):543–549.
- Porter, B. D., Lin, A. S. P., Peister, A., Hutmacher, D., and Guldberg, R. E. (2007). Noninvasive image analysis of 3d construct mineralization in a perfusion bioreactor. *Biomaterials*, 28(15):2525–2533.
- Radisic, M., Malda, J., Epping, E., Geng, W., Langer, R., and Vunjak-Novakovic, G. (2006). Oxygen gradients correlate with cell density and cell viability in engineered cardiac tissue. *Biotechnology and bioengineering*, 93(2):332–343.
- Raimondi, M. T., Boschetti, F., Falcone, L., Migliavacca, F., Remuzzi, A., and Dubini, G. (2004). The effect of media perfusion on three-dimensional cultures of human chondrocytes: integration of experimental and computational approaches. *Biorheology*, 41(3-4):401–10.
- Rauh, J., Milan, F., Gunther, K. P., and Stiehler, M. (2011). Bioreactor systems for bone tissue engineering. *Tissue Eng Part B Rev*, 17(4):263–80.
- Rico, F., Roca-Cusachs, P., Gavara, N., Farre, R., Rotger, M., and Navajas, D. (2005). Probing mechanical properties of living cells by atomic force microscopy with blunted pyramidal cantilever tips. *Phys Rev E Stat Nonlin Soft Matter Phys*, 72(2 Pt 1):021914.
- Rumpler, M., Woesz, A., Dunlop, J. W. C., van Dongen, J. T., and Fratzl, P. (2008). The effect of geometry on three-dimensional tissue growth. *Journal of the Royal Society Interface*, 5(27):1173–1180.
- Sacco, R., Causin, P., Zunino, P., and Raimondi, M. T. (2011). A multiphysics/multiscale 2d numerical simulation of scaffold-based cartilage regeneration under interstitial perfusion in a bioreactor. *Biomechanics and modeling in mechanobiology*, 10(4):577–589.
-

- Saki, N., Jalalifar, M. A., Soleimani, M., Hajizamani, S., and Rahim, F. (2013). Adverse effect of high glucose concentration on stem cell therapy. *International journal of hematology-oncology and stem cell research*, 7(3):34.
- Salter, E., Goh, B., Hung, B., Hutton, D., Ghone, N., and Grayson, W. L. (2012). Bone tissue engineering bioreactors: a role in the clinic? *Tissue Eng Part B Rev*, 18(1):62–75.
- Sanz-Herrera, J. A. and Reina-Romo, E. (2011). Cell-biomaterial mechanical interaction in the framework of tissue engineering: insights, computational modeling and perspectives. *International journal of molecular sciences*, 12(11):8217–8244.
- Sethian, J. A. (1996). A fast marching level set method for monotonically advancing fronts. *Proc Natl Acad Sci U S A*, 93(4):1591–5. Sethian, J A eng 1996/02/20 00:00 Proc Natl Acad Sci U S A. 1996 Feb 20;93(4):1591-5.
- Sethian, J. A. (1999). Fast marching methods. *Siam Review*, 41(2):199–235.
- Shapiro, F. (2008). Bone development and its relation to fracture repair. the role of mesenchymal osteoblasts and surface osteoblasts. *Eur Cell Mater*, 15(53):e76.
- Shemesh, T., Geiger, B., Bershadsky, A. D., and Kozlov, M. M. (2005). Focal adhesions as mechanosensors: a physical mechanism. *Proc Natl Acad Sci U S A*, 102(35):12383–8.
- Shin, J., Kim, S., Jeong, D., Lee, H. G., Lee, D., Lim, J. Y., and Kim, J. (2012). Finite element analysis of schwarz p surface pore geometries for tissue-engineered scaffolds. *Mathematical Problems in Engineering*, 2012.
- Shraiman, B. I. (2005). Mechanical feedback as a possible regulator of tissue growth. *Proceedings of the National Academy of Sciences of the United States of America*, 102(9):3318–3323.
- Shrivats, A. R., McDermott, M. C., and Hollinger, J. O. (2014). Bone tissue engineering: state of the union. *Drug discovery today*, 19(6):781–786.
- Sikavitsas, V. I., Bancroft, G. N., Lemoine, J. J., Liebschner, M. A. K., Dauner, M., and Mikos, A. G. (2005). Flow perfusion enhances the calcified matrix deposition of marrow stromal cells in biodegradable nonwoven fiber mesh scaffolds. *Annals of Biomedical Engineering*, 33(1):63–70.
- Sikavitsas, V. I., Bancroft, G. N., and Mikos, A. G. (2002). Formation of three dimensional cell/polymer constructs for bone tissue engineering in a spinner flask and a rotating wall vessel bioreactor. *Journal of biomedical materials research*, 62(1):136–148.
-

- Sliogeryte, K., Thorpe, S. D., Lee, D. A., Botto, L., and Knight, M. M. (2014). Stem cell differentiation increases membrane-actin adhesion regulating cell blebability, migration and mechanics. *Scientific reports*, 4.
- Slomka, N. and Gefen, A. (2010). Confocal microscopy-based three-dimensional cell-specific modeling for large deformation analyses in cellular mechanics. *Journal of biomechanics*, 43(9):1806–1816.
- Sobral, J. M., Caridade, S. G., Sousa, R. A., Mano, J. F., and Reis, R. L. (2011). Three-dimensional plotted scaffolds with controlled pore size gradients: Effect of scaffold geometry on mechanical performance and cell seeding efficiency. *Acta Biomater*, 7(3):1009–1018.
- Song, M. J., Dean, D., and Tate, M. L. K. (2013). Mechanical modulation of nascent stem cell lineage commitment in tissue engineering scaffolds. *Biomaterials*, 34(23):5766–5775.
- Sonnaert, M., Kerckhofs, G., Papantoniou, I., Van Vlierberghe, S., Boterberg, V., Dubruel, P., Luyten, F. P., Schrooten, J., and Geris, L. (2015). Multifactorial optimization of contrast-enhanced nanofocus computed tomography for quantitative analysis of neo-tissue formation in tissue engineering constructs. *PloS one*, 10(6):e0130227.
- Sonnaert, M., Papantoniou, I., Bloemen, V., Kerckhofs, G., Luyten, F. P., and Schrooten, J. (2014). Human periosteal-derived cell expansion in a perfusion bioreactor system: proliferation, differentiation and extracellular matrix formation. *J Tissue Eng Regen Med*.
- Spencer, T. J., Hidalgo-Bastida, L. A., Cartmell, S. H., Halliday, I., and Care, C. M. (2013). In silico multi-scale model of transport and dynamic seeding in a bone tissue engineering perfusion bioreactor. *Biotechnology and Bioengineering*, 110(4):1221–1230.
- Spitters, T. W., Mota, C. M., Uzoechi, S. C., Slowinska, B., Martens, D. E., Moroni, L., and Karperien, M. (2014). Glucose gradients influence zonal matrix deposition in 3d cartilage constructs. *Tissue Engineering Part A*, 20(23-24):3270–3278.
- Stiehler, M., Banger, C., Baatrup, A., Lind, M., Kassem, M., and Mygind, T. (2009). Effect of dynamic 3d culture on proliferation, distribution, and osteogenic differentiation of human mesenchymal stem cells. *Journal of Biomedical Materials Research Part A*, 89(1):96–107.
- Tijskens, E., Ramon, H., and De Baerdemaeker, J. (2003). Discrete element modelling for process simulation in agriculture. *Journal of sound and vibration*, 266(3):493–514.
-

- Tinevez, J.-Y., Schulze, U., Salbreux, G., Roensch, J., Joanny, J.-F., and Paluch, E. (2009). Role of cortical tension in bleb growth. *Proceedings of the National Academy of Sciences*, 106(44):18581–18586.
- Truscello, S., Schrooten, J., and Van Oosterwyck, H. (2011). A computational tool for the upscaling of regular scaffolds during in vitro perfusion culture. *Tissue Engineering Part C: Methods*, 17(6):619–630.
- U.S.-FDA (2014). Reporting of computational modeling studies in medical device submissions - draft guidance for industry and food and drug administration staff. Technical report, U.S. Food and Drug Administration.
- Vaez Ghaemi, R., Vahidi, B., Sabour, M. H., Haghighipour, N., and Alihemmati, Z. (2015). Fluid structure interactions analysis of shear induced modulation of a mesenchymal stem cell: An image based study. *Artificial Organs*.
- Van Bael, S., Chai, Y. C., Truscello, S., Moesen, M., Kerckhofs, G., Van Oosterwyck, H., Kruth, J. P., and Schrooten, J. (2012). The effect of pore geometry on the in vitro biological behavior of human periosteum-derived cells seeded on selective laser-melted ti6al4v bone scaffolds. *Acta Biomater*, 8(7):2824–34.
- Van Bael, S., Kerckhofs, G., Moesen, M., Pyka, G., Schrooten, J., and Kruth, J. P. (2011). Micro-ct-based improvement of geometrical and mechanical controllability of selective laser melted ti6al4v porous structures. *Materials Science and Engineering a-Structural Materials Properties Microstructure and Processing*, 528(24):7423–7431.
- van Gastel, N., Depypere, M., Stockmans, I., Schrooten, J., Maes, F., Luyten, F., and Carmeliet, G. (2012). Interactions between periosteal cells and blood vessels during bone autograft healing: implications for tissue engineering strategies. *Journal of Tissue Engineering and Regenerative Medicine*, 6(1):310–310.
- van Lenthe, G. H., Hagenmüller, H., Bohner, M., Hollister, S. J., Meinel, L., and Müller, R. (2007). Nondestructive micro-computed tomography for biological imaging and quantification of scaffold–bone interaction in vivo. *Biomaterials*, 28(15):2479–2490.
- Vaughan, T., Mullen, C., Verbruggen, S., and McNamara, L. (2014). Bone cell mechanosensation of fluid flow stimulation: a fluid–structure interaction model characterising the role integrin attachments and primary cilia. *Biomechanics and modeling in mechanobiology*, pages 1–16.
- Vaughan, T., Voisin, M., Niebur, G., and McNamara, L. (2015). Multiscale modeling of trabecular bone marrow: Understanding the micromechanical environment of mesenchymal stem cells during osteoporosis. *Journal of biomechanical engineering*, 137(1):011003.
-

- Verbruggen, S. W., Vaughan, T. J., and McNamara, L. M. (2014). Fluid flow in the osteocyte mechanical environment: a fluid-structure interaction approach. *Biomech Model Mechanobiol*, 13(1):85–97.
- Viceconti, M., Morley-Fletcher, E., Henney, A., Contin, M., El-Arifi, K., McGregor, C., Karlström, A., and Wilkinson, E. (2015). In silico clinical trials: How computer simulation will transform the biomedical industry, avicenna – a strategy for in silico clinical trials.
- Volkmer, E., Drosse, I., Otto, S., Stangelmayer, A., Stengele, M., Kallukalam, B. C., Mutschler, W., and Schieker, M. (2008). Hypoxia in static and dynamic 3d culture systems for tissue engineering of bone. *Tissue Engineering Part A*, 14(8):1331–1340.
- Voronov, R., Vangordon, S., Sikavitsas, V. I., and Papavassiliou, D. V. (2010). Computational modeling of flow-induced shear stresses within 3d salt-leached porous scaffolds imaged via micro-ct. *J Biomech*, 43(7):1279–86.
- Voronov, R. S., Vangordon, S. B., Shambaugh, R. L., Papavassiliou, D. V., and Sikavitsas, V. I. (2012). 3d tissue engineered construct analysis via conventional high resolution microct without x-ray contrast. *Tissue Eng Part C Methods*.
- Wang, X., Wenk, E., Zhang, X., Meinel, L., Vunjak-Novakovic, G., and Kaplan, D. L. (2009). Growth factor gradients via microsphere delivery in biopolymer scaffolds for osteochondral tissue engineering. *Journal of Controlled Release*, 134(2):81–90.
- Wang, Y.-K. and Chen, C. S. (2013). Cell adhesion and mechanical stimulation in the regulation of mesenchymal stem cell differentiation. *Journal of cellular and molecular medicine*, 17(7):823–832.
- Weinbaum, S., Cowin, S., and Zeng, Y. (1994). A model for the excitation of osteocytes by mechanical loading-induced bone fluid shear stresses. *Journal of biomechanics*, 27(3):339–360.
- Wendt, D., Marsano, A., Jakob, M., Heberer, M., and Martin, I. (2003). Oscillating perfusion of cell suspensions through three-dimensional scaffolds enhances cell seeding efficiency and uniformity. *Biotechnology and bioengineering*, 84(2):205–214.
- Whittaker, R. J., Booth, R., Dyson, R., Bailey, C., Parsons Chini, L., Naire, S., Payvandi, S., Rong, Z., Woollard, H., Cummings, L. J., Waters, S. L., Mawasse, L., Chaudhuri, J. B., Ellis, M. J., Michael, V., Kuiper, N. J., and Cartmell, S. (2009). Mathematical modelling of fibre-enhanced perfusion inside a tissue-engineering bioreactor. *J Theor Biol*, 256(4):533–46.
-

- Williams, K. A., Saini, S., and Wick, T. M. (2002). Computational fluid dynamics modeling of steady state momentum and mass transport in a bioreactor for cartilage tissue engineering. *Biotechnology progress*, 18(5):951–963.
- Wuertz, K., Godburn, K., and Iatridis, J. C. (2009). Msc response to ph levels found in degenerating intervertebral discs. *Biochem Biophys Res Commun*, 379(4):824–9.
- Yang, L., Effler, J. C., Kutscher, B. L., Sullivan, S. E., Robinson, D. N., and Iglesias, P. A. (2008). Modeling cellular deformations using the level set formalism. *BMC Syst Biol*, 2:68.
- Yeatts, A. B. and Fisher, J. P. (2011). Bone tissue engineering bioreactors: dynamic culture and the influence of shear stress. *Bone*, 48(2):171–181.
- Yu, X., Botchwey, E. A., Levine, E. M., Pollack, S. R., and Laurencin, C. T. (2004). Bioreactor-based bone tissue engineering: the influence of dynamic flow on osteoblast phenotypic expression and matrix mineralization. *Proceedings of the National Academy of Sciences of the United States of America*, 101(31):11203–11208.
- Zeltinger, J., Landeen, L. K., Alexander, H. G., Kidd, I. D., and Sibanda, B. (2001a). Development and characterization of tissue-engineered aortic valves. *Tissue Eng*, 7(1):9–22.
- Zeltinger, J., Sherwood, J. K., Graham, D. A., Mueller, R., and Griffith, L. G. (2001b). Effect of pore size and void fraction on cellular adhesion, proliferation, and matrix deposition. *Tissue Eng*, 7(5):557–72.
- Zeng, Y., Cowin, S., and Weinbaum, S. (1994). A fiber matrix model for fluid flow and streaming potentials in the canaliculi of an osteon. *Annals of biomedical engineering*, 22(3):280–292.
- Zermatten, E., Vetsch, J. R., Ruffoni, D., Hofmann, S., Müller, R., and Steinfeld, A. (2014). Micro-computed tomography based computational fluid dynamics for the determination of shear stresses in scaffolds within a perfusion bioreactor. *Annals of biomedical engineering*, 42(5):1085–1094.
- Zhang, J., Johnson, P. C., and Popel, A. S. (2009). Effects of erythrocyte deformability and aggregation on the cell free layer and apparent viscosity of microscopic blood flows. *Microvasc Res*, 77(3):265–72.
- Zhang, X., Awad, H. A., O’Keefe, R. J., Guldberg, R. E., and Schwarz, E. M. (2008). A perspective: engineering periosteum for structural bone graft healing. *Clin Orthop Relat Res*, 466(8):1777–87.
- Zhao, F. and Ma, T. (2005). Perfusion bioreactor system for human mesenchymal stem cell tissue engineering: dynamic cell seeding and construct development. *Biotechnology and bioengineering*, 91(4):482–493.
-

-
- Zhao, F., Vaughan, T. J., and McNamara, L. M. (2014). Multiscale fluid-structure interaction modelling to determine the mechanical stimulation of bone cells in a tissue engineered scaffold. *Biomech Model Mechanobiol*.
- Zhao, F., Vaughan, T. J., and McNamara, L. M. (2015). Quantification of fluid shear stress in bone tissue engineering scaffolds with spherical and cubical pore architectures. *Biomechanics and modeling in mechanobiology*, pages 1–17.
- Zhou, X., Holsbeeks, I., Impens, S., Sonnaert, M., Bloemen, V., Luyten, F., and Schrooten, J. (2013). Noninvasive real-time monitoring by alamarblue((r)) during in vitro culture of three-dimensional tissue-engineered bone constructs. *Tissue Eng Part C Methods*, 19(9):720–9.
-

APPENDIX A

REINITIALIZATION OF THE LEVEL-SET WITH *MSHDIST*

In this section, the reinitialization procedure of the level-set function using *mshdist* is described. Generally, advecting a signed distance function will distort the level set, making the gradient too flat (low) or too steep (high) near the interface. This could cause changes in the interface location and loss of regularity, potentially resulting in numerical errors. To tackle this issue, it is necessary to reinitialize the level set function to a signed distance function. For this purpose, the free software *mshdist* (Dapogny and Frey, 2012) was used. The software takes a function with a zero level as input, and outputs a signed distance function with preservation of the interface. Practically, this procedure was periodically used in the neotissue growth model. For every added percent of scaffold filling, the re-initialization procedure was run and a new distance function was computed.

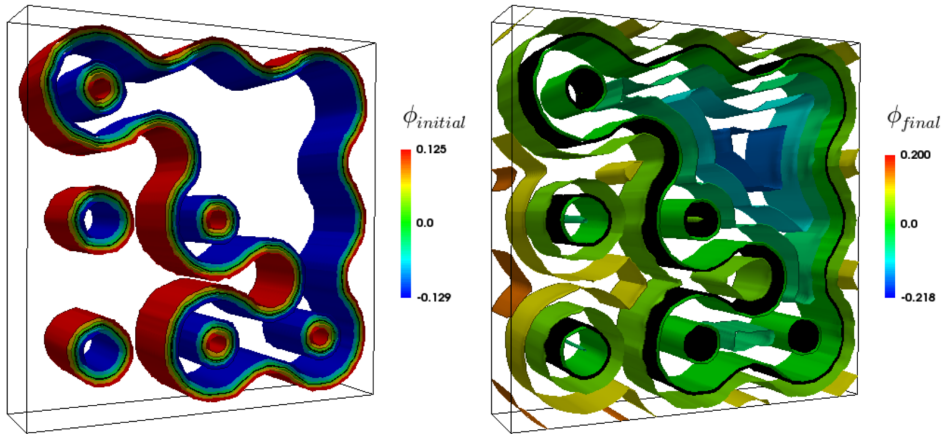


Figure A.1: Illustration of the reinitialization of the level-set with *mshdist*. **(Left)** initial configuration with the interface in black in the 3D Prometheus logo. **(Right)** output of *mshdist*, a signed distance function is propagated from the interface

APPENDIX B

TRIPLY PERIODIC MINIMAL SURFACE SCAFFOLD GENERATION

In order to generate the complex scaffold geometries introduced in chapter 7, a procedure has been developed using FreeFem++, *mshdist* (see appendix A) and *mmg3d-v5* (Dapogny et al., 2014) as shown in Fig. B.1. First of all, the equation corresponding to the desired geometry is projected on a homogenous cylinder mesh. Subsequently, a signed distance function to the zero level is calculated using *mshdist*. After taking the absolute value of the opposite of the distance function, adding a value corresponding to the scaffold struts thickness and “cutting” top and bottom with suitable function, a final distance function to the scaffold surface is calculated. Thanks to *mmg3d-v5*, a mesh conform to the scaffold surface is generated, and, using the FreeFem++ function “trunc”, the volume corresponding to the scaffold is removed. Finally a remeshing procedure (also using *mmg3d-v5*) is applied to have a fine mesh within the scaffold region and a coarser mesh outside of the scaffold region.

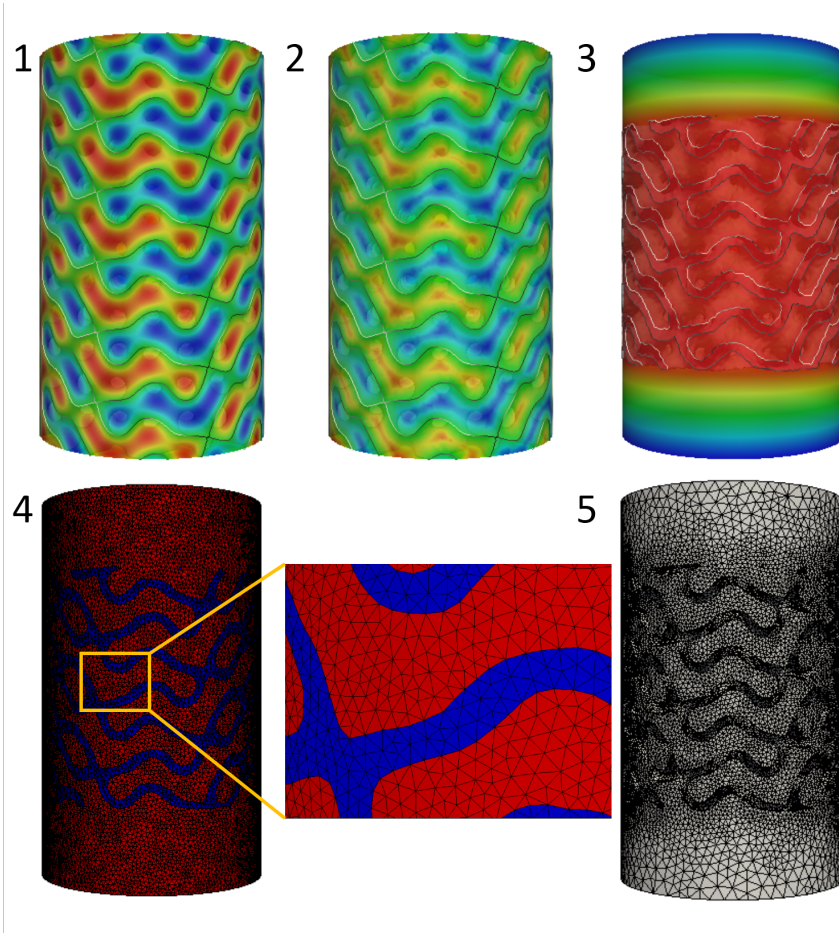


Figure B.1: Overall process to generate the $G7$ scaffold and computational domain presented in chapter 7. **(1)** Projection of the corresponding equation on a regular homogenous mesh. **(2)** A distance function to the zero level is calculated. **(3)** Projection of a distance function to the interface representing the scaffold. **(4)** Generation of a conform mesh to the scaffold interface thanks to *mmg3d-v5*. **(5)** Remeshing of the final computational mesh.

APPENDIX C

ALGORITHM FOR MODEL PRESENTED IN CHAPTER 7

In order to better understand the implementation of the model described in chapter 7, the following algorithm is introduced.

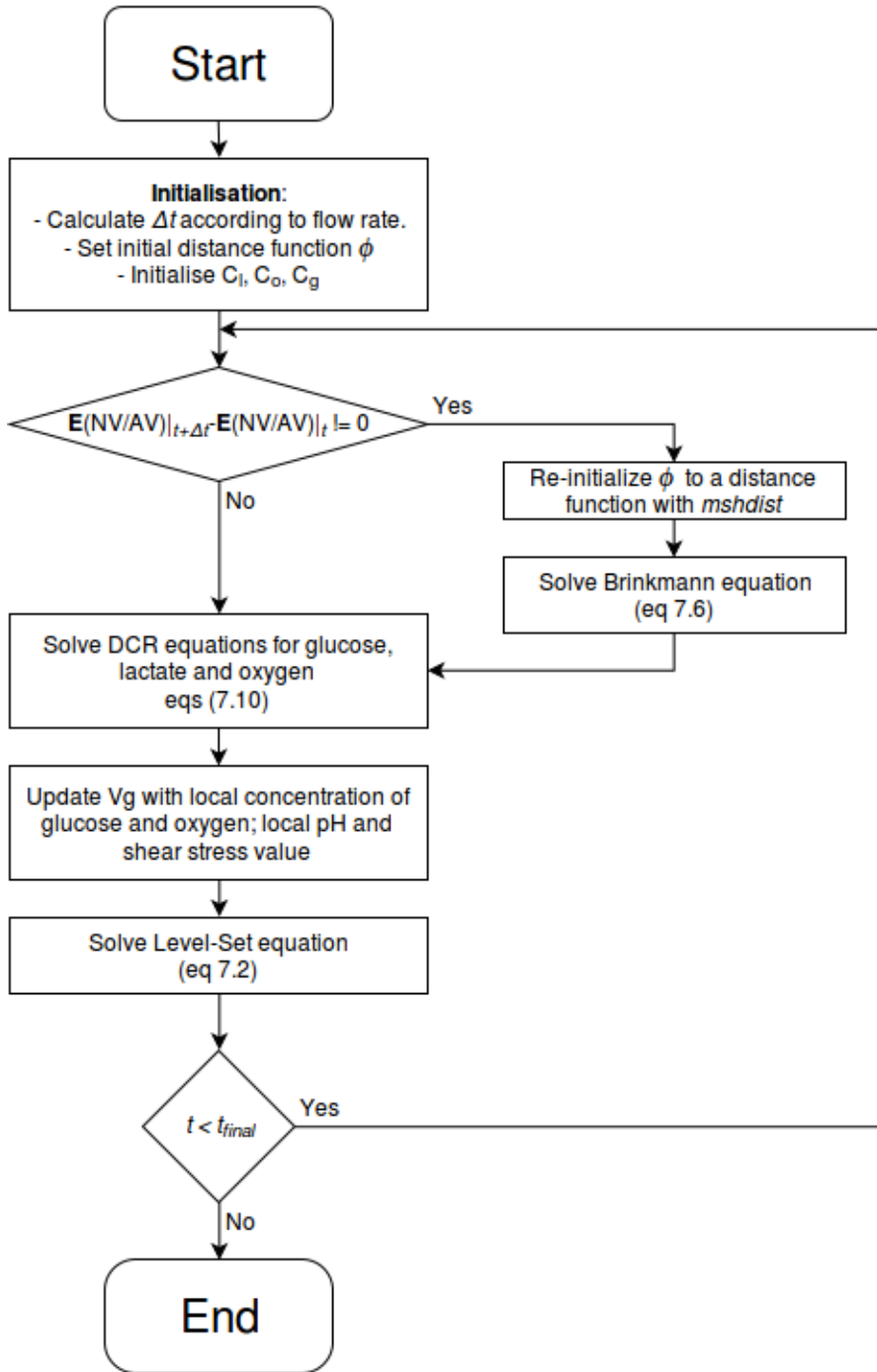


Figure C.1: Algorithm for model presented in chapter 7.

APPENDIX D

DEFORMABLE CELL MODEL

In order to better describe the deformable cell model presented in chapter 8, the following section is extracted from the Materials & Methods in (Odenthal et al., 2013).

D.1 Elastic model of the cortex

In the deformable cell model, the cortex nodes interact through viscoelastic potentials. In the most simple approach, a linear elastic spring could be used. For a given displacement of nodes i and j , the elastic spring force over a connection is:

$$F_{\text{Linear}} = k_s (d_{ij} - d_{ij}^*), \quad (\text{D.1})$$

in which d_{ij} and d_{ij}^* are the actual distance and equilibrium distance between connected node i and j . The linear spring stiffness is called k_s . For red blood cells, two non-linear spring models have been used in literature: the finite extensible non-linear elastic model (FENE) and the worm-like chain model (WLC) (Fedosov et al., 2010). These models express that upon stretching, the biopolymers of the cytoskeleton – a sub-membranous network of spectrin connections for RBCs – first uncoil, providing relatively little resistance, but when completely stretched out, become practically non-extensible.

Between two connected nodes i and j , the FENE attractive potential reads:

$$U_{\text{FENE}} = -\frac{k_s}{2} d_{\text{max}}^2 \log \left[1 - \left(\frac{d_{ij}}{d_{\text{max}}} \right)^2 \right], \quad (\text{D.2})$$

where d_{max} is the maximal distance, and k_s the stretching constant. The force derived from this is:

$$F_{\text{FENE}} = -k_s d_{ij} \left[1 - \left(\frac{d_{ij}}{d_{\text{max}}} \right)^2 \right]^{-1}. \quad (\text{D.3})$$

It is convenient to denote the term $\frac{d_{\text{max}}}{d_{ij}^*}$ by x_{max} , the fraction of maximal extension and equilibrium distance.

FENE springs exert purely attractive forces. In order to account for the (limited) incompressibility of the spectrin, a simple power law is used (power L):

$$F_{\text{POW}} = \frac{k_c}{d_{ij}^L} \quad (\text{D.4})$$

The incompressibility coefficient k_c can be derived for the assumption that the total force must vanish for $d_{ij} \equiv d_{ij}^*$:

$$k_c = k_s (d_{ij}^*)^{L+1} \left[1 - \left(\frac{d_{ij}^*}{d_{\text{max}}} \right)^2 \right]^{-1} \quad (\text{D.5})$$

In the present model, we set $L = 2$, as suggested by (Fedosov et al., 2010). In addition to this purely elastic potential, we also include dissipation as per the Kelvin-Voigt model by adding a parallel dashpot with the damping constant c :

$$F_{\text{Dashpot}} = -c \hat{n}_{ij} \cdot \vec{v}_{ij}. \quad (\text{D.6})$$

Here, $\hat{n}_{ij} \cdot \vec{v}_{ij}$ is the projection of the relative velocity of a pair of connected cortex nodes on their connecting axis. The force is also applied in the direction of the connection.

Whereas in-plane stretching and compressive forces can be calculated purely based on the distance between two neighboring cortex nodes, bending forces are calculated for two neighboring triangles. The bending moment between two adjacent triangles is given as

$$M = k_b \sin(\theta - \theta^*). \quad (\text{D.7})$$

Here, k_b is the model parameter determining the bending rigidity, θ is the instantaneous angle and θ^* the spontaneous angle between a pair of triangles with a common edge. A corresponding force is applied to the non-common points of each of the two triangles, with a compensating force applied to the points on the common edge, ensuring that the total force on the cell remains unchanged. This type of bending-stiffness is commonly found in the literature for RBC models, eg. by (Fedosov et al., 2011) and (Discher et al., 1998) - a more general analysis is provided by (Boal and Rao, 1992).

Additionally, both a global and local area constraint is used, making sure that both the individual triangle areas and the total area of the red blood cell can not strongly increase or decrease. As described by (Fedosov et al., 2011), this is achieved by a local force with magnitude:

$$F_{A,\text{local}} = k_a(A - A^*), \quad (\text{D.8})$$

in which A is the triangle area, A^* the resting triangle area and k_a the local constraint constant. The magnitude of the global force is formulated as:

$$F_{A,\text{global}} = k_d(A_{\text{tot}} - A_{\text{tot}}^*), \quad (\text{D.9})$$

where A_{tot} is the total RBC area, A_{tot}^* the total resting area and k_d the global constraint constant. For both constants, values were taken from (Fedosov et al., 2010). These forces are applied in the plane of each triangle in the direction from the barycenter of the triangle.

Finally, we add a volume constraint since for short timescales, the total cytosol volume of the cell can be considered constant. As for the area, magnitude of the force takes the form

$$F_{\text{volume}} = k_V(V - V^*), \quad (\text{D.10})$$

with the instantaneous cell volume V and the initial cell volume V^* .

CURRICULUM VITAE

Personal data

Name: Yann Guyot
Date and place of birth: 05/12/1986, Tours, France
Address: rue César Franck, 11, 4000, Liège
Tel: +32 4 91 22 97 17
Email: yguyot@ulg.ac.be

Education

2011-2015: PhD student at the Biomechanics Research Unit, University of Liège, Liège, Belgium
2011: Internship at Liphy (Interdisciplinary Laboratory of Physics), University Joseph Fourier, Grenoble, France.
Thesis: 'Modeling and numerical simulations of two-phase flow'
2009-2011: Master of Mathematics, Modeling and Simulation, University of Pau et des pays de l'Adour, Pau, France
2006-2009: Bachelor of Applied Mathematics, University Paris 7 Denis Diderot, Paris, France

Awards

Finalist for the European Society of Biomechanics (ESB) student award for : **Guyot, Y.**, Papantoniou, I., Schrooten, J., & Geris, L. (2014, July). A Multiphysics approach to calculate shear stresses during neotissue growth in perfusion bioreactor. Paper presented at 7th world congress of biomechanics, Boston, USA.

Bibliography

Articles in internationally reviewed academic journals

Guyot, Y., Smeets, B., Odenthal, T., Subramani, R., Luyten, F., Ramon, H., Papantoniou, I. & Geris, L., Immersed Boundary Models for quantifying flow-Induced mechanical stimuli on stem cells seeded on 3d scaffolds in perfusion bioreactors. *PLoS Computational Biology*. Submitted.

Guyot, Y.; Papantoniou, I.; Luyten, F. P. & Geris, L. Coupling curvature-dependent and shear stress stimulated neotissue growth in dynamic bioreactor cultures: a 3D computational model of a complete scaffold. *Biomechanics and modeling in mechanobiology*. Accepted for publication.

Guyot, Y., Luyten, F. P., Schrooten, J., Papantoniou, I., & Geris, L. (2015). A three-dimensional computational fluid dynamics model of shear stress distribution during neotissue growth in a perfusion bioreactor. *Biotechnology and bioengineering*, 112(12), 2591-2600.

Guyot, Y., Papantoniou, I., Chai, Y. C., Van Bael, S., Schrooten, J., & Geris, L. (2014). A computational model for cell/ECM growth on 3D surfaces using the level set method: a bone tissue engineering case study. *Biomechanics and modeling in mechanobiology*, 13(6), 1361-1371.

Papantoniou, I., **Guyot, Y.**, Sonnaert, M., Kerckhofs, G., Luyten, F. P., Geris, L., & Schrooten, J. (2014). Spatial optimization in perfusion bioreactors improves bone tissueengineered construct quality attributes. *Biotechnology and bioengineering*, 111(12), 2560-2570.

Doyeux, V., **Guyot, Y.**, Chabannes, V., Prud'Homme, C., & Ismail, M. (2013). Simulation of two-fluid flows using a finite element/level set method. Application to bubbles and vesicle dynamics. *Journal of Computational and Applied Mathematics*, 246, 251-259.

Meeting abstracts, presented at international and local conferences and symposia

Guyot, Y., Papantoniou, I., Schrooten, J., & Geris, L. (2014, October). Investigation of shear stress evolution during neotissue growth in a perfusion bioreactor using 3d multiphysics modeling. Paper presented at 12th International Symposium on Computer Methods in Biomechanics and Biomedical Engineering, Amsterdam, Netherlands.

Manhas, V., **Guyot, Y.**, Chai, Y. C., Kerckhofs, G., Schrooten, J., & Geris, L. (2014, October). Investigating local Ca²⁺ concentration in calcium phosphate scaffolds for bone tissue engineering applications. Paper presented at 12th International Symposium: Computer Methods in Biomechanics and Biomedical Engineering, Amsterdam, Netherlands.

Guyot, Y., Papantoniou, I., Schrooten, J., & Geris, L. (2014, September). A Multiphysics model of neotissue growth in a perfusion bioreactor. Paper presented at Virtual Physiological Human Conference 2014, Trondheim, Norway.

Guyot, Y., Papantoniou, I., Schrooten, J., & Geris, L. (2014, July). 3D Modeling of shear stress development during neotissue growth in a perfusion bioreactor. Paper presented at 11th world congress on computational mechanics, Barcelona, Spain.

Guyot, Y., Papantoniou, I., Schrooten, J., & Geris, L. (2014, July). A Multiphysics approach to calculate shear stresses during neotissue growth in perfusion bioreactor. Paper presented at 7th world congress on biomechanics, Boston, USA.

Manhas, V., **Guyot, Y.**, Chai, Y. C., Kerckhofs, G., Schrooten, J., & Geris, L. (2014, June). In silico assessment of local Ca²⁺ concentrations in calcium phosphate scaffolds for bone tissue engineering. Poster session presented at 7th World Congress of Biomechanics, Boston, USA.

Manhas, V., **Guyot, Y.**, Chai, Y. C., Kerckhofs, G., & Geris, L. (2013, October 24). Assessing local Ca²⁺ concentrations in calcium phosphate scaffolds by computational modeling. Poster session presented at 2nd Belgian Symposium on Tissue Engineering, Leuven, Belgium.

Guyot, Y., Papantoniou, I., Chai, Y. C., Schrooten, J., & Geris, L. (2013, October). Modeling cell/matrix growth in three dimensional scaffolds under dynamic culture conditions. Paper presented at Belgium symposium of tissue engineering. Leuven, Belgium.

Guyot, Y., Papantoniou, I., Chai, Y. C., Schrooten, J., & Geris, L. (2013, September 11). A Model for cell/ECM growth on 3D surface: a coupling of level set method and brinkman equation. Paper presented at International Conference on Computational Bioengineering, Leuven, Belgium.

Guyot, Y., Papantoniou, I., Chai, Y. C., Schrooten, J., & Geris, L. (2013, August 26). Multiphysics modeling of cell/matrix growth on 3D structures. Paper presented at European Society of Biomechanics. Patras, Greece.

Guyot, Y., Papantoniou, I., Chai, Y. C., Van Bael, S., Schrooten, J., & Geris, L. (2013, April 03). A Mathematical model for cell/matrix growth on 3D surfaces using the level set method. Paper presented at CMBBE, Salt Lake City, USA.

Guyot, Y., Papatoniou, I., Chai, Y. C., Van Bael, S., Schrooten, J., & Geris, L. (2012, September). Mathematical Level-Set Modelling of Cell Growth on 3D Surfaces. Poster session presented at Belgian symposium for tissue engineering, Leuven, Belgium.



Prometheus, Division of Skeletal Tissue Engineering
KU Leuven
<http://www.mtm.kuleuven.be/Prometheus>

Biomechanics Research Unit,
University of Liège
yguyot@ulg.ac.be
<http://www.biomech.ulg.ac.be>

